SCUOLA DI DOTTORATO
UNIVERSITÀ DEGLI STUDI DI MILANO-BICOCCA

Dipartimento di

MATEMATICA E APPLICAZIONI

Dottorato di Ricerca in MATEMATICA   Ciclo XXXV

Curriculum in FISICA MATEMATICA

Mathematical Models of the Lymph Flow: Analysis and Simulations

Cognome: Girelli   Nome: Alberto

Matricola: 861031

Supervisore: Prof. Alessandro Musesti

Coordinatore: Prof. Pierluigi Colli

ANNO ACCADEMICO 2021/2022

Abstract

The lymphatic system is an important component of the circulatory network, responsible for the transportation of interstitial fluid throughout the body. The interstitial fluid is called *lymph* when inside the lymphatics. The movement of lymph plays a key role in transporting immune cells, proteins, cancer metastasis, drugs, and so on. Moreover, impaired lymph transport can result in lymphœdema, a condition that consists of an accumulation of interstitial fluid in the tissues.

The goal of this thesis is to develop mathematical models that describe the lymph behavior in the lymphatic system, in particular its flow through lymphangions and lymph nodes. We analyze these models, solve them explicitly in simplified geometries, and propose numerical simulations to handle more general scenarios.

First of all, we propose a model of the lymph flow in a lymphangion, that is the part of the lymphatic vessel between two valves. Due to its geometry, we are able to develop a 1D model using the theory of quasilinear hyperbolic systems. Several models try to describe the lymph flow in a lymphangion; we proposed a model with a phenomenological description of the wall behavior, taking into account the shear stress inhibition and regulation phenomena related to the contractions.

After that, we focus most of our attention to model the lymph flow through a lymph node because, to our knowledge, it has not been extensively explored from a mechanical perspective. Moreover, there is evidence that the lymph nodes are essential for regulating lymph transport due to the fluid exchange with the blood vessels within them. Indeed, secondary lymphœdema often results from damage to or removal of lymph nodes. Due to the complex structure and functioning of the lymph node, the attempt to describe the motion of the lymph within it has inspired us with some very interesting mathematical models which have been worth studying in detail.

Sommario

Il sistema linfatico è una componente importante del sistema circolatorio, responsabile del trasporto del fluido interstiziale in tutto il corpo. Il fluido interstiziale si chiama *linfa* quando si trova all'interno del sistema linfatico. Il movimento della linfa svolge un ruolo chiave nel trasporto di cellule immunitarie, proteine, metastasi tumorali, farmaci e così via. Inoltre, un trasporto linfatico compromesso può causare linfedema, una patologia che consiste in un accumulo di fluido interstiziale nei tessuti.

L'obiettivo di questa tesi è quello di sviluppare modelli matematici che descrivono il comportamento della linfa nel sistema linfatico, in particolare il suo flusso attraverso linfangioni e linfonodi. Analizziamo questi modelli, li risolviamo esplicitamente in geometrie semplificate e proponiamo simulazioni numeriche per affrontare scenari più generali.

Innanzitutto proponiamo un modello del flusso linfatico in un linfangione, cioè la parte del vaso linfatico compresa tra due valvole. Grazie alla sua geometria, siamo in grado di sviluppare un modello 1D utilizzando la teoria dei sistemi iperbolici quasilineari. Diversi modelli tentano di descrivere il flusso linfatico in un linfangione; abbiamo proposto un modello con una descrizione fenomenologica del comportamento della parete, tenendo conto dei fenomeni di inibizione e regolazione dello shear stress legati alle contrazioni.

Successivamente, ci concentriamo nel modellare il flusso linfatico attraverso un linfonodo perché, per quanto ci risulta, non è stato ampiamente esplorato da un punto di vista meccanico. Inoltre, alcune evidenze suggeriscono che i linfonodi sono essenziali per la regolazione del trasporto della linfa a causa dello scambio di fluidi con i vasi sanguigni al loro interno. In effetti, il linfedema secondario spesso deriva dal danneggiamento o dalla rimozione dei linfonodi. A causa della struttura e del funzionamento complessi del linfonodo, abbiamo elaborato alcuni modelli matematici interessanti per descrivere il movimento della linfa all'interno di esso, che è stato interessante approfondire.

Acknowledgements

I would like to take this opportunity to express my sincere gratitude to everyone who has supported and inspired me throughout my PhD.

First and foremost, I would like to express my deepest gratitude to my supervisor Prof. Alessandro Musesti and to Prof. Giulia Giantesio for their invaluable support and guidance throughout my research and my PhD journey. Their expert knowledge and indispensable feedback were fundamental in helping me complete this work and to overcome numerous challenges along the way.

I am also grateful to Prof. Raimondo Penta for giving me the opportunity to have a wonderful experience in Glasgow and for his precious collaboration that considerably enriched this work and made a significant contribution to my academic growth.

I would like to express my gratitude to the thesis referees for their constructive criticism, which has significantly contributed to improving the quality of my thesis.

I am thankful to my friends for sharing with me the most important experiences over the years and providing me with much-needed breaks from academic work.

Finally, I would like to thank my family for their love and encouragement throughout my PhD. Their belief in me and my abilities has been a constant source of motivation and inspiration.

To the staff of the department of "Trapianto Midollo Osseo/Ematologia" of the "Spedali Civili di Brescia", in the hopes that this work may contribute in some way to the advancement of knowledge of the lymphatic system.

Introduction

Motivation of the Thesis

The lymphatic system is a crucial component of the circulatory system, responsible for lymph transport throughout the body. Lymph flow plays a crucial role in transporting immune cells, proteins, cancer metastasis, drugs, and so on. Moreover, inadequate lymph transport leads to lymphœdema, a condition that consists of an accumulation of interstitial fluid in the tissues, leading to distension, inflammation, fatty tissue proliferation, and fibrosis [1]. Despite its importance, the study of the lymphatic system has received much less attention than the study of the blood circulation system, particularly in the realm of mathematical modeling. Mathematical models of the blood circulation system have been extensively researched and developed over the years, providing valuable insights into the dynamics and functions of this system (see [2]). Instead [3], one of the first mathematical models of the lymphatic vessels, was published only in 1975.

The scope of this thesis is to propose and analyze mathematical models that describe the lymph flow through the lymphatic system, in particular through lymphangions and lymph nodes. We direct most of our attention on modeling the lymph flow through a lymph node (LN) because, as far as we know, only a few models in the literature try to describe the behavior of the LN from a mechanical point of view [4–10] or mimic the LN mechanical properties in a LN-on-a-chip model [11–13]. The intricate structure and function of the lymph node have generated interesting mathematical questions about the lymphatic flow within it, making it a valuable subject for detailed study. The mathematical models in this thesis are designed to be as general as possible for potential use in other applications.

However, we also present a model describing the lymph within the lymphangions, taking into account previous works. Indeed, as we mentioned before, the first model of the lymphatic system [3] refers to lymphangions treated as a 0D model. Ref. [14] is the first that takes into account the spatial dimension of the lymphangion using a 1D simplified model. In [15–18] they use a 0D model solved taking into account real physiological data obtained by experiments. The 1D extension of these models using the theory of quasilinear hyperbolic systems is considered in [19–21]. Moreover, some recent works use finite element simulations to take into account more spatial dimensions [22–27], but with several simplifications given by the complexity of the problem. Finally, some models focus more on the wall behavior of the lymphangions [28–30].

Organization of the Thesis

The thesis is organized as follows. In Chapter 2 we recall well-known theoretical aspects that we will use in the entire work. In particular, in Section 2.1 we recall the equations of motion that govern the fluid flow. In Section 2.2 we summarize the main properties and definitions related to the *Gegenbauer functions.* In Section 2.3 we explain some aspects of the axisymmetric flow and stream function given in [31]. In Section 2.4 we recall the *asymptotic homogenization technique* with an example. Finally, in Section 2.5 we use the well-known theory of quasilinear hyperbolic systems to derive the governing equations that describe an incompressible Newtonian fluid flowing in a compliant pipe in 1D.

In Chapter 3 we propose a model of a 1D lymphangion using the theory of quasilinear hyperbolic systems. First of all, we found the critical thresholds, which refer to certain critical values or conditions that determine whether a system will exhibit a global in-time regular smooth solution or whether it will experience a finite-time singularity formation, with a general pressure in a simplified setting (we do not consider the valve behavior). Moreover, we highlight the role of the viscosity μ in the singularity of the solution. After that, we study a general 1D mathematical model that describes the lymphangion. We take into account the valve behavior and the contractions (with the inhibitory effect due to *eNOS*-shear stress) of the lymphangion. We use a largely phenomenological description of the wall behavior; we choose this type of approach because we are more interested in the fluid behavior and we want to run more feasible numerical simulations. In general, there can be other terms that influence and are important for the contraction of the lymphangion wall due to high deformations of the latter and that it would be worth studying in detail [28–30]. The results presented in this chapter are not yet complete, hence they may be subject to future modifications or updates.

In Chapter 4 we advance a mathematical model for the lymph flow in a lymph node in a cylindrical geometry with a laminar flow and driven by a pulsatile pressure gradient [9]. The model proposed here is very idealized and is a starting point for more advanced studies on the subject.

In Chapter 5 we put forward a mathematical model for the flow of the interstitial fluid (lymph) in an idealized spherical and spheroidal popliteal lymph node [10]. We assume a small Reynolds number as a result of the small velocities within the lymph nodes [1], hence we can model the flow into the LC by Darcy-Brinkman equation, and the flow inside the SCS by Stokes equation (see Section 2.1). As we mentioned before, the lymph has a relevant pulsatile behavior, and we take it into account in our model. We obtain an explicit solution in spherical geometry using the stream function approach (see Section 2.3). Then we solve it numerically in a more general setting and geometry (using a numerical scheme validated with the explicit solution).

So far, we did not take into consideration the blood vessels (and the consequent exchange of fluids) inside the lymphoid compartment (LC) of the latter; hence, in Chapter 6 we use the *asymptotic homogenization technique* (see Section 2.4) to couple two different phases: the matrix phase (described by the Darcy-Brinkman equation) and the blood vessel phase (described by the Darcy equation), both in a steady setting, with inhomogeneous body forces. First of all, we analyze the obtained macroscale model in a more general setting. After that, we find an explicit solution in a spherical domain, describing the interaction between the matrix phase and the blood vessel phase in the LC: we analyze this solution with physiological data obtained from the literature of an idealized spherical mouse popliteal lymph node. Moreover, we couple the free-fluid region (the subcapsular sinus, SCS) and the porous region (LC) using numerical simulations.

Finally, in Chapter 7 we present a multiscale model using the asymptotic homogenization technique with a time-dependent Darcy-Brinkman equation that describes the fluid flow in both phases (matrix phase and blood vessel phase) with inhomogeneous body forces as our starting point. We consider the Darcy-Brinkman equation's time dependence because we have that the inlet flow is time-dependent (see Section 1.1). The time-dependent term leads to the macroscopic *Darcy's law with memory* [32, 33]. After that, we solve the problem using numerical simulations. The results presented in this chapter are recent and not yet complete, and we present them as a future research direction.

Contents

Chapter 1

Physiology of the Lymphatic System

The primary function of the lymphatic system is to transport excess *interstitial fluid* from the interstitial space back to the blood circulation, *via* the thoracic duct. Interstitial fluid is mainly composed of water and contains sugars, salts, fatty acids, amino acids, coenzymes, hormones, neurotransmitters, white blood cells, and cell waste products (it accounts for 26% of the water in the human body). Along with the excess interstitial fluid, excess proteins and waste are transported back to circulation [1, 34].

The lymphatic system is composed of a network of vessels, capillaries, and organs [35]. The interstitial fluid (called *lymph* when inside the lymphatics) enters through the small *lymphatic capillaries* (also called *initial* or *terminal lymphatics*); the interstitial fluid absorbed by the terminal lymphatics is pumped by passive and active contractions of the larger lymphatic vessels. These vessels are the results of a gradual combination of the terminal lymphatics, which are called *pre-collectors* and *collectors* lymphatics, *trunks* and *ducts* [34]. Moreover, inside the lymphatic vessels there is a series of *one-way valves* which prevent retrograde flows. The part of the vessel between two valves is called *lymphangion*. Lymphangions can perform rhythmic contractions because their walls are innervated with sympathetic and parasympathetic nerves [28, 29, 34].

The lymphatic system acts as a priority way for the carriage of the immune cells, facilitating the immune response, and it plays an important role in the dissemination of cancer and transplantation [34, 36]. Indeed, the lymphatic system is an integral part of the immune system thanks to the *lymph nodes*: they are organs scattered all across the lymphatic system and their function is to filter the interstitial fluid and break down bacteria, viruses, and waste [34, 37].

Lymph transport has an important function in transporting immune cells, proteins, cancer metastasis, and so on [12, 37]. The lymphatic system can be a route to deliver drugs to the lymph nodes (LNs) in case of certain pathologies; recent evidence shows that nanotechnology is one of the main approaches to improve the lymphatic uptake of drugs [38].

Inadequate lymph transport can lead to a condition called lymphœdema, where excess interstitial fluid accumulates in the tissues, causing swelling, inflammation, an increase in fatty tissue, and fibrosis [1]. This condition can be caused by congenital disorders (primary lymphœdema), or damage to or removal of lymph nodes (secondary lymphœdema) [39]. This is one of the diseases that emphasizes the importance of studying the lymph flow through the whole lymphatic system.

We refer to [1, 34, 35, 37] to have a more detailed review of the lymph flow in the lymphatic system.

1.1 Lymphatic Vessels

The lymphatic vessels are divided into three macro-categories: *lymphatic capillaries* (or *terminal lymphatics*), *pre-collecting lymphatics*, and *collecting lymphatics* [34]. The primary function of the lymphatic capillaries is to act as a one-way valve system, allowing interstitial fluid to flow into them from the interstitial space when the interstitial pressure is high and then to close in order to stop back-flow when the interstitial pressure is low [40]; they are supported by anchoring filaments ($6 - 10$ nm in diameter) that help them not to collapse when interstitial fluid pressure increases [34].

The interstitial fluid that is drained by the lymphatic capillaries flows into the *pre-collecting lymphatics*. The walls of the pre-collectors are formed by smooth muscle that allows these vessels to perform spontaneous contractions. However, portions without muscle exist, and in these parts, the endothelial layer is similar to that of lymphatic capillaries; thus, these parts of pre-collectors are allowed to absorb fluid. So, the pre-collectors have a dual role: absorption and propulsion of lymph. Moreover, the pre-collecting lymphatics contain bicuspid one-way valves like the capillary vessels, but their distribution is more irregular [34].

From the pre-collecting lymphatics the lymph goes to the *collecting lymphatics*. These vessels are larger than the pre-collecting and initial lymphatics, and the primary lymphatic valves are absent. They contain another type of valve that prevents retrograde flow: the *secondary valve* [34].

The mechanical behavior of lymphatic vessels is nonlinear, nearly elastic, and varies in properties between different regions. They also have a tendency to experience large deformation under normal physiological loading [28, 41].

The lymphatic vessel wall is lined by *lymphatic endothelial cells* (LECs), specialized cells of the lymphatic system [30, 37].

The part of the vessel between two valves is known as *lymphangion* (Figure 1.1). Lymphangions are innervated with sympathetic and parasympathetic nerves that can perform rhythmic contractions. Lymphangions are essential in the regulation of the lymph flow through the lymphatic system: indeed, the combination of lymphangion contractions and valves action is the main feature that helps fluid to move against a pressure gradient given by the pulsation of the heart and to return into the blood circulation [1, 19, 34].

Collecting lymphatics contraction begins when tension (rather than stretch) surpasses a threshold [1]. The frequency and strength of the contraction depend on a lot of factors, such as the circumferential stretch of the vessel wall and the wall shear stress [19, 28, 29, 41, 43].

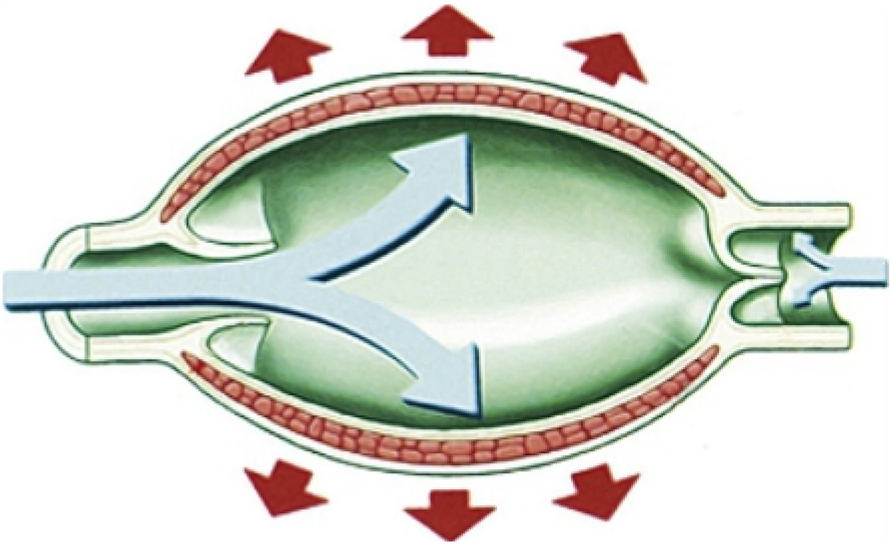

Figure 1.1: A schematic image of a lymphangion, taken from [34, 42].

The lymphangion has a pump-conduit dual role. When the lymph flows against an adverse pressure gradient, it has a pump behavior: it means that the lymphangion contracts and pushes the lymph towards the next lymphangion, and the valves prevent retrograde flow given by this adverse pressure gradient. Instead, if there is a favorable pressure gradient, the contractions are inhibited by *nitric oxide NO* and the lymphangion has a conduit function [18, 43]. The most important sources of *NO* in the lymphatic system (and in particular in the lymphangions) are [30]:

- *eNOS*: production of *NO* via *lymphatic endothelial cells* (LECs) due to the shear stress;
- *iNOS*: production of *NO* via *inducible NO synthase* in immune cells [44, 45];
- *nNOS*: production via nerve tissue.

The inhibition is motivated by the fact that, if we have a favorable pressure gradient, the contractions of the lymphangion wall can be an obstacle that leads to non-optimal fluid transport.

The secondary lymphatic valves that are in the collecting lymphatic vessels (and separate the lymphangions) have a complex structure and functionality. These valves are biased to stay open, and the threshold needed to open/close these valves depends on the transmural pressure (that is the difference between the pressure and the external pressure given by the interstitial space) near the valve [15, 16, 24, 46]. Moreover, these valves present a small gap that stays open [22–24]. It follows that, when a contraction of the wall occurs, there is a small retrograde flow that happens before the valve closure [47, 48].

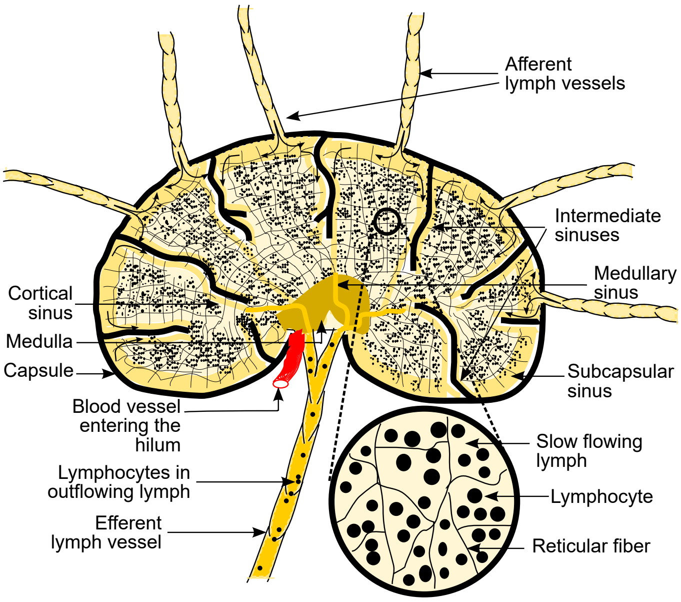

Figure 1.2: A schematic image of a lymph node (adapted from Wikipedia).

1.2 Lymph Nodes

The structure of the lymph node is highly complex and not easily visualized: a schematic image is shown in Figure 1.2.

Lymph nodes are lymphoid organs that are important for the immune response of our system. The lymph enters the lymph node from the afferent lymphatic vessels with a pulsatile behavior (due to the contraction of the lymphangion wall), and goes into the *subcapsular sinus* (SCS), which is composed of two layers of specialized *lymphatic endothelial cells* (LECs); here we can find *macrophages* and antigen-presenting cells (APCs), known as *Dentritic cells* (DCs), that regulate *antigens*, bacteria, etc... [37].

Macrophages are a type of white blood cells of the immune system which carry out a process called *phagocytosis*, which consists of digesting pathogens, such as cancer cells, microbes, cellular debris, and foreign substances, which do not have proteins that are specific to healthy body cells on their surface. This process acts to defend the host against infection and injury. Besides phagocytosis, macrophages play a critical role in innate immunity (nonspecific defense) and help initiate adaptive immunity (specific defense) by recruiting other immune cells such as lymphocytes.

Dendritic cells (DCs) are antigen-presenting cells (APCs) of the immune system. Their main function is to process antigens and present them to the T cells of the immune system to start the adaptive immune response.

The main difference between DCs and macrophages is that DCs function is to process antigen material and present it to the T cells and to start the adaptive immune response; on the other hand, macrophages clean up waste and remove pathogens, and then present their peptide to other cells for further help.

LECs are formed by vascular endothelial growth factor receptor-3 (VEGFR-

3), lymphatic vessel endothelial hyaluronan receptor 1 (LYVE-1), mucin type-1 protein podoplanin (podoplanin), and lymphatic-specific transcription factor (PROX-1) [36].

The majority of the lymph (about $\approx 90\%$ [5]) flows in the SCS, and the remaining part enters into the *lymphoid compartment* (LC) through a conduit system network formed by *fibroblastic reticular cells* (FRC), which form the parenchyma of the LN; due to this conformation, LNs are organs with high resistance to flow [49]. We can see a representation of the FRC network in Figure 1.3. Moreover, it seems that the LNs have also the function to regulate the lymph transport between a high-pressure zone (afferent lymphatic vessel) and a low-pressure zone (efferent lymphatic vessel), due to the fluid absorption of the lymph into the blood vessels in the node to establish an equilibrium of forces across the blood vessels membrane given by the *Starling's law* [39, 50–52]. Indeed, the secondary lymphœdema often results from damage to or removal of lymph nodes [1, 39].

The LN is a highly vascularized organ [53, 54]. The blood vessels inside the LN are important for giving nutrients and oxygen to the cells; during an infection, the vascularization must increase to ensure support for the increasing number of cells (creating new blood vessels, which will be destroyed at the end of the infection). Due to this vascularization inside the LN, there is a fluid exchange between the lymph (inside the FRC network) and the fluid inside the blood vessels of the lymph node; this is generally driven by Starling's law [55, 56], which regulates the fluid exchange between two phases separated by a membrane. This fluid exchange depends on the difference of pressure between the phases and the osmotic pressure, *i.e.*, the concentration difference of proteins between the two phases. This fluid exchange is demonstrated by the fact that the concentration of proteins in the efferent lymphatic vessel is higher than in the afferent one [34, 50–52].

Lymph flow inside LNs has an important function; indeed, fluid flow biases macromolecular distribution, enhances ligand expression, aligns extracellular matrix, and shapes active mechanisms of cell migration [37]. Fluid flow through endothelial monolayers and FRC network enhances the expression of chemokines that direct leucocyte localization and migration patterns [37]. Moreover, increased flows enhance proliferation and drug sensitivity in diffuse large B cell lymphoma [57]. Fluid flow is important to study tumor metastasis [12] and drug transport too [38, 58].

Part of the DCs (in particular the migratory DC) is carried by lymphatic vessels to help the LN, thanks also to the *chemokines*.

When the lymph enters the SCS, it transports antigens, signal molecules, and immunological cells. The SCS wall is formed by LEC, and the "roof" contains the receptor CCRL1 (ACKR4) and, bonding with the chemokines CCL19 and CCL21, creates a chemokine gradient that moves the DC from the SCS into the LC (parenchyma) [36]. Spatially confined expression of CCRL1 was necessary and sufficient for the creation of functional chemokine gradients [60]. Moreover, the SCS is an important site for preventing the systemic spread of microorganisms and viruses [61]. The lymph flow plays an important role in tumor transport through the lymphatic system and in tumor metastasis, and the lymphatic endothelium of

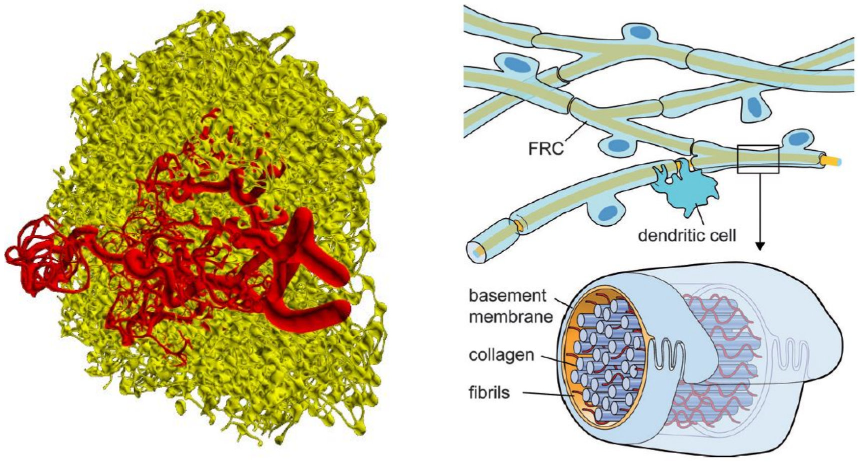

Figure 1.3: A reconstruction of the conduit system inside the lymphoid compartment of the lymph node. The figure on the left is taken from [59], the figure on the right is taken from [49].

the sinus represents a barrier to the entry of tumor cells into the lymph node [62].

Just under the “floor” of the SCS, there are the B-cell follicles (formed by B-type lymphocytes, they respond to chemokine CXCL13), and the remaining part is formed by the T-cell zone (formed by T-type lymphocytes) [34, 37]. The SCS floor protects the above mentioned zone from the direct contact of the afferent lymph; LECs in the sinus floor possess tight junctions and a basal membrane, indicating a diffusion barrier. The LECs lining the SCS and the LECs that form the peripherical lymphatics (lymphatic capillaries) are different (for example the surface markers and junctional molecules expression are different) [62].

The bigger particles ($> 70\,kDa$) cannot enter the conduits formed by FRC and remain in the SCS, where they are confined and filtered by specialized cells of the LEC (in the boundary), see Figure 1.3. However, there is some evidence indicating that the selectivity of the FRC network is not based solely on the size of the molecules; indeed, selected macromolecules (such as antibodies) can gain access to the LN parenchyma [63]; antibodies and large molecules that are physically unable to enter the conduit system may get transported by dynamin-dependent vesicular transcytosis across LECs lining the SCS into the LN parenchyma [64]. Moreover, throughout the conduit system there are antigen presenting cells (APC) that filter the lymph from antigens and present them to the lymphocytes [49].

The FRCs that ensheet the conduits in which the lymph flow sometimes have openings in which we can find a DC that searches antigens and bacteria in the conduit system (see Figure 1.3). Once the DC has found an antigen, they need to present it to the T-cells to start the immunological response; here the FRC in the T-cell zone produces chemokines CCL19 and CCL21 that drive T cells and DC to facilitate the interaction between them [49, 65–67].

While the DCs crawl against the FRC network searching for antigens, the interaction between $PDPN^+$ in FRC and CLEC-2 in DC induces the remodeling of the cytoskeleton of the FRC [65–67]. There is an elongation of the FRC, the

LN gets bigger to make more room for the lymphocytes, thanks also to the $LT\beta R$ (derived from DC) that promotes the survival of FRC's modulating PDPN (PDPN holds off the elongation of the FRC) [37, 49, 65–67].

It has been shown that B cells do not get instantly stimulated when encountering antigens. Instead, they accumulate antigens over time, suggesting multiple rounds of antigen acquisition. The extremely low velocity in the porous region is highly desirable as it allows sufficient time for antigens and/or antigen-bearing cells to find and interact with lymphocytes and triggers their activation [11].

Chapter 2

Theoretical Background

In this chapter we recall some well-known theoretical backgrounds that we use to model and study the fluid flow in lymphangions and lymph nodes.

In Section 2.1 we recall the classical fluid flow equations for a Newtonian fluid that flows in a free-fluid region and a porous medium. In Section 2.2 we summarize the definitions and properties of the *Gegenbauer functions* [31, 68, 69], and we will use these properties in Section 2.3 (and further on), where we describe the *stream function* approach used to solve a creeping fluid motion. As a reference to this theory, we use [31]. In Section 2.4 we describe the *asymptotic homogenization technique*, which is used to study multiscale problems and to derive the macroscale one, saving information about the microscale as the derived models encode the role of the microstructure in their coefficients. As a reference, we use [70]. Finally, in Section 2.5 we briefly describe the well-known *theory of quasilinear hyperbolic systems* [71, 72] and we derive the simplified 1D model used to describe the fluid flow in a deformable tube, referring to [56, 73, 74].

2.1 Equations of Motion

In this section, we recall the equations of motion that we will use in the whole thesis.

To describe the motion of a fluid, the classical choice is to use Eulerian formalism. The classical system of differential equations that describe the balance of momentum and the balance of mass without any source or sink is

$$\begin{cases} \rho \dfrac{d\boldsymbol{v}}{dt} = \rho \boldsymbol{f} + \nabla \cdot \mathbf{T}, \\ \dfrac{\partial \rho}{\partial t} + \nabla \cdot (\rho \boldsymbol{v}) = 0, \end{cases} \tag{2.1}$$

in the whole domain $\Omega \subset \mathbb{R}^3$, where $\boldsymbol{v}$ is the *velocity of the fluid*, $\boldsymbol{f}$ is the *density of force per unit of mass*, $\mathbf{T}$ is the *Cauchy stress tensor*, and ρ is the *fluid density.* We can assume the lymph to be a homogeneous and incompressible fluid, which means that the fluid can change its shape but not its volume; it follows that the second equation of (2.1) becomes

$$\nabla \cdot \boldsymbol{v} = 0, \tag{2.2}$$

where $\rho = \rho_0$ is constant.

Since the particles in the lymph have little influence on the lymph flow [1], we can assume that the fluid is *Newtonian*, which means that the local strain rate depends linearly on the viscous stresses arising from its flow (an example of Newtonian fluid is water). The Cauchy stress tensor for an incompressible Newtonian fluid is

$$\boldsymbol{T} = -p\boldsymbol{I} + 2\mu\boldsymbol{D}(\boldsymbol{v}), \tag{2.3}$$

where p is the *pressure* of the fluid and it is the Lagrange multiplier associated with the constraint of incompressibility, $\boldsymbol{I}$ is the *identity tensor*, μ is the *viscosity* of the fluid and

$$\boldsymbol{D}(\boldsymbol{v}) = \frac{1}{2}\left(\nabla\boldsymbol{v} + \nabla\boldsymbol{v}^T\right)$$

is a traceless second-order tensor field and it is the *symmetric part of the velocity gradient.* By the chain rule the material derivative of the velocity is

$$\frac{d\boldsymbol{v}}{dt} = \frac{\partial\boldsymbol{v}}{\partial t} + (\nabla\boldsymbol{v})\,\boldsymbol{v}. \tag{2.4}$$

Substituting (2.3) and (2.4) into (2.1), we obtain the *Navier-Stokes equation*

$$\begin{cases} \rho_0\dfrac{\partial\boldsymbol{v}}{\partial t} + \rho_0(\nabla\boldsymbol{v})\,\boldsymbol{v} = \rho_0\boldsymbol{f} - \nabla p + \nabla\cdot(\mu\boldsymbol{D}(\boldsymbol{v})), \\ \nabla\cdot\boldsymbol{v} = 0, \end{cases} \tag{2.5}$$

that is closed by a set of boundary conditions and an inital condition

$$\boldsymbol{v}(\boldsymbol{x}, 0) = \boldsymbol{v}_0(\boldsymbol{x}), \tag{2.6}$$

that must verify

$$\nabla\cdot\boldsymbol{v}_0(\boldsymbol{x}) = 0. \tag{2.7}$$

In the case where μ is constant, the system (2.5) becomes

$$\begin{cases} \rho_0\dfrac{\partial\boldsymbol{v}}{\partial t} + \rho_0(\nabla\boldsymbol{v})\,\boldsymbol{v} = \rho_0\boldsymbol{f} - \nabla p + \mu\Delta\boldsymbol{v}, \\ \nabla\cdot\boldsymbol{v} = 0. \end{cases} \tag{2.8}$$

We define the Reynolds number as [31, 56]

$$Re = \frac{\rho_0 LU}{\mu}, \tag{2.9}$$

where L is a *characteristic length* and U is a *characteristic velocity.* The Reynolds number is a measure of how much the viscous term is relevant with respect to the inertial term. In the case where $Re \ll 1$, we have that the system (2.5) can be approximated as

$$\begin{cases} \rho_0 \dfrac{\partial \boldsymbol{v}}{\partial t} = \rho_0 \boldsymbol{f} - \nabla p + \mu \Delta \boldsymbol{v}, \\ \nabla \cdot \boldsymbol{v} = 0; \end{cases} \tag{2.10}$$

this is called *Stokes equation*, and it is often used to describe flow with slow velocity or with small characteristic length.

2.1.1 Porous Media

A porous medium is a solid material in which there are pores (*i.e.* voids) topologically connected [75, 76]. The description of the fluid flow governed by the Stokes equation inside a porous medium is in general very complex; hence here we formulate the *macroscale* description of the fluid flow inside a porous medium obtained by smoothing out the microscopic complexity given by the pore structure.

The main equation used to describe a fluid flow inside a porous medium is the *Darcy's law*, which was formulated by Henry Darcy based on the results of experiments on the flow of water through beds of sand [77]; Darcy's law linearly relates the fluid discharge to the pressure difference (or pressure gradient) via the hydraulic conductivity tensor and the volume loads (applied externally). Hence we have

$$\boldsymbol{v} = -\mathbf{W} \left(\nabla p - \rho_0 \boldsymbol{f} \right), \tag{2.11}$$

where $\boldsymbol{v}$ is the average velocity of the fluid, $\mathbf{W}$ is the *hydraulic conductivity tensor* which takes into account the geometrical and viscous properties of the porous flow, and is given by

$$\mathbf{W} = \frac{\mathbf{K}}{\mu}, \tag{2.12}$$

where $\mathbf{K}$ is the *permeability tensor* and takes into account the microscale geometry of the porous medium, and μ is the viscosity. We highlight that the velocity described by the Darcy's law (2.11) is different than in the previous Section; indeed, here we have an average velocity, and it is the velocity relative to that of the solid, which in our case is zero (we are assuming that the matrix is non-deformable).

Darcy's law can be obtained using the *homogenization theory* (for more details, see Section 2.4). Equation (2.11) comes together with the incompressibility condition (2.2), and it follows that Darcy's law can be rewritten as

$$\nabla \cdot \left(-\mathbf{W} \nabla p \right) = \rho_0 \nabla \cdot \left(\mathbf{W} \boldsymbol{f} \right), \tag{2.13}$$

that is a diffusion differential equation in terms of the pressure p and needs to be closed by some boundary conditions for the pressure.

There is another important differential equation that describes the fluid flow of an incompressible Newtonian fluid inside a rigid porous matrix: the *Darcy-Brinkman* equation, that is

$$\begin{cases} \rho_0 \dfrac{\partial \boldsymbol{v}}{\partial t} = \rho_0 \boldsymbol{f} - \nabla p + \mu_e \Delta \boldsymbol{v} - \mathbf{W}^{-1} \boldsymbol{v}, \\ \nabla \cdot \boldsymbol{v} = 0, \end{cases} \tag{2.14}$$

where μ_e is the *effective viscosity* and satisfy [78]

$$\frac{\mu_e}{\mu} \approx 1. \tag{2.15}$$

This equation has been introduced by Brinkman adding a Laplacian (viscous) term (called Brinkman term) to the classical Darcy equation [79], weighed by an effective viscosity μ_e, and has been used widely to analyze high-porosity porous media. Moreover, if we have an interaction between a free-fluid region and a porous region, we have that the Darcy-Brinkman equation allows us to study in more detail the interface (and the boundary layer) between them [80]; in general, the Darcy-Brinkman formulation allows us to specify in more details the boundary conditions [81], having a differential form similar to the Stokes' one.

2.2 Gegenbauer Functions

In this section we summarize the main properties and definitions related to the *Gegenbauer functions.* We refer to [31, 68, 69].

The Gegenbauer functions $G_n^{(\lambda)}(x)$ of the first kind are polynomials and are solutions of the *Gegenbauer differential equation* of integer n:

$$(1-x^2)y''(x) - (2\lambda+1)xy'(x) + n(n+2\lambda)y = 0. \tag{2.16}$$

If $\lambda = \frac{1}{2}$, the Gegenbauer equation reduces to the *Legendre equation*, whose solutions are the *Legendre polynomials* $P_\nu^{(\mu)}(x)$; if $\lambda = 1$, the equation reduces to the Chebyshev differential equation, and the Gegenbauer polynomials reduce to the *Chebyshev polynomials* of the second kind. Now we focus on the $\lambda = -\frac{1}{2}$ case. We have:

$$G_0(x) = 1, \tag{2.17}$$

$$G_1(x) = -x, \tag{2.18}$$

$$G_n(x) = \frac{1}{2n-1}\left[P_{n-2}(x) - P_n(x)\right] = \frac{1}{(n-1)!}\frac{d^{n-2}}{dx^{n-2}}\left(\frac{x^2-1}{2}\right)^{n-1}, \tag{2.19}$$

for $n \geq 2$, where we denote by $G_n(x)$ the Gegenbauer polynomial $G_n^{(-\frac{1}{2})}(x)$ and by $P_n(x)$ the Legendre polynomial $P_n^{(0)}(x)$. There is another linear independent solution of the Gegenbauer equation, that is the *Gegenbauer function of the second kind* $H_n^{(\lambda)}(x)$, given by:

$$H_0(x) = -x = G_1(x), \tag{2.20}$$

$$H_1(x) = -1 = -G_0(x), \tag{2.21}$$

$$H_n(x) = \frac{1}{2n-1}\left[Q_{n-2}(x) - Q_n(x)\right] = \frac{1}{2}G_n(x)\begin{cases} \ln\left(\dfrac{1+x}{1-x}\right) + K_n(x), & |x| < 1, \\ \ln\left(\dfrac{x+1}{x-1}\right) + K_n(x), & |x| > 1, \end{cases} \tag{2.22}$$

for $n \geq 2$, where we denote by $H_n(x)$ the Gegenbauer function of the second kind $H_n^{(-\frac{1}{2})}(x)$, by $Q_n(x)$ the Legendre polynomial $Q_n^{(0)}(x)$ of the second kind and we have:

$$K_n(x) = -\sum_{k=1}^{n/2,(n+1)/2} \frac{2n-4k+1}{(2k-1)(n-k)} \left[1 - \frac{(2k-1)(n-k)}{n(n-1)}\right] G_{n-2k+1}(x). \tag{2.23}$$

We recall some important properties of the Gegenbauer polynomials [31, 68, 69, 82]:

$$\frac{d}{dx} G_n^{(\lambda)}(x) = 2\lambda G_{n-1}^{(\lambda+1)}(x), \tag{2.24}$$

$$(n+\lambda) G_n^{(\lambda)}(x) = \lambda \left(G_n^{(\lambda+1)}(x) - G_{n-2}^{(\lambda+1)}(x)\right), \tag{2.25}$$

$$\begin{aligned} &4\lambda(n+\lambda+1)(1-x^2) G_n^{(\lambda+1)}(x) \\ &= -(n+1)(n+2) G_{n+2}^{(\lambda)}(x) + (n+2\lambda)(n+2\lambda+1) G_n^{(\lambda)}(x), \end{aligned} \tag{2.26}$$

$$\frac{d}{dx}\left[\left(1-x^2\right)^{\lambda-\frac{1}{2}} G_n^{(\lambda)}(x)\right] = -\frac{(n+1)(n+2\lambda-1)}{2(\lambda-1)} \left(1-x^2\right)^{\lambda-\frac{3}{2}} G_{n+1}^{(\lambda-1)}(x), \tag{2.27}$$

$$\frac{d^2}{dx^2} G_n(x) = -\frac{n(n-1)}{1-x^2} G_n(x), \tag{2.28}$$

$$x^2 G_n(x) = \alpha_n G_{n-2}(x) + \gamma_n G_n(x) + \beta_n G_{n+2}(x), \tag{2.29}$$

where

$$\begin{aligned} \alpha_n &= \frac{(n-2)(n-3)}{4(n-\frac{1}{2})(n-\frac{3}{2})}, \\ \beta_n &= \frac{(n+1)(n+2)}{4(n-\frac{1}{2})(n+\frac{1}{2})}, \\ \gamma_n &= \frac{(2n^2-2n-3)}{4(n+\frac{1}{2})(n-\frac{3}{2})}. \end{aligned}$$

We have that the Gegenbauer polynomials are *orthogonal polynomials* for $x \in [-1,1]$, normalized by:

$$\int_{-1}^{1} (1-x^2)^{\lambda-\frac{1}{2}} \left[G_n^{(\lambda)}(x)\right]^2 dx = 2^{1-2\lambda}\pi \frac{\Gamma(n+2\lambda)}{(n+\lambda)\left[\Gamma(\lambda)\right]^2 \Gamma(n+1)} \quad \text{for } \lambda > -\frac{1}{2}, \tag{2.30}$$

where Γ is the *Gamma function*. For $\lambda = -\frac{1}{2}$ we have:

$$\int_{-1}^{1} \frac{\left[G_n(x)\right]^2}{1-x^2} dx = \frac{2}{n(n-1)(2n-1)}. \tag{2.31}$$

This allows the expansion of an arbitrary function in series. In the case of Gegenbauer polynomials of order $\lambda = -\frac{1}{2}$ we have:

$$f(x) = \sum_{n=0}^{\infty} a_n G_n(x), \tag{2.32}$$

and the orthogonality condition leads to

$$a_n = \frac{1}{2} n(n-1)(2n-1) \int_{-1}^{1} \frac{f(x) G_n(x)}{1-x^2} dx. \tag{2.33}$$

If we fix the case $\lambda = \frac{1}{2}$, we can write the expansion of an arbitrary function in a series of Legendre polynomials:

$$g(x) = \sum_{n=0}^{\infty} b_n P_n(x), \tag{2.34}$$

and the orthogonality condition leads to

$$b_n = \frac{1}{2}(2n+1) \int_{-1}^{1} g(x) P_n(x) dx. \tag{2.35}$$

Furthermore, we have that the even-order Gegenbauer polynomials are even function of x, and the odd-order ones are odd function of x. Hence we have:

$$G_0(x) = -H_1(x) = \sum_{n=1}^{\infty} (4n-1) G_{2n}(x), \tag{2.36}$$

$$G_1(x) = H_0(x) = -\sum_{n=1}^{\infty} (4n+1) G_{2n+1}(x); \tag{2.37}$$

this means that the Gegenbauer functions $G_0(x)$, $G_1(x)$, $H_0(x)$ and $H_1(x)$ are *linearly dependent* of the Gegenbauer functions of $n \geq 2$, and the Gegenbauer functions $G_n(x)$ with $n \geq 2$ are *linearly independent* and *orthonormal* thanks to equation (2.31). These properties can be generalized for every λ using the orthogonal property (2.30).

2.3 Axisimmetric Flow and Stream Functions

In this section we recall some aspects of the axisymmetric flow and stream function given in [31]. Indeed, thanks to the property of axisymmetry, a 3D problem can be treated introducing the *stream function*, reducing the equations of motion to the search of a single scalar function.

We have that an *axisymmetrical fluid motion* is one for which

$$\frac{\partial \boldsymbol{v}}{\partial \phi} = 0, \quad \mathbf{e}_\phi \cdot \boldsymbol{v} = \mathbf{0}, \tag{2.38}$$

where $\boldsymbol{v}$ is the *fluid velocity* and ϕ is the *azimuthal angle*. It follows that the velocity $\boldsymbol{v}$ is *independent* of the azimuthal angle ϕ and the azimuthal component

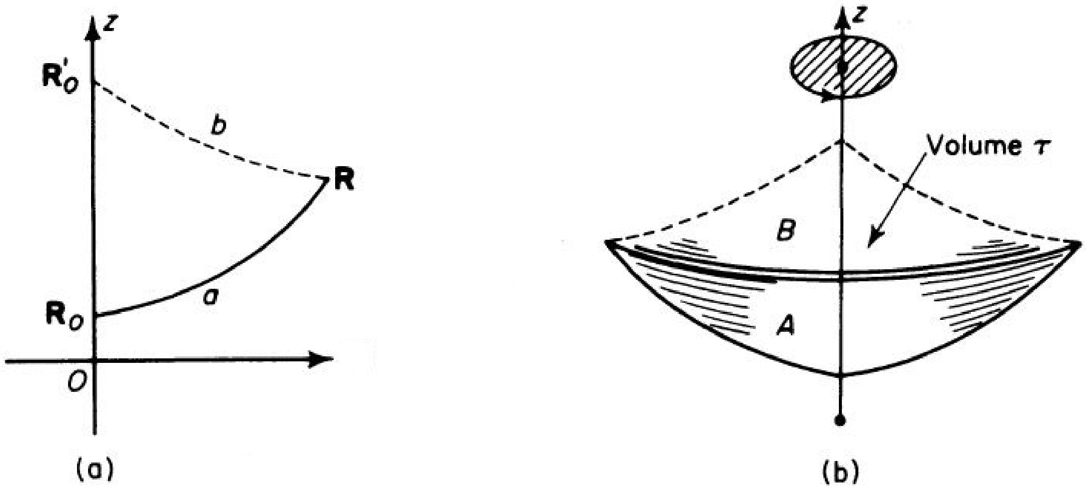

Figure 2.1: Definition drawing for axisymmetric flow. The Figure is taken from [31].

of the velocity is everywhere zero. If we assume this property, we can neglect the azimuthal coordinate and study the flow only with respect to the other coordinates.

We suppose the *incompressibility* of the fluid (equation (2.2)):

$$\nabla \cdot \boldsymbol{v} = 0. \tag{2.39}$$

The definition of the stream function ψ for the incompressible velocity field is as follows [31]. Given a point $\boldsymbol{R}$, we call a the curve that connects this point to any point $\boldsymbol{R}_0$ lying along the axis of symmetry (see Figure 2.1 (a)). Upon rotation of this curve through an angle of 2π, we generate a surface (see Figure 2.1 (b)). We denote with Q the instantaneous volumetric flow rate through this surface. Thanks to the incompressibility assumption, we have that Q, at any instant, is therefore uniquely determined by a position vector $\boldsymbol{X}$. In particular, it is independent of the choice of the curve a joining $\boldsymbol{X}$ to the axis. We define the quantity called *stream function*, at some point $\boldsymbol{X}$, as [31]:

$$\psi = \psi(\boldsymbol{X}; t) = \frac{Q}{2\pi}. \tag{2.40}$$

According to this definition, $\psi = 0$ on the axis of revolution. This quantity is often referred to as *Stokes stream function* (or *Stokes current function*). The existence of a stream function depends on certain hypotheses of symmetry and incompressibility.

We focus on the spherical coordinate system (see [31] for a generic coordinate system):

$$\boldsymbol{v} = v_r \boldsymbol{e}_r + v_\theta \boldsymbol{e}_\theta + v_\phi \boldsymbol{e}_\phi, \tag{2.41}$$

where r is the *radial coordinate*, θ is the *polar coordinate* and ϕ is the *azimuthal coordinate*. Due to the axisymmetric assumption, we have that

$$\boldsymbol{v} = \boldsymbol{v}(r, \theta) = v_r(r, \theta) \boldsymbol{e}_r + v_\theta(r, \theta) \boldsymbol{e}_\theta. \tag{2.42}$$

In spherical coordinates, the connection between the velocity $\boldsymbol{v}$ and the stream function ψ is given by

$$Q = \int_A \boldsymbol{v} \cdot \boldsymbol{n} dS = \int_{R_0}^{R} \int_0^{2\pi} \boldsymbol{v} \cdot \boldsymbol{n} r \sin\theta d\phi ds, \tag{2.43}$$

where s is the *arc length* and $\boldsymbol{n}$ is a unit outer normal to the surface. The stream function is (remembering that $\psi = 0$ on the axis of revolution)

$$\psi = \int_{R_0}^{R} d\psi = \int_{R_0}^{R} \nabla\psi \cdot d\boldsymbol{R} = \int_{R_0}^{R} \boldsymbol{t} \cdot \nabla\psi ds, \tag{2.44}$$

where $\boldsymbol{t}$ is a unit tangent vector to the meridian curve. From equation (2.43), it follows that

$$\psi = \int_{R_0}^{R} \boldsymbol{v} \cdot \boldsymbol{n} r \sin\theta ds, \tag{2.45}$$

hence we have, thanks to the arbitrariness of s:

$$\boldsymbol{v} \cdot \boldsymbol{n} r \sin\theta = \boldsymbol{t} \cdot \nabla\psi. \tag{2.46}$$

Recalling that

$$\boldsymbol{t} = \boldsymbol{n} \times \boldsymbol{e}_\phi, \tag{2.47}$$

we have

$$\boldsymbol{n} \cdot (\boldsymbol{v} r \sin\theta - \boldsymbol{e}_\phi \times \nabla\psi) = 0, \tag{2.48}$$

and, due to the arbitrariness of $\boldsymbol{n}$, we have

$$\boldsymbol{v} r \sin\theta - \boldsymbol{e}_\phi \times \nabla\psi = \boldsymbol{0}, \tag{2.49}$$

so that

$$\boldsymbol{v} = -\nabla \times \left(\frac{\psi}{r \sin\theta} \boldsymbol{e}_\phi \right). \tag{2.50}$$

Starting from the classical steady Stokes equation:

$$\mu \Delta \boldsymbol{v} = \nabla p, \tag{2.51}$$

where $\boldsymbol{v}$ is the velocity and p is the pressure, we can rewrite the Laplacian term $\Delta\boldsymbol{v}$ as

$$\Delta\boldsymbol{v} = \nabla\left(\nabla \cdot \boldsymbol{v}\right) - \nabla \times \left(\nabla \times \boldsymbol{v}\right), \tag{2.52}$$

and, due to the incompressibility, we have

$$\Delta\boldsymbol{v} = -\nabla \times \left(\nabla \times \boldsymbol{v}\right). \tag{2.53}$$

Hence we have

$$\nabla p + \nabla \times \left(\nabla \times \boldsymbol{v}\right) = \boldsymbol{0}. \tag{2.54}$$

If we call the *vorticity*

$$\omega = \nabla \times \boldsymbol{v}, \tag{2.55}$$

we have

$$\omega = \nabla \times \boldsymbol{v} = \nabla \times \nabla \times \left(-\frac{\psi}{r \sin\theta} \boldsymbol{e}_\phi \right) = -\frac{1}{r \sin\theta} \left[\frac{\partial^2 \psi}{\partial r^2} + \frac{\sin^2\theta}{r^2} \frac{\partial}{\partial \theta} \left(\frac{1}{\sin\theta} \frac{\partial \psi}{\partial \theta} \right) \right] \boldsymbol{e}_\phi, \tag{2.56}$$

and, if we define

$$\mathrm{E}^2 = \frac{\partial^2}{\partial r^2} + \frac{\sin\theta}{r^2} \frac{\partial}{\partial\theta} \left(\frac{1}{\sin\theta} \frac{\partial}{\partial\theta} \right) \tag{2.57}$$

we have

$$\omega = -\frac{\boldsymbol{e}_\phi}{r \sin\theta} \, \mathrm{E}^2 \, \psi. \tag{2.58}$$

Moreover, we have

$$\nabla \times \nabla \times \omega = -\frac{\boldsymbol{e}_\phi}{r \sin\theta} \, \mathrm{E}^2 \left(\mathrm{E}^2 \, \psi \right). \tag{2.59}$$

Hence, if we apply $\nabla\times$ to the equation (2.54), we obtain the following equation of motion (note that $\nabla \times \nabla p = 0$):

$$\mathrm{E}^2 \left(\mathrm{E}^2 \, \psi \right) = 0. \tag{2.60}$$

In the case of the Darcy-Brinkman equation (with constant permeability) or the pulsatile Stokes equation (see Section 5), we have the following differential equation for the motion:

$$\mu \Delta \boldsymbol{v} + q \boldsymbol{v} = \nabla p, \tag{2.61}$$

where q is a constant. Following the computations above, we obtain the following equation of motion:

$$\mathrm{E}^2 \left(\mathrm{E}^2 \, \psi \right) + q \, \mathrm{E}^2 \, \psi = 0. \tag{2.62}$$

Once ψ has been found, from equation (2.50) we can determine the components of $\boldsymbol{v}$ with these relations

$$v_r = -\frac{1}{r^2 \sin\theta} \frac{\partial \psi}{\partial \theta} = \frac{1}{r^2} \frac{\partial \psi}{\partial \zeta}, \quad v_\theta = \frac{1}{r \sin\theta} \frac{\partial \psi}{\partial r} = \frac{1}{r\sqrt{1-\zeta^2}} \frac{\partial \psi}{\partial r}, \tag{2.63}$$

where $\zeta = \cos\theta$.

The pressure may be obtained from equation (2.61):

$$\begin{aligned} \nabla p &= \mu \left(\Delta \boldsymbol{v} - \sigma \boldsymbol{v} \right) = -\mu \left(\nabla \times \omega + \sigma \boldsymbol{v} \right) \\ &= -\mu \left[\nabla \times \left(\frac{\boldsymbol{e}_\phi}{r \sin\theta} \, \mathrm{E}^2 \, \psi \right) - \sigma \nabla \times \left(\frac{\boldsymbol{e}_\phi}{r \sin\theta} \psi \right) \right] \\ &= -\mu \left[\frac{\boldsymbol{e}_\phi}{r \sin\theta} \times \nabla \left(\mathrm{E}^2 \, \psi \right) - \sigma \frac{\boldsymbol{e}_\phi}{r \sin\theta} \times \nabla \psi \right], \end{aligned} \tag{2.64}$$

hence we can find the pressure by integrating the following relations, respectively (with $\nabla = \frac{\partial}{\partial r} \boldsymbol{e}_r + \frac{1}{r} \frac{\partial}{\partial \theta} \boldsymbol{e}_\theta$) [31, 83]:

$$\begin{cases} \dfrac{\partial p}{\partial r} = \dfrac{\mu}{r^2} \dfrac{\partial}{\partial \zeta} \left[\left(\mathrm{E}^2 - \sigma \right) \psi \right] \\ \dfrac{\partial p}{\partial \zeta} = -\dfrac{\mu}{1-\zeta^2} \dfrac{\partial}{\partial r} \left[\left(\mathrm{E}^2 - \sigma \right) \psi \right]. \end{cases} \tag{2.65}$$

2.3.1 Steady General Solution

We want to find the general solution of the equation (2.60) following [31].

We have that the solution of (2.60) is in the form:

$$\psi = \psi^{(1)} + \psi^{(2)}, \tag{2.66}$$

where $\psi^{(1)}$ and $\psi^{(2)}$ solve:

$$\mathrm{E}^2\,\psi^{(1)} = 0, \tag{2.67}$$

and

$$\mathrm{E}^2\,\psi^{(2)} = W, \tag{2.68}$$

where W solves

$$\mathrm{E}^2\,W = 0. \tag{2.69}$$

We start by finding the solution of equation (2.67). We use the separation of variables $\psi^{(1)} = R(r)Z(\zeta)$ (where $\zeta = \cos\theta$) and, substituting into equation (2.67), we have:

$$\frac{r^2}{R}\frac{d^2R}{dr^2} + \frac{1-\zeta^2}{Z}\frac{d^2Z}{d\zeta^2} = 0. \tag{2.70}$$

This equation can be true only if the terms in r and in ζ are equal to a constant, say $n(n-1)$, with $n \in \mathbb{N}$. This leads to the second-order equations

$$r^2\frac{d^2R}{dr^2} - n(n-1)R = 0, \tag{2.71}$$

$$(1-\zeta^2)\frac{d^2Z}{d\zeta^2} + n(n-1)Z = 0. \tag{2.72}$$

Degenerate cases occur for $n = 0, 1$. The solution of (2.71) is:

$$R(r) = \alpha_n r^n + \beta_n r^{-n+1}. \tag{2.73}$$

The second equation (2.72) is in the form of the Gegenbauer equation of order $-\dfrac{1}{2}$ (see Section 2.2) and has the solution

$$Z(\zeta) = \nu_n G_n(\zeta) + \delta_n H_n(\zeta), \tag{2.74}$$

where G_n is the *Gegenbauer polynomial of the first kind of order* $-\dfrac{1}{2}$ and H_n is the *Gegenbauer function of the second kind of order* $-\dfrac{1}{2}$. The Gegenbauer function of the second kind degenerate at $\zeta = \pm 1$; for this reason, we have that $\delta_n = 0$. Hence, by putting together the above equations, we obtain:

$$\psi^{(1)} = \sum_{n=0}^{\infty} \left(\alpha_n r^n + \beta_n r^{-n+1}\right) G_n(\zeta). \tag{2.75}$$

Remark 1. *The choice of the constant as* $n(n-1)$, $n \in \mathbb{N}$ *is due to the fact that the Gegenbauer polynomials of the first kind* $G_\alpha^{-1/2}(\zeta)$ *have a singularity at* $\zeta = -1$ *except for* α *integer [84].*

For the solution of equation (2.68), we have (using the separation of variables):

$$\psi^{(2)} = \sum_{n=0}^{\infty} \pi(r) G_n(\zeta); \tag{2.76}$$

applying the operator E^2 to the above equation, using the Gegenbauer differential equation (Section 2.2) and using equations (2.68) and (2.69), we have:

$$\frac{d^2 \pi_n}{dr^2} - n(n-1)\frac{\pi_n}{r^2} = a_n r^n + b_n r^{-n+1}, \tag{2.77}$$

for which a particular solution is

$$\pi_n(r) = \frac{a_n r^{n+2}}{2(2n+1)} - \frac{b_n r^{-n+3}}{2(2n-3)} = C_n r^{n+2} + D_n r^{-n+3}. \tag{2.78}$$

Hence, a complete solution for the equation (2.60) is of the form:

$$\psi(r,\theta) = \sum_{n=0}^{\infty} \left(A_n r^n + B_n r^{-n+1} + C_n r^{n+2} + D_n r^{\cdot n+3} \right) G_n(\zeta). \tag{2.79}$$

Furthermore, the values $n = 0$ and 1 lead to infinite tangential velocities. Hence we have

$$\psi(r,\theta) = \sum_{n=2}^{\infty} \left(A_n r^n + B_n r^{-n+1} + C_n r^{n+2} + D_n r^{\cdot n+3} \right) G_n(\zeta). \tag{2.80}$$

From the equation for the pressure (2.65), we have (removing the terms with $n = 0, 1$):

$$\frac{1}{\mu} p = -\sum_{n=2}^{\infty} \left[\frac{2(2n+1)}{n-1} C_n r^{n-1} + \frac{2(2n-3)}{n} D_n r^{-n} \right] P_{n-1}(\zeta), \tag{2.81}$$

where P_n is the *Legendre function of order* n (see Section 2.2).

2.4 Asymptotic Homogenization

The *asymptotic homogenization* technique allows the modeling of multiscale phenomena. In general, we can have different scales in which our problem is defined, but it is impossible (analytically and computationally) to take into account all the information of the microscale; moreover, experimental measurements usually provide average information on a macroscale. The asymptotic homogenization technique allows us to describe a multiscale phenomenon on the macroscale, saving microscale information. In this subsection we recap the main assumptions that we need to use the technique. The asymptotic homogenization technique is based on the *two-scale convergence* [32, 85–88]. To write this section, we refer to [70]. To perform the asymptotic homogenization, we need the following assumptions:

- *length scale separation*: We assume that there exist two distinct spatial scales, referred to as the *microscale* d and the *macroscale* L, such that their ratio is
$$\epsilon = \frac{d}{L} \ll 1. \tag{2.82}$$
When $\epsilon \sim 1$ we have a poor separation of scale [78].

- *spatial variations decoupling*: We call the non-dimensional physical spatial coordinate $\tilde{\boldsymbol{x}}$. We assume that the unknowns and the coefficients in our boundary value problem (BVP) are functions of two formally independent spatial variables $\boldsymbol{x}, \boldsymbol{y}$ such that
$$\boldsymbol{x} = \tilde{\boldsymbol{x}}, \quad \boldsymbol{y} = \frac{\tilde{\boldsymbol{x}}}{\epsilon}, \tag{2.83}$$
where $\boldsymbol{x}$ is referred to as the *macroscale* variable and $\boldsymbol{y}$ is referred to as the *microscale* variable. In particular, all the unknowns of our BVP depend on the variables $(\boldsymbol{x}, \boldsymbol{y})$, with $\boldsymbol{x} \in (0,1)^n$ and $\boldsymbol{y} \in (0,+\infty)^n$. This means that in the one-dimensional case:
$$\frac{d(\cdot)}{d\tilde{x}} = \frac{\partial(\cdot)}{\partial x}\frac{dx}{d\tilde{x}} + \frac{dy}{d\tilde{x}}\frac{\partial(\cdot)}{\partial y} = \frac{\partial(\cdot)}{\partial x} + \frac{1}{\epsilon}\frac{\partial(\cdot)}{\partial y}. \tag{2.84}$$
Instead, for the multidimensional case, we have:
$$\nabla_{\tilde{\boldsymbol{x}}} = \nabla_{\boldsymbol{x}} + \frac{1}{\epsilon}\nabla_{\boldsymbol{y}}. \tag{2.85}$$

- *power series expansion*: We assume that all the multiscale unknowns $\boldsymbol{u}(\boldsymbol{x}, \boldsymbol{y})$ can be formally represented by a regular expansion in power series of ϵ:
$$\boldsymbol{u}(\boldsymbol{x}, \boldsymbol{y}) \equiv \boldsymbol{u}^{\epsilon}(\boldsymbol{x}, \boldsymbol{y}) = \sum_{l=0}^{\infty} \boldsymbol{u}^{(l)}(\boldsymbol{x}, \boldsymbol{y})\epsilon^{l}. \tag{2.86}$$

The hypotheses above are the essential assumptions that we need for using the asymptotic homogenization technique. Typically, other assumptions are also made, which are:

- *local periodicity*: This hypothesis means that the unknowns and the coefficients of our problem are $\boldsymbol{y}$-periodic. This assumption allows us to study fine scale variations of the fields on a restricted portion of the domain. For this reason, we can define an average operator only in a portion of the microscale domain Ω:
$$\langle(\cdot)\rangle_{\Omega} = \frac{1}{|\Omega|}\int_{\Omega}(\cdot)d\boldsymbol{y}. \tag{2.87}$$
This hypothesis can be replaced by the weaker hypothesis of *local boundedness and regularity* by introducing a new average operator
$$\langle(\cdot)\rangle_{\Omega} = \lim_{R\to\infty}\frac{1}{\frac{4}{3}\pi R^3}\int_{\Omega\cap B_R}(\cdot)d\boldsymbol{y}, \tag{2.88}$$

where Ω is the domain and B_R is a ball of radius R (see [89]). The strength of the local-periodicity hypothesis is that we can focus our attention only to a small portion of the domain, and this is computationally less expensive.

When the separation of scales is obvious, *i.e.* $\epsilon \ll 1$, whatever the organization on the local scale, the macroscopic behavior of the material will be qualitatively the same and, for this reason, we can justify the use of the local periodicity assumption for treating real non-periodic materials. Instead, the closer the macroscopic scale gets to the microscopic scale, *i.e.* $\epsilon \to 1$, the more sensitive it becomes to local fluctuations, and consequently to the organization of the microstructure (see [90], Chapter 3).

- *macroscopic uniformity*: We neglect geometrical variations of the cell with respect to the coarse scale variable $\boldsymbol{x}$. Therefore, it is sufficient to consider one periodic cell at each macroscale point $\boldsymbol{x}$ to completely capture the fine scale structure, and we have (since Ω does not depend on the macroscale $\boldsymbol{x}$):

  $$\nabla_{\boldsymbol{x}} \cdot \int_{\Omega} (\cdot) d\boldsymbol{y} = \int_{\Omega} \nabla_{\boldsymbol{x}} \cdot (\cdot) d\boldsymbol{y}. \tag{2.89}$$

  If this assumption does not hold, we have to be careful in using the right type of Reynolds transport theorem.

Remark 2. *The two-scale asymptotic expansion presented in* (2.86) *is of fundamental importance for the asymptotic homogenization technique, but, unfortunately, from a mathematical point of view, there is no reason for the expansion* (2.86) *to hold true. Therefore, an additional step is necessary to provide a rigorous justification of the homogenization result achieved heuristically through this expansion approach. This is the purpose of the two-scale convergence. Essentially, the two-scale convergence provides a rigorous justification for the first term of the expansion* (2.86) *when applied to any bounded sequence* $\boldsymbol{u}^{\epsilon}$. *This implies that a two-scale limit* $\boldsymbol{u}^{(0)}(\boldsymbol{x}, \boldsymbol{y})$ *exists. Indeed, any sequence* $\boldsymbol{u}^{\epsilon}$ *which admits an asymptotic expansion of the type*

$$\boldsymbol{u}^{\epsilon}(\boldsymbol{x}) = \boldsymbol{u}^{(0)}(\boldsymbol{x}, \frac{\boldsymbol{x}}{\epsilon}) + \epsilon \boldsymbol{u}^{(1)}(\boldsymbol{x}, \frac{\boldsymbol{x}}{\epsilon}) + ...,$$

where the functions $\boldsymbol{u}^{(i)}(\boldsymbol{x}, \boldsymbol{y})$ *are smooth and* Y*-periodic in* y*, two-scale converges to* $\boldsymbol{u}^{(0)}(\boldsymbol{x}, \boldsymbol{y})$ *(the first term of the expansion). The first term* $\boldsymbol{u}^{(0)}(\boldsymbol{x}, \boldsymbol{y})$ *of the asymptotic expansion can be rigorously justified to exist through two scale convergence, even if the expansion itself does not hold. We refer to [32, 85–88] for more information about the two scale convergence.*

2.4.1 Example: Asymptotic Homogenization of the Stokes Problem - Darcy's Law

Here we propose an example taken from [70] to see how asymptotic homogenization can be used to describe the fluid flow through a porous medium. We identify the whole physical domain with the open set $\Omega \in \mathbb{R}^3$, $\Omega = \Omega_f \cup \Omega_s$, where Ω_f is

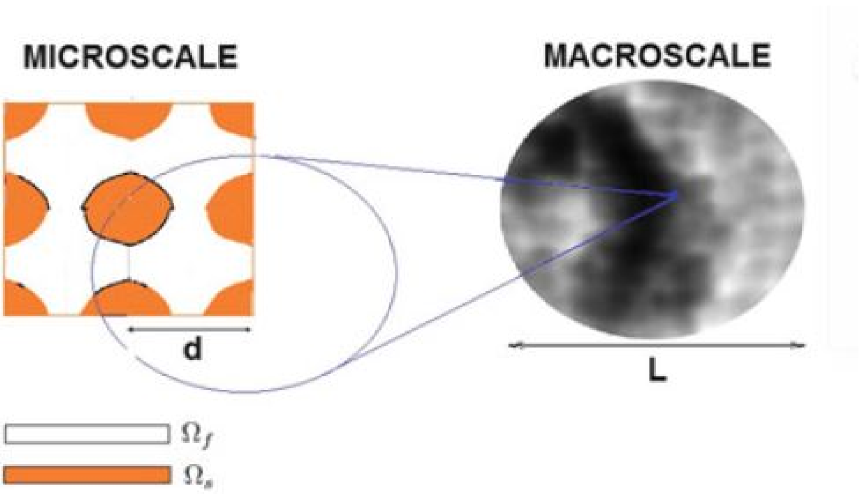

Figure 2.2: The domain microstructure (left) and macrostructure (right) with the geometrical variations smoothed out. The picture is taken from [70].

the fluid region and Ω_s is the solid region (that represents the structure of the porous domain). As we mentioned above, we need two scales d and L such that $\epsilon = \dfrac{d}{L} \ll 1$. We identify our microscale d with the pore radius, and the macroscale L with the average size of the whole domain. We can see a representation of the geometry in Figure 2.2.

We suppose that the fluid that flows through the pores is a Newtonian fluid described by the steady Stokes equation, see Section 2.1:

$$\mu \Delta_{\boldsymbol{x}} \boldsymbol{v} = \nabla p \quad \boldsymbol{x} \in \Omega_f, \tag{2.90}$$

$$\nabla_{\boldsymbol{x}} \cdot \boldsymbol{v} = 0 \quad \boldsymbol{x} \in \Omega_f, \tag{2.91}$$

$$\boldsymbol{v} = \boldsymbol{0}, \quad \text{on } \Gamma, \tag{2.92}$$

where μ is the fluid viscosity, $\boldsymbol{v}$ is the fluid velocity, p is the fluid pressure and $\Gamma = \partial\Omega_f \cap \partial\Omega_s$.

To proceed with the asymptotic homogenization technique, we need to non-dimensionalize equations (2.90–2.92); hence we rescale our relevant quantities in the following way:

$$\boldsymbol{x} = L\boldsymbol{x}', \quad \boldsymbol{v} = \frac{Cd^2}{\mu}\boldsymbol{v}', \quad p = CLp', \tag{2.93}$$

where C is the *magnitude of the characteristic pressure gradient*. The rescaling of the velocity is suggested by the parabolic profile of a viscous fluid flowing in a straight cylindrical channel of radius d:

$$\frac{Cd^2}{\mu}. \tag{2.94}$$

The differential operators become:

$$\nabla_{\boldsymbol{x}} = \frac{1}{L}\nabla_{\boldsymbol{x}'}, \quad \Delta_{\boldsymbol{x}} = \frac{1}{L^2}\Delta_{\boldsymbol{x}'}, \tag{2.95}$$

and the non-dimensional Stokes problem reads (leaving the primes):

$$\epsilon^2 \Delta_{\boldsymbol{x}} \boldsymbol{v} = \nabla p \quad \boldsymbol{x} \in \Omega_f, \tag{2.96}$$

$$\nabla_{\boldsymbol{x}} \cdot \boldsymbol{v} = 0 \quad \boldsymbol{x} \in \Omega_f, \tag{2.97}$$

$$\boldsymbol{v} = \mathbf{0} \quad \text{on } \Gamma. \tag{2.98}$$

Substituting the power series expansion (2.86) for $\boldsymbol{v}$ and p and the spatial variations decoupling, we have

$$\boldsymbol{v}(\boldsymbol{x},\boldsymbol{y}) \equiv \boldsymbol{v}^{\epsilon}(\boldsymbol{x},\boldsymbol{y}) = \sum_{l=0}^{\infty} \boldsymbol{v}^{(l)}(\boldsymbol{x},\boldsymbol{y})\epsilon^l, \tag{2.99}$$

$$p(\boldsymbol{x},\boldsymbol{y}) \equiv p^{\epsilon}(\boldsymbol{x},\boldsymbol{y}) = \sum_{l=0}^{\infty} p^{(l)}(\boldsymbol{x},\boldsymbol{y})\epsilon^l; \tag{2.100}$$

moreover, substituting (2.85) into equations (2.96–2.98), we obtain:

$$\epsilon^3 \Delta_{\boldsymbol{x}} \boldsymbol{v}^{\epsilon} + \epsilon^2 \nabla_{\boldsymbol{x}} \cdot (\nabla_{\boldsymbol{y}} \boldsymbol{v}^{\epsilon}) + \epsilon^2 \nabla_{\boldsymbol{y}} \cdot (\nabla_{\boldsymbol{x}} \boldsymbol{v}^{\epsilon}) + \epsilon \Delta_{\boldsymbol{y}} \boldsymbol{v}^{\epsilon} = \nabla_{\boldsymbol{y}} p^{\epsilon} + \epsilon \nabla_{\boldsymbol{x}} p^{\epsilon} \quad \text{in } \Omega_f, \tag{2.101}$$

$$\nabla_{\boldsymbol{y}} \cdot \boldsymbol{v}^{\epsilon} + \epsilon \nabla_{\boldsymbol{x}} \cdot \boldsymbol{v}^{\epsilon} = 0 \quad \text{in } \Omega_f, \tag{2.102}$$

$$\boldsymbol{v}^{\epsilon} = \mathbf{0} \quad \text{on } \Gamma. \tag{2.103}$$

Now we equate the same powers of ϵ of the above equations. Equating the terms of order ϵ^0 of equation (2.101), we have

$$\nabla_{\boldsymbol{y}} p^{(0)}(\boldsymbol{x},\boldsymbol{y}) = 0 \implies p^{(0)} = p^{(0)}(\boldsymbol{x}), \tag{2.104}$$

which means that the pressure term of order ϵ^0 does not depends on the microscale $\boldsymbol{y}$. If we equate the terms of order ϵ^0 from equations (2.102) and (2.103), we have

$$\nabla_{\boldsymbol{y}} \cdot \boldsymbol{v}^{(0)} = 0 \quad \text{in } \Omega_f \tag{2.105}$$

$$\boldsymbol{v}^{(0)} = \mathbf{0} \quad \text{on } \Gamma. \tag{2.106}$$

Equating the terms ϵ^1 in equations (2.101-2.103) we get to the following equations:

$$\Delta_{\boldsymbol{y}} \boldsymbol{v}^{(0)} = \nabla_{\boldsymbol{y}} p^{(1)} + \nabla_{\boldsymbol{x}} p^{(0)} \quad \text{in } \Omega_f, \tag{2.107}$$

$$\nabla_{\boldsymbol{y}} \cdot \boldsymbol{v}^{(1)} + \nabla_{\boldsymbol{x}} \cdot \boldsymbol{v}^{(0)} = 0 \quad \text{in } \Omega_f, \tag{2.108}$$

$$\boldsymbol{v}^{(1)} = \mathbf{0}, \quad \text{on } \Gamma. \tag{2.109}$$

If we collect the equations (2.107), (2.105) and (2.106) together, we obtain the following *auxiliary Stokes problem* for the fields $(\boldsymbol{v}^{(0)}, p^{(1)})$:

$$\begin{cases} \Delta_{\boldsymbol{y}} \boldsymbol{v}^{(0)} = \nabla_{\boldsymbol{y}} p^{(1)} + \nabla_{\boldsymbol{x}} p^{(0)} \quad \text{in } \Omega_f, \\ \nabla_{\boldsymbol{y}} \cdot \boldsymbol{v}^{(0)} = 0 \quad \text{in } \Omega_f, \\ \boldsymbol{v}^{(0)} = \mathbf{0}, \quad \text{on } \Gamma, \end{cases} \tag{2.110}$$

with the property of $\boldsymbol{y}$-periodicity on the external boundary of the cell $\partial\Omega_f \setminus \Gamma$. We note from equation (2.104) that the term $\nabla_{\boldsymbol{x}} p^0$ only depends on the macroscale $\boldsymbol{x}$ and this term is the forcing term of the motion. From the linearity of the system (2.110), we formulate the following ansatz for the solution

$$\boldsymbol{v}^{(0)} = -\mathbf{W}\nabla_{\boldsymbol{x}} p^{(0)}, \tag{2.111}$$

$$p^{(1)} = -\boldsymbol{p} \cdot \nabla_{\boldsymbol{x}} p^{(0)} + \bar{p}(\boldsymbol{x}); \tag{2.112}$$

the above expressions represent the unique solution (up to a $\boldsymbol{y}$-constant arbitrary function $\bar{p}(\boldsymbol{x})$) of the auxiliary Stokes problem (2.110), provided that $\mathbf{W}$ and $\boldsymbol{p}$ solve the following cell problem

$$\begin{cases} \Delta_{\boldsymbol{y}} \mathbf{W} = (\nabla_{\boldsymbol{y}} \boldsymbol{p})^T - \mathbf{I} & \text{in } \Omega_f, \\ \nabla_{\boldsymbol{y}} \cdot \mathbf{W} = 0 & \text{in } \Omega_f, \\ \mathbf{W} = \mathbf{0} & \text{on } \Gamma, \end{cases} \tag{2.113}$$

and we close the problem (2.113) imposing $\boldsymbol{y}$-periodic conditions on $\partial\Omega_f \setminus \Gamma$ and the condition

$$\langle \boldsymbol{p} \rangle_{\Omega_f} = 0$$

to ensure the solution uniqueness, where $\langle (\cdot) \rangle_{\Omega_f}$ is the *average operator* defined as

$$\langle (\cdot) \rangle_{\Omega_f} = \frac{1}{|\Omega_f|} \int_{\Omega_f} (\cdot) dV. \tag{2.114}$$

If we apply the average operator (2.114) to the ansatz of the solution (2.111), we obtain the macroscale governing equation relating the leading order velocity and pressure, namely

$$\langle \boldsymbol{v}^0 \rangle_{\Omega_f} = -\langle \mathbf{W} \rangle_{\Omega_f} \nabla_{\boldsymbol{x}} p^0, \tag{2.115}$$

i.e., the *Darcy's law.* Moreover, applying (2.114) to equation (2.108) and using the divergence theorem and the local periodicity assumption (see Section 2.4), we have

$$\nabla_{\boldsymbol{x}} \cdot \langle \boldsymbol{v}^0 \rangle_{\Omega_f} = 0. \tag{2.116}$$

Moreover, we have

$$\nabla_{\boldsymbol{x}} \cdot \langle \boldsymbol{v}^0 \rangle_{\Omega_f} = \nabla_{\boldsymbol{x}} \cdot \left(-\langle \mathbf{W} \rangle_{\Omega_f} \nabla_{\boldsymbol{x}} p^0 \right) = 0, \tag{2.117}$$

that is a Darcy's law with permeability $\langle \mathbf{W} \rangle_{\Omega_f}$, where $\mathbf{W}$ results from the problem (2.113) on the periodic cell Ω.

2.5 Quasilinear Hyperbolic Systems for Balance Law

In this section we briefly recall the theory of the quasilinear hyperbolic system for balance law, and then we will apply it to the case of an incompressible Newtonian fluid flowing in a deformable pipe.

In general, we have

$$\frac{d}{dt}\left(\int_{\Omega(t)} udV\right) = \int_{\Omega(t)} fdV, \tag{2.118}$$

where $u(x,t)$ is a density, $f(x,t)$ is the density source and Ω is the domain. Using the Reynolds transport theorem, we have that a *balance law* has the form:

$$\int_{\Omega(t)} \frac{\partial u}{\partial t} dV = -\int_{\partial\Omega(t)} \mathbf{J}\cdot\mathbf{n}dS + \int_{\Omega(t)} fdV, \tag{2.119}$$

where $\mathbf{J}(x,t) = \boldsymbol{v}u$ is the current density. The first quantity represents the variation over time of a certain quantity, the second term represents the flux of the quantity at the boundary and the third is a source/sink term. Using the localization theorem, we have:

$$\frac{\partial u}{\partial t} + \operatorname{div}\mathbf{J} = f. \tag{2.120}$$

If we have several balance laws, we can write a system of balance laws in this form [71, 72]

$$\frac{\partial \mathbf{U}}{\partial t} + \frac{\partial \mathbf{F}^\alpha(\mathbf{U})}{\partial \boldsymbol{x}^\alpha} = \mathbf{B}(\mathbf{U}) \tag{2.121}$$

and setting

$$\mathbf{H}^\alpha(\mathbf{U}) = \frac{\partial \mathbf{F}^\alpha}{\partial \mathbf{U}}(\mathbf{U}), \tag{2.122}$$

we have:

$$\frac{\partial \mathbf{U}}{\partial t} + \mathbf{H}^\alpha(\mathbf{U})\frac{\partial \mathbf{U}^\alpha}{\partial \boldsymbol{x}^\alpha} = \mathbf{B}(\mathbf{U}). \tag{2.123}$$

The system is called *linear* if the matrix $\boldsymbol{H}^\alpha$ is constant and $\mathbf{B}$ is linear in $\boldsymbol{U}$, *semilinear* if the matrix $\boldsymbol{H}^\alpha$ is constant and *quasilinear* otherwise.

Definition 1. *A system (2.123) of m equations is said to be* hyperbolic *at a point $(\boldsymbol{x},t)$ if $\boldsymbol{H}^\alpha$ has m* real *eigenvalues $\lambda_1,...,\lambda_m$ and a corresponding set of m* linearly independent right eigenvectors $K(1),...,K(m)$. *The system is said to be* strictly hyperbolic *if the eigenvalues λ_i are all distinct.*

The eigenvalues λ are called *characteristic velocity* and represent the velocity of the front waves. In the quasilinear case, they depend on the solution u (hence the system can lose the hyperbolicity for some values). The physical interpretation of the properties of the eigenvalues is as follows [71, 72]:

- The eigenvalues λ must be real so that the propagation can actually happen;
- $\det\mathbf{H}^0 \neq 0$ excludes the fact that there is some $\lambda \to \infty$, that means an infinite velocity of propagation of the front waves;

2.5.1 Derivation of the Equations for the Motion of the Fluid

We derive the governing equations that describe an incompressible Newtonian fluid flowing in a compliant pipe. We follow the approach using the asymptotic analysis described in [73, 74], but the derivation of these equations with other approaches is possible [56].

The incompressible axisymmetric Navier-Stokes equations without body forces in cylindrical coordinates (r, θ, z), where the z coordinate is aligned with the axis of symmetry of the channel and, assuming that the angular velocity is zero, are (where $\boldsymbol{v} = v_r \boldsymbol{e}_r + v_z \boldsymbol{e}_z$ is the velocity of our motion):

$$\frac{\partial v_r}{\partial t} + v_r \frac{\partial v_r}{\partial r} + v_z \frac{\partial v_r}{\partial z} + \frac{1}{\rho_0} \frac{\partial p}{\partial r} = \nu \left[\frac{\partial^2 v_r}{\partial r^2} + \frac{1}{r} \frac{\partial v_r}{\partial r} - \frac{v_r}{r^2} + \frac{\partial^2 v_r}{\partial z^2} \right], \tag{2.124}$$

$$\frac{\partial v_z}{\partial t} + v_r \frac{\partial v_z}{\partial r} + v_z \frac{\partial v_z}{\partial z} + \frac{1}{\rho_0} \frac{\partial p}{\partial z} = \nu \left[\frac{\partial^2 v_z}{\partial r^2} + \frac{1}{r} \frac{\partial v_z}{\partial r} + \frac{\partial^2 v_z}{\partial z^2} \right], \tag{2.125}$$

and the incompressibility condition

$$\frac{\partial v_z}{\partial z} + \frac{1}{r} \frac{\partial (r v_r)}{\partial r} = 0. \tag{2.126}$$

If we introduce V_r and V_z the characteristic radial and axial velocities, L the characteristic length, and R the characteristic inner vessel radius, we have the following non-dimensional variables:

$$r' = \frac{r}{R}, \quad z' = \frac{z}{L}, \quad t' = \frac{V_z}{L} t, \quad v'_z = \frac{v_z}{V_z}, \quad v'_r = \frac{v_r}{V_r}, \quad p' = \frac{p}{\rho_0 v^2}, \tag{2.127}$$

noticing that, for our flow regime

$$\frac{R}{L} = \frac{V_r}{V_z} = \epsilon \ll 1. \tag{2.128}$$

The incompressibility condition (2.126) in non-dimensional variables is (leaving the primes)

$$\frac{\partial (r v_r)}{\partial r} + \frac{V_z R}{V_r L} \frac{\partial (r v_z)}{\partial z} = 0; \tag{2.129}$$

noting that

$$\frac{V_z R}{V_r L} = 1, \tag{2.130}$$

we have

$$\frac{\partial (r v_r)}{\partial r} + \frac{\partial (r v_z)}{\partial z} = 0. \tag{2.131}$$

The momentum equations (2.125) and (2.124) in non-dimensional variables are (leaving the primes)

$$\frac{\partial v_z}{\partial t} + v_z \frac{\partial v_z}{\partial z} + v_r \frac{\partial v_z}{\partial r} + \frac{\partial p}{\partial z} = \frac{L \nu}{V_z R^2} \left(\frac{\partial^2 v_z}{\partial r^2} + \frac{1}{r} \frac{\partial v_z}{\partial r} + \epsilon^2 \frac{\partial^2 v_z}{\partial z^2} \right), \tag{2.132}$$

$$-\frac{\partial p}{\partial r} = \epsilon^2 \left[\frac{\partial v_r}{\partial t} + v_z \frac{\partial v_r}{\partial z} + v_r \frac{\partial v_r}{\partial r} - \frac{L\nu}{V_z R^2} \left(\frac{\partial^2 v_r}{\partial r^2} + \frac{1}{r}\frac{\partial v_r}{\partial r} - \frac{v_r}{r^2} + \epsilon^2 \frac{\partial^2 v_r}{\partial z^2} \right) \right]. \tag{2.133}$$

From equation (2.133), we obtain

$$\frac{\partial p}{\partial r} = 0. \tag{2.134}$$

Using the following relations

$$\frac{\partial (r v_r v_z)}{\partial r} = v_z \frac{\partial (r v_r)}{\partial r} + r v_r \frac{\partial v_z}{\partial r}, \tag{2.135}$$

$$\frac{\partial (r v_z^2)}{\partial z} = v_z \frac{\partial (r v_z)}{\partial z} + r v_z \frac{\partial v_z}{\partial z}, \tag{2.136}$$

and by using the incompressibility condition (2.131), we observe that the first terms of these relations on the right-hand side are the same but with opposite sign; hence we can rewrite (2.132) in the form

$$\frac{\partial (r v_z)}{\partial t} + \frac{\partial (r v_z^2)}{\partial z} + \frac{\partial (r v_r v_z)}{\partial r} + \frac{\partial (r p)}{\partial z} = \frac{L\nu}{V_z R^2} \left(\frac{\partial}{\partial r} \left(r \frac{\partial v_z}{\partial r} \right) \right). \tag{2.137}$$

We can integrate equations (2.137) and (2.131) over r from $r = 0$ to $r = \tilde{R}$ (where $\tilde{R}$ is the inner radius), and we obtain

$$\frac{\partial}{\partial t} \left[\int_0^{\tilde{R}} r v_z dr \right] - [r v_z]_{\tilde{R}} \frac{\partial \tilde{R}}{\partial t} + \frac{\partial}{\partial z} \left[\int_0^{\tilde{R}} r v_z^2 dr \right] - \left[r v_z^2 \right]_{\tilde{R}} \frac{\partial \tilde{R}}{\partial z} + [r v_r v_z]_{\tilde{R}} + \int_0^{\tilde{R}} r \frac{\partial p}{\partial z} dr = \frac{L\nu}{V_z R^2} \left[r \frac{\partial v_z}{\partial r} \right]_{\tilde{R}}, \tag{2.138}$$

and

$$\frac{\partial}{\partial z} \left[\int_0^{\tilde{R}} v_z r dr \right] - [v_z r]_{\tilde{R}} \frac{\partial \tilde{R}}{\partial z} + [r v_r]_{\tilde{R}} = 0. \tag{2.139}$$

We assume the streamline condition at the wall, that means

$$[v_r]_{\tilde{R}} = \frac{\partial \tilde{R}}{\partial t} + \frac{\partial \tilde{R}}{\partial z} [v_z]_{\tilde{R}}. \tag{2.140}$$

If we define the average velocity

$$\bar{u} = \frac{1}{\tilde{R}^2} \int_0^{\tilde{R}} 2 r v_z dr, \tag{2.141}$$

and the parameter α (called *Coriolis coefficient*)

$$\alpha = \frac{1}{\tilde{R}^2 \bar{u}^2} \int_0^{\tilde{R}} 2 r v_z^2 dr, \tag{2.142}$$

equations (2.138) and (2.139) become

$$\frac{\partial\left(\tilde{R}^2\bar{u}\right)}{\partial t}+\frac{\partial\left(\alpha\tilde{R}^2\bar{u}^2\right)}{\partial z}+\tilde{R}^2\frac{\partial p}{\partial z}=2\frac{L\nu}{V_zR^2}\tilde{R}\left[\frac{\partial v_z}{\partial r}\right]_{\tilde{R}},\tag{2.143}$$

and

$$\frac{\partial\left(\tilde{R}^2\bar{u}\right)}{\partial z}+2\tilde{R}\frac{\partial\tilde{R}}{\partial t}=0.\tag{2.144}$$

In terms of dimensional quantities, these equations are:

$$\frac{\partial A\bar{u}}{\partial t}+\frac{\partial\left(\alpha A\bar{u}^2\right)}{\partial z}+\frac{A}{\rho_0}\frac{\partial p}{\partial z}=2\pi\nu R\left[\frac{\partial v_z}{\partial r}\right]_{\tilde{R}},\tag{2.145}$$

$$\frac{\partial A}{\partial t}+\frac{\partial\left(A\bar{u}\right)}{\partial z}=0,\tag{2.146}$$

where $A>0$ is the cross-sectional area of the tube.

To obtain the equations written in terms of the averaged quantities we need to specify the axial velocity profile v_z. A typical approximation for the velocity profile is [91]

$$v_z=\frac{\gamma+2}{\gamma}\bar{u}\left[1-\left(\frac{r}{R}\right)^{\gamma}\right],\tag{2.147}$$

with $\gamma=2$ for a Newtonian fluid. From equations (2.142) and (2.147), we obtain the relationship

$$\gamma=\frac{2-\alpha}{\alpha-1}\tag{2.148}$$

and equation (2.145) becomes

$$\frac{\partial\left(A\bar{u}\right)}{\partial t}+\frac{\partial\left(\alpha A\bar{u}^2\right)}{\partial z}+\frac{A}{\rho_0}\frac{\partial p}{\partial z}=-2\pi\frac{\alpha}{\alpha-1}\nu\bar{u}.\tag{2.149}$$

If we introduce the quantity

$$Q=A\bar{u},\tag{2.150}$$

we can rewrite equations (2.146) and (2.149) in the form

$$\frac{\partial A}{\partial t}+\frac{\partial Q}{\partial z}=0,\tag{2.151}$$

$$\frac{\partial Q}{\partial t}+\frac{\partial}{\partial z}\left(\alpha\frac{Q^2}{A}\right)+\frac{A}{\rho_0}\frac{\partial p}{\partial z}=-2\pi\frac{\alpha}{\alpha-1}\nu\frac{Q}{A}.\tag{2.152}$$

To close the system (2.151)–(2.152), the pressure term needs to be specified and, in general, it is a function of the cross-sectional area A. From the fact that $\frac{\partial p}{\partial r}=0$ (the pressure is constant along the r coordinate), we have that the pressure here takes into account the wall effect and contraction. Hence we have that the pressure is in the form

$$p=p_{ext}+\phi(A;A_0,\beta_1,....,\beta_m),\tag{2.153}$$

where ϕ is a suitable function of the vessel area A, the initial datum A_0 and some mechanical parameters $\beta_1, ..., \beta_m$ and must have the following properties

$$\frac{\partial \phi}{\partial A} > 0, \quad \phi(A_0; A_0, \beta_1, ..., \beta_m) = 0. \tag{2.154}$$

For an analysis of the pressure, we refer to [56, 92].

We can rewrite the equations (2.151) and (2.152) in the form of (2.123):

$$\frac{\partial U}{\partial t} + \mathbf{H}(U)\frac{\partial U}{\partial z} + B(U) = \mathbf{0}, \tag{2.155}$$

where

$$U = \begin{bmatrix} A \\ Q \end{bmatrix}, \tag{2.156}$$

$$\mathbf{H}(U) = \begin{bmatrix} 0 & 1 \\ c_1^2 - \alpha\left(\frac{Q}{A}\right)^2 & 2\alpha\frac{Q}{A} \end{bmatrix}, \tag{2.157}$$

$$c_1 = \sqrt{\frac{A}{\rho_0}\frac{\partial \phi}{\partial A}}, \tag{2.158}$$

$$B(U) = \begin{bmatrix} 0 \\ \frac{2\pi\alpha}{\alpha - 1}\nu\frac{Q}{A} + \frac{A}{\rho_0}\frac{\partial \phi}{\partial A_0}\frac{dA_0}{dz} + \frac{A}{\rho_0}\frac{\partial \phi}{\partial \beta_1}\frac{d\beta_1}{dz} + ... + \frac{A}{\rho_0}\frac{\partial \phi}{\partial \beta_m}\frac{d\beta_m}{dz} \end{bmatrix}. \tag{2.159}$$

The eigenvalues of (2.157) are

$$\lambda_{1,2} = \alpha\frac{Q}{A} \pm \sqrt{c_1^2 + \left(\frac{Q}{A}\right)^2 \alpha(\alpha - 1)}, \tag{2.160}$$

and, from the fact that $\alpha \geq 1$, $A > 0$ and $\frac{\partial \phi}{\partial A} > 0$, we have that the two eigenvalues are real and distinct, hence we have that system (2.155) is *strictly hyperbolic.*

We can rewrite the system (2.155) in terms of the *characteristic variables.* Let $(\boldsymbol{l}_1, \boldsymbol{l}_2)$ and $(\boldsymbol{r}_1, \boldsymbol{r}_2)$ be two pairs of sets of right and left eigenvectors of the matrix $\mathbf{H}$, respectively. The matrices $\mathbf{L}$, $\mathbf{R}$ and $\mathbf{G}$ are defined as

$$\mathbf{L} = \begin{bmatrix} \boldsymbol{l}_1^T \\ \boldsymbol{l}_2^T \end{bmatrix}, \quad \mathbf{R} = \begin{bmatrix} \boldsymbol{r}_1 & \boldsymbol{r}_2 \end{bmatrix}, \quad \mathbf{G} = \operatorname{diag}(\lambda_1, \lambda_2), \tag{2.161}$$

and we have

$$\mathbf{LR} = \boldsymbol{I}, \quad \mathbf{H} = \mathbf{LGR}. \tag{2.162}$$

System (2.155) can be rewritten as

$$\mathbf{L}\frac{\partial U}{\partial t} + \mathbf{GLH}(U)\frac{\partial U}{\partial z} + \mathbf{L}B(U) = \mathbf{0}; \tag{2.163}$$

if there exist two variables W_1 and W_2 such that

$$\frac{\partial W_1}{\partial U} = \boldsymbol{l}_1, \quad \frac{\partial W_2}{\partial U} = \boldsymbol{l}_2, \tag{2.164}$$

we will call them the *characteristic variables* of our hyperbolic system. By setting $W = [W_1, W_2]$, we have

$$\frac{\partial W}{\partial t} + \mathbf{G}\frac{\partial W}{\partial z} + G = \mathbf{0}, \tag{2.165}$$

where

$$G = \mathbf{L}B - \frac{\partial W}{\partial A_0}\frac{dA_0}{dz} - \frac{\partial W}{\partial \beta_1}\frac{d\beta_1}{dz} - ... - \frac{\partial W}{\partial \beta_m}\frac{d\beta_m}{dz}. \tag{2.166}$$

Chapter 3

One-Dimensional Model of a Lymphangion

The part of the vessel between two valves is known as *lymphangion*. Lymphangions are innervated with sympathetic and parasympathetic nerves that can perform rhythmic contractions. Lymphangions are essential in the regulation of the lymph flow through the lymphatic system: indeed, the combination of lymphangion contractions and valve action is the main device that helps lymph move against a pressure gradient given by the pulsation of the heart and to return into the blood circulation. We refer to Chapter 1 for a more complete description of the lymphatic system and lymphatic vessels.

In this chapter we propose a 1D model using the *theory of quasilinear hyperbolic systems* exposed in Section 2.5 to describe the fluid flow in a lymphangion. First of all, in Section 3.1 we find the critical thresholds, which refer to certain critical values or conditions that determine whether a system will exhibit a global in-time smooth solution or it will experience a finite-time singularity formation, with a general pressure in an infinitely long cylindrical domain. Moreover, we highlight the role of the viscosity μ in the singularity of the solution. The novelty of the critical thresholds that we find with respect to the ones found in [93] is that we take into account a generic constitutive law for the pressure. In Section 3.2 we study a general 1D mathematical model that describes the lymph flow in a lymphangion and takes into account the valve behavior and the contractions (with the inhibitory effect due to *eNOS* – shear stress) of the lymphangion. For the valve behavior, we use the model presented in [94] and used in [19] with physiological parameters given in the literature [15, 46]. For the wall contraction behavior, we fit physiological data found in [17, 18]: the description of the wall behavior is largely phenomenological, but we choose this type of approach because we are more interested in the fluid behavior, and we want to run more feasible numerical simulations. In Section 3.3 we describe the numerical schemes that we use to solve the models presented in Section 3.2. In Section 3.4 we recap the physiological parameters from the literature. Finally, in Section 3.5 we show the numerical results of our problem and compare them with results and data found in the literature. The results presented in this chapter are not yet complete and have to be considered preliminary. Since the research is ongoing, further analysis is needed before any definitive conclusions can be reached. We are still working on the subject.

3.1 Critical Thresholds

In this section we want to find the critical threshold related to a 1D flow problem (presented in Section 2.5) with a general pressure and in an infinitely long cylindrical domain. This threshold is related to certain critical values or conditions that determine whether a system will exhibit a global in-time smooth solution or it will experience a finite-time singularity formation. In [93] the authors found the critical threshold for this flow with a specific constitutive law for the pressure of the form $p(A) = G_0\left(\left(\frac{A}{A_0}\right)^{1/2} - 1\right)$, where G_0 describes the stiffness of the vessel wall. This pressure choice is typical to the aorta and blood vessels [56, 74, 93]. We want to find the critical thresholds with a generic constitutive law for the pressure.

We recall equations (2.151) and (2.152):

$$\frac{\partial A}{\partial t} + \frac{\partial Q}{\partial z} = 0, \tag{3.1}$$

$$\frac{\partial Q}{\partial t} + \frac{\partial}{\partial z}\left(\alpha \frac{Q^2}{A}\right) + \frac{A}{\rho_0}\frac{\partial p}{\partial z} = -2\pi\nu\left(\gamma + 2\right)\frac{Q}{A}, \tag{3.2}$$

where the constants are introduced in Section 2.5. The eigenvalues of our problem are

$$\lambda_{1,2} = \frac{Q}{A} \mp \sqrt{\frac{A}{\rho_0}\frac{\partial p}{\partial A}} = \bar{u} \mp c_1(A), \tag{3.3}$$

where

$$c_1(A) = \sqrt{\frac{A}{\rho_0}\frac{\partial p}{\partial A}}. \tag{3.4}$$

We need some hypothesis to start with:

- we fix $\alpha = 1$;
- we impose $\dfrac{\partial p}{\partial A} > 0$ to have hyperbolicity (see Section 2.5);
- we call $\bar{f} = 2(\gamma + 2)\pi\nu$ and we assume $\bar{f} > 0$;
- we need to choose the constitutive pressure law such that $\dfrac{\partial \lambda_2}{\partial A} > 0$ and $\dfrac{\partial \lambda_1}{\partial A} < 0$.

System (3.1)–(3.2) becomes

$$\frac{\partial A}{\partial t} + \frac{\partial Q}{\partial z} = 0, \tag{3.5}$$

$$\frac{\partial Q}{\partial t} + \frac{\partial}{\partial z}\left(\frac{Q^2}{A}\right) + \frac{A}{\rho_0}\frac{\partial p}{\partial z} = -\bar{f}\frac{Q}{A}, \tag{3.6}$$

and has the following Riemann invariants [56, 93]:

$$R^{\pm} = \frac{Q}{A} \pm m(A) = \bar{u} \pm m(A), \tag{3.7}$$

where

$$m(A) = \int_{A_0}^{A} \frac{c_1(\tau)}{\tau} d\tau, \tag{3.8}$$

$$\bar{u} = \frac{1}{2}\left(R^+ + R^-\right), \tag{3.9}$$

$$A = m^{-1}\left(\frac{1}{2}\left(R^+ - R^-\right)\right), \tag{3.10}$$

and they satisfy

$$\begin{cases} \dfrac{\partial R^-}{\partial t} + \lambda_1 \dfrac{\partial R^-}{\partial z} = -\bar{f}\dfrac{\bar{u}}{A} & t > 0,\ z \in \mathbb{R}, \\ \dfrac{\partial R^+}{\partial t} + \lambda_2 \dfrac{\partial R^+}{\partial z} = -\bar{f}\dfrac{\bar{u}}{A} & t > 0,\ z \in \mathbb{R}, \end{cases} \tag{3.11}$$

with the initial data

$$R^{\pm}(z, 0) = R_0^{\pm}(z) = \bar{u}_0(z) \pm m\left(A_0(z)\right). \tag{3.12}$$

Thanks to the reformulated system (3.11), there exists a uniform invariant region for the system (3.5)–(3.6), see [93, 95]. Hence there exist $0 < A_{\min} < A_{\max}$ and $Q_{\min} < Q_{\max}$ dependent on the initial data (A_0, Q_0), such that

$$(A(z,t), Q(z,t)) \in D = [A_{\min}, A_{\max}] \times [Q_{\min}, Q_{\max}], \quad \forall z \in \mathbb{R},\ t > 0.$$

We introduce the quantities

$$s^{\pm} := \frac{\partial R^{\pm}}{\partial z}, \tag{3.13}$$

differentiate the system (3.11) with respect to z and use the definition (3.13):

$$\begin{cases} \dfrac{\partial s^-}{\partial t} + \lambda_1 \dfrac{\partial s^-}{\partial z} + \left(\dfrac{\partial \lambda_1}{\partial A}\dfrac{\partial A}{\partial z}\right) s^- = \dfrac{\partial}{\partial z}\left(-\bar{f}\dfrac{\bar{u}}{A}\right), \\ \dfrac{\partial s^+}{\partial t} + \lambda_2 \dfrac{\partial s^+}{\partial z} + \left(\dfrac{\partial \lambda_2}{\partial A}\dfrac{\partial A}{\partial z}\right) s^+ = \dfrac{\partial}{\partial z}\left(-\bar{f}\dfrac{\bar{u}}{A}\right). \end{cases} \tag{3.14}$$

Differentiating (3.8) with respect to z, we have

$$m'(A)\frac{\partial A}{\partial z} = \frac{1}{2}\left(\frac{\partial R^+}{\partial z} - \frac{\partial R^-}{\partial z}\right),$$

and hence we have

$$\frac{\partial A}{\partial z} = \frac{A}{2c_1(A)}\left(s^+ - s^-\right). \tag{3.15}$$

We differentiate A along the characteristic $x_1'(t) = \lambda_1$ and we obtain

$$A' := \left(\frac{\partial}{\partial t} + \lambda_1 \frac{\partial}{\partial z}\right) A = \frac{(R^+)' - (R^-)'}{2\dfrac{\partial m}{\partial A}} = \frac{(\lambda_1 - \lambda_2)\dfrac{\partial R^+}{\partial z}}{2\dfrac{c_1(A)}{A}}$$

$$= \frac{-c_1(A)\dfrac{\partial R^+}{\partial z}}{\dfrac{c_1(A)}{A}} = -As^+. \tag{3.16}$$

We define the quantities

$$g := \int_{A_{\min}}^{A} \frac{\bar{f}}{2\xi^2}\,(1+\delta)\, e^{h(\xi)} d\xi \tag{3.17}$$

where

$$h = \frac{\bar{u}}{c_1(A)}, \quad \delta \ll 1, \tag{3.18}$$

and we have

$$g' = \frac{\bar{f}}{2A}\,(1+\delta)\, e^{h(\xi)} A'; \tag{3.19}$$

$$b^{\pm} := \frac{\bar{f}}{2A}\,(1+\delta) - w^{\pm} = \frac{\bar{f}}{2A}\left(1 \mp \frac{\bar{u}}{c_1(A)}\right), \tag{3.20}$$

where

$$w^{\pm} = \frac{\bar{f}}{2A}\left(\delta \pm \frac{\bar{u}}{c_1(A)}\right). \tag{3.21}$$

Moreover, we assume that

$$\left|\frac{\bar{u}_{\max}}{c_1(A_{\min})}\right| < \delta \ll 1, \tag{3.22}$$

and hence we have

$$|w^{\pm}| = \left|\frac{\bar{f}}{2A}\left(\delta \pm \frac{\bar{u}}{c_1(A)}\right)\right| \ll 1. \tag{3.23}$$

We note that, due to the low velocities of the flow in the lymphatic system, the above assumption is valid in the lymphangion case.

We can rewrite the term $\frac{\partial}{\partial z}\left(-\bar{f}\frac{\bar{u}}{A}\right)$ as:

$$\begin{aligned}
\frac{\partial}{\partial z}\left(-\bar{f}\frac{\bar{u}}{A}\right) =& \frac{\partial}{\partial z}\left(-\frac{\bar{f}}{2A}(R^{+}+R^{-})\right)\\
=& -\frac{\bar{f}}{2A}\left(1+\frac{\bar{u}}{c_1(A)}-\frac{\bar{u}}{c_1(A)}\right)\left(s^{+}+s^{-}\right)+\frac{\bar{f}}{2A^2}\frac{\partial A}{\partial z}\left(R^{+}+R^{-}\right)\\
=& -b^{-}s^{-}-\frac{\bar{f}}{2A}s^{+}-\frac{\bar{f}}{2A}\frac{\bar{u}}{c_1(A)}s^{+}+\frac{\bar{f}}{2A}\frac{\bar{u}}{c_1(A)}\left(s^{+}-s^{-}\right)\\
&+\frac{\bar{f}}{2A}\frac{\bar{u}}{c_1(A)}\left(s^{+}+s^{-}\right)=-b^{-}s^{-}-\frac{\bar{f}}{2A}s^{+}+\frac{\bar{f}}{2A}\frac{\bar{u}}{c_1(A)}s^{+}\\
=& -b^{-}s^{-}-\frac{\bar{f}}{2A}(1+\delta-\delta)s^{+}+\frac{\bar{f}}{2A}\frac{\bar{u}}{c_1(A)}s^{+}\\
=& -b^{-}s^{-}-\frac{\bar{f}}{2A}(1+\delta)s^{+}+\frac{\bar{f}}{2A}\delta s^{+}+\frac{\bar{f}}{2A}\frac{\bar{u}}{c_1(A)}s^{+}\\
=& -b^{-}s^{-}-\frac{\bar{f}}{2A}(1+\delta)s^{+}+w^{+}s^{+}. \qquad (3.24)
\end{aligned}$$

Substituting (3.15)–(3.16)–(3.23)–(3.24) into the first equation of (3.14), we obtain

$$\left(s^{-}\right)'-\frac{\partial\lambda_1}{\partial A}\frac{1}{2c_1(A)}A's^{-}-\frac{\partial\lambda_1}{\partial A}\frac{A}{2c_1(A)}\left(s^{-}\right)^2=-b^{-}s^{-}-\frac{\bar{f}}{2A}(1+\delta)s^{+}. \quad (3.25)$$

Recalling (3.4), we define

$$\bar{h}=\frac{1}{2}\ln\left(c_1(A)\right), \quad (3.26)$$

$$r^{\pm}=e^{\bar{h}}s^{\pm}; \quad (3.27)$$

multiplying (3.25) by $e^{\bar{h}}$, using the definitions (3.17)–(3.19) and after some computations, we obtain

$$\left(r^{-}-g\right)'-\frac{\partial\lambda_1}{\partial A}\frac{A}{2c_1(A)e^{\bar{h}}}\left(r^{-}\right)^2+b^{-}r^{-}=0. \quad (3.28)$$

The case with r^{+} is similar, and the final equation is

$$\left(r^{+}-q\right)'+\frac{\partial\lambda_2}{\partial A}\frac{A}{2c_1(A)e^{\bar{h}}}\left(r^{+}\right)^2+b^{+}r^{+}=0. \quad (3.29)$$

We recall Lemma 4.1 from [93]

Lemma 1. *Consider an equation of the form*

$$\frac{dB}{dt}+a(t)\left(B-b_1(t)\right)\left(B-b_2(t)\right)=0, \quad B(0)=B_0, \quad (3.30)$$

with $\inf a>0$, $b_1\le b_2$ *and such that* a, b_1 *and* b_2 *are uniformly bounded. We have:*

I) If the initial data B_0 is such that $B_0 < \min b_1$, then the solution of (3.30) *has a finite time blow up at t_*, $0 < t_* \leq t^* < \infty$*

$$\lim_{t \to t_*} B(t) = -\infty,$$

where t^* satisfies

$$\int_0^{t^*} a(s)ds = \frac{1}{\min b_2 - \min b_1} \ln \left(1 + \frac{\min b_2 - \min b_1}{\min b_1 - B_0} \right),$$

which equals to $\dfrac{1}{\min b_2 - B_0}$ if $\min b_2 = \min b_1$.

II) If there exists a constant $\bar{b}$ such that

$$b_1(t) \leq \bar{b} \leq b_2(t),$$

then (3.30) *admits a unique global bounded solution satisfying*

$$\bar{b} \leq B(t) \leq \max\{B_0, \max b_2\}$$

provided that $B_0 \geq \bar{b}$.

Setting

$$a^-(t) = -\frac{\partial \lambda_1}{\partial A} \frac{A}{2c_1(A)e^{\bar{h}}} > 0, \tag{3.31}$$

$$a^+(t) = \frac{\partial \lambda_2}{\partial A} \frac{A}{2c_1(A)e^{\bar{h}}} > 0, \tag{3.32}$$

$$B(t) = r^{\pm} - q, \quad b_2 = -g, \quad b_1 = -g - \frac{b^{\pm}}{a}, \tag{3.33}$$

we can use Lemma 1 to obtain the main result of this section.

Theorem 1. *Assume that the initial data (A_0, Q_0) are such that* (3.22) *holds.*

I) If at least at one point $z \in \mathbb{R}$, either

$$r^{\pm}(0, z) < g(A_0) + \inf_{(A,Q) \in D} \left(-g(A) - \frac{b^{\pm}(A,Q)}{a^{\pm}(A)} \right) \tag{3.34}$$

holds, then the solution of system (3.28)–(3.29) *must develop a singularity at finite time.*

II) If

$$\inf_{(A,Q) \in D} \left(\frac{b^{\pm}(A,Q)}{a^{\pm}(A)} \right) \geq \sup_{A \in I} g(A) - \inf_{A \in I} g(A) + C\bar{f}\delta, \tag{3.35}$$

where $\delta > 0$, and $C > 0$ depending only on initial data $(A_0, Q_0)(z)$, and $I = [A_{min}, A_{max}]$, then the solution of system (3.28)–(3.29) *remains smooth for all time, provided that for every $z \in \mathbb{R}$*

$$r^{\pm}(0, z) \geq g(A_0(z)) + \sup_{(A,Q) \in D} \left(-g(A) - \frac{b^{\pm}(A,Q)}{a^{\pm}(A)} \right) + C\bar{f}\delta. \tag{3.36}$$

Moreover, the right hand side of (3.36) *is non-positive.*

Proof. We first prove that under condition (3.35), the right hand side of (3.35) is non-positive:

$$
\begin{aligned}
& g(A_0(z)) + \sup_{(A,Q)\in D}\left(-g(A) - \frac{b^{\pm}(A,Q)}{a^{\pm}(A)}\right) + C\bar{f}\delta \\
& \leq g(A_0(z)) + \sup_{(A,Q)\in D}(-g(A)) + \sup_{(A,Q)\in D}\left(-\frac{b^{\pm}(A,Q)}{a^{\pm}(A)}\right) + C\bar{f}\delta \\
& \leq \sup_{A\in I} g(A) - \inf_{A\in I} g(A) - \inf_{(A,Q)\in D}\frac{b^{\pm}(A,Q)}{a^{\pm}(A)} + C\bar{f}\delta \leq 0. \qquad (3.37)
\end{aligned}
$$

Under the conditions (3.22)–(3.23), equations (3.28)–(3.29) for $r^{\pm}$ are perturbations of ordinary differential equations of the form

$$
\frac{d}{dt}(r-g) + ar^2 + br = 0, \quad r(0) = r_0. \qquad (3.38)
$$

The above equation can be written as

$$
\frac{dB}{dt} + a(t)\left(B - b_1(t)\right)\left(B - b_2(t)\right) = 0, \quad B(0) = B_0, \qquad (3.39)
$$

where

$$
B(t) = r^{\pm} - q, \quad b_2 = -g, \quad b_1 = -g - \frac{b^{\pm}}{a}, \qquad (3.40)
$$

and we can use Lemma 1. □

We found specific limits when singularities occur in solutions and when smooth solutions can exist globally in a 1D model of fluid flow through a deformable pipe with a generic pressure. These limits are determined by the initial slope of the Riemann invariants and the initial cross-section. Our results confirm previous findings [93] that the presence of viscous damping delays shock formation and that the class of initial data for which global smooth solutions exist is richer than the one predicted by inviscid theory. As in [93], we can extend our results to the case where α is not equal to 1 but the difference $\alpha - 1$ is small.

3.2 Mathematical Model

In this section we summarize the mathematical models we use to describe the fluid flow inside a lymphangion and the action of the valves. First of all, we assume the lymph to be a Newtonian incompressible fluid similar to water [1]. The one-dimensional flow equations for a deformable vessel (see Section 2.5) are

$$
\frac{\partial A}{\partial t}(z,t) + \frac{\partial Q}{\partial z}(z,t) = 0, \qquad (3.41)
$$

$$
\frac{\partial Q}{\partial t}(z,t) + \alpha\frac{\partial}{\partial z}\left(\frac{Q(z,t)^2}{A(z,t)}\right) + \frac{A(z,t)}{\rho_0}\frac{\partial p}{\partial z}(z,t) = -\frac{2(\gamma+2)\pi\mu}{\rho_0}\frac{Q}{A}, \qquad (3.42)
$$

where $A(z,t)$ is the *cross sectional area*,

$$Q(z,t) = A(z,t)\bar{u}(z,t) \tag{3.43}$$

is the *mean flux*, $\bar{u}(z,t)$ is the *average velocity*, ρ_0 is the *density*, γ is a parameter dependent on the chosen velocity profile, and μ is the *viscosity*.

To close the system formed by equations (3.41)–(3.42), an additional relation between pressure $p(z,t)$ and cross-sectional area $A(z,t)$ is required and, inspired by [19], we choose the *tube law*:

$$p(z,t) = K(z,t)\psi(A(z,t);A_0(z)) + g(z,t) + p_{ext}(z,t), \quad \frac{\partial p}{\partial A} > 0, \tag{3.44}$$

with

$$\psi(A(z,t);A_0(z)) = \left(\frac{A(z,t)}{A_0(z)}\right)^{m(t)} - \left(\frac{A(z,t)}{A_0(z)}\right)^{n(t)} + C(t)\left[\left(\frac{A(z,t)}{A_0(z)}\right)^{x(t)} - 1\right], \tag{3.45}$$

where $p(z,t)$ is the *internal pressure*, $p_{ext}(z,t)$ is the *external pressure*, $p(z,t) - p_{ext}(z,t)$ is the *transmural pressure*, $A_0(z)$ is the *vessel cross-sectional area at zero transmural pressure* (equilibrium), $K(z,t)$, $g(z,t)$, $m(t)$, $n(t)$, $x(t)$ and $C(t)$ are time-dependent coefficients that must satisfy the relations $m \geq 0, n \leq 0, z \geq 0$, and $C \geq 0$ for every t to guarantee the hyperbolicity of the problem.

Since we suppose that the lymphangion contracts as a whole, the function K is given by [14, 19]

$$K(t) = K_{min} + s(t)(K_{max} - K_{min}), \tag{3.46}$$

where $s(t)$ is explicitly given as in [17, 18], and K_{min} and K_{max} are constants. We suppose that p_{ext} is constant in space and time, which means a uniform external pressure. Moreover, we have that the functions g, m, n, z and C depend only on time in the following way:

$$g(t) = g_1 + s(t)(g_2 - g_1),$$

$$\begin{aligned} m(t) &= m_1 + s(t)(m_2 - m_1), \\ n(t) &= n_1 + s(t)(n_2 - n_1), \\ x(t) &= x_1 + s(t)(x_2 - x_1), \\ C(t) &= C_1 + s(t)(C_2 - C_1), \end{aligned}$$

where g_1, g_2, $m_1 \geq 0, m_2 \geq 0, n_1 \leq 0, n_2 \leq 0, z_1 \geq 0, z_2 \geq 0, C_1 \geq 0, C_2 \geq 0$ are constant parameters given by the literature and by fitting the data in [17] (see Figure 3.2). We assume that g, m, n, z, and C depend on t to better fit the contraction data found in [17]; indeed, we have that the form of the pressure curve in the relaxation state is different with respect to the curve in the contracted state. In general, there can be other terms that are important for the contraction of the lymphangion wall due to the high deformations of the latter and that it would be worth studying in detail [28–30], but here we want to keep our model as simple as possible to have a more computationally feasible simulation and because we want to focus more on the fluid flow instead of the vessel wall.

The time-dependent parameter $s(t)$ describes the pulsation of the lymphangion and is taken as in [18]:

$$s(t) = \frac{m_{\text{scal}}}{2}\left[1 - \cos\left(2\pi f\left(\frac{t - t_c}{m_{\text{scal}}}\right)\right)\right], \tag{3.47}$$

where $\frac{1}{f}$ is the duration of systole (without the inhibitory effect given by the wall shear stress), t_c is the time in which the contraction starts, and m_{scal} is given by

$$m_{\text{scal}} = \left(\frac{1/f}{1/f + t_d}\right)^{\beta_m}, \tag{3.48}$$

where β_m is a parameter, and t_d is the time delay added to the relaxing time t_r (fitted by [17, 18]) due to the inhibition of the shear stress, and is given by [18]

$$t_{d0} = k_{tW}\left[\bar{\tau}(t_0) - \tau_{\text{thr}}\right] \tag{3.49}$$

for the initial time $t = t_0$ and

$$t_d(t_1) = k_{tW}\frac{1}{t_1 - t_0}\int_{t_0}^{t_1}\left[\bar{\tau}(t) - \tau_{\text{thr}}\right] dt \tag{3.50}$$

for a general time step $t = t_1$, where $\bar{\tau}(t)$ is the *average shear stress* of the fluid given by

$$\bar{\tau}(t) = \frac{1}{L}\int_0^L\left[\bar{u}(z,t)\mu\frac{\gamma + 2}{\sqrt{A(z,t)/\pi}}\right] dz, \tag{3.51}$$

where L is the length of the lymphangion and τ_{thr} is a fixed threshold. Hence we have that the relaxation time t_r is given by, fitting the data in [17]:

$$t_r = (60/((-1.39((\ln(1+(\overline{\Delta p})))^2) + 12.6\ln(1+(\overline{\Delta p})) + 0.647))), \quad \Delta p < 0 \tag{3.52}$$

where

$$\overline{\Delta p} = \int_{t_c}^{t_c+1/f}\Delta p dt, \tag{3.53}$$

or it is normalized as $t_r = 1\,\text{s}$ when $\Delta p \geq 0$, as in [18]; hence the total relaxation time T_r (the time in which the next pulsation starts) is

$$T_r = t_r + t_d, \tag{3.54}$$

where in the case $\Delta p \leq 0$ we have $t_d = 0$ (and in this case $T_r = t_r$).

Using this type of contraction state $s(t)$, we take into account the inhibition of the active lymph pump due to the shear stress given by the lymph flow [18, 43].

To model the valves we use the same approach as [19, 94] but the parameters are fitted to real data given by [15, 16, 24, 46]. The model is given by

$$\begin{cases} \dfrac{dQ_v}{dt} = \dfrac{1}{L(\xi)}\left(\Delta p(t) - R(\xi)Q_v - B(\xi)Q_v|Q_v|\right), \\ \dfrac{d\xi}{dt} = f_\xi(\xi, t), \end{cases} \tag{3.55}$$

where Q_v is the fluid flow passing through the valve, $\xi(t) \in [0,1]$ is the valve state ($\xi = 0$ is close and $\xi = 1$ is fully open),

$$\Delta p(t) = p_u(t) - p_d(t), \tag{3.56}$$

with p_u the upstream pressure and p_d the downstream pressure. Moreover, we have that

$$B(\xi) = \frac{\rho_0}{2A_{\text{eff}}^2(\xi)}, \tag{3.57}$$

$$L(\xi) = \rho_0 \frac{L_{\text{eff}}}{A_{\text{eff}}(\xi)}, \tag{3.58}$$

$$R(\xi) = \frac{2(\gamma+2)\pi\mu}{A_{\text{eff}}^2(\xi)}, \tag{3.59}$$

where B is the *Bernoulli resistance*, L is the *lymphatic inertia*, R is the *viscous resistance to flow*, L_{eff} is the effective valve length, A_{eff} is the effective area given by

$$A_{\text{eff}}(\xi) = A_{\text{eff,min}} + \xi(t)\left(A_{\text{eff,max}} - A_{\text{eff,min}}\right), \tag{3.60}$$

$$A_{\text{eff,min}} = M_{\text{rg}} A_0, \tag{3.61}$$

$$A_{\text{eff,max}} = M_{\text{st}} A_0, \tag{3.62}$$

where $0 \leq M_{\text{rg}} \leq 1$ is the *minimum valve closure* and $0 \leq M_{\text{st}} \leq 1$ is the *maximum valve opening.* Moreover, f_ξ is given by

$$f_\xi(\xi, t) = \begin{cases} K_{vo}\left(1-\xi\right)\left(\Delta p(t) - \Delta p_{\text{open}}\right) & \Delta p(t) > \Delta p_{\text{open}}, \\ K_{vc}\xi\left(\Delta p(t) - \Delta p_{\text{close}}\right) & \Delta p(t) < \Delta p_{\text{close}}, \\ 0 & \text{elsewhere}, \end{cases} \tag{3.63}$$

with K_{vo} is the valve opening rate and K_{vc} the valve closure rate, Δp_{open} is the opening threshold pressure and Δp_{close} is the closing threshold pressure.

3.3 Numerical Methods

This section describes the numerical methods adopted to solve the model exposed in the previous section. The algorithm is the following:

I) Fix the inlet and the outlet pressure p_{in} and p_{out}; p_{in} is the upstream pressure for the inlet valve and p_{out} is the downstream pressure for the outlet valve, the remaining downstream and upstream pressure are calculated according to equations (3.44) and (3.45).

II) Solve system (3.55) with the Lobatto IIIC method to obtain the flux value Q_v for the inlet and the outlet valve (we need to solve the system twice).

III) Use Q_v to obtain the inlet and outlet condition on the flux (3.72) and (3.73) and, consequently, the boundary cross-sectional area from equations (3.76) and (3.77).

IV) Solve system (3.41)–(3.42) with the two-step Lax-Wendroff method (3.69).

We implement these steps explicitly in Scilab.

As far as step (II) is concerned, the system of ODEs (3.55) is solved using the Lobatto IIIC method (as in [19]), which is a second-order implicit Runge-Kutta method.

For the system of equations (3.41) and (3.42) (step (IV)), we use the finite difference method, in particular, the *two step Lax-Wendroff scheme* [92, 96, 97]; to use this method, we need the conservative form of the system of equations (3.41) and (3.42), that in our case is

$$\frac{\partial U}{\partial t} + \frac{\partial F}{\partial z} = S(U), \tag{3.64}$$

where

$$U = \begin{bmatrix} A \\ Q \end{bmatrix}, \tag{3.65}$$

$$F = \begin{bmatrix} Q \\ \alpha\left(\frac{Q^2}{A}\right) + \frac{K(t)}{\rho_0} A_0 \left[\frac{m}{m+1}\left(\frac{A}{A_0}\right)^{m+1} - \frac{n}{n+1}\left(\frac{A}{A_0}\right)^{n+1} + C\frac{z}{z+1}\left(\frac{A}{A_0}\right)^{z+1}\right] \end{bmatrix}, \tag{3.66}$$

and

$$S = \begin{bmatrix} 0 \\ -\frac{2(\gamma+2)\pi\mu}{\rho_0}\frac{Q}{A} \end{bmatrix}. \tag{3.67}$$

We discretize the one-dimensional space variable with a uniform grid of width Δz; the time variable is discretized with a time-step Δt that must satisfy the *Courant-Friedrichs-Lewy condition* to have the stability of the numerical method, that is

$$\Delta t \le \frac{\Delta z}{\max\left(|\bar{u}| + \sqrt{\frac{A}{\rho_0}\frac{\partial p}{\partial A}}\right)}. \tag{3.68}$$

We call U_j^n the discretization of U at the n-time node t_n and j-space node x_j. The method takes the form

$$U_j^{n+1} = U_j^n - \frac{\Delta t}{\Delta x}\left(F(U_{j+1/2}^{n+1/2}) - F(U_{j-1/2}^{n+1/2})\right) + \frac{\Delta t}{2}\left(S(U_{j+1/2}^{n+1/2}) + S(U_{j-1/2}^{n+1/2})\right), \tag{3.69}$$

where

$$U_{j+1/2}^{n+1/2} = \frac{1}{2}\left(U_{j+1}^n + U_j^n\right) - \frac{\Delta t}{2\Delta x}\left(F(U_{j+1}^n) - F(U_j^n)\right) + \frac{\Delta t}{4}\left(S(U_{j+1}^n) + S(U_j^n)\right), \tag{3.70}$$

$$U_{j-1/2}^{n+1/2} = \frac{1}{2}\left(U_j^n + U_{j-1}^n\right) - \frac{\Delta t}{2\Delta x}\left(F(U_j^n) - F(U_{j-1}^n)\right) + \frac{\Delta t}{4}\left(S(U_j^n) + S(U_{j-1}^n)\right). \tag{3.71}$$

We need to impose the boundary condition for the first space step z_0 and for the last space step z_N ($0 = z_0 < z_1 < ... < z_N = L$) (step (III)); for both, we impose as boundary condition the flux Q_v passing through the valves, that is the solution of the system (3.55). Hence we have

$$Q_0^{n+1} = Q_v^i, \tag{3.72}$$

$$Q_N^{n+1} = Q_v^o, \tag{3.73}$$

where Q_0^{n+1} and Q_N^{n+1} are the fluxes evaluated at the points (z_0, t^{n+1}) and (z_N, t^{n+1}), respectively; Q_v^i is the flux passing through the inlet valve and Q_v^o is the flux passing through the outlet valve.

The boundary conditions for the cross-sectional areas A_0^n and A_N^n are then calculated according to the first equation of (3.69) [98], and we have, for the inlet condition,

$$A_0^{n+1} = A_0^n - \frac{\Delta t}{\Delta z}\left(Q_{1/2}^{n+1/2} - Q_{-1/2}^{n+1/2}\right), \tag{3.74}$$

where $Q_{-1/2}^{n+1}$ can be calculated in this way:

$$Q_0^{n+1/2} = \frac{1}{2}\left(Q_{-1/2}^{n+1/2} + Q_{1/2}^{n+1/2}\right) \implies Q_{-1/2}^{n+1/2} = 2Q_0^{n+1/2} - Q_{1/2}^{n+1/2}. \tag{3.75}$$

Then (3.74) becomes

$$A_0^{n+1} = A_0^n - 2\frac{\Delta t}{\Delta z}\left(Q_{1/2}^{n+1/2} - Q_0^{n+1/2}\right), \tag{3.76}$$

where $Q_0^{n+1/2}$ is given by the flux boundary condition (3.72) and $Q_{1/2}^{n+1/2}$ is calculated by equation (3.70).

For the outlet condition, we have (by similar computations)

$$A_N^{n+1} = A_N^n + 2\frac{\Delta t}{\Delta z}\left(Q_{N-1/2}^{n+1/2} - Q_N^{n+1/2}\right), \tag{3.77}$$

where $Q_N^{n+1/2}$ is given by the flux boundary condition (3.73) and $Q_{N-1/2}^{n+1/2}$ is calculated by equation (3.71).

3.4 Parameters

In this section, we describe the physiological parameters used in the model given in section 3.2. We suppose that the lymph is a Newtonian fluid similar to water, with a viscosity μ of 0.01 g/(cm s) and a density ρ_0 of 1 g/(cm^3). Moreover, for a Newtonian fluid, we have $\gamma = 2$ and $\alpha = \frac{4}{3}$ [74, 91].

For the parameters that describe the valve behavior, we use physiological or estimated data of a mesenteric lymphangion of a mouse. For the parameters Δp_{open} and Δp_{close}, we use the data found in [46] and fitted in [15]; the parameter curves are shown in Figure 3.1. As we can see, we have that the parameters Δp_{open} and Δp_{close} depend on the transmural pressure $p - p_{ext}$ in this way:

$$\Delta p_{\text{open}} = a_o - b_o p_{\text{tm,o}} - c_o\left[1 - \exp(-d_o(p_{\text{tm,o}}^2))\right], \tag{3.78}$$

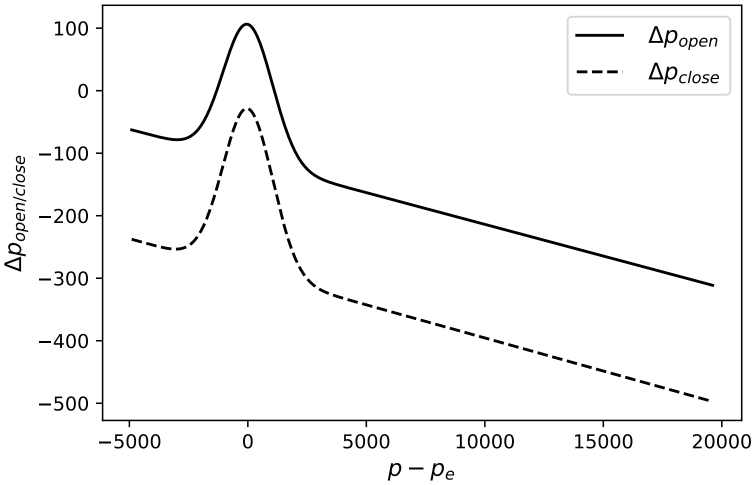

Figure 3.1: The variation of $\Delta p_{\text{open/close}}$ with respect to the transmural pressure (in dyne/cm^2), where for the opening valve threshold is $p_{\text{in}} - p_{ext}$, and for the closing valve threshold is $p_{\text{out}} - p_{ext}$.

$$\Delta p_{\text{close}} = O_{\text{scale}}\left[a_c - b_c p_{\text{tm,c}} - c_c\left(1 - \exp(-d_v(p^2_{\text{tm,c}}))\right)\right], \tag{3.79}$$

where $p_{\text{tm,o}} = p_{\text{in}} - p_{ext}$ is the transmural pressure for the opening valve threshold and $p_{\text{tm,c}} = p_{\text{out}} - p_{ext}$ is the transmural pressure for the closing valve threshold. The parameters $a_o = 106.14$, $b_o = 0.01$, $c_o = 218.5$, $d_o = 4.6 \times 10^{-7}$, $O_{\text{scale}} = 0.22103$, $a_c = -129.7$, $b_c = 0.0479$, $c_c = 1180.7498$, and $d_c = 4.54 \times 10^{-7}$ are obtained fitting the curves to the data as in [15]. These data have physiological meaning: first of all, we have that the opening and closing valve threshold both depend on the transmural pressure; second, we have that the thresholds are mostly negative, and this means that the valves are biased to stay open [16, 22, 24]. The other valve parameters are $M_{\text{rg}} = 0$, $M_{\text{st}} = 1$ [19], $K_{\text{vo}} = K_{\text{vc}} = 100\,\text{cm}^2/\,(s \text{ dyne})$ (estimated), $L_{\text{eff}} = 0.06$ cm (estimated).

Now we need to find the parameters for the pressure described in (3.44) and in (3.45). First of all, we need the value of A_0, that is the value of the cross-sectional area at zero transmural pressure. As we can see from the data obtained in [17] and shown in Figure 3.2, the value of A_0 changes in time because it is different for the relaxed and contracted state. For this reason we added the term $g(t)$ in the relation (3.44). We assume a value of A_0 in between the contracted and relaxed value, that is $A_0 = \pi\left(4 \times 10^{-3}\right)^2$ cm^2 $= 5 \times 10^{-5}\,\text{cm}^2$. To do this, we fitted the curves to experimental data given in [17], and we found $K_{min} = 1150\,\text{dyne/cm}^2$, $K_{max} = 793\,\text{dyne/cm}^2$, $g_1 = -500\,\text{dyne/cm}^2$, $g_2 = 2526\,\text{dyne/cm}^2$, $m_1 = 0.1$, $m_2 = 1.8$, $n_1 = -0.8$, $n_2 = -0.67$, $x_1 = 15.4$, $x_2 = 14.1$, $C_1 = 10^{-10}$, and $C_2 = 1.6 \times 10^{-9}$. We can see the fitting curves in Figure 3.2.

The parameters that regulate the inhibitory effect [18] are $f = 0.5\,\frac{1}{\text{s}}$, $k_{tW} = 1.2\,\frac{\text{s}}{\frac{\text{dyne}}{\text{cm}^2}}$, $\beta_m = 0.65$, and $\tau_{\text{thr}} = 1.1\,\frac{\text{dyne}}{\text{cm}^2}$. We have that the value of the parameter τ_{thr} is less than the one used in [18] (which is $3\,\frac{\text{dyne}}{\text{cm}^2}$); indeed, they found that this parameter may overestimate the value of any equivalent biological threshold

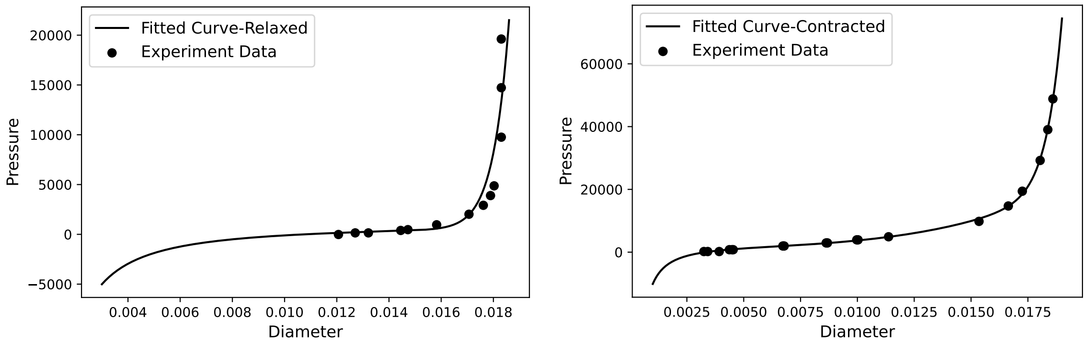

Figure 3.2: The variation of the transmural pressure $p - p_{ext}$ (in dyne/cm^2) with respect to the diameter D (in μm) in a relaxed (left) and in a contracted (right) state, given by the experiments of [17] (dots) and the fitted curve from the tube law described in equation (3.45).

which pertained to the circumstances of the mesenteric experiments of [43].

The values of the parameters are summarized in Table 3.1.

3.5 Numerical Results

In this section we show some numerical results of the models presented in the previous sections and we compare the results with those found in the literature.

The first simulation that we run is with the values $p_{\text{in}} = 2.5\,\text{cmH2O} \approx 2450\,\frac{\text{dyne}}{\text{cm}^2}$, $p_{\text{out}} = 5\,\text{cmH2O} \approx 4900\,\frac{\text{dyne}}{\text{cm}^2}$, and $p_{\text{ext}} = 1\,\text{cmH2O} \approx 980\,\frac{\text{dyne}}{\text{cm}^2}$, as in [24]. We show the results over time in Figure 3.3. The behavior and the values that we found are in agreement with [24]. When a contraction starts, there is a small delay as the inlet valve begins to close, and this implies a small retrograde flow at the start; when the outlet valve opens, the flow starts to get out of the lymphangion until the contraction starts to decrease and the outlet valve to close, in which case there is a small outlet retrograde flow. After that, the lymphangion fills up with an inlet positive flow when the contraction is about to end. There is a very steep transition between the open and close valve state, hence the values of K_{vo} and K_{vc} may overestimate the real ones (see [24]).

We note in Figure 3.3 that, when the valve are both closed, the diameter is constant in time; this is due to the fact that, at these times, we have that Q_v^i and Q_v^o are both zero, which implies that $\dfrac{\partial Q}{\partial z} = 0$, and we have, from equation (3.41)

$$\frac{\partial A}{\partial t} = 0 \implies \frac{\partial D}{\partial t} = 0, \tag{3.80}$$

where D is the lymphangion diameter, and it follows that D is constant in these times.

To see the inhibition effect on our model, we perform the same experiments presented in [18, 43]. We run the simulations with different (favorable) pressure

Name	Physiological Range/Value	Description
L	$0.3\,\mathrm{cm}$	Lymphangion length [19]
μ	$0.01\,\frac{\mathrm{g}}{\mathrm{cm\ s}}$	Viscosity [1, 17]
γ	2	Viscous Parameter [74, 91]
α	$\frac{4}{3}$	Coriolis parameter [74, 91]
ρ_0	$1\,\frac{\mathrm{g}}{\mathrm{cm}^3}$	Density [1, 17]
Δp_{open}	equation (3.78)	Valve opening threshold
$\Delta p_{\mathrm{close}}$	equation (3.78)	Valve closing threshold
a_o	106.14	Fitted parameter in equation (3.78)
b_o	0.01	Fitted parameter in equation (3.78)
c_o	218.5	Fitted parameter in equation (3.78)
d_o	4.6×10^{-7}	Fitted parameter in equation (3.78)
O_{scale}	0.22103	Fitted parameter in equation (3.79)
a_c	-129.7	Fitted parameter in equation (3.79)
b_c	0.0479	Fitted parameter in equation (3.79)
c_c	1180.7498	Fitted parameter in equation (3.79)
d_c	4.54×10^{-7}	Fitted parameter in equation (3.79)
M_{rg}	0	Minimum valve closure [22, 24]
M_{st}	1	Maximum valve opening [19, 94]
K_{vo}	$100\,\frac{1}{\mathrm{s}\frac{\mathrm{dyne}}{\mathrm{cm}^2}}$	Valve opening rate (estimated)
K_{vc}	$100\,\frac{1}{\mathrm{s}\frac{\mathrm{dyne}}{\mathrm{cm}^2}}$	Valve closing rate (estimated)
L_{eff}	$0.06\ \mathrm{cm}$	Effective valve length (estimated)
A_0	$5 \times 10^{-5}\,\mathrm{cm}^2$	Cross-sectional area at zero transmural pressure (estimated and [17])
K_{min}	$1150\,\frac{\mathrm{dyne}}{\mathrm{cm}^2}$	Fitted parameter in equation (3.45)
K_{max}	$793\,\frac{\mathrm{dyne}}{\mathrm{cm}^2}$	Fitted parameter in equation (3.45)
g_1	$-500\,\frac{\mathrm{dyne}}{\mathrm{cm}^2}$	Fitted parameter in equation (3.44)
g_2	$2526\,\frac{\mathrm{dyne}}{\mathrm{cm}^2}$	Fitted parameter in equation (3.44)
m_1	0.1	Fitted parameter in equation (3.45)
m_2	1.8	Fitted parameter in equation (3.45)
n_1	-0.8	Fitted parameter in equation (3.45)
n_2	-0.67	Fitted parameter in equation (3.45)
x_1	15.4	Fitted parameter in equation (3.45)
x_2	14.1	Fitted parameter in equation (3.45)
C_1	10^{-10}	Fitted parameter in equation (3.45)
C_2	1.6×10^{-9}	Fitted parameter in equation (3.45)
f	$0.5\ 1/\mathrm{s}$	Systole frequency [17–19]
k_{tW}	$1.2\,\frac{s}{\frac{\mathrm{dyne}}{\mathrm{cm}^2}}$	Inhibition parameter [18].
β_m	0.65	Inhibition parameter [18]
τ_{thr}	$1.1\,\frac{\mathrm{dyne}}{\mathrm{cm}^2}$	Wall shear stress threshold (estimated)

Table 3.1: Physiological and estimated parameters.

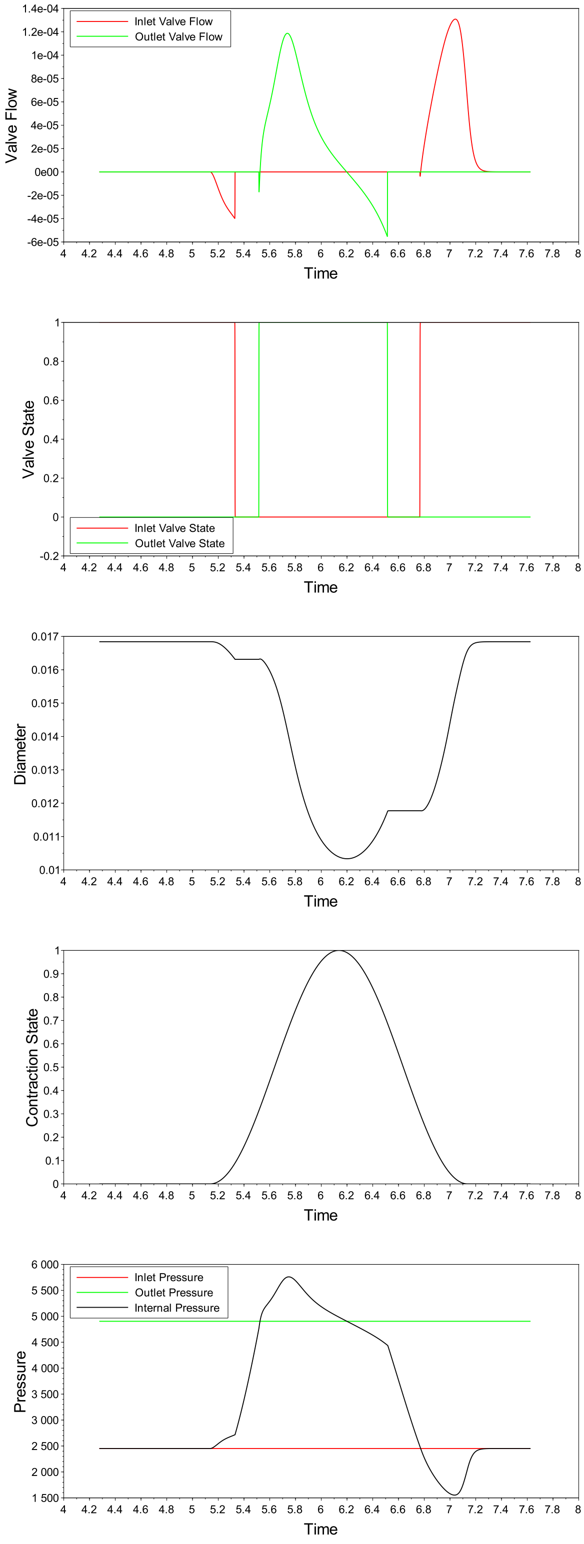

Figure 3.3: The numerical results with $p_{\text{in}} \approx 2450\,\frac{\text{dyne}}{\text{cm}^2}$, $p_{\text{out}} \approx 4900\,\frac{\text{dyne}}{\text{cm}^2}$, and $p_{\text{ext}} \approx 980\,\frac{\text{dyne}}{\text{cm}^2}$, with respect to time. In the first plot we can see the fluid flow passing through the valves (in $\frac{\text{cm}^3}{s}$), in the second the valve state (1 – open valve, 0 – close valve), in the third the lymphangion diameter (in cm), in the fourth the contraction state, and in the last the pressure (inlet, outlet, and calculated at the center of the lymphangion, in $\frac{\text{dyne}}{\text{cm}^2}$).

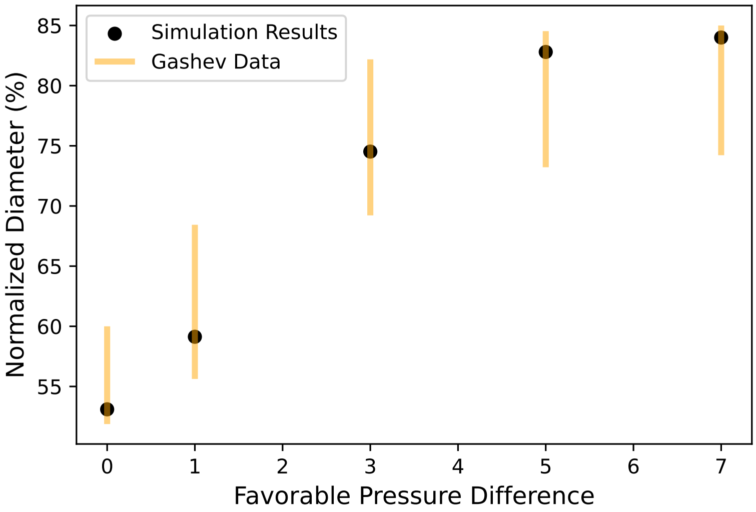

Figure 3.4: The data obtained by the results of our model compared with the results found in [43], with favorable pressure difference calculated as in equations (3.81) and (3.82) in cmH2O, with $p_{\text{ext}} = 1\,\text{cmH2O} \approx 980\,\frac{\text{dyne}}{\text{cm}^2}$.

differences

$$\Delta p = p_{\text{in}} - p_{\text{out}} = 0, 1, 3, 5, 7\,\text{cmH2O} \approx 0, 980, 2940, 4900, 6865\,\frac{\text{dyne}}{\text{cm}^2}, \tag{3.81}$$

and

$$\frac{1}{2}\left(p_{\text{in}} + p_{\text{out}}\right) = 5\,\text{cmH2O} \approx 4900\,\frac{\text{dyne}}{\text{cm}^2}, \tag{3.82}$$

with $p_{\text{ext}} = 1\,\text{cmH2O} \approx 980\,\frac{\text{dyne}}{\text{cm}^2}$.

We can see the results in Figure 3.4. The *normalized diameter* is calculated as

$$\frac{D_{\text{syst}}}{D_{\text{diast}}} \times \text{freq}, \tag{3.83}$$

where D_{syst} is the *systolic diameter* (the diameter when the lymphangion is contracted), D_{diast} is the *diastolic diameter* (the diameter when the lymphangion is relaxed), and freq is the frequency in the case $\Delta p = 0$ cmH2O in [43]. As we can see, the value of our numerical results are in agreement with the value found in the mesenteric experiments of [43].

3.6 Conclusions

In this chapter we proposed a mathematical model for the flow of the interstitial fluid (lymph) in a lymphangion. We assumed the lymph to be an incompressible fluid similar to water so that we could use the governing equations derived in Section 2.5. First of all, inspired by [93], we found the critical threshold related to the model of a fluid flow through a compliant pipe. In our more general case we confirmed the results presented in [93], which says first of all that shock formation due to the viscous damping term is delayed compared with the shock formation without viscous damping (which is physically expected) and second that the class of initial data for which global smooth solutions exist is richer than the one predicted by inviscid theory.

Moreover, we proposed a model in which we described a more realistic lymphangion; to describe the valve behavior we used the model presented in [94] with physiological parameters found in the literature [15, 46] or estimated; the valve behavior is in agreement with the literature [15, 17, 24, 46]. For the contraction behavior, we fitted physiological data found in [17, 18]: as we mentioned before, the description of the wall behavior is largely phenomenological; we chose this type of approach because we were more interested in the fluid behavior and we wanted to run more feasible numerical simulations, but keeping realistic wall behavior results.

We compared our numerical results with experiments and results found in literature [17, 24, 43], and we found that the proposed model agrees with those data.

Chapter 4

Simplified Cylindrical Model of a Lymph Node

The aim of this chapter is to propose a mathematical model for the flow of the interstitial fluid in a lymph node in a cylindrical geometry with a laminar flow driven by a pulsatile pressure gradient [9]. The model proposed here is very idealized and is a starting point for more advanced studies on the subject. To begin with, we assume that the lymph node is essentially composed of two parts: a porous medium, characterized by a permeability constant K, surrounded by a thin channel in which lymph can flow freely. We describe the motion of the interstitial fluid within the lymph node using the Darcy-Brinkman equation in the porous core and the Navier-Stokes equation in the external channel. The motion is induced by a pulsatile gradient of pressure, so it has to be non-stationary. The lymph is composed mainly of water [1], hence we assume the incompressibility of the fluid. The geometry of the problem is summarized in Figure 4.1.

In Sections 4.1 and 4.2 we find an explicit solution in the case of a cylindrical lymph node with a laminar flow in the presence of a pulsatile pressure gradient. More precisely, in Section 4.1 we employ the Fourier method in order to write the solution as a series expansion of Bessel functions, while in Section 4.2 we find the explicit solution for the long-time periodic behavior.

The results found in this chapter are published in [9].

4.1 Solving the Problem in a very Simplified Geometry

As mentioned in Section 1.2, the geometry of a lymph node is very complex. To begin with, we will assume a much more simplified geometry, so that we can find an explicit expression for the solution even in the presence of a pulsatile pressure gradient. We can see the geometry of our problem in Figure 4.1. More precisely, the lymph node is here represented by a cylinder and it is permeated by an incompressible homogeneous Newtonian fluid. The incompressibility constraint is motivated by the fact that the interstitial fluid is essentially a water solvent [1].

The region $r \in [0, R_1]$ represents the lymphoid compartment (LC), and the

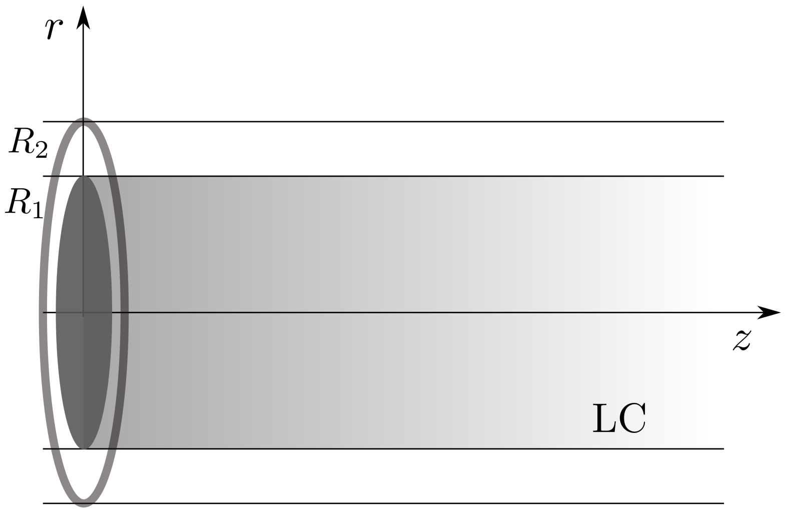

Figure 4.1: Physical configuration and coordinate system.

region $r \in [R_1, R_2]$ represents the subcapsular sinus (SCS). For simplicity, we assume that the boundaries do not perform any contraction. This assumption is motivated by the fact that the contractions of the boundaries of the lymph node have a very long period with respect to the pressure gradient [99].

We treat the part of the lymph inside the LC as a porous medium, describing the flow by the Darcy-Brinkman equation, while outside the LC we use the Navier-Stokes equation. Hence, the flow of the fluid in the absence of body forces is governed by

$$\rho_0 \frac{\partial \boldsymbol{v}}{\partial t} + \rho_0 (\nabla \boldsymbol{v}) \boldsymbol{v} = -\nabla p - \frac{\mu}{K} \boldsymbol{v} + \mu \Delta \boldsymbol{v} \tag{4.1}$$

for $r \in [0, R_1]$ (inside the LC) and by

$$\rho_0 \frac{\partial \boldsymbol{v}}{\partial t} + \rho_0 (\nabla \boldsymbol{v}) \boldsymbol{v} = -\nabla p + \mu \Delta \boldsymbol{v} \tag{4.2}$$

for $r \in (R_1, R_2]$ (outside the LC), together with the incompressibility constraint

$$\nabla \cdot \boldsymbol{v} = 0.$$

Here ρ_0 is the constant density of the lymph, μ the constant viscosity, K the (constant) permeability of the LC and $\boldsymbol{v}$ and p are the velocity and the pressure field of the lymph, respectively.

Thanks to the symmetry of this idealized problem, we look for a laminar velocity field of the form

$$\boldsymbol{v} = v_z(r, t) \boldsymbol{e}_z, \tag{4.3}$$

where $\boldsymbol{e}_z$ is the axis of the cylinder and r the radial coordinate. In particular, the incompressibility constraint $\nabla \cdot \boldsymbol{v} = 0$ is automatically satisfied.

Notice that the laminarity assumption is quite restrictive, especially because it prevents any flow of the fluid from the LC to the external region, and *vice versa.*

As far as the boundary and initial conditions are concerned, we assume:

$$v_z(R_2,t) = 0 \text{ (no-slip condition)}, \tag{4.4}$$

$$v_z(0,t) \text{ bounded}, \tag{4.5}$$

$$v_z \in C^1 \text{ (smoothness condition)}, \tag{4.6}$$

$$v_z(r,0) = v_{z0}(r) \text{ (initial condition)}. \tag{4.7}$$

Then, equations $(4.1)_1$ and $(4.2)_1$ reduce to

$$\begin{aligned} &\frac{\partial v_z}{\partial t} - \nu \frac{1}{r}\frac{\partial}{\partial r}\left(r\frac{\partial v_z}{\partial r}\right) + \frac{\nu}{K}v_z = g(t) \quad && r \in [0,R_1], \\ &\frac{\partial v_z}{\partial t} - \nu \frac{1}{r}\frac{\partial}{\partial r}\left(r\frac{\partial v_z}{\partial r}\right) = g(t) && r \in (R_1,R_2], \end{aligned} \tag{4.8}$$

where we put $-\frac{1}{\rho_0}\frac{\partial p}{\partial z} = g(t)$ and $\nu = \mu/\rho_0$. Introducing the *characteristic function of a set* A

$$\chi_A(x) = \begin{cases} 1 & \text{if } x \in A \\ 0 & \text{if } x \notin A \end{cases} \tag{4.9}$$

then (4.8) can be written as

$$\frac{\partial v_z}{\partial t} - \nu \frac{1}{r}\frac{\partial}{\partial r}\left(r\frac{\partial v_z}{\partial r}\right) + \chi_{[0,R_1]}\frac{\nu}{K}v_z = g(t). \tag{4.10}$$

Denoting with $v_z^{(1)}$ the solution in $[0,R_1]$ and with $v_z^{(2)}$ the solution in $(R_1,R_2]$, the smoothness condition (4.6) implies that, for every t:

$$v_z^{(1)}(R_1,t) = v_z^{(2)}(R_1,t), \quad \frac{\partial v_z^{(1)}}{\partial r}(R_1,t) = \frac{\partial v_z^{(2)}}{\partial r}(R_1,t). \tag{4.11}$$

The problem is a linear PDE in the form

$$\frac{1}{\nu}\frac{\partial v_z}{\partial t} + Lv_z = \frac{1}{\nu}g(t), \tag{4.12}$$

where

$$Lu = -\frac{1}{r}\frac{\partial}{\partial r}\left(r\frac{\partial u}{\partial r}\right) + \chi_{[0,R_1]}\frac{1}{K}u \tag{4.13}$$

is a linear operator; hence it is useful to characterize the eigenvalues (λ_k) and the eigenfunctions (ϕ_k) of the operator L in (4.13):

$$L\phi_k = \lambda_k\phi_k \tag{4.14}$$

with $\phi_k(0)$ bounded, $\phi_k(R_2) = 0$ and ϕ_k of class C^1 in R_1.

4.1.1 Eigenvalues of the Linear Operator

It is easy to prove that the eigenvalues λ_k are positive; however, it is convenient to consider the two cases $\lambda_k < 1/K$ and $\lambda_k \geq 1/K$. Since by a standard change of variables the equation $L\phi_k = \lambda_k \phi_k$ can be put in the form of a Bessel equation with $\nu = 0$, then the eigenfunctions can be written as a linear combination of J_0 and Y_0, the Bessel functions of order 0 of the first and second kind, respectively:

$$\phi_k(r) := \begin{cases} \bar{A}_k J_0\left(r\sqrt{\lambda_k - \dfrac{1}{K}}\right) + \bar{B}_k Y_0\left(r\sqrt{\lambda_k - \dfrac{1}{K}}\right) & r \in [0, R_1] \\ A_k J_0\left(r\sqrt{\lambda_k}\right) + B_k Y_0\left(r\sqrt{\lambda_k}\right) & r \in (R_1, R_2]. \end{cases} \tag{4.15}$$

Notice that in the case $\lambda_k < 1/K$ the argument of the Bessel functions in the first case is imaginary, hence we can rewrite it as

$$\bar{A}_k I_0\left(r\sqrt{\frac{1}{K} - \lambda_k}\right) + \bar{B}_k K_0\left(r\sqrt{\frac{1}{K} - \lambda_k}\right) \quad r \in [0, R_1], \tag{4.16}$$

by using the *modified* Bessel functions I_0, K_0.

Now we impose the boundedness at $r = 0$, the smoothness at $r = R_1$ and the vanishing boundary condition at $r = R_2$. Since Y_0 and K_0 are unbounded in the origin, we must impose $\bar{B}_k = 0$, obtaining the following linear system:

$$\begin{cases} \bar{A}_k J_0\left(R_1\sqrt{\lambda_k - \dfrac{1}{K}}\right) - A_k J_0\left(R_1\sqrt{\lambda_k}\right) - B_k Y_0\left(R_1\sqrt{\lambda_k}\right) = 0 \\ -\bar{A}_k\sqrt{\lambda_k - \dfrac{1}{K}} J_1\left(R_1\sqrt{\lambda_k - \dfrac{1}{K}}\right) + A_k\sqrt{\lambda_k} J_1\left(R_1\sqrt{\lambda_k}\right) + B_k\sqrt{\lambda_k} Y_1\left(R_1\sqrt{\lambda_k}\right) = 0 \\ A_k J_0\left(R_2\sqrt{\lambda_k}\right) + B_k Y_0\left(R_2\sqrt{\lambda_k}\right) = 0 \end{cases} \tag{4.17}$$

where we should replace

$$J_0\left(R_1\sqrt{\lambda_k - \frac{1}{K}}\right) \quad \text{with} \quad I_0\left(R_1\sqrt{\frac{1}{K} - \lambda_k}\right) \tag{4.18}$$

$$-\sqrt{\lambda_k - \frac{1}{K}} J_1\left(R_1\sqrt{\lambda_k - \frac{1}{K}}\right) \quad \text{with} \quad \sqrt{\frac{1}{K} - \lambda_k} I_1\left(R_1\sqrt{\frac{1}{K} - \lambda_k}\right) \tag{4.19}$$

in the case $\lambda_k < 1/K$. The first two equations in (4.17) come from the smoothness at R_1 and the last equation from the boundary condition (and we used the fact that $J_0' = -J_1$, $Y_0' = -Y_1$ and $I_0' = I_1$). Then the eigenvalues of the linear operator L defined in (4.13) can be found imposing that the linear system (4.17) has nontrivial solutions, *i.e.*

$$\det \mathsf{A} = 0, \tag{4.20}$$

where A is the 3×3 matrix of the linear system in the unknowns $\bar{A}_k, A_k, B_k$. Figure 4.2 represents a numerical plot of the curve $y = \det \mathsf{A}$: as one can see,

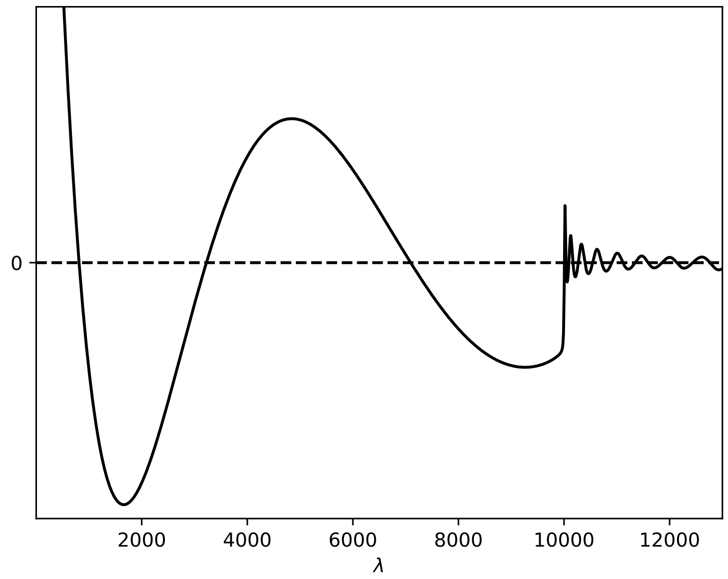

Figure 4.2: The graph of the function $y = \det \mathsf{A}$ for $R_1 = 0.9\,\mathrm{cm}$, $R_2 = 1\,\mathrm{cm}$, $K = 10^{-4}\,\mathrm{cm}^2$. For a better presentation, we normalized the function dividing by the quantity $1 + J_0\Big(R_1\sqrt{\lambda - \frac{1}{K}}\Big)$.

there is an increasing unbounded sequence (λ_k) of simple zeroes of the equation. In that case there are three eigenvalues smaller than $1/K$, the first eigenvalue being $\lambda_1 \simeq 813.305$.

Then, for every eigenvalue λ_k one can solve the linear system (4.17), finding the coefficients $\bar{A}_k, A_k, B_k$ and hence the corresponding eigenfunction ϕ_k from equation (4.15), up to a multiplicative factor.

4.1.2 Orthogonality of the eigenfunctions

By standard methods one can prove that two eigenfunctions ϕ_k, ϕ_h defined in (4.15), corresponding to different eigenvalues λ_k, λ_h, are orthogonal with respect to the weighted scalar product in L^2 (keeping in mind that r is the radial coordinate), namely:

$$\lambda_k \neq \lambda_h \quad \Rightarrow \quad \int_0^{R_2} r\phi_k(r)\phi_h(r)\,dr = 0. \tag{4.21}$$

Indeed, the two eigenfunctions satisfy the equations

$$r\frac{\partial^2 \phi_k}{\partial r^2} + \frac{\partial \phi_k}{\partial r} - r\chi_{[0,R_1]}\frac{1}{K}\phi_k + r\lambda_k\phi_k = 0, \tag{4.22}$$

$$r\frac{\partial^2 \phi_h}{\partial r^2} + \frac{\partial \phi_h}{\partial r} - r\chi_{[0,R_1]}\frac{1}{K}\phi_h + r\lambda_h\phi_h = 0. \tag{4.23}$$

Multiplying the first equation by ϕ_h and the second by ϕ_k and taking the difference, we get

$$\frac{\partial}{\partial r}\left(r\Big(\phi_h\frac{\partial\phi_k}{\partial r}-\phi_k\frac{\partial\phi_h}{\partial r}\Big)\right)=(\lambda_h-\lambda_k)r\phi_k\phi_h. \tag{4.24}$$

Integrating between 0 and R_2 and keeping into account that $\phi_k(R_2)=\phi_h(R_2)=0$, we obtain

$$(\lambda_k-\lambda_h)\int_0^{R_2} r\phi_k(r)\phi_h(r)\,dr=0, \tag{4.25}$$

which gives the orthogonality whenever $\lambda_k\neq\lambda_h$. Moreover, by using the formulas (see [100, (10) p. 134])

$$\int xJ_0^2(x)\,dx=\frac{x^2}{2}[J_0^2(x)+J_1^2(x)], \tag{4.26}$$

$$\int xY_0^2(x)\,dx=\frac{x^2}{2}[Y_0^2(x)+Y_1^2(x)], \tag{4.27}$$

$$\int xI_0^2(x)\,dx=\frac{x^2}{2}[I_0^2(x)-I_1^2(x)], \tag{4.28}$$

$$\int xJ_0(x)Y_0(x)\,dx=\frac{x^2}{2}[J_0(x)Y_0(x)+J_1(x)Y_1(x)], \tag{4.29}$$

one can prove that

$$\begin{aligned}\int_0^{R_2} r\phi_k^2(r)\,dr=&\frac{R_1^2}{2K\lambda_k}\left[\bar{A}_kJ_1\Big(R_1\sqrt{\lambda_k-\frac{1}{K}}\Big)\right]^2\\&+\frac{R_2^2}{2}\left[A_kJ_1\left(R_2\sqrt{\lambda_k}\right)+B_kY_1\left(R_2\sqrt{\lambda_k}\right)\right]^2\end{aligned} \tag{4.30}$$

in case $\lambda_k\geq 1/K$, and

$$\begin{aligned}\int_0^{R_2} r\phi_k^2(r)\,dr=&-\frac{R_1^2}{2K\lambda_k}\left[\bar{A}_kI_1\Big(R_1\sqrt{\frac{1}{K}-\lambda_k}\Big)\right]^2\\&+\frac{R_2^2}{2}\left[A_kJ_1\left(R_2\sqrt{\lambda_k}\right)+B_kY_1\left(R_2\sqrt{\lambda_k}\right)\right]^2\end{aligned} \tag{4.31}$$

in case $\lambda_k<1/K$. From now on we will assume that the sequence of eigenfunctions is *normalized*, that is

$$\int_0^{R_2} r\phi_k^2(r)\,dr=1. \tag{4.32}$$

4.1.3 Fourier Coefficients and Long-Time Behavior

In order to give an explicit form of the solution of the PDE (4.12), let us introduce the Fourier coefficients

$$c_k:=\int_0^{R_2} r\phi_k(r)\,dr, \tag{4.33}$$

so that

$$\sum_{k=1}^{\infty}c_k\phi_k(r)=1. \tag{4.34}$$

By using the formula (see [100, (1) p. 132])

$$\int r Z_0(r)\, dr = r Z_1(r), \quad Z = J, Y, I \tag{4.35}$$

we have

$$c_k = \frac{R_1 \bar{A}_k}{K\lambda_k \sqrt{\lambda_k - \frac{1}{K}}} J_1\Big(R_1\sqrt{\lambda_k - \frac{1}{K}}\Big) + \frac{R_2}{\sqrt{\lambda_k}}\left[A_k J_1\left(R_2\sqrt{\lambda_k}\right) + B_k Y_1\left(R_2\sqrt{\lambda_k}\right)\right] \tag{4.36}$$

in case $\lambda_k \geq 1/K$ and

$$c_k = \frac{R_1 \bar{A}_k}{K\lambda_k \sqrt{\frac{1}{K} - \lambda_k}} I_1\Big(R_1\sqrt{\frac{1}{K} - \lambda_k}\Big) + \frac{R_2}{\sqrt{\lambda_k}}\left[A_k J_1\left(R_2\sqrt{\lambda_k}\right) + B_k Y_1\left(R_2\sqrt{\lambda_k}\right)\right] \tag{4.37}$$

in case $\lambda_k < 1/K$.

Taking the solution in the form

$$v_z(r,t) = \sum_{k=1}^{\infty} v_k(t)\phi_k(r), \tag{4.38}$$

we can rewrite (4.12) as

$$\frac{1}{\nu}\sum_{k=1}^{\infty} v_k'(t)\phi_k(r) + \sum_{k=1}^{\infty} \lambda_k v_k(t)\phi_k(r) = \frac{g(t)}{\nu}\sum_{k=1}^{\infty} c_k\phi_k(r). \tag{4.39}$$

Multiplying by $r\phi_k(r)$ and integrating on $[0, R_2]$, we find the sequence of ODEs

$$\frac{1}{\nu}v_k'(t) + \lambda_k v_k(t) = \frac{c_k}{\nu}g(t), \qquad k \geq 1, \tag{4.40}$$

which can be easily solved:

$$v_k(t) = e^{-\nu\lambda_k t}\left(v_k(0) + c_k\int_0^t e^{\nu\lambda_k\tau}g(\tau)\, d\tau\right). \tag{4.41}$$

The coefficients $v_k(0)$ can be computed by writing the Fourier coefficients of the initial datum

$$v_z(r,0) = v_{z0}(r), \quad r \in [0, R_2], \tag{4.42}$$

that is

$$v_k(0) = \int_0^{R_2} v_{z0}(r)\phi_k(r)\, dr, \tag{4.43}$$

$$\sum_{k=1}^{\infty} v_k(0)\phi_k(r) = v_{z0}(r). \tag{4.44}$$

Since $\lambda_k > 0$, it is easy to see that for $t \to +\infty$ one has

$$v_k(t) \approx e^{-\nu\lambda_k t}c_k\int_0^t e^{\nu\lambda_k\tau}g(\tau)\, d\tau, \tag{4.45}$$

R_1	$0.9\,\mathrm{cm}$
R_2	$1\,\mathrm{cm}$
ρ_0	$1\,\mathrm{g\,cm^{-3}}$
μ	$0.015\,\mathrm{g\,cm^{-1}\,s^{-1}}$
C	$0.05\,\mathrm{g\,cm^{-2}\,s^{-2}}$
G	$20\,\mathrm{g\,cm^{-2}\,s^{-2}}$
ω	π
K	$10^{-4}\,\mathrm{cm^2}$

Table 4.1: Numerical values of the parameters inspired by the physical quantities of the lymph node [6] or estimated.

hence the long-time behavior of the solution does not depend on the initial datum.

As an example, let us assume a harmonic pulsatile pressure gradient of the form

$$\frac{\partial p}{\partial z} = C + G\cos\omega t, \tag{4.46}$$

where C is the pressure drop of the basic flow and the constants G, ω determine the pulsatility of the motion. Then

$$g(t) = -\frac{1}{\rho_0}(C + G\cos\omega t) \tag{4.47}$$

and one can explicitly compute the Fourier coefficients for the long-time behavior:

$$v_k(t) \approx -\frac{G\nu\lambda_k\omega\sin\omega t + G\nu^2\lambda_k^2\cos\omega t + C\omega^2 + C\nu^2\lambda_k^2}{\nu\lambda_k\rho_0(\omega^2+\nu^2\lambda_k^2)}. \tag{4.48}$$

The long-time solution then behaves as

$$-\sum_{k=1}^{\infty}\frac{G\nu\lambda_k\omega\sin\omega t + G\nu^2\lambda_k^2\cos\omega t + C\omega^2 + C\nu^2\lambda_k^2}{\nu\lambda_k\rho_0(\omega^2+\nu^2\lambda_k^2)}\phi_k(r), \tag{4.49}$$

which is represented in Figure 4.3 using the first 40 eigenfunctions and the values in Table 4.1. We can notice a periodic profile with a period of 2 s.

4.2 The explicit expression of the long-time solution

In this section, we give an explicit form of the long-time periodic solution of the problem. Actually, we look for an explicit solution of (4.10) of the form

$$v_z(r,t) = v_p(r) + Re\left(U(r)e^{i\omega t}\right), \tag{4.50}$$

where $U(r)$ has to be determined and v_p is the velocity of the Poiseuille part of the flow.

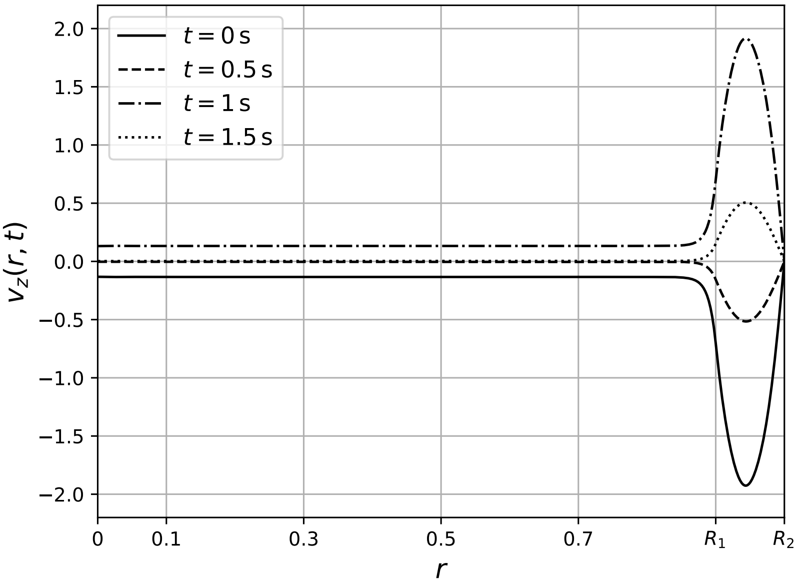

Figure 4.3: The long-time behavior of the solution. The parameters are given in Table 4.1.

We recall that the Poiseuille flow refers to the steady laminar solution of problem (4.1)-(4.2). Hence we search a solution $\boldsymbol{v} = v_p(r)\boldsymbol{e}_z$ of

$$-\nu\frac{1}{r}\frac{\partial}{\partial r}\left(r\frac{\partial v_p}{\partial r}\right) + \chi_{[0,R_1]}\frac{\nu}{K}v_p = -\frac{1}{\rho_0}C, \tag{4.51}$$

where C is the pressure drop in z-direction. Moreover, v_p satisfies the following boundary conditions

$$v_p(R_2) = 0 \text{ (no-slip condition)}, \tag{4.52}$$

$$v_p(0) \text{ bounded}, \tag{4.53}$$

$$v_p \in C^1 \text{ (smoothness condition)}. \tag{4.54}$$

After some calculations, we get

$$v_p(r) = \begin{cases} Re\left(-\dfrac{C}{\mu}K + c_5 J_0(\xi_p(r))\right) & r \in [0, R_1], \\ Re\left(\dfrac{C}{4\mu}r^2 + c_6 \log r + c_7\right) & r \in (R_1, R_2], \end{cases} \tag{4.55}$$

where J_0 is the Bessel functions of order 0 of the first kind,

$$\xi_p(r) = ir/\sqrt{K}, \tag{4.56}$$

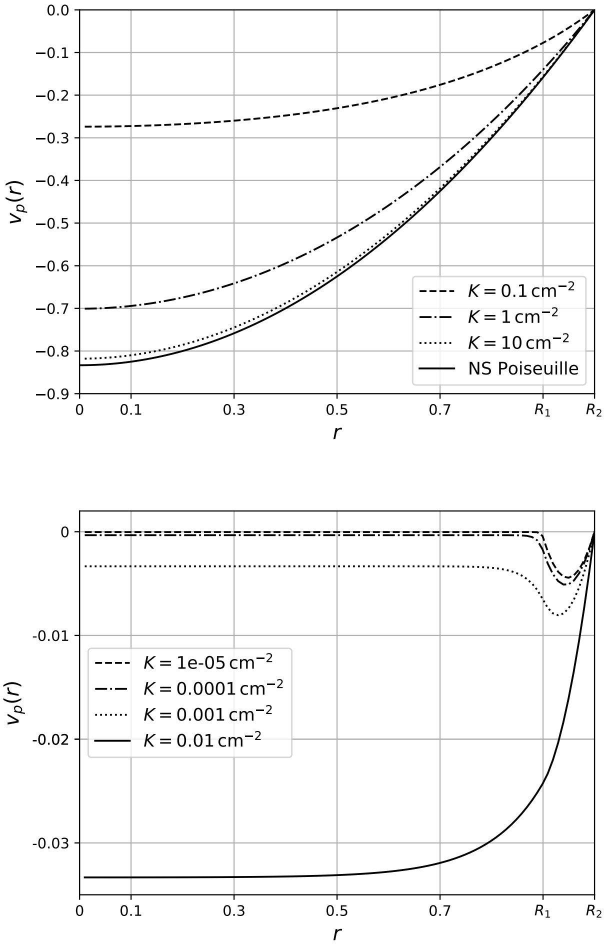

Figure 4.4: Profile of the Poiseuille flow given in (4.55), for several values of the permeability K.

and c_5, c_6, c_7 are obtained by the boundary conditions and are

$$c_5 = -\frac{1}{aJ_1(\xi_p(R_1))}\left(\frac{C}{2\mu}R_1 + \frac{c_6}{R_1}\right), \tag{4.57}$$

$$c_6 = -\frac{C}{4\mu}\frac{4K + R_1^2 - R_2^2 + 2R_1\frac{J_0(\xi_p(R_1))}{aJ_1(\xi_p(R_1))}}{\frac{J_0(\xi_p(R_1))}{aR_1J_1(\xi_p(R_1))} - \log\frac{R_2}{R_1}}, \tag{4.58}$$

$$c_7 = -\frac{C}{4\mu}R_2^2 - c_6\log R_2, \tag{4.59}$$

where $a = \frac{i}{\sqrt{K}}$.

The behavior of v_p is shown in Figure 4.4 for several values of K. One can see that the profile of the velocity is similar to the classical Poiseuille profile for large values of K, while if $K \leq 0.001$ then the porous region LC slows the passage of the flow.

We now put (4.50) in (4.10) and simplify the exponential part, obtaining

$$U''(r) + \frac{1}{r}U'(r) - \left(\chi_{[0,R_1]}\frac{1}{K} + \frac{i\rho_0\omega}{\mu}\right)U(r) = \frac{G}{\mu}, \tag{4.60}$$

which is a second order ODE in the form of a Bessel equation. Hence, its solution can be written in the form:

$$U(r) = \begin{cases} -\dfrac{GK}{\mu + i\rho_0\omega K} + \bar{A}J_0(\xi_K(r)) + \bar{B}Y_0(\xi_K(r)) & r \in [0, R_1], \\ \dfrac{iG}{\omega\rho_0} + AJ_0(\xi(r)) + BY_0(\xi(r)) & r \in (R_1, R_2], \end{cases} \tag{4.61}$$

with J_0 and Y_0 are Bessel functions of the first and second kind and ξ_K, ξ are complex variables related to the radius r:

$$\xi_K(r) = i\sqrt{\frac{1}{K} + \frac{i\omega\rho_0}{\mu}}r, \qquad \xi(r) = \frac{i-1}{\sqrt{2}}\sqrt{\frac{\omega\rho_0}{\mu}}r. \tag{4.62}$$

The constants $\bar{A}$, $\bar{B}$, A and B have to be determined using the boundary conditions.

From the no-slip condition (4.4), we have

$$U(R_2) = 0 \quad \Rightarrow \quad \frac{iG}{\omega\rho_0} + AJ_0(\xi(R_2)) + BY_0(\xi(R_2)) = 0, \tag{4.63}$$

while the boundedness in $r = 0$ (4.5) gives

$$\bar{B} = 0. \tag{4.64}$$

Finally, we impose condition (4.6) and after some calculations we get

$$\begin{aligned}
\Xi =& \frac{\xi_K'(r)}{\xi'(r)} = \frac{\sqrt{2}}{2}(1-i)\sqrt{\frac{\mu + iK\rho_0\omega}{K\rho_0\omega}}, \qquad &(4.65)\\
d =& J_0(\xi(R_2))Y_1(\xi(R_1)) - Y_0(\xi(R_2))J_1(\xi(R_1)), &(4.66)\\
f =& J_0(\xi(R_2))Y_0(\xi(R_1)) - Y_0(\xi(R_2))J_0(\xi(R_1)), &(4.67)\\
A =& -\frac{iG}{\omega\rho_0}\frac{Y_1(\xi(R_1))}{d} - \Xi\bar{A}\frac{Y_0(\xi(R_2))J_1(\xi_K(R_1))}{d}, &(4.68)\\
B =& \frac{iG}{\omega\rho_0}\frac{J_1(\xi(R_1))}{d} + \Xi\bar{A}\frac{J_0(\xi(R_2))J_1(\xi_K(R_1))}{d}, &(4.69)\\
\bar{A} =& \frac{iG}{\omega\rho_0}\frac{-d + Y_1(\xi(R_1))J_0(\xi(R_1)) - J_1(\xi(R_1))Y_0(\xi(R_1))}{\Xi J_1(\xi_K(R_1))f - J_0(\xi_K(R_1))d} &(4.70)\\
&- \frac{GK}{\mu + iK\rho_0\omega}\frac{d}{\Xi J_1(\xi_K(R_1))f - J_0(\xi_K(R_1))d}. &(4.71)
\end{aligned}$$

Plotting the solution (4.50) we obtain again the results of Figure. 4.3. In Figure. 4.5 we show the velocity profile at a fixed time for some values of the permeability K.

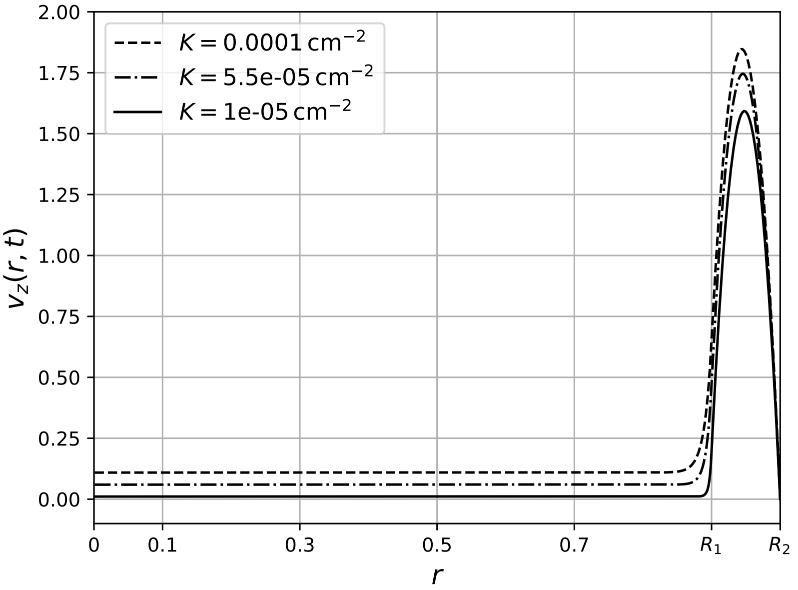

Figure 4.5: Trend of the velocity when K varies at $t = 1.2\,\mathrm{s}$. The values of the parameters not explicitly mentioned in the figure are given in Table 4.1.

4.3 Conclusions

We studied the interstitial fluid flow in a lymph node driven by a pulsatile pressure gradient. The lymph node is here assumed to be essentially composed of a porous core, where the fluid is governed by the Darcy-Brinkman equation and a thin layer in which the lymph can flow freely following the Navier-Stokes equation. We further assumed laminarity to get an explicit solution in terms of Bessel functions. We studied the eigenvalues and the eigenvectors of the motion explicitly, and we found an increasing unbounded sequence of eigenvalues. Moreover, we proved the orthogonality of the eigenvectors.

The exact solution we found showed that the porous part slows the motion; as expected, this behavior explains why the majority of the lymph entering the lymph node does not enter the LC [34]. We remark that our results are qualitative: the material parameters here are chosen according to [6] or estimated, and they do not come from any medical or experimental data.

Chapter 5

Simplified Spherical and Spheroidal Model of a Lymph Node

In this chapter we propose a mathematical model for the flow of the interstitial fluid (lymph) in a lymph node. We assume the lymph to be an incompressible fluid similar to water; moreover, we assume a small Reynolds number as a result of the small velocities within the lymph nodes [1], hence we can model the flow into the lymphoid compartment (LC) by Darcy-Brinkman equation (due to the high porosity and the time-dependence of the flow [11, 101]), and the flow inside the subcapsular sinus (SCS) by Stokes equation (see Section 2.1). The lymph enters the lymph node from the lymphatic vessels, which have one-way valves that prevent retrograde flow and a wall structure composed of sinus-lining cells: such cells control and generate active pulsation of the wall, pumping the lymph from a segment between two valves to another (see Chapter 1)[1, 35]. This means that the lymph has a relevant pulsatile behavior, and we take it into account in our model.

In Section 5.1 we describe the behavior of the lymph explicitly in a spherical geometry, supposing that the fluid flow inside the lymph node is axisymmetric with respect to the azimuthal angle, so that we can assume a simplified two-dimensional geometry and we can use the stream function approach to find an explicit solution (see Section 2.3 and [31]). We remark that the solution given in Section 5.1.1 is quite general and can be used also for other choices of boundary conditions. Finally, in Section 5.2 we compare our results with some finite element simulations obtained using the open source software FreeFEM [102].

The results found in this chapter are published in [10].

5.1 Explicit result in a simplified case

Let us model the lymph node (LN) as a spherical region: the subcapsular sinus (SCS) is a thin spherical shell with radii $R_1 < R_2$ of creeping fluid flowing near the external wall of the LN, while the lymphoid compartment (LC) is a sphere of radius R_1 of porous material. We use spherical coordinates (r, θ, ϕ), where r is the radial distance, θ the polar angle and ϕ the azimuthal angle; moreover, we suppose axial symmetry with respect to the azimuthal angle ϕ.

Assuming that the lymph, which flows inside the LN, is an incompressible Newtonian fluid, and that the Reynolds number is small [1], we have the equations

$$\begin{cases} \rho_0 \dfrac{\partial \boldsymbol{v}}{\partial t}(r,\theta,t) = -\nabla p(r,\theta,t) + \mu_e \Delta \boldsymbol{v}(r,\theta,t) - \dfrac{\mu}{k}\boldsymbol{v}(r,\theta,t) & r \in [0, R_1] \\ \rho_0 \dfrac{\partial \boldsymbol{v}}{\partial t}(r,\theta,t) = -\nabla p(r,\theta,t) + \mu \Delta \boldsymbol{v}(r,\theta,t) & r \in [R_1, R_2] \\ \nabla \cdot \boldsymbol{v}(r,\theta,t) = 0 \end{cases} \tag{5.1}$$

where ρ_0 is the constant density, $\boldsymbol{v}$ the velocity, p is the pressure, μ the viscosity of the lymph, μ_e the *effective viscosity*, k the *permeability*. The second equation in (5.1) is the *Stokes equation* and describes the motion in the subcapsular sinus, the first is the *Darcy-Brinkman equation*, which is used for modeling the flow in the porous region of the LC, while the last equation models the incompressibility of the fluid. Here we assume a constant homogeneous permeability k [11, 101]. The effective viscosity μ_e in general differs from the classical viscosity μ because μ_e keeps into account the Brinkman correction [79, 103]. Furthermore, assuming that the flow is time periodic with period T, we write the time dependence of the velocity and of the pressure as a Fourier expansion

$$\boldsymbol{v}(r,\theta,t) = \sum_{m=-\infty}^{\infty} \boldsymbol{v}_m(r,\theta) e^{im\omega t}, \quad p(r,\theta,t) = \sum_{m=-\infty}^{\infty} p_m(r,\theta) e^{im\omega t}, \tag{5.2}$$

where $\omega = 2\pi/T$.

5.1.1 Solving the equations

Now we want to compute the general solution of system (5.1) in terms of the Fourier expansion (5.2). Here we try to be as general as possible, without imposing any boundary condition, so that our solution can be used in several situations. We will deal with suitable boundary conditions for our specific problem in Section 5.1.3.

By using (5.2), system (5.1) becomes

$$\begin{cases} \Delta \boldsymbol{v}_m(r,\theta) - \left(\dfrac{\mu}{k\mu_e} + \dfrac{im\omega\rho_0}{\mu_e}\right)\boldsymbol{v}_m(r,\theta) = \dfrac{1}{\mu_e}\nabla p_m(r,\theta) & \text{in } [0, R_1], \\ \Delta \boldsymbol{v}_m(r,\theta) - \dfrac{im\omega\rho_0}{\mu}\boldsymbol{v}_m(r,\theta) = \dfrac{1}{\mu}\nabla p_m(r,\theta) & \text{in } [R_1, R_2], \\ \nabla \cdot \boldsymbol{v}_m(r,\theta) = 0, \end{cases} \tag{5.3}$$

which can be written in compact form as

$$\begin{cases} \Delta \boldsymbol{v}_m(r,\theta) - q_m(r)\boldsymbol{v}_m(r,\theta) = \dfrac{1}{\mu}\nabla p_m(r,\theta) \\ \nabla \cdot \boldsymbol{v}_m(r,\theta) = 0, \end{cases} \quad m \in \mathbb{Z}, \tag{5.4}$$

where $\mathbb{Z}$ is the set of integers, while q_m is given by

$$q_m(r) = \begin{cases} \dfrac{\mu}{k\mu_e} + \dfrac{im\omega\rho_0}{\mu_e} & \text{in } [0, R_1], \\ \dfrac{im\omega\rho_0}{\mu} & \text{in } [R_1, R_2]. \end{cases} \tag{5.5}$$

Now, writing $\boldsymbol{v}_m = v_{r,m}\mathbf{e}_r + v_{\theta,m}\mathbf{e}_\theta$, we introduce the *stream function* ψ_m (see Section 2.3 and [31]) as

$$v_{r,m}(r,\theta) = -\frac{1}{r^2 \sin\theta}\frac{\partial\psi_m}{\partial\theta}, \quad v_{\theta,m}(r,\theta) = \frac{1}{r\sin\theta}\frac{\partial\psi_m}{\partial r}. \tag{5.6}$$

Moreover, it is useful to perform the change of variable $\zeta := \cos\theta$, so that the previous relations become

$$v_{r,m}(r,\zeta) = \frac{1}{r^2}\frac{\partial\psi_m}{\partial\zeta}, \quad v_{\theta,m}(r,\zeta) = \frac{1}{r\sqrt{1-\zeta^2}}\frac{\partial\psi_m}{\partial r}. \tag{5.7}$$

By introducing the operator

$$\mathrm{E}^2 = \frac{\partial^2}{\partial r^2} + \frac{(1-\zeta^2)}{r^2}\frac{\partial^2}{\partial\zeta^2}, \tag{5.8}$$

we can rewrite (5.4) as

$$\mathrm{E}^2\left(\mathrm{E}^2\,\psi_m(r,\zeta)\right) - q_m(r)\,\mathrm{E}^2\,\psi_m(r,\zeta) = 0, \quad m \in \mathbb{Z}, \tag{5.9}$$

while for the pressure we have

$$\begin{cases} \dfrac{\partial p_m}{\partial r} = \dfrac{\mu}{r^2}\dfrac{\partial}{\partial\zeta}\left((\mathrm{E}^2 - q_m(r))\,\psi_m\right) \\ \dfrac{\partial p_m}{\partial\zeta} = -\dfrac{\mu}{1-\zeta^2}\dfrac{\partial}{\partial r}\left((\mathrm{E}^2 - q_m(r))\,\psi_m\right) \end{cases} \quad m \in \mathbb{Z}. \tag{5.10}$$

Focusing on the case $m \neq 0$, we have that the solution can be written as

$$\psi_m(r,\zeta) = \psi_{1,m}(r,\zeta) + \psi_{2,m}(r,\zeta), \tag{5.11}$$

where

$$\mathrm{E}^2\,\psi_{1,m}(r,\zeta) = 0, \quad \mathrm{E}^2\,\psi_{2,m}(r,\zeta) - q_m(r)\psi_{2,m}(r,\zeta) = 0. \tag{5.12}$$

We can now solve (5.12): by using the separation of variables

$$\psi_{1,m}(r,\zeta) = R(r)Z(\zeta), \tag{5.13}$$

substituting in the first equation of (5.12) we get

$$\frac{r^2}{R}\frac{d^2R}{dr^2} + \frac{1-\zeta^2}{Z}\frac{d^2Z}{d\zeta^2} = 0. \tag{5.14}$$

As the first term of (5.14) depends only on r and the second term only on ζ, the two have to be constant, say $n(n-1)$ with $n \in \mathbb{N}$ [84], where $\mathbb{N}$ is the set of natural numbers. Hence (5.14) becomes

$$r^2 \frac{d^2R}{dr^2} - n(n-1)R = 0, \tag{5.15}$$

$$\left(1-\zeta^2\right) \frac{d^2Z}{d\zeta^2} + n(n-1)Z = 0. \tag{5.16}$$

The solution of (5.15) is given by

$$R^{(n)}(r) = A^{(n)}r^n + B^{(n)}r^{1-n}, \tag{5.17}$$

for some constants $A^{(n)}, B^{(n)}$, while (5.16) is the *Gegenbauer equation*, whose solutions are the *Gegenbauer functions* G_n, H_n with order $-1/2$, of the first and second kind, respectively. Hence the solution of the first equation of (5.12) becomes

$$\psi_{1,m} = \sum_{n=0}^{\infty} \left[\left(A_m^{(n)}r^n + B_m^{(n)}r^{1-n}\right) G_n(\zeta) + \left(C_m^{(n)}r^n + D_m^{(n)}r^{1-n}\right) H_n(\zeta)\right]$$

for some constants $A_m^{(n)}, B_m^{(n)}, C_m^{(n)}, D_m^{(n)}$. Since H_n is not smooth in $\zeta = \pm 1$ and G_0, G_1 lead to an infinite tangential velocity, the solution simplifies as

$$\psi_{1,m}(r,\zeta) = \sum_{n=2}^{\infty} \left(A_m^{(n)}r^n + B_m^{(n)}r^{1-n}\right) G_n(\zeta), \tag{5.18}$$

for some constants $A_m^{(n)}, B_m^{(n)}$.

The second equation of (5.12) is

$$\frac{\partial^2 \psi_{2,m}}{\partial r^2} + \frac{1-\zeta^2}{r^2}\frac{\partial^2 \psi_{2,m}}{\partial \zeta^2} - q_m(r)\psi_{2,m} = 0 \tag{5.19}$$

and, using again the separation of variables,

$$\psi_{2,m}(r,\zeta) = R(r)Z(\zeta), \tag{5.20}$$

by a similar procedure as before, we obtain

$$\frac{d^2R}{dr^2} - q_m R - \frac{n(n-1)}{r^2}R = 0, \tag{5.21}$$

$$(1-\zeta^2)\frac{d^2Z}{d\zeta^2} + n(n-1)Z = 0. \tag{5.22}$$

Equation (5.21) is a Bessel equation, hence the solution can be written as

$$R^{(n)}(r) = \alpha^{(n)}\sqrt{r}J_{n-\frac{1}{2}}\left(-i\sqrt{q_m}r\right) + \beta^{(n)}\sqrt{r}Y_{n-\frac{1}{2}}\left(-i\sqrt{q_m}r\right), \tag{5.23}$$

where J_s, Y_s are the *Bessel functions of the first and second kind*, respectively. Equation (5.22) is the same Gegenbauer equation as (5.16), hence the solution of (5.19) is given by

$$\psi_{2,m} = \sum_{n=2}^{\infty} \left[\alpha_m^{(n)}\sqrt{r}J_{n-\frac{1}{2}}\left(-i\sqrt{q_m}r\right) + \beta_m^{(n)}\sqrt{r}Y_{n-\frac{1}{2}}\left(-i\sqrt{q_m}r\right)\right] G_n(\zeta), \tag{5.24}$$

and the general solution $\psi_m = \psi_{1,m} + \psi_{2,m}$ is

$$\psi_m(r,\zeta) = \sum_{n=2}^{\infty} \Big[A_m^{(n)} r^n + B_m^{(n)} r^{1-n} + \alpha_m^{(n)} \sqrt{r} J_{n-\frac{1}{2}} (-i\sqrt{q_m} r) + \beta_m^{(n)} \sqrt{r} Y_{n-\frac{1}{2}} (-i\sqrt{q_m} r) \Big] G_n(\zeta). \quad (5.25)$$

Now we want to employ the definition of q_m, so that we have to distinguish between the Stokes and the Darcy-Brinkman case. Let us denote with $A_m^{(n)}$, $B_m^{(n)}$, $\alpha_m^{(n)}$, $\beta_m^{(n)}$ the constants of the Stokes case ($R_1 \le r \le R_2$) and with $\bar{A}_m^{(n)}$, $\bar{B}_m^{(n)}$, $\bar{\alpha}_m^{(n)}$, $\bar{\beta}_m^{(n)}$ those of the Darcy-Brinkman case ($0 \le r \le R_1$). Using (5.5), we obtain, for any $m \neq 0$,

$$\begin{aligned} \psi_m^S(r,\zeta) = \sum_{n=2}^{\infty} \Bigg[& A_m^{(n)} r^n + B_m^{(n)} r^{1-n} + \alpha_m^{(n)} \sqrt{r} J_{n-\frac{1}{2}} \left(-i\sqrt{\frac{i\rho_0 m\omega}{\mu}} r \right) \\ & + \beta_m^{(n)} \sqrt{r} Y_{n-\frac{1}{2}} \left(-i\sqrt{\frac{i\rho_0 m\omega}{\mu}} r \right) \Bigg] G_n(\zeta), \end{aligned} \quad (5.26)$$

$$\psi_m^B(r,\zeta) = \sum_{n=2}^{\infty} \left[\bar{A}_m^{(n)} r^n + \bar{\alpha}_m^{(n)} \sqrt{r} J_{n-\frac{1}{2}} \left(-i\sqrt{\frac{i\rho_0 m\omega}{\mu_e} + \frac{\mu}{\mu_e k}} r \right) \right] G_n(\zeta), \quad (5.27)$$

where the superscript S denotes the Stokes case and B the Darcy-Brinkman case, and we used the fact that $r = 0$ is in the domain of ψ^B, so that $\bar{B}_m^{(n)} = \bar{\beta}_m^{(n)} = 0$ in view of the non degeneracy of the solution.

Regarding the pressure, we use (5.10) to obtain

$$p_m^S(r,\zeta) = C_m^S + im\omega\rho_0 \sum_{n=2}^{\infty} \left[\frac{A_m^{(n)}}{n-1} r^{n-1} - \frac{B_m^{(n)}}{n} r^{-n} \right] P_{n-1}(\zeta) \quad (5.28)$$

in the Stokes case, and

$$p_m^B(r,\zeta) = C_m^B + \left(im\omega\rho_0 + \frac{\mu}{k} \right) \sum_{n=2}^{\infty} \frac{\bar{A}_m^{(n)}}{n-1} r^{n-1} P_{n-1}(\zeta) \quad (5.29)$$

in the Darcy-Brinkman case, where P_n are the Legendre polynomials of the first kind.

For $m = 0$ we get the well-known steady solution of the Stokes equation discussed in Section 2.3.1

$$\begin{cases} \psi_0^S = \sum_{n=2}^{\infty} \left(A_0^{(n)} r^n + B_0^{(n)} r^{1-n} + C_0^{(n)} r^{n+2} + D_0^{(n)} r^{-n+3} \right) G_n(\zeta), \\ p_0^S = C_0^S - \mu \sum_{n=2}^{\infty} \left[\frac{2(2n+1)}{n-1} C_0^{(n)} r^{n-1} + \frac{2(2n-3)}{n} D_0^{(n)} r^{-n} \right] P_{n-1}(\zeta) \end{cases} \quad (5.30)$$

and for the Darcy-Brinkman equation we have

$$\begin{cases} \psi_0^B = \sum_{n=2}^{\infty} \left[\bar{A}_0^{(n)} r^n + \bar{B}_0^{(n)} \sqrt{r} J_{n-\frac{1}{2}} \left(-i\sqrt{\frac{\mu}{\mu_e k}} r \right) \right] G_n(\zeta), \\ p_0^B = C_0^B + \frac{\mu}{k} \sum_{n=2}^{\infty} \left[\frac{\bar{A}_0^{(n)}}{n-1} r^{n-1} \right] P_{n-1}(\zeta). \end{cases} \quad (5.31)$$

5.1.2 Geometrical and physiological parameters

We use an idealized spherical geometry based on the data obtained from a murine (popliteal) lymph node: the radius is $R_2 = 0.5\,\mathrm{mm}$, the subcapsular sinus (SCS) thickness is $h = 10\,\mu\mathrm{m}$, the afferent and efferent lymphatic vessels have the same radius $R_{LV} = 40\,\mu\mathrm{m}$ [5, 11, 12, 60, 62, 104, 105]. With these data, we have that more than 90% of the lymph takes the peripheral path without entering the LC in a pulsation cycle [5, 51, 52].

The inlet and outlet conditions are imposed in the upper and lower lymphatic vessel (near $\theta = 0$ and $\theta = \pi$, respectively) as a pulsatile flow of the form

$$v_{in}(\theta, t) = \frac{L}{\pi R_{LV}^2} f(t) H(\cos\theta), \tag{5.32}$$

where L is the maximum lymph mean flow of the inlet lymphatic vessel. Here we assume $L = 10^{-3}\,\mathrm{mm}^3/\mathrm{s}$, as measured in [47], and $f(t)$ is a periodic function. The function H is given by

$$H(\zeta) = \begin{cases} 1 & \zeta \in [-1, -1 + \zeta_0] \\ 0 & \zeta \in (-1 + \zeta_0, 1 - \zeta_0) \\ -1 & \zeta \in [1 - \zeta_0, 1], \end{cases} \tag{5.33}$$

where the constant $0 < \zeta_0 < 1$ describes the inlet and outlet regions, and is given by

$$\zeta_0 = \cos\left[\arcsin\left(\frac{R_{LV}}{\sqrt{R_{LV}^2 + R_2^2}}\right)\right] = \frac{R_2}{\sqrt{R_{LV}^2 + R_2^2}}. \tag{5.34}$$

Notice that we are assuming that the inlet and outlet velocities are the same.

The lymph is modeled as an incompressible Newtonian fluid similar to water [1] with viscosity $\mu = 1\,\mathrm{mg/(mm\,s)}$ and density $\rho_0 = 1\,\mathrm{mg/mm^3}$. The permeability is considered homogeneous [101] with value $k = 3.84 \times 10^{-9}\,\mathrm{mm}^2$ [11]. The effective viscosity is taken as $\mu_e = \frac{\mu}{\phi}$ [106, 107], where ϕ is the *porosity* taken as $\phi = 0.75$ [11]. The parameters are summarized in Table 5.1.

5.1.3 Boundary conditions

We now want to impose suitable boundary conditions to our general solution. We give a *Dirichlet condition* at the external boundary and the *Ochoa-Tapia boundary conditions* [106, 109] at the interface between the porous zone LC and the free-fluid region SCS. In this way we can close the problem and find a unique solution.

More precisely, we will assume the *no-slip condition* for the velocity on R_2, except near $\theta = 0, \pi$, where we impose the inlet/outlet flow (5.32). For simplicity, given the small diameter of the afferent/efferent lymphatic vessel, we impose the inlet/outlet condition only for the radial velocity v_r, but we could use the same procedure to impose boundary condition for v_θ too. For the boundary conditions on the internal radius R_1, the Ochoa-Tapia boundary conditions imply the continuity of radial and tangential velocity, the continuity of the normal stress tensor and a jump-condition on the shear stress.

Variable name	Value	Description
R_2	$0.5\,\mathrm{mm}$	external radius [12]
h	$10\,\mu\mathrm{m}$	height of SCS [5, 12, 108]
R_1	$R_2 - h$	internal radius
R_{LV}	$40\,\mu\mathrm{m}$	lymphatic vessel radius [12]
μ	$1\,\mathrm{mg/(mm\,s)}$	viscosity [1]
ϕ	0.75	porosity [11]
μ_e	$\frac{\mu}{\phi}$	effective viscosity [106, 109]
ρ_0	$1\,\mathrm{mg/mm^3}$	density [1]
β	0.7	stress jump
k	$3.84 \times 10^{-9}\,\mathrm{mm^2}$	permeability [11]
L	$10^{-3}\,\mathrm{mm^3/s}$	maximum lymph fluid mean flow [47]

Table 5.1: Physiological parameters of Section 5.1.2.

Thanks to the above conditions, we can determine for every n the six unknown constants in equations (5.26)-(5.27). For the sake of brevity, we rewrite the stream functions as

$$\psi_m^{S/B}(r,\zeta) = \sum_{n=2}^{\infty} \tilde{\psi}_{m,n}^{S/B}(r) G_n(\zeta), \quad p_m^{S/B} = \sum_{n=2}^{\infty} \tilde{p}_{m,n}^{S/B}(r) P_{n-1}(\zeta). \tag{5.35}$$

Expanding the step function $H(\zeta)$ in (5.33) in terms of Legendre polynomials, we get

$$H(\zeta) = \sum_{n=2}^{\infty} b_{n-1} P_{n-1}(\zeta), \tag{5.36}$$

where

$$b_n = \frac{2n+1}{2} \int_{-1}^{1} H(\zeta) P_n(\zeta) d\zeta = \frac{2n+1}{2} \left(\int\limits_{-1}^{-1+\zeta_0} P_n(\zeta) d\zeta - \int\limits_{1-\zeta_0}^{1} P_n(\zeta) d\zeta \right) \tag{5.37}$$

and we kept into account that $b_0 = 0$ since H is an odd function.

To impose the boundary condition, we need to expand in Fourier series the time dependence of (5.32), as we did in (5.2). Writing

$$f(t) = \sum_{m=-\infty}^{\infty} f_m e^{im\omega t}, \tag{5.38}$$

it follows that

$$\begin{aligned} v_{in}(\zeta,t) &= \frac{L}{\pi R_{LV}^2} H(\zeta) \sum_{m=-\infty}^{\infty} f_m e^{im\omega t} \\ &= \frac{L}{\pi R_{LV}^2} \sum_{n=2}^{\infty} \sum_{m=-\infty}^{\infty} b_{n-1} P_{n-1}(\zeta) f_m e^{im\omega t}. \end{aligned} \tag{5.39}$$

Now we impose the boundary condition $v_r(R_2,\zeta,t) = v_{in}(\zeta,t)$: recalling the relation $G_n'(\zeta) = -P_{n-1}(\zeta)$, by $(5.7)_1$ we obtain

$$\frac{1}{R_2^2}\psi_m^S(R_2,\zeta) = -\frac{L}{\pi R_{LV}^2}\sum_{n=2}^{\infty} b_{n-1}G_n(\zeta), \tag{5.40}$$

whence

$$\tilde{\psi}_{m,n}^S(R_2) = -\frac{R_2^2 L}{\pi R_{LV}^2} b_{n-1} f_m \tag{5.41}$$

for any $m \in \mathbb{Z}$ and $n \geq 2$, where we used the linear independence of the Gegenbauer polynomials.

By the no-slip boundary condition on v_θ, recalling $(5.7)_2$ it follows that

$$\frac{\partial \psi_{m,n}^S}{\partial r}(R_2,\zeta) = 0 \quad \Rightarrow \quad \frac{\partial \tilde{\psi}_{m,n}^S}{\partial r}(R_2) = 0, \tag{5.42}$$

where we used again the linear independence of the Gegenbauer polynomials.

We now write in terms of the stream function the Ochoa-Tapia boundary conditions on the internal radius R_1 [110], using the linear independence of Legendre and Gegenbauer polynomials:

- Continuity of v_r:

$$v_{r,m}^S(R_1,\zeta) = v_{r,m}^B(R_1,\zeta) \quad \Rightarrow \quad \tilde{\psi}_{m,n}^S(R_1) = \tilde{\psi}_{m,n}^B(R_1). \tag{5.43}$$

- Continuity of v_θ:

$$v_{\theta,m}^S(R_1,\zeta) = v_{\theta,m}^B(R_1,\zeta) \quad \Rightarrow \quad \frac{\partial \tilde{\psi}_{m,n}^S}{\partial r}(R_1) = \frac{\partial \tilde{\psi}_{m,n}^B}{\partial r}(R_1). \tag{5.44}$$

- Continuity of normal stress:

$$T_{rr,m}^S(R_1,\zeta) = T_{rr,m}^B(R_1,\zeta), \tag{5.45}$$

  where

$$T_{rr,m} = -p_m + 2\mu\frac{\partial v_{r,m}}{\partial r}; \tag{5.46}$$

  we can write this condition as

$$\begin{aligned} &-\tilde{p}_{m,n}^S(R_1,\zeta) + 4\mu\frac{1}{R_1^3}\tilde{\psi}_{m,n}^S(R_1,\zeta) - 2\mu\frac{1}{R_1^2}\frac{\partial \tilde{\psi}_{m,n}^S}{\partial r}(R_1,\zeta) \\ &\quad = -\tilde{p}_{m,n}^B(R_1,\zeta) + 4\mu_e\frac{1}{R_1^3}\tilde{\psi}_{m,n}^B(R_1,\zeta) - 2\mu_e\frac{1}{R_1^2}\frac{\partial \tilde{\psi}_{m,n}^B}{\partial r}(R_1,\zeta). \end{aligned} \tag{5.47}$$

- The stress jump condition:

$$T_{r\theta,m}^S(R_1,\zeta) - T_{r\theta,m}^B(R_1,\zeta) = \frac{\beta\mu}{\sqrt{k}}v_{\theta,m}^B(R_1,\zeta), \tag{5.48}$$

where β is the *slip constant* which has to be estimated experimentally. Since the expression of the shear stress is

$$T_{r\theta,m} = \mu\left[\frac{1}{r}\frac{\partial v_{r,m}}{\partial\theta} - \frac{v_{\theta,m}}{r} + \frac{\partial v_{\theta,m}}{\partial r}\right], \tag{5.49}$$

in the term $\frac{\partial v_{r,m}}{\partial\theta} = -\sqrt{1-\zeta^2}\frac{\partial v_{r,m}}{\partial\zeta}$ there is a second derivative of the Gegenbauer polynomials, so that we need the following property [68, 82]:

$$G''_n(\zeta) = -\frac{n(n-1)}{1-\zeta^2}G_n(\zeta). \tag{5.50}$$

Hence we have:

$$\begin{aligned}\frac{\partial v_{r,m}}{\partial\theta} &= -\sqrt{1-\zeta^2}\frac{1}{r^2}\frac{\partial^2\psi_m}{\partial\zeta^2}\\ &= -\frac{\sqrt{1-\zeta^2}}{r^2}\sum_{n=2}^{\infty}\tilde{\psi}_{m,n}(r)G''_n(\zeta) = \frac{\sqrt{1-\zeta^2}}{r^2}\sum_{n=2}^{\infty}n(n-1)\tilde{\psi}_{m,n}(r)G_n(\zeta).\end{aligned} \tag{5.51}$$

After some computations, eq. (5.48) can be written as

$$\begin{aligned}&\mu\left[\frac{n(n-1)}{R_1^3}\tilde{\psi}^S_m(R_1) - \frac{2}{R_1^2}\frac{\partial\tilde{\psi}^S_{m,n}}{\partial r}(R_1) + \frac{1}{R_1}\frac{\partial^2\tilde{\psi}^S_{m,n}}{\partial r^2}(R_1)\right]\\ &\quad - \mu_e\left[\frac{n(n-1)}{R_1^3}\tilde{\psi}^B_{m,n}(R_1) - \frac{2}{R_1^2}\frac{\partial\tilde{\psi}^B_{m,n}}{\partial r}(R_1) + \frac{1}{R_1}\frac{\partial^2\tilde{\psi}^B_{m,n}}{\partial r^2}(R_1)\right]\\ &\qquad = \frac{\beta\mu}{\sqrt{k}}\frac{1}{R_1}\frac{\partial\tilde{\psi}^B_{m,n}}{\partial r}(R_1).\end{aligned} \tag{5.52}$$

From (5.41)–(5.44), (5.47) and (5.52), for every $m \in \mathbb{Z}$ and $n \geq 2$ we obtain a linear system in the unknowns $(A^{(n)}_m, B^{(n)}_m, \alpha^{(n)}_m, \beta^{(n)}_m, \bar{A}^{(n)}_m, \bar{\alpha}^{(n)}_m)$, which are the constants of integration of equations (5.26)-(5.27), and the same holds for the steady case when $m = 0$ in the unknowns $(A^{(n)}_0, B^{(n)}_0, C^{(n)}_0, D^{(n)}_0, \bar{A}^{(n)}_0, \bar{B}^{(n)}_0)$ which are the constants of integration of eqs. $(5.30)_1$–$(5.31)_1$.

Moreover, we fix the value of the pressure in one point to find the constants in equation (5.28)–(5.30) and have a physiological pressure value. By (5.47), it follows that $C^S_m = C^B_m$ and $C^B_0 = C^S_0$. We fix the pressure (with respect to time) at the exit point $(r,\zeta) = (R_2,-1)$ by using the same time function of (5.32), that is,

$$p(t) = \bar{p}f(t) = \bar{p}\sum_{m=-\infty}^{\infty} f_m e^{im\omega t}. \tag{5.53}$$

Hence we can find the pressure constants by imposing

$$p^S_m(R_2,-1) = \bar{p}f_m, \quad m \in \mathbb{Z} \tag{5.54}$$

where $p^S_m(r,\zeta)$ is given in (5.28) for $m \neq 0$, and in $(5.30)_2$ for $m = 0$.

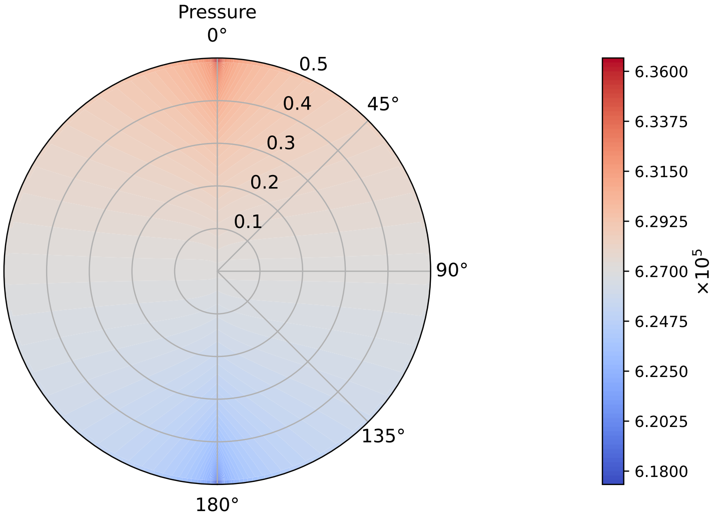

Figure 5.1: Pressure distribution in mPa with fixed pressure $p = 6.18 \times 10^5$ mPa at the outlet.

5.1.4 Explicit results

This section is devoted to show some plots related to the explicit solution and to make some considerations about the proposed model.

Following [17], we choose a time function of the form

$$f(t) = \frac{1 - \cos \pi t}{2}. \tag{5.55}$$

We notice that in this case the period of a pulsatile flow in the lymph node is 2 s, hence $\omega = \pi$, and $f_m = 0$ for $m \neq -1, 0, 1$.

In this model we do not take into account the inhibition and the autoregulation of the contractions in the lymphangion, given by several factors like shear stress and pressure [1, 18] (see Chapters 1 and 3); a further extension of this model can be the coupling with a lymphangion model for taking into account these phenomena.

In Figure 5.1, we plot the pressure distribution in the LN with the fixed constant $\bar{p} = 6.18 \times 10^5$ mPa (corresponding to the lower limit of the pressure found in [111]); as we can see, the values of the pressure belong to the range given in that paper and, due to the incompressibility of the flow, the pressure translates from a higher value in the inlet zone to a lower value in the outlet zone. We can choose to fix any pressure at the outlet, and we have the same pressure distribution with different values (for example with the fixed pressure of $\bar{p} = 4 \times 10^5$ mPa ≈ 3 mmHg as in [5]).

Figure 5.2 provides the Stokes shear stress given by the formula:

$$T_{r\theta} = \sum_{m \in \{-1,0,1\}} \mu \left[\frac{1}{r} \frac{\partial v_{r,m}}{\partial \theta} - \frac{v_{\theta,m}}{r} + \frac{\partial v_{\theta,m}}{\partial r} \right] e^{im\pi t}, \tag{5.56}$$

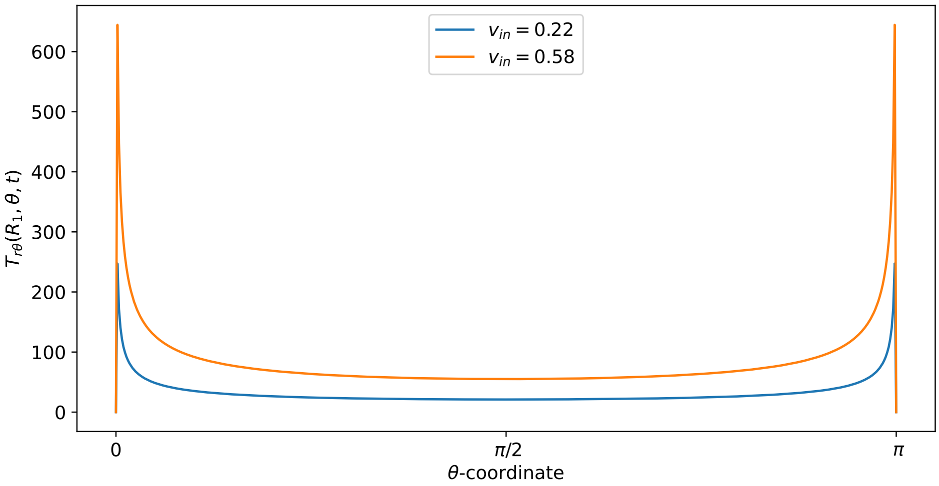

Figure 5.2: Shear stress $T_{r\theta}(r, \theta, t)$ in mPa with respect to the polar angle ($\theta = 0$ near the inlet flow and $\theta = \pi$ near the outlet flow) calculated at $t = 1\,\mathrm{s}$ and in the internal radius R_1 with different boundary velocities in mm/s (where $v_{in} \approx 0.22$ corresponds to $L = 10^{-3}\,\mathrm{mm}^3/\mathrm{s}$ and $v_{in} \approx 0.58$ corresponds to $L = 2.2 \times 10^{-3}\,\mathrm{mm}^3/\mathrm{s}$).

(in mPa) at time $t = 1\,\mathrm{s}$, where we have the maximum value of the velocity (and, consequently, of the shear stress) and radius $r = R_1$ (this is the shear stress at the exterior of the LC). We plot the shear stress value with two different boundary velocities: $v_{in} \approx 0.22$ corresponds to the physiological value of $L = 10^{-3}\,\mathrm{mm}^3/\mathrm{s}$, given in Table 5.1, found in [47], and $v_{in} \approx 0.58$ appears in [5]. As we can see, the shear stress is similar to the one reported in [5, 12]; that is, higher near the inlet flow and lower near $\theta = \frac{\pi}{2}$. The same behavior occurs in the velocity too (see Figure 5.3). This trend is interesting because the cell adhesion to the exterior of the LC is proportional to the shear stress [12], hence the majority of the cells adhere (and then enter in the LC) near the inlet zone of the lymphatic vessel. Indeed, in our model the inlet shear stress is the same as the outlet one due to the choice of the same inlet/outlet velocity and the incompressibility of the fluid; however, usually a part of the lymph enters in the blood capillaries in the LC [51, 52], so that the shear stress in the outer zone reduces.

As we can see in Figure 5.3 and in Figure 5.4, for $\theta > 0$ the tangential component $\boldsymbol{v}_\theta$ of the velocity in the SCS is the larger one. From the first picture in Figure 5.3 one can see that the fluid flow in the porous medium is flat and starts increasing near the interface that connects the LC to the SCS, showing a non-differentiable point due to the Ochoa-Tapia boundary conditions (indeed, we do not impose the continuity of the derivative of $\boldsymbol{v}_\theta$).

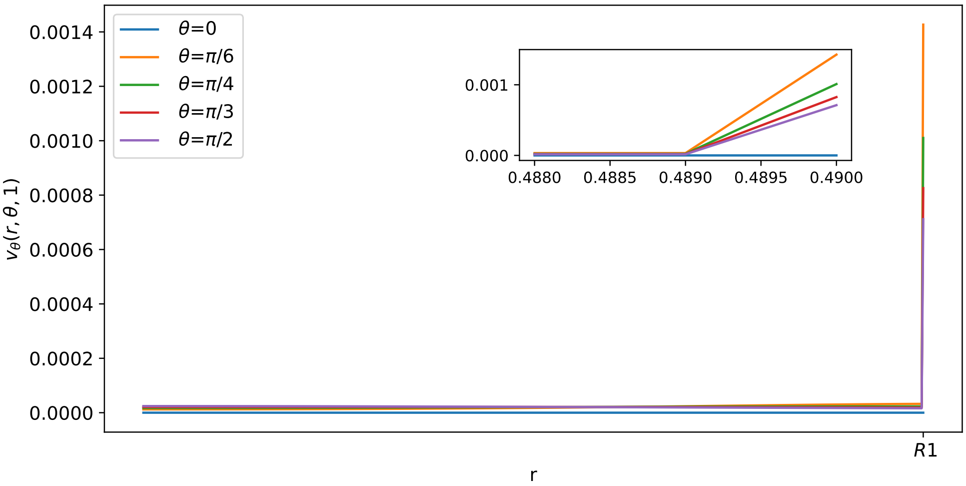

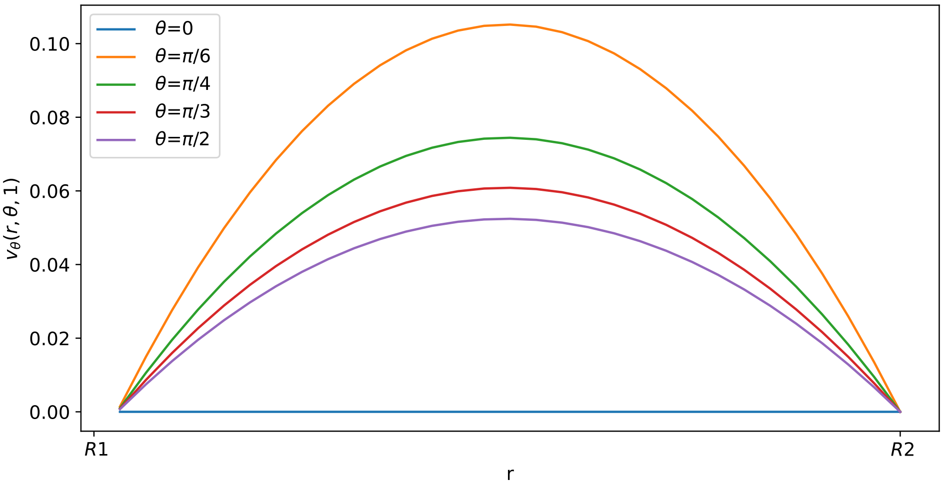

Figure 5.3: Tangential component of the velocity in mm/s with respect to the radius at different angles at $t = 1\,\mathrm{s}$. The first picture corresponds to the tangential velocity in the LC (porous part), and the second corresponds to the tangential velocity in the SCS (free-fluid region).

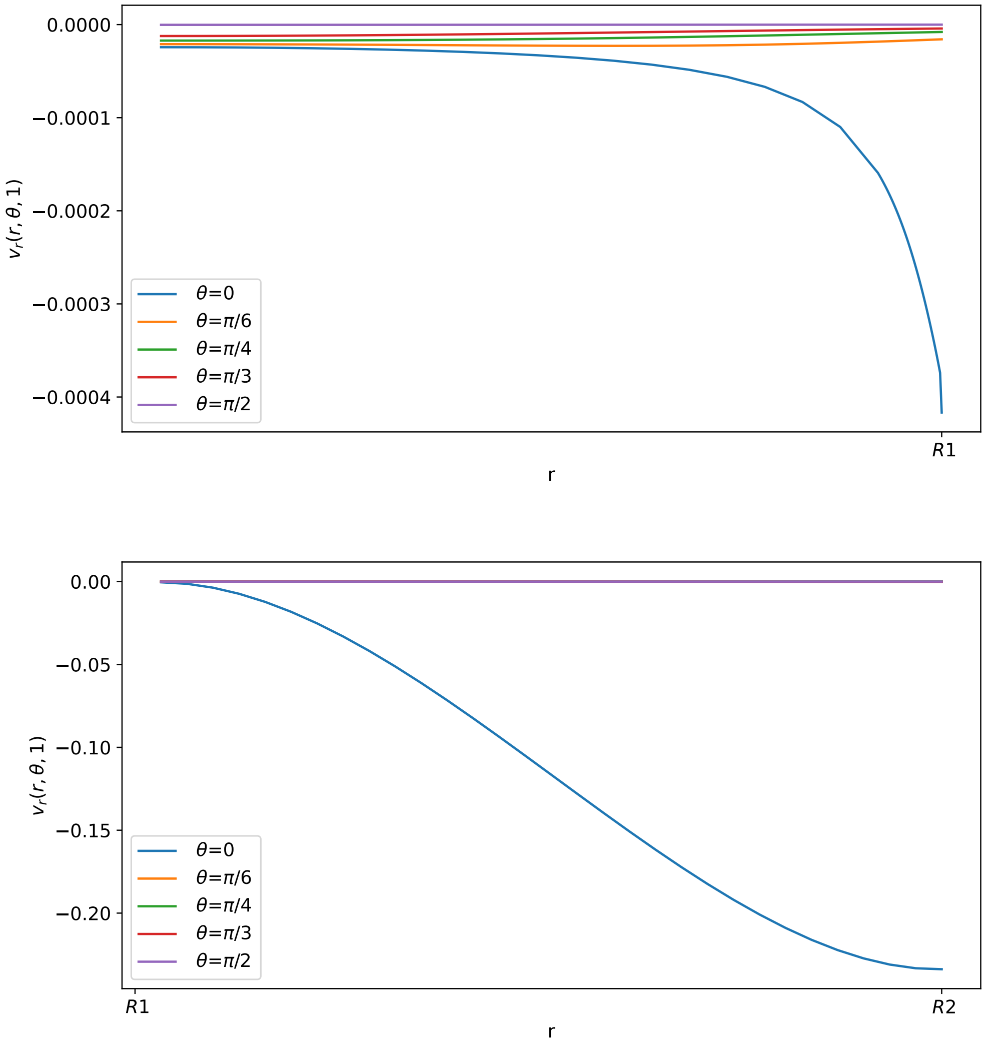

Figure 5.4: Normal component of the velocity in mm/s with respect to the radius at different angles at $t = 1\,\mathrm{s}$.

5.2 Numerical simulation

The explicit model found in the previous Section uses several simplifications. In this section we propose some numerical simulations to describe a more general fluid flow in a lymph node.

We define two different domains and we call Ω^S the domain of the SCS in which we have the Stokes equation, and Ω^B the LC domain in which we have the Darcy-Brinkman equation. The boundaries of the domain are $\partial\Omega^S = \Gamma^S_D \cup \Gamma^S_N$, where Γ^S_D is the part of the boundary with Dirichlet boundary condition and Γ^S_N is the one with the Neumann boundary condition and for the domain Ω^B are $\partial\Omega^B = \Gamma^B_D \cup \Gamma^B_N$, where Γ^B_D is the part of the boundary with Dirichlet boundary condition and Γ^B_N is the one with the Neumann boundary condition. We call the boundary interface of the two domains $\Gamma = \partial\Omega^S \cap \partial\Omega^B$. We define the normal $\boldsymbol{n}$ at the interface Γ as the external normal to Ω^B. Moreover, we define the spaces $W^I = \{\boldsymbol{w} \in H^1(\Omega^I) : \boldsymbol{w}_{\Gamma_D} = 0\}$, $W^I_g = \{\boldsymbol{v} \in H^1(\Omega^I) : \boldsymbol{v}_{\Gamma_D} = g\}$, $Q^I = \{q \in L^2(\Omega^I), \text{ with } \int_{\Omega^I} q = 0 \text{ if } \Gamma_D = \partial\Omega^I\}$, where $I = S, B$.

The weak formulation of our problem is (supposing a constant density $\rho = \rho_0$ and viscosity $\nu = \mu/\rho_0$): find $\boldsymbol{v} \in W^S_g$, $p \in Q^S$, $\boldsymbol{v}_b \in W^B_g$ and $p_b \in Q^B$ such that

$$\int_{\Omega^S} \frac{\partial \boldsymbol{v}}{\partial t} \cdot \boldsymbol{w} dV - \frac{1}{\rho_0} \int_{\Omega^S} p \nabla \cdot \boldsymbol{w} dV + \nu \int_{\Omega^S} \mathbf{D}(\boldsymbol{v}) : \mathbf{D}(\boldsymbol{w}) dV + \frac{1}{\rho_0} \int_{\Gamma^S_N} \boldsymbol{T}\boldsymbol{w} \cdot \boldsymbol{n} dS$$
$$+ \int_{\Omega^B} \frac{\partial \boldsymbol{v}_b}{\partial t} \cdot \boldsymbol{w}_b dV - \frac{1}{\rho_0} \int_{\Omega^B} p_b \, \nabla \cdot \boldsymbol{w}_b dV + \nu_e \int_{\Omega^B} \mathbf{D}(\boldsymbol{v}_b) : \mathbf{D}(\boldsymbol{w}_b) dV$$
$$- \frac{1}{\rho_0} \int_{\Gamma^B_N} \boldsymbol{T}_e \boldsymbol{w}_b \cdot \boldsymbol{n} dS + \nu \int_{\Omega^B} \boldsymbol{K}^{-1} \boldsymbol{v}_b \cdot \boldsymbol{w}_b dV + \int_{\Omega^S} \nabla \cdot \boldsymbol{v} q dV + \int_{\Omega^B} \nabla \cdot \boldsymbol{v}_b q_b dV = 0, \tag{5.57}$$

for all $\boldsymbol{w} \in W^S_g$, $\boldsymbol{w}_b \in W^B_g$ such that $\boldsymbol{w} = \boldsymbol{w}_b$ on Γ, and for all $q \in Q^S$ and $q_b \in Q^B$. In equation (5.57) we have that $\boldsymbol{v}$ is the *velocity* in Ω^S, $p \in Q$ is the *pressure* in Ω^S, $\boldsymbol{v}_b$ is the *velocity* in Ω^B, $p_b \in Q$ is the pressure in Ω^B, $\mathbf{D}(\boldsymbol{v}) = 1/2(\nabla \boldsymbol{v} + \nabla \boldsymbol{v}^T)$, $\boldsymbol{T} = -p\boldsymbol{I} + \mu \left[\nabla \boldsymbol{v} + \nabla \boldsymbol{v}^T\right]$, $\nu_e = \mu_e/\rho_0$, $\boldsymbol{K}$ is the *permeability tensor* (in the case of Section 5.1, $\boldsymbol{K} = k\boldsymbol{I}$), $\boldsymbol{T}_e = -p_b\boldsymbol{I} + \mu_e \left[\nabla \boldsymbol{v}_b + \nabla \boldsymbol{v}_b^T\right]$.

Now we want to write the weak formulation for the boundary condition 5.1.3; we have that the continuity of the velocity is verified automatically, and, for the stress-jump condition, we have [107] (on the interface Γ):

$$\int_\Gamma \boldsymbol{T}\boldsymbol{w} \cdot \boldsymbol{n} dS - \int_\Gamma \boldsymbol{T}_e \boldsymbol{w} \cdot \boldsymbol{n} dS = \int_\Gamma \mu \mathbf{B} \sqrt{\boldsymbol{K}^{-1}} \boldsymbol{v}_b \cdot \boldsymbol{w} dS, \tag{5.58}$$

where $\mathbf{B}$ is the *slip tensor* (in the case of Section 5.1.3, $\mathbf{B} = \beta\boldsymbol{I}$).

The boundary conditions in the external wall (inlet condition and no-slip boundary condition) are imposed by the penalty method. Moreover, we add the Grad-div stabilization terms

$$\gamma_1 \int_{\Omega^{S/B}} \nabla \cdot \boldsymbol{v} \cdot \nabla \cdot \boldsymbol{w} dV + \gamma_2 \int_{\Omega^{S/B}} \nabla \cdot \left(\frac{\partial \boldsymbol{v}}{\partial t}\right) \cdot \nabla \cdot \boldsymbol{w} dV \tag{5.59}$$

in either Stokes and Darcy-Brinkman domains [112–115]. Thanks to this stabilization term, we have the stability for the Darcy-Brinkman equation (see [116]). For the numerical discretization, we use a BDF2 method for the time discretization, instead, we use $\mathbb{P}_k^d - \mathbb{P}_k$ element pairs (where k is the polynomials order and d is the dimension) with the Brezzi-Pitkäranta stabilization, which consists in adding the term $\epsilon \int_{\Omega^S} \nabla p \cdot \nabla q dV + \epsilon \int_{\Omega^B} \nabla p_b \cdot \nabla q_b dV$ to the discretization of the equation (5.57), with $\epsilon \approx h_T^2$, where h_T is the maximum diameter of the triangle of the finite element triangulation. The weak formulation here proposed has been implemented using the open source software FreeFEM [102].

5.2.1 Numerical Test

In this section we want to qualitatively compare the results obtained with the numerical simulation with the explicit results exposed in Section 5.1. For that reason, we use the same geometry and parameters exhibited in Section 5.1.2; hence, in the external boundary we will impose only Dirichlet boundary condition (Γ_N is empty), subdivided as $\Gamma_D = \Gamma_{\text{in}} \cup \Gamma_{\text{out}} \cup \Gamma_{\text{BC}}$, where we are imposing the inlet and the outlet flow in Γ_{in} and Γ_{out}, respectively, given by the equation (5.32) with $L = 10^{-3}\,\text{mm}^3/\text{s}$, and the no-slip boundary condition in Γ_{BC}. The numerical stabilization parameters are estimated as $\gamma_2 = 0$, while $\gamma_1 = 300$ in Ω^S and $\gamma_1 = 10^6$ in Ω^B.

In Figure 5.5, Figure 5.6, and Figure 5.7, we can see the tangential and radial velocity, and the shear stress, respectively. We can see that the results are very similar to the ones explicitly found in Section 5.1.4: in order to remove some small oscillations in the internal velocity near R_1, we needed to use a finer mesh, which meant a greater computational cost for every time step. We can do only a qualitative comparison between the numerical solution of this section and the explicit solution in Section 5.1.4 because we do not have available and precise physiological data of the lymph node and we have an error in both cases: in the explicit result from the truncation of the sum, and here due to the finite element approximation. Qualitatively, we have the same behavior and values here and in the explicit result.

5.2.2 Numerical results

In this section we want to show a more complete numerical simulation using the method given in Section 5.2.

We use a spherical idealized 2D geometry with the same parameters given in Section 5.1.2; hence we suppose that the permeability tensor $\boldsymbol{K}$ is homogeneous and constant (this is not a limiting assumption, see [5, 11, 101]) and the same with the slip tensor $\mathbf{B} = \beta \boldsymbol{I}$. Moreover, we add to the simulation domain a part to the inlet and outlet lymphatic vessel (see Figure 5.10 and Figure 5.8).

As we mention in Section 5.1.2, more than 90% of the lymph takes a peripheral path; the lymph that enters in the LC does not remain in the LC but gets out due to the incompressibility of the lymph, because we are not taking into account the fluid exchange behavior given by the blood vessels inside the LN.

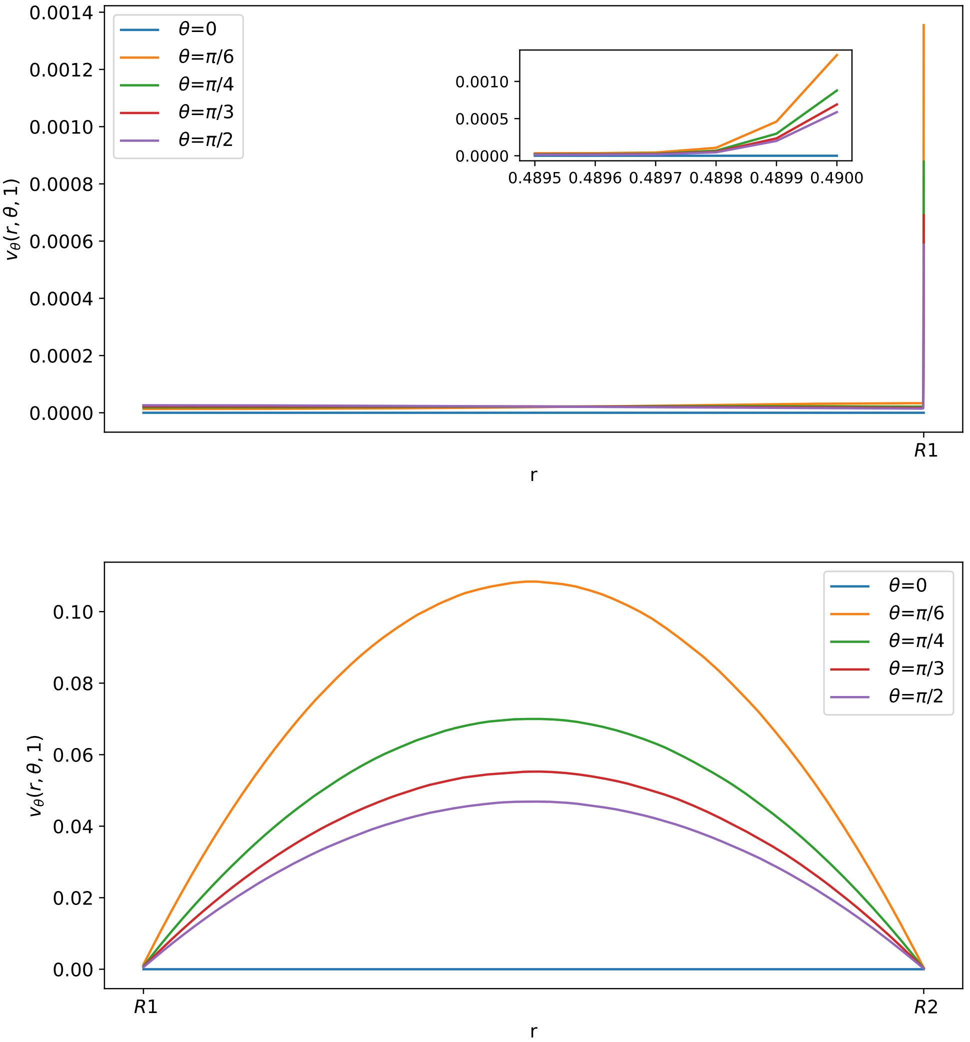

Figure 5.5: Tangential component of the velocity in mm/s with respect to the radius at different angles at $t = 1\,\mathrm{s}$. The first graph corresponds to the tangential velocity in the LC (porous part), and the second corresponds to the tangential velocity in the SCS (free-fluid region).

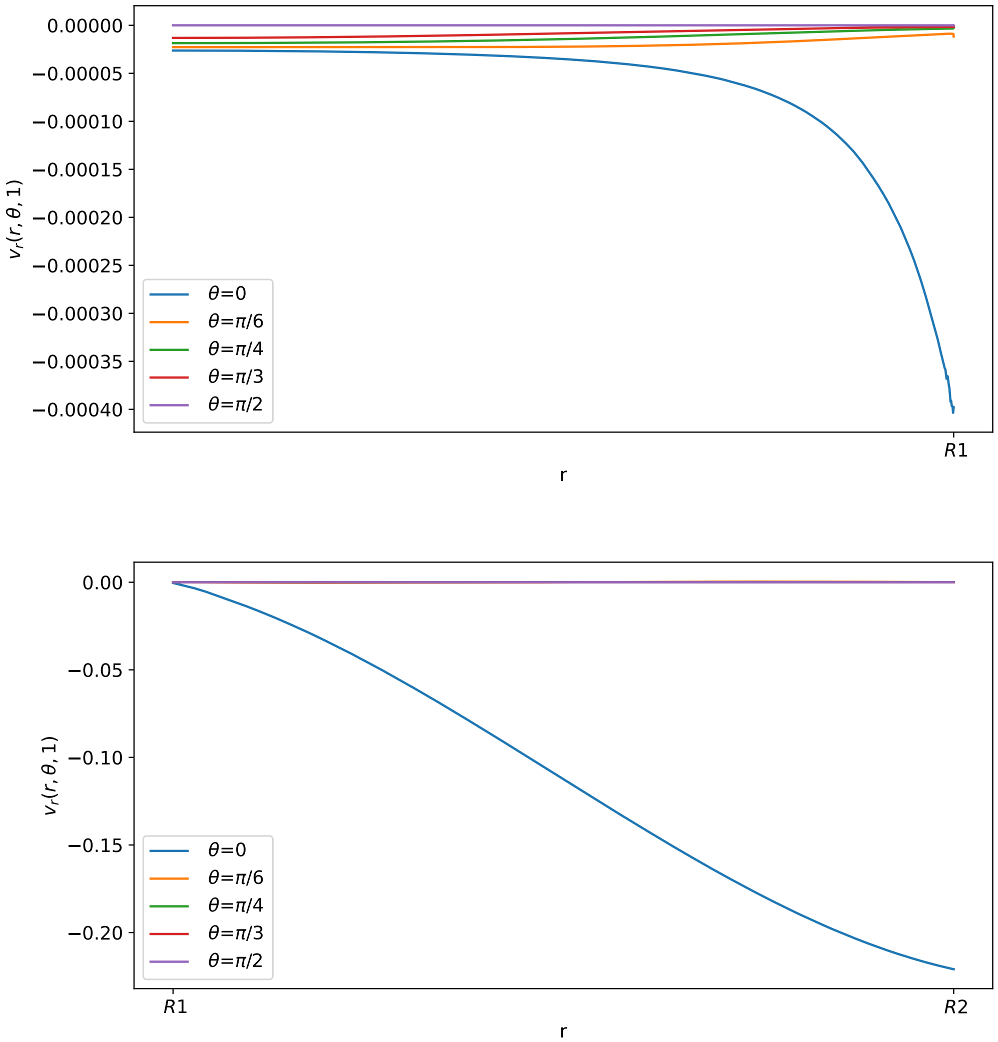

Figure 5.6: Normal component of the velocity in mm/s with respect to the radius at different angles at $t = 1\,\text{s}$. The first graph corresponds to the tangential velocity in the LC (porous part), and the second corresponds to the tangential velocity in the SCS (free-fluid region).

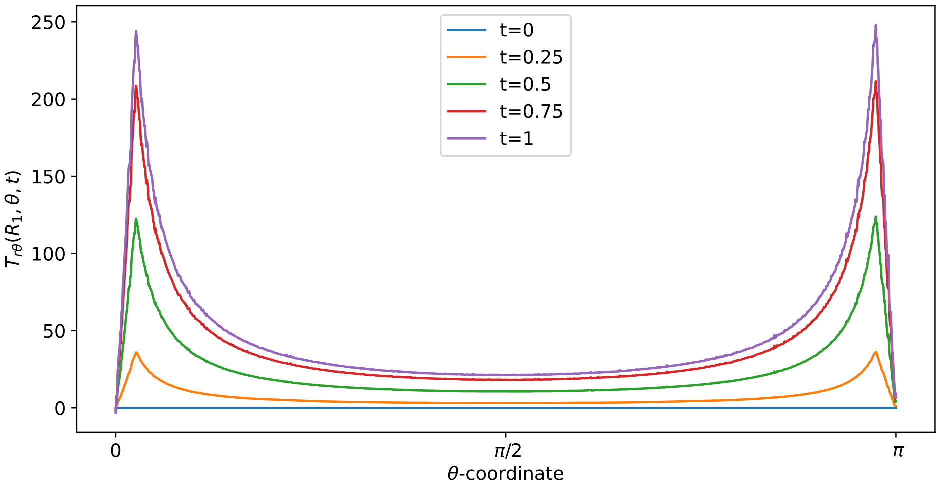

Figure 5.7: Shear stress in mPa with respect to the polar coordinates calculated at a fixed radius $r = R_1$ in different times.

Unlike the explicit case, here the boundary conditions do not concern the inlet and outlet velocity, but only the inlet one, and in the outlet we impose the pressure.

The inlet condition is imposed in the upper lymphatic vessel as a uniform pulsatile flow in the y direction with the equation (5.32).

For the outlet condition, we need to fix the stress. For clarity and for a simpler interpretation, we fix the pressure $\bar{p}(t)$ in this way:

$$\begin{aligned}\left[\int_{\Gamma_N^S} \boldsymbol{T}\boldsymbol{w}\cdot\boldsymbol{n}dS\right]_{|\bar{p}} &= \left[\int_{\Gamma_N^S} \left(-p\boldsymbol{I} + \mu\left[\nabla\boldsymbol{v} + \nabla\boldsymbol{v}^T\right]\right)\boldsymbol{w}\cdot\boldsymbol{n}dS\right]_{|\bar{p}} \\ &= \int_{\Gamma_N^S} \left(-\bar{p}\boldsymbol{I} + \mu\left[\nabla\boldsymbol{v} + \nabla\boldsymbol{v}^T\right]\right)\boldsymbol{w}\cdot\boldsymbol{n}dS. \end{aligned} \tag{5.60}$$

We use the numerical parameters given in Section 5.2.1. In Figure 5.8, we can see the pressure distribution in the LN with $\bar{p} = 6.18 \times 10^5 f(t)\,\mathrm{mPa}$ ($= 6.3\,\mathrm{cmH_2O}$ as the inferior limit in the range of pressure found in [111] and as in the explicit results in Section 5.1.4), where $f(t)$ is the one given by the equation (5.55). As we can see, the pressure distribution is similar to the one in Figure 5.1 and it is in range with the corresponding results. If one has $\bar{p} = 4 \times 10^5 f(t)\,\mathrm{mPa}$ ($= 3\,\mathrm{mmHg}$ as in [5]), the behavior of the pressure is similar to the one showed in Figure 5.8 (so that we omit the picture), with a range of values comparable to [5].

In Figure 5.9, we can see the shear stress over time (in mPa). At time $t = 1\,\mathrm{s}$, we have the maximum value of the velocity (and, consequently, of the shear stress) and the shear stress is similar to the one found in the explicit result (the blue curve with $v_{in} \approx 0.22$ plotted in Figure 5.2), that is in range with the values found in [5, 12].

We can see the norm and the velocity behavior in more details in Figure 5.10. The tangential velocity (the most relevant one) is shown in Figure 5.11. As expected, the maximum velocity is in the SCS near the inlet and the outlet region.

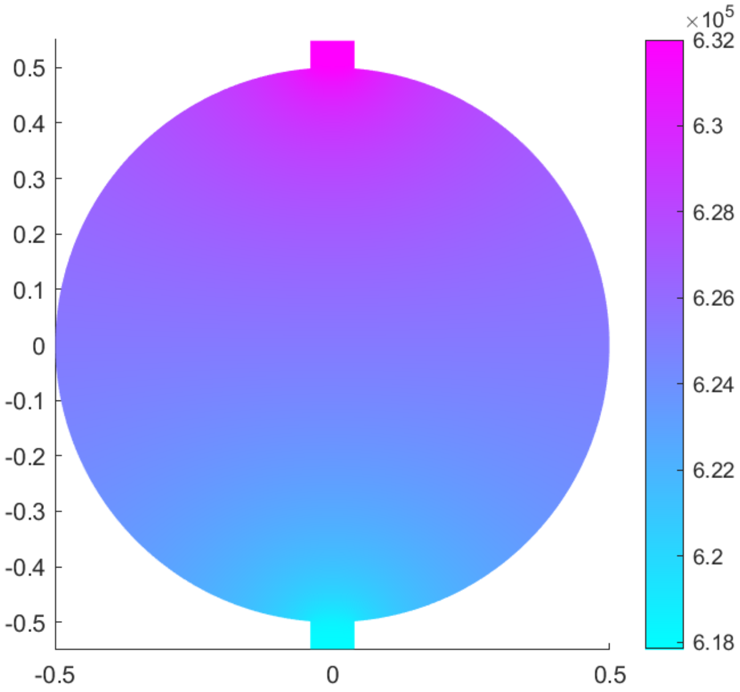

Figure 5.8: Pressure distribution in mPa with fixed pressure $\bar{p} = 6.18 \times 10^5$ mPa at outlet.

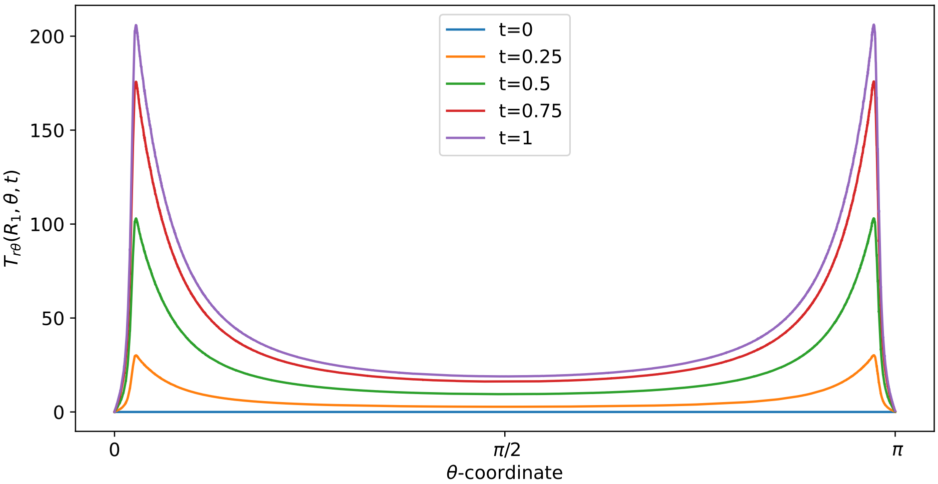

Figure 5.9: Shear stress in mPa with respect to the polar angle ($\theta = 0$ near the inlet flow and $\theta = \pi$ near the outlet flow) calculated at different times.

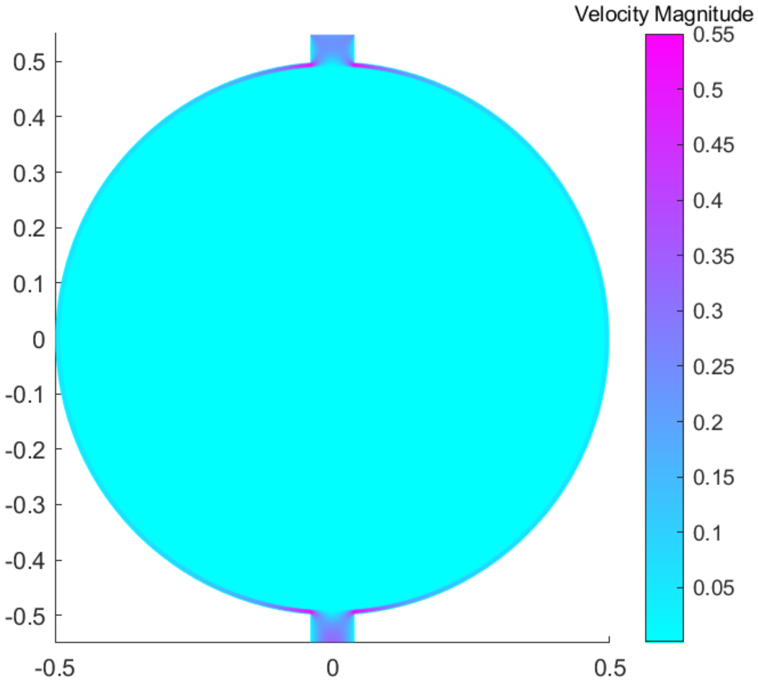

Figure 5.10: Velocity magnitude in mm/s at $t = 1\,\mathrm{s}$ (maximum velocity).

In particular, we can see that the maximum velocity is between the connections of the SCS with the afferent/efferent vessel; then the velocity decrease with respect to the polar coordinate θ, reaching the minimum at $\theta = \pi/2$. Moreover, even if we do not impose the outlet velocity equal to the inlet one, we have that this is true due to the incompressibility; hence our assumption used to find the explicit solution is not too limiting in this case.

5.3 Oblate Spheroidal Lymph Node

In this section, we want to use the numerical simulations described and tested in the previous sections to a lymph node with a more realistic geometry, which is an oblate spheroid [5, 8, 9, 12] of this form

$$\begin{bmatrix} x \\ y \end{bmatrix} = \begin{bmatrix} a\cos\theta \\ b\sin\theta \end{bmatrix}, \tag{5.61}$$

with major semiaxis $a = 0.5$ mm, minor semiaxis $b = 0.35$ mm, and subcapsular sinus thickness $h = 10$ μm. It follows that the parametric equation that describes the LC geometry is

$$\begin{bmatrix} x \\ y \end{bmatrix} = \begin{bmatrix} a\cos\theta \\ b\sin\theta \end{bmatrix} - h\frac{\begin{bmatrix} \frac{2}{a^2}\cos\theta \\ \frac{2}{b^2}\sin\theta \end{bmatrix}}{\left\| \begin{bmatrix} \frac{2}{a^2}\cos\theta \\ \frac{2}{b^2}\sin\theta \end{bmatrix} \right\|}. \tag{5.62}$$

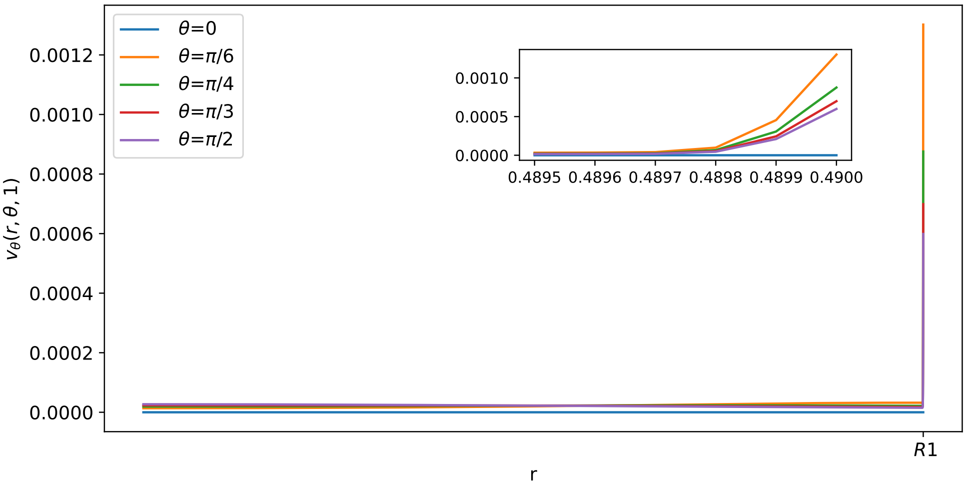

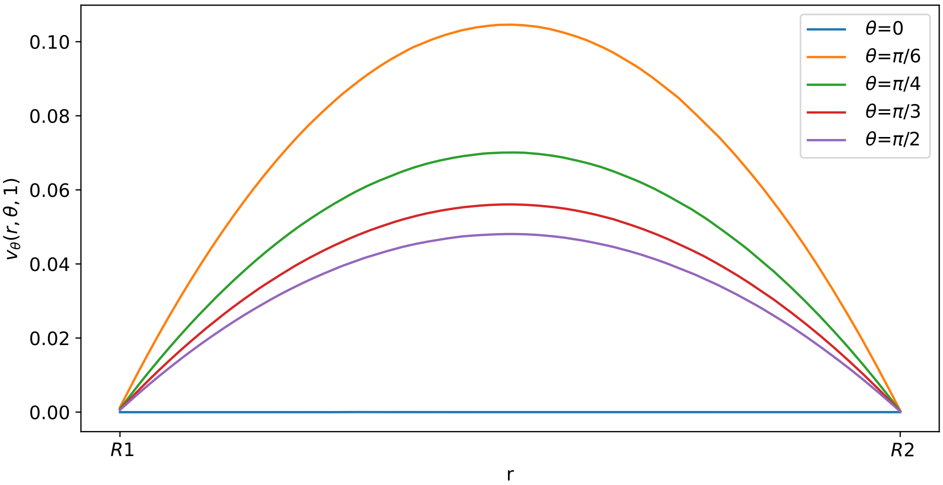

Figure 5.11: Tangential component of the velocity in mm/s with respect to the radius at different angles at $t = 1\,\text{s}$. The first graph corresponds to the tangential velocity in the LC (porous part), and the second corresponds to the tangential velocity in the SCS (free-fluid region).

The other parameters remain as in the previous sections (see Section 5.1.2). We can see the geometry of our problem in Figure 5.14. We study the same problem presented in Section 5.2.2 in the geometry presented above to compare the two cases.

We plot the velocity results defining

$$\begin{bmatrix} x \\ y \end{bmatrix} = \begin{bmatrix} a\cos\theta \\ b\sin\theta \end{bmatrix} - d\frac{\begin{bmatrix} \frac{2}{a^2}\cos\theta \\ \frac{2}{b^2}\sin\theta \end{bmatrix}}{\left\| \begin{bmatrix} \frac{2}{a^2}\cos\theta \\ \frac{2}{b^2}\sin\theta \end{bmatrix} \right\|}, \tag{5.63}$$

varying d (when $d = h$ we obtain the interface between the SCS and the LC and when $d = 0$ we obtain the external spheroidal domain). In Figure 5.12 we can see the tangential velocity component with respect to d at time $t = 1\,\mathrm{s}$. As in the case we have studied in Section 5.2.2, the maximum velocity is in the SCS near the inlet and the outlet region. In particular, we can see that the maximum velocity is between the connections of the SCS with the afferent/efferent vessel; then the velocity decreases with respect to the polar coordinate θ, reaching the minimum at $\theta = \pi/2$. Figure 5.13 shows the same behavior for the shear stress. The velocity behavior is the same as in the spherical case, but here the tangential velocity is lower. We can see this also in Figure 5.14, where we have the velocity magnitude plot; as we can see, the velocity behavior is qualitatively similar to the spherical case. Despite this, the shear stress, in this case, is very similar to the spherical one, as shown in Figure 5.13.

In Figure 5.15, we can see the pressure distribution over the spheroidal lymph node; as we can see, the behavior is the same and the values are very close to the spherical case.

We can conclude that although there is some difference between the spherical and spheroidal cases, qualitatively we have the same behavior. Moreover, the shear stress at the external surface of the LC and the pressure are very close, which means that the spherical shape we chose as a simplified lymph node geometry is a pretty good approximation for a qualitative study of the fluid flow in a lymph node.

5.4 Conclusions

We proposed a model that describes the pulsatile lymph flow inside a simplified spherical and spheroidal lymph node (LN), using the Darcy-Brinkman equation to describe the lymph flow in the lymphoid compartment (LC, the porous part) and the Stokes equation to describe the flow inside the subcapsular sinus (SCS, the free fluid region). We found the explicit solution in terms of Gegenbauer polynomials and we showed the trend of the velocity, the pressure, and the shear stress inside the LN; after that, we used this explicit solution to validate the numerical simulations of the model. Finally, we performed a more general numerical simulation with finite elements.

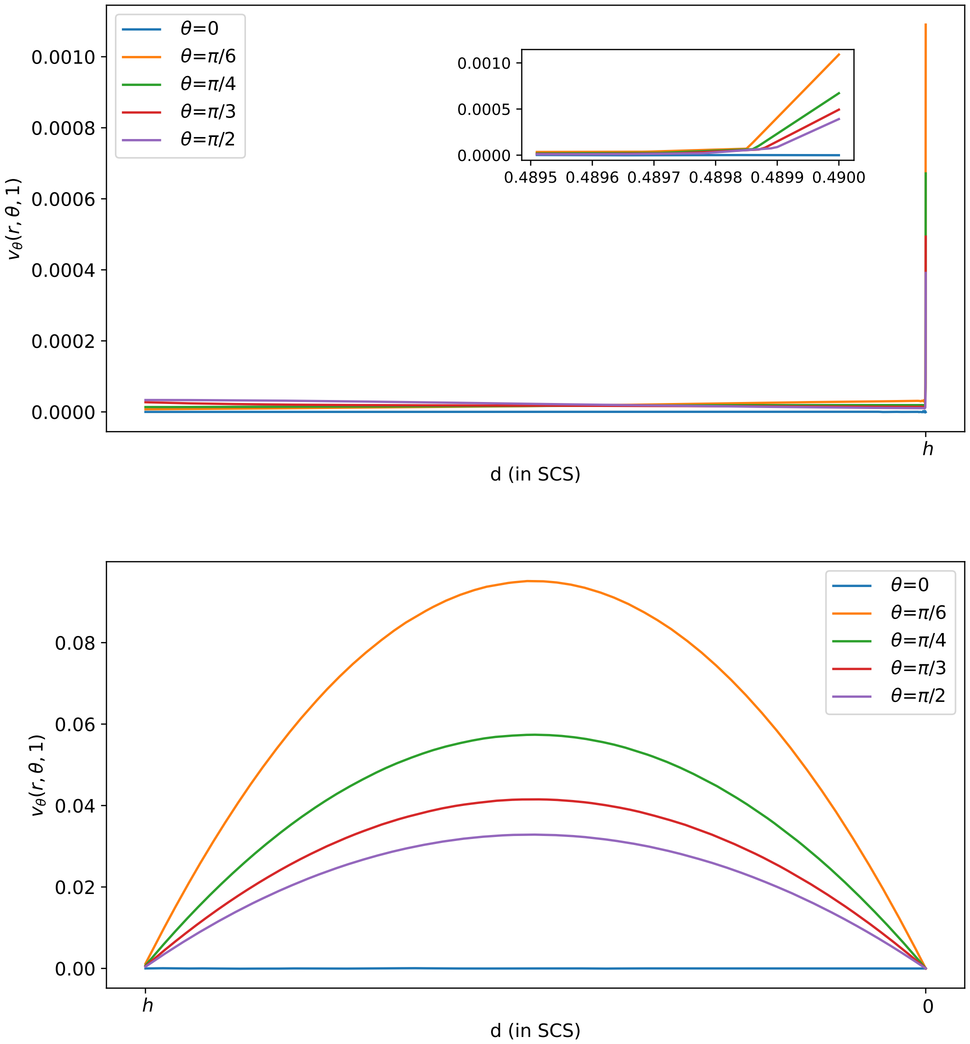

Figure 5.12: Tangential component of the velocity in mm/s with respect to d at different angles at $t = 1\,\mathrm{s}$. The first graph corresponds to the tangential velocity in the LC (porous part), and the second corresponds to the tangential velocity in the SCS (free-fluid region).

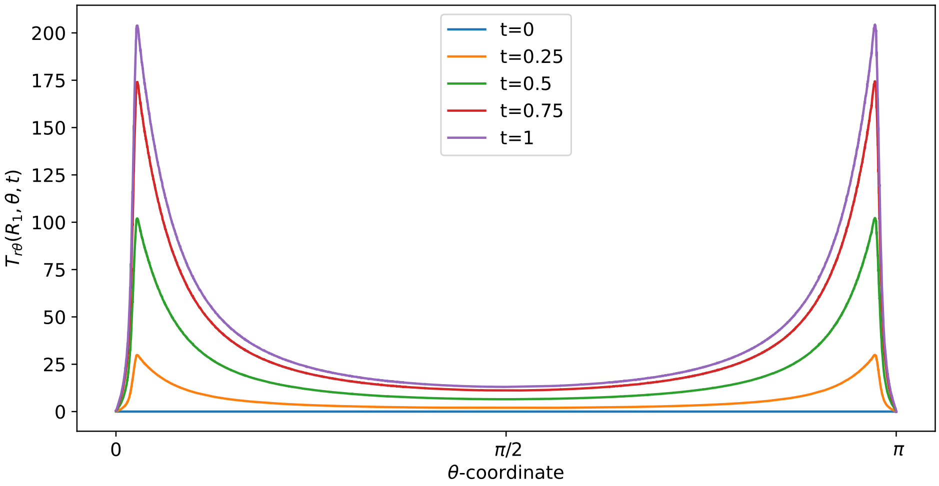

Figure 5.13: Shear stress in mPa with respect to the polar angle ($\theta = 0$ near the inlet flow and $\theta = \pi$ near the outlet flow) calculated at different times.

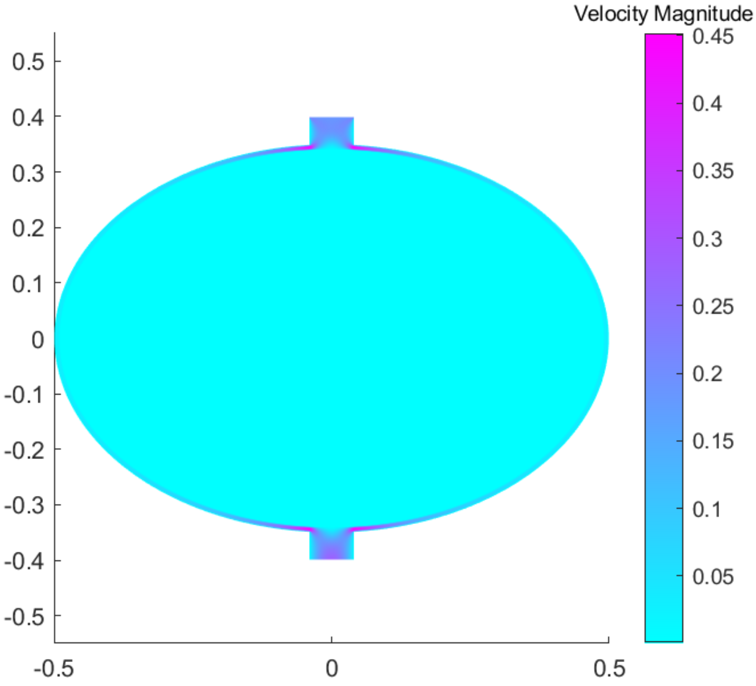

Figure 5.14: Velocity magnitude in mm/s at $t = 1\,\mathrm{s}$ (maximum velocity).

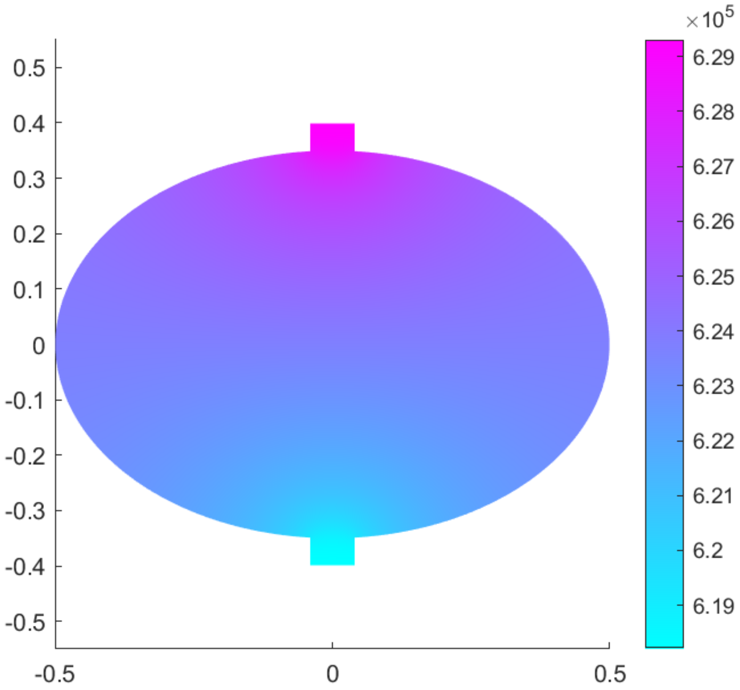

Figure 5.15: Pressure in mPa at $t = 1\,\text{s}$ (maximum velocity).

This model allows us to better understand the fluid behavior inside the LN and how it changes with respect to time. The results obtained by our model are in agreement with the literature [5–7, 11, 12]. We remark that the Ochoa-Tapia boundary condition minimally affects the fluid behavior in the SCS. Still, it affects the flow in the LC, inducing a velocity profile which is not smooth at the interface between the LC and SCS regions.

Particular attention has been given to the shear stress, because a lot of biological phenomena in the LN depend on it. Among them is the cell adhesion to the exterior of the LC, which is proportional to the shear stress: this is important because inside the LC there is a connection between the lymphatic system and the blood system, and some cells can get access from here to the blood circulation (for instance, tumor cells [12]). Moreover, shear stress drives drug delivery and can affect pathologies like B-cell lymphoma [57, 117]. In our model we found that the shear stress is higher near the inlet and the outlet regions, and decreases with respect to the polar angle θ, reaching the minimum at $\theta = \pi/2$; hence we believe that the majority of the cell adhesion is located near these two critical regions, which are the connections of the SCS with the afferent/efferent vessels.

If we compare the model proposed in this chapter with the one proposed in chapter 4, we have that the difference lies not only in the geometry, but also in the different and more general interface conditions (the Ochoa-Tapia interface conditions) and in the fact that here we are not supposing a laminar flow.

Finally, we compared the spherical and the spheroidal case and we could conclude that although there was some difference between the two cases, qualitatively we had the same behavior. Moreover, the shear stress at the external surface of the LC and the pressure are very close, which means that the spherical shape we chose as a simplified lymph node geometry is a pretty good approximation.

Chapter 6

Multiscale Darcy/Darcy-Brinkman Coupling with Application to a Vascularized Lymph Node

The motion of an incompressible Newtonian fluid inside a rigid porous matrix can be macroscopically described by Darcy's law, which was formulated by Henry Darcy based on the results of experiments on the flow of water through beds of sand [77] (see Section 2.1 and Section 2.4).

There is another important differential equation that describes the fluid flow of an incompressible Newtonian fluid inside a rigid porous matrix: the Darcy-Brinkman equation (see Section 2.1). This equation has been introduced by Brinkman adding a Laplacian (viscous) term (called Brinkman term) to the classical Darcy equation [79], weighed by an effective viscosity μ_e. It has been used widely to analyze high-porosity porous media. Moreover, if we have an interaction between a free-fluid region and a porous region, we have that the Darcy-Brinkman equation allows us to study in more detail the interface (and the boundary layer) between them [80]; in general, the Darcy-Brinkman formulation allows us to specify the boundary conditions [81], having a differential form similar to the Stokes one.

Despite its practical feedback, the Darcy-Brinkman equation is theoretically less justified than Darcy's law from a multiscale point of view [32, 78, 118] and is computationally more demanding. Moreover, Darcy and Darcy-Brinkman equations have very different differential structures.

In this chapter we present a multiscale model using the *asymptotic homogenization technique* (see Section 2.4) that couples the Darcy and the Darcy-Brinkman equation, with inhomogeneous body forces [119].

We consider a multiscale volume load that drives the coarse scale fluid flow acting on both the Darcy and the Darcy-Brinkman problems. The above-mentioned source involves both the cell average of the body force and an additional contribution related to the solution of another cell problem driven solely by fine scale variations of the given force. Such forces can arise from the application of electromagnetic fields, on magnetorheological fluids and electrolytes percolating heterogeneous tissues.

The derivation of the macroscopic equations related to this problem is as general as possible, so we can use this model to describe plenty of multiscale phenomena. However, the motivation that drives us to study this model is the application of the latter to the movement of fluid within a lymph node. Lymph nodes are essential organs in our immune and lymphatic system, and we refer to Section 1.2 for a detailed description of them. Essentially, lymph nodes are formed by a thin channel near the wall (*subcapsular sinus*, SCS) where the fluid can flow freely surrounding a porous core (*lymphoid compartment*, LC) that is the *parenchyma* of the lymph node [120], where the fluid can enter from the SCS through a conduit system network [49, 59, 101] formed by fibroblastic reticular cells (FRC). In particular, we focus our attention on the porous region of the lymph node (the LC) and the fluid exchange between the node and the blood vessels, which are only in this part of the node [5, 53, 54]; using the hypothesis of axisymmetry and isotropy of the porous medium, we found an explicit solution and analyze it by varying physiological parameters related to the lymph node. After that, we solve the general case coupling the fluid flow in the SCS with the fluid flow in the LC using numerical simulations obtained using COMSOL Multiphysics.

In Section 6.1, we define the starting equations of our problem. We formulate the balance equations of Continuum Mechanics and the corresponding boundary conditions. In Section 6.2 we use the asymptotic homogenization technique to find the equations that describe the motion of the fluid at the macroscale, one starting with the Darcy-Brinkman equation and the other with the Darcy equation, and to describe the fluid exchange between them. In Section 6.3, we find the macroscopic equations by averaging the leading order terms of the asymptotic expansion. In Section 6.4 we analyze the difference in having as a microscale cell problem Darcy, Darcy-Brinkman, or Stokes, finding an explicit result to the microscale cell problem in a specific case. In Section 6.5, we find the macroscopic explicit solution in a sphere with axisymmetry and isotropic permeability in terms of Bessel's and Legendre's polynomials. In Section 6.6 we analyze the solution found in Section 6.5 with lymph node physiological data obtained from the literature. Finally, in Section 6.7 we study numerically the fluid flow in a lymph node coupling the free-fluid region (SCS) with the porous region (LC) using lymph node physiological data.

The results presented in this chapter have not yet been published, but a preprint is in preparation.

6.1 Statement of the Problem

Let us consider a domain $\Omega = \Omega_v \cup \Omega_m$, where Ω_m and Ω_v are the portions of the domain that indicate two different phases. The labels m and v stand for the *matrix* and the *vessel* regions, respectively.

We use Darcy equation with inhomogeneous body forces to describe the fluid flow in the domain Ω_v [119]:

$$\begin{cases} \boldsymbol{v}_v(\boldsymbol{x}) = -\hat{\boldsymbol{K}}_v(\boldsymbol{x}) \left(\nabla p_v(\boldsymbol{x}) - \boldsymbol{f}_v(\boldsymbol{x})\right) & \text{in } \Omega_v \\ \nabla \cdot \boldsymbol{v}_v(\boldsymbol{x}) = 0 & \text{in } \Omega_v. \end{cases} \tag{6.1}$$

The Darcy-Brinkman equation with inhomogeneous body forces in the phase Ω_m can be written as:

$$\begin{cases} -\nabla p_m(\boldsymbol{x}) - \hat{\boldsymbol{K}}_m^{-1}(\boldsymbol{x})\boldsymbol{v}_m(\boldsymbol{x}) + \mu_e \Delta \boldsymbol{v}_m(\boldsymbol{x}) + \boldsymbol{f}_m(\boldsymbol{x}) = \boldsymbol{0} & \text{in } \Omega_m \\ \nabla \cdot \boldsymbol{v}_m(\boldsymbol{x}) = 0 & \text{in } \Omega_m. \end{cases} \tag{6.2}$$

Here we are considering two fluid phases: one in Ω_v and one in Ω_m. For $\gamma = v, m$, $\boldsymbol{v}_\gamma$ is the velocity of the fluid, p_γ the pressure, $\boldsymbol{f}_\gamma$ the external force density, $\hat{\boldsymbol{K}}_\gamma(\boldsymbol{x})$ is *hydraulic conductivity tensor*, which is given by the permeability tensor divided by the viscosity μ of the fluid, and μ_e is the *effective viscosity.* We assume that the hydraulic conductivity tensor is symmetric and positive definite, that is

$$\hat{\boldsymbol{K}}_\gamma(\boldsymbol{x}) = \hat{\boldsymbol{K}}_\gamma^T(\boldsymbol{x}), \quad \forall \boldsymbol{a} \neq \boldsymbol{0} : \boldsymbol{a} \cdot \hat{\boldsymbol{K}}_\gamma(\boldsymbol{x}) \cdot \boldsymbol{a} > 0. \tag{6.3}$$

As our starting points are the Darcy and Darcy-Brinkman representations, the pore structure is considered already smoothed out, and the microscale geometry information is encoded in the hydraulic conductivity $\hat{\boldsymbol{K}}_\gamma(\boldsymbol{x})$.

The interface conditions are prescribed as follows:

$$\begin{cases} \boldsymbol{v}_v(\boldsymbol{x}) \cdot \boldsymbol{n} = \boldsymbol{v}_m(\boldsymbol{x}) \cdot \boldsymbol{n} = L_p(p_m(\boldsymbol{x}) - p_v(\boldsymbol{x}) - \bar{p}) & \text{on } \Gamma \\ \boldsymbol{v}_m(\boldsymbol{x}) \cdot \boldsymbol{t} = -\dfrac{\sqrt{\hat{\mathfrak{K}}_m(\boldsymbol{x})}}{\alpha} \left[\left(\boldsymbol{n} \cdot \nabla\right) \boldsymbol{v}_m(\boldsymbol{x})\right] \cdot \boldsymbol{t} & \text{on } \Gamma, \end{cases} \tag{6.4}$$

where $\Gamma = \partial\Omega_m \cap \partial\Omega_v$ is the interface between the domains Ω_v and Ω_m, $\hat{\mathfrak{K}}_m(\boldsymbol{x})$ is the *permeability* of the hydraulic conductivity tensor $\hat{\boldsymbol{K}}_m(\boldsymbol{x})$, $\boldsymbol{n}$ the outer normal to Ω_m, $\boldsymbol{t}$ any tangential vector to Γ, $\bar{p}$ is a constant and α is a constant that must be found with experiments. The second equation of (6.4) is the *Beavers-Joseph-Saffman boundary condition* [121–125], which is a quite general interface condition on the tangent component of the velocity. We remark that we need the $\sqrt{\hat{\mathfrak{K}}_m(\boldsymbol{x})}$ to have the same dimensions in both sides of the equation [122]. Instead, for the normal component of the velocity, we impose the interface condition described by the first equation of (6.4). We impose this type of interface condition having in mind biological applications of this model (such as lymph nodes, tumors, etc...); indeed, if we have $\bar{p} = \sigma\left(\pi_m - \pi_v\right)$, we obtain the *Starling equation* [55, 56], which describes the fluid exchange between two different phases, where σ is the *Staverman's reflection coefficient*, π_v the *oncotic pressure of phase* Ω_v and π_m the *oncotic pressure of phase* Ω_m. For simplicity, in this work, we assume that the oncotic pressures π_v and π_m are constant, although in general, they can depend on the concentration of solutes which vary over time and space [126]. The quantity L_p is given by experimental measurements and depends on both the geometry and the tissue wall material of the intersection Γ. Nevertheless, our model remains valid for other choices of boundary conditions.

Now we want to write the Darcy-Brinkman equation and the interface conditions in a non-dimensional form; we define the following non-dimensional quantities (denoted with a prime symbol):

$$p = Pp', \quad \boldsymbol{v} = U\boldsymbol{v}', \quad \epsilon = \frac{d}{L}, \tag{6.5}$$

where P is the *characteristic pressure*, U is the *characteristic velocity*, d is the *fine scale length* and L is the *coarse scale length*. C is a *representative pressure gradient* (with $P = CL$), say:

$$C = \frac{U}{K_{\text{ref}}}, \tag{6.6}$$

where K_{ref} is the representative (scalar) value for the hydraulic conductivity given by

$$K_{\text{ref}} \approx \frac{d^2}{\mu}, \tag{6.7}$$

and we set

$$\boldsymbol{K}' = \frac{\hat{\boldsymbol{K}}}{K_{\text{ref}}}, \qquad \boldsymbol{f}'_m = \frac{\boldsymbol{f}_m}{C}. \tag{6.8}$$

Substituting into (6.2) and omitting the primes, we obtain:

$$\begin{cases} -\nabla p_m(\boldsymbol{x}) - \boldsymbol{K}_m^{-1}(\boldsymbol{x})\boldsymbol{v}_m(\boldsymbol{x}) + \hat{\mu}\Delta\boldsymbol{v}_m(\boldsymbol{x}) + \boldsymbol{f}_m(\boldsymbol{x}) = \boldsymbol{0} & \text{in } \Omega_m, \\ \nabla \cdot \boldsymbol{v}_m(\boldsymbol{x}) = 0 & \text{in } \Omega_m, \end{cases} \tag{6.9}$$

where

$$\hat{\mu} = \frac{K_{\text{ref}}\,\mu_e}{L^2}. \tag{6.10}$$

Assuming that $\mu_e \approx \mu$, we have $\hat{\mu} = O(\epsilon^2)$.

Substituting these equations into (6.1) and (6.9), we obtain the non-dimensional equations:

$$\begin{cases} \boldsymbol{v}_v(\boldsymbol{x}) = -\boldsymbol{K}_v(\boldsymbol{x})\left(\nabla p_v(\boldsymbol{x}) - \boldsymbol{f}_v(\boldsymbol{x})\right) & \text{in } \Omega_v \\ \nabla \cdot \boldsymbol{v}_v(\boldsymbol{x}) = 0 & \text{in } \Omega_v, \end{cases} \tag{6.11}$$

$$\begin{cases} -\nabla p_m(\boldsymbol{x}) - \boldsymbol{K}_m^{-1}(\boldsymbol{x})\boldsymbol{v}_m(\boldsymbol{x}) + \epsilon^2\mu^*\Delta\boldsymbol{v}_m(\boldsymbol{x}) + \boldsymbol{f}_m(\boldsymbol{x}) = \boldsymbol{0} & \text{in } \Omega_m, \\ \nabla \cdot \boldsymbol{v}_m(\boldsymbol{x}) = 0 & \text{in } \Omega_m, \end{cases} \tag{6.12}$$

where $\mu^* = \dfrac{\mu_e}{\mu}$.

Now we want to non-dimensionalize the interface conditions (6.4): by the Starling equation, the flux J_v passing through the interface between the two phases is given by

$$J_v = L_p\bar{S}\left(p_m(\boldsymbol{x},t) - p_v(\boldsymbol{x},t) - \bar{p}\right), \tag{6.13}$$

where $\bar{S}$ is the total exchange surface density. From the fact that d is related to the distance between the vessels of the domain Ω_v, we have

$$\bar{S} \propto \frac{L}{d} = \frac{1}{\epsilon}. \tag{6.14}$$

It is likely that the measured flux of a specific area of tissue will remain finite, even if the number of capillaries and their total surface area within that volume increases; hence we need to scale the interface condition by ϵ to have a finite flux. The same conclusion can be recovered also for the Beavers-Joseph-Saffman interface condition (see [126] for more details). Then, substituting into equation (6.4) we have:

$$\begin{cases} \boldsymbol{v}_v(\boldsymbol{x}) \cdot \boldsymbol{n} = \boldsymbol{v}_m(\boldsymbol{x}) \cdot \boldsymbol{n} = \epsilon L_p(p_m(\boldsymbol{x}) - p_v(\boldsymbol{x}) - \bar{p}) & \text{on } \Gamma \\ \boldsymbol{v}_m(\boldsymbol{x}) \cdot \boldsymbol{t} = -\epsilon \dfrac{\sqrt{\boldsymbol{\mathcal{K}}_m(\boldsymbol{x})}}{\alpha} \left[(\boldsymbol{n} \cdot \nabla) \, \boldsymbol{v}_m(\boldsymbol{x}) \right] \cdot \boldsymbol{t} & \text{on } \Gamma. \end{cases} \tag{6.15}$$

6.2 Asymptotic Homogenization

In this section, we employ the asymptotic homogenization technique (Section 2.4) [32, 70] to derive a continuum macroscale model for the systems (6.11)–(6.15). Since we suppose $\epsilon = \frac{d}{L} \ll 1$, we enforce the sharp length scale separation between d (fine scale) and L (coarse scale) and we decouple spatial scales by introducing a new local variable

$$\boldsymbol{y} = \frac{\boldsymbol{x}}{\epsilon}, \tag{6.16}$$

where $\boldsymbol{x}$ and $\boldsymbol{y}$ represent the coarse and fine scale spatial coordinates, respectively. They have to be formally considered independent variables. From now on, p_γ, $\boldsymbol{v}_\gamma$, $\boldsymbol{K}_\gamma$ and $\boldsymbol{f}_\gamma$ (where $\gamma = m, v$) are assumed to depend on both $\boldsymbol{x}$ and $\boldsymbol{y}$.

Before we start with the asymptotic homogenization technique, we recall some assumptions concerning the geometry of the multiscale problem (see Section 2.4):

- *Local periodicity*: we assume that p_γ, $\boldsymbol{v}_\gamma$, $\boldsymbol{K}_\gamma$ and $\boldsymbol{f}_\gamma$ are $\boldsymbol{y}$-periodic. This assumption allows us to study fine scale variations of the fields on a restricted portion of the domain. In particular, we have that Ω is the periodic cell domain, and Ω_m and Ω_v are the portions of the domain Ω related to the two different phases.

- *Macroscopic uniformity*: we neglect geometric variations of the cell and inclusions with respect to the coarse scale variable $\boldsymbol{x}$. Thanks to this assumption, we can consider only one periodic cell Ω_γ for every macroscale point $\boldsymbol{x}$, and we have that

$$\nabla_{\boldsymbol{x}} \cdot \int_{\Omega_\gamma} (\cdot) d\boldsymbol{y} = \int_{\Omega_\gamma} \nabla_{\boldsymbol{x}} \cdot (\cdot) d\boldsymbol{y}. \tag{6.17}$$

The differential operator transforms accordingly

$$\nabla \to \nabla_{\boldsymbol{x}} + \frac{1}{\epsilon} \nabla_{\boldsymbol{y}}. \tag{6.18}$$

Now we employ a power series representation with respect to ϵ as follows (with $\gamma = m, v$):

$$\boldsymbol{v}_\gamma(\boldsymbol{x}, \boldsymbol{y}) \equiv \boldsymbol{v}^\epsilon_\gamma(\boldsymbol{x}, \boldsymbol{y}) = \sum_{l=0}^{\infty} \boldsymbol{v}^{(l)}_\gamma(\boldsymbol{x}, \boldsymbol{y})\epsilon^l, \tag{6.19}$$

$$p_\gamma(\boldsymbol{x}, \boldsymbol{y}) \equiv p^\epsilon_\gamma(\boldsymbol{x}, \boldsymbol{y}) = \sum_{l=0}^{\infty} p^{(l)}_\gamma(\boldsymbol{x}, \boldsymbol{y})\epsilon^l, \tag{6.20}$$

$$\boldsymbol{f}_\gamma(\boldsymbol{x}, \boldsymbol{y}) \equiv \boldsymbol{f}^\epsilon_\gamma(\boldsymbol{x}, \boldsymbol{y}) = \sum_{l=0}^{\infty} \boldsymbol{f}^{(l)}_\gamma(\boldsymbol{x}, \boldsymbol{y})\epsilon^l. \tag{6.21}$$

Substituting the power series representations (6.19), (6.20), (6.21) and the differential operator (6.18) into the non-dimensionalized Darcy equation (6.11), the Darcy-Brinkman equation (6.12) and the interface conditions (6.15), we have:

$$\begin{cases} \epsilon\boldsymbol{v}^\epsilon_v(\boldsymbol{x}, \boldsymbol{y}) + \epsilon\boldsymbol{K}_v(\boldsymbol{x}, \boldsymbol{y})\nabla_{\boldsymbol{x}} p^\epsilon_v(\boldsymbol{x}, \boldsymbol{y}) + \boldsymbol{K}_v(\boldsymbol{x}, \boldsymbol{y})\nabla_{\boldsymbol{y}} p^\epsilon_v(\boldsymbol{x}, \boldsymbol{y}) \\ \qquad\qquad - \epsilon\boldsymbol{K}_v(\boldsymbol{x}, \boldsymbol{y})\boldsymbol{f}^\epsilon_v(\boldsymbol{x}, \boldsymbol{y}) = \boldsymbol{0} & \text{in } \Omega_v, \\ \epsilon\nabla_{\boldsymbol{x}} \cdot \boldsymbol{v}^\epsilon_v(\boldsymbol{x}, \boldsymbol{y}) + \nabla_{\boldsymbol{y}} \cdot \boldsymbol{v}^\epsilon_v(\boldsymbol{x}, \boldsymbol{y}) = 0 & \text{in } \Omega_v, \end{cases} \tag{6.22}$$

$$\begin{cases} -\epsilon\nabla_{\boldsymbol{x}} p^\epsilon_m(\boldsymbol{x}, \boldsymbol{y}) - \nabla_{\boldsymbol{y}} p^\epsilon_m(\boldsymbol{x}, \boldsymbol{y}) - \epsilon\boldsymbol{K}^{-1}_m(\boldsymbol{x}, \boldsymbol{y})\boldsymbol{v}^\epsilon_m(\boldsymbol{x}, \boldsymbol{y}) \\ + \mu^*\epsilon^3\Delta_{\boldsymbol{x}}\boldsymbol{v}^\epsilon_m(\boldsymbol{x}, \boldsymbol{y}) + \mu^*\epsilon\Delta_{\boldsymbol{y}}\boldsymbol{v}^\epsilon_m(\boldsymbol{x}, \boldsymbol{y}) + \mu^*\epsilon^2\nabla_{\boldsymbol{x}} \cdot (\nabla_{\boldsymbol{y}}\boldsymbol{v}^\epsilon_m(\boldsymbol{x}, \boldsymbol{y})) & \text{in } \Omega_m \\ + \mu^*\epsilon^2\nabla_{\boldsymbol{y}} \cdot (\nabla_{\boldsymbol{x}}\boldsymbol{v}^\epsilon_m(\boldsymbol{x}, \boldsymbol{y})) + \epsilon\boldsymbol{f}^\epsilon_m(\boldsymbol{x}, \boldsymbol{y}) = \boldsymbol{0} \\ \epsilon\nabla_{\boldsymbol{x}} \cdot \boldsymbol{v}^\epsilon_m(\boldsymbol{x}, \boldsymbol{y}) + \nabla_{\boldsymbol{y}} \cdot \boldsymbol{v}^\epsilon_m(\boldsymbol{x}, \boldsymbol{y}) = 0 & \text{in } \Omega_m, \end{cases} \tag{6.23}$$

$$\begin{cases} \boldsymbol{v}^\epsilon_v(\boldsymbol{x}) \cdot \boldsymbol{n} = \boldsymbol{v}^\epsilon_m(\boldsymbol{x}) \cdot \boldsymbol{n} = \epsilon L_p(p^\epsilon_m(\boldsymbol{x}) - p^\epsilon_v(\boldsymbol{x}) - \bar{p}) & \text{on } \Gamma \\ \boldsymbol{v}^\epsilon_m(\boldsymbol{x}) \cdot \boldsymbol{t} = -\epsilon\dfrac{\sqrt{\mathcal{K}_m(\boldsymbol{x})}}{\alpha}\left[\left(\boldsymbol{n} \cdot \left(\nabla_{\boldsymbol{x}} + \dfrac{1}{\epsilon}\nabla_{\boldsymbol{y}}\right)\right)\boldsymbol{v}^\epsilon_m(\boldsymbol{x})\right] \cdot \boldsymbol{t} & \text{on } \Gamma. \end{cases} \tag{6.24}$$

If we collect the terms of order ϵ^0 in systems (6.22) and (6.23):

$$\nabla_{\boldsymbol{y}} p^{(0)}_v(\boldsymbol{x}, \boldsymbol{y}) = \boldsymbol{0} \quad \Rightarrow \quad p^{(0)}_v = p^{(0)}_v(\boldsymbol{x}), \tag{6.25}$$

$$\nabla_{\boldsymbol{y}} p^{(0)}_m(\boldsymbol{x}, \boldsymbol{y}) = \boldsymbol{0} \quad \Rightarrow \quad p^{(0)}_m = p^{(0)}_m(\boldsymbol{x}), \tag{6.26}$$

$$\nabla_{\boldsymbol{y}} \cdot \boldsymbol{v}^{(0)}_v(\boldsymbol{x}, \boldsymbol{y}) = 0, \tag{6.27}$$

$$\nabla_{\boldsymbol{y}} \cdot \boldsymbol{v}^{(0)}_m(\boldsymbol{x}, \boldsymbol{y}) = 0, \tag{6.28}$$

and for the interface conditions (6.24):

$$\boldsymbol{v}^{(0)}_m(\boldsymbol{x}, \boldsymbol{y}) \cdot \boldsymbol{n} = \boldsymbol{v}^{(0)}_v(\boldsymbol{x}, \boldsymbol{y}) \cdot \boldsymbol{n} = \boldsymbol{0} \text{ on } \Gamma, \tag{6.29}$$

$$\boldsymbol{v}^{(0)}_m(\boldsymbol{x}, \boldsymbol{y}) \cdot \boldsymbol{t} = -\frac{\sqrt{\mathcal{K}_m(\boldsymbol{x}, \boldsymbol{y})}}{\alpha}\left[\left(\boldsymbol{n} \cdot \nabla_{\boldsymbol{y}}\right)\boldsymbol{v}^{(0)}_m(\boldsymbol{x}, \boldsymbol{y})\right] \cdot \boldsymbol{t} \text{ on } \Gamma. \tag{6.30}$$

Collecting the terms of order ϵ^1 in systems (6.22), (6.23) and in the interface conditions (6.24), we obtain:

$$\begin{aligned}\boldsymbol{v}_v^{(0)}(\boldsymbol{x},\boldsymbol{y}) + \boldsymbol{K}_v(\boldsymbol{x},\boldsymbol{y})\nabla_{\boldsymbol{x}} p_v^{(0)}(\boldsymbol{x}) + \boldsymbol{K}_v(\boldsymbol{x},\boldsymbol{y})\nabla_{\boldsymbol{y}} p_v^{(1)}(\boldsymbol{x},\boldsymbol{y}) \\ - \boldsymbol{K}_v(\boldsymbol{x},\boldsymbol{y})\boldsymbol{f}_v^{(0)}(\boldsymbol{x},\boldsymbol{y}) = \boldsymbol{0} \quad \text{on } \Omega_v,\end{aligned} \tag{6.31}$$

$$\nabla_{\boldsymbol{x}} \cdot \boldsymbol{v}_v^{(0)}(\boldsymbol{x},\boldsymbol{y}) + \nabla_{\boldsymbol{y}} \cdot \boldsymbol{v}_v^{(1)}(\boldsymbol{x},\boldsymbol{y}) = 0 \quad \text{on } \Omega_v, \tag{6.32}$$

$$\begin{aligned}-\nabla_{\boldsymbol{x}} p_m^{(0)}(\boldsymbol{x}) - \nabla_{\boldsymbol{y}} p_m^{(1)}(\boldsymbol{x},\boldsymbol{y}) - \boldsymbol{K}_m^{-1}(\boldsymbol{x},\boldsymbol{y})\boldsymbol{v}_m^{(0)}(\boldsymbol{x},\boldsymbol{y}) + \mu^* \Delta_{\boldsymbol{y}} \boldsymbol{v}_m^{(0)}(\boldsymbol{x},\boldsymbol{y}) \\ + \boldsymbol{f}_m^{(0)}(\boldsymbol{x},\boldsymbol{y}) = \boldsymbol{0} \quad \text{on } \Omega_m,\end{aligned} \tag{6.33}$$

$$\nabla_{\boldsymbol{x}} \cdot \boldsymbol{v}_m^{(0)}(\boldsymbol{x},\boldsymbol{y}) + \nabla_{\boldsymbol{y}} \cdot \boldsymbol{v}_m^{(1)}(\boldsymbol{x},\boldsymbol{y}) = 0 \quad \text{on } \Omega_m, \tag{6.34}$$

$$\boldsymbol{v}_m^{(1)}(\boldsymbol{x},\boldsymbol{y}) \cdot \boldsymbol{n} = \boldsymbol{v}_v^{(1)}(\boldsymbol{x},\boldsymbol{y}) \cdot \boldsymbol{n} = L_p \left(p_m^{(0)}(\boldsymbol{x}) - p_v^{(0)}(\boldsymbol{x}) - \bar{p}\right) \quad \text{on } \Gamma, \tag{6.35}$$

$$\boldsymbol{v}_m^{(1)}(\boldsymbol{x},\boldsymbol{y}) \cdot \boldsymbol{t} = -\frac{\sqrt{\mathcal{K}_m(\boldsymbol{x},\boldsymbol{y})}}{\alpha} \left[\left(\boldsymbol{n} \cdot \nabla_{\boldsymbol{x}}\right) \boldsymbol{v}_m^{(0)}(\boldsymbol{x},\boldsymbol{y}) + \left(\boldsymbol{n} \cdot \nabla_{\boldsymbol{y}}\right) \boldsymbol{v}_m^{(1)}(\boldsymbol{x},\boldsymbol{y})\right] \quad \text{on } \Gamma. \tag{6.36}$$

Applying the $\nabla_{\boldsymbol{y}}\cdot$ operator to the equation (6.31) and using the equation (6.27), we obtain

$$\begin{aligned}\nabla_{\boldsymbol{y}} \cdot \left[\boldsymbol{K}_v(\boldsymbol{x},\boldsymbol{y})\nabla_{\boldsymbol{x}} p_v^{(0)}(\boldsymbol{x}) + \boldsymbol{K}_v(\boldsymbol{x},\boldsymbol{y})\nabla_{\boldsymbol{y}} p_v^{(1)}(\boldsymbol{x},\boldsymbol{y}) - \boldsymbol{K}_v(\boldsymbol{x},\boldsymbol{y})\boldsymbol{f}_v^{(0)}(\boldsymbol{x},\boldsymbol{y})\right] \\ = 0 \quad \text{in } \Omega_v,\end{aligned} \tag{6.37}$$

and the boundary condition (6.29) becomes:

$$\begin{aligned}\left[\boldsymbol{K}_v(\boldsymbol{x},\boldsymbol{y})\nabla_{\boldsymbol{x}} p_v^{(0)}(\boldsymbol{x}) + \boldsymbol{K}_v(\boldsymbol{x},\boldsymbol{y})\nabla_{\boldsymbol{y}} p_v^{(1)}(\boldsymbol{x},\boldsymbol{y}) - \boldsymbol{K}_v(\boldsymbol{x},\boldsymbol{y})\boldsymbol{f}_v^{(0)}(\boldsymbol{x},\boldsymbol{y})\right] \cdot \boldsymbol{n} \\ = 0 \quad \text{on } \Gamma.\end{aligned} \tag{6.38}$$

Since the problem is linear and the vector function $\nabla_{\boldsymbol{x}} p^{(0)}$ is $\boldsymbol{y}$-constant, we state the following ansatz of the solution:

$$p_v^{(1)}(\boldsymbol{x},\boldsymbol{y}) = \boldsymbol{g}_v(\boldsymbol{x},\boldsymbol{y}) \cdot \nabla_{\boldsymbol{x}} p_v^{(0)}(\boldsymbol{x}) + \tilde{g}_v(\boldsymbol{x},\boldsymbol{y}). \tag{6.39}$$

Equation (6.39) is a solution of the problem (6.37) and (6.38) (up to a $\boldsymbol{y}$-constant function), provided that the auxiliary vectors $\boldsymbol{g}_v$ and $\tilde{g}_v$ solve the following cell problems:

$$\begin{cases}\nabla_{\boldsymbol{y}} \cdot \left[\nabla_{\boldsymbol{y}} \boldsymbol{g}_v(\boldsymbol{x},\boldsymbol{y}) \boldsymbol{K}_v(\boldsymbol{x},\boldsymbol{y})^T\right] = -\nabla_{\boldsymbol{y}} \cdot \boldsymbol{K}_v(\boldsymbol{x},\boldsymbol{y})^T, & \text{in } \Omega_v \\ \left[\nabla_{\boldsymbol{y}} \boldsymbol{g}_v(\boldsymbol{x},\boldsymbol{y}) \boldsymbol{K}_v(\boldsymbol{x},\boldsymbol{y})^T\right] \cdot \boldsymbol{n} = -\boldsymbol{K}_v(\boldsymbol{x},\boldsymbol{y})^T \cdot \boldsymbol{n} & \text{on } \Gamma,\end{cases} \tag{6.40}$$

and:

$$\begin{cases}\nabla_{\boldsymbol{y}} \cdot \left[\boldsymbol{K}_v(\boldsymbol{x},\boldsymbol{y}) \nabla_{\boldsymbol{y}} \tilde{g}_v(\boldsymbol{x},\boldsymbol{y})\right] = \nabla_{\boldsymbol{y}} \cdot \boldsymbol{K}_v(\boldsymbol{x},\boldsymbol{y}) \boldsymbol{f}_v^0(\boldsymbol{x},\boldsymbol{y}), & \text{in } \Omega_v \\ \left[\boldsymbol{K}_v(\boldsymbol{x},\boldsymbol{y}) \nabla_{\boldsymbol{y}} \tilde{g}_v(\boldsymbol{x},\boldsymbol{y})\right] \cdot \boldsymbol{n} = \boldsymbol{K}_v(\boldsymbol{x},\boldsymbol{y}) \boldsymbol{f}_v^0(\boldsymbol{x},\boldsymbol{y}) \cdot \boldsymbol{n} & \text{on } \Gamma.\end{cases} \tag{6.41}$$

Moreover, we need to have $\langle \boldsymbol{g}_v(\boldsymbol{x}, \boldsymbol{y}) \rangle_{\Omega_v} = 0$ and $\langle \tilde{g}_v(\boldsymbol{x}, \boldsymbol{y}) \rangle_{\Omega_m} = 0$ to ensure the uniqueness of the solution, where $\langle \cdot \rangle_{\Omega_\gamma}$ is defined as

$$\langle h \rangle_{\Omega_\gamma} = \frac{1}{|\Omega_\gamma|} \int_{\Omega_\gamma} h d\boldsymbol{y}. \tag{6.42}$$

Putting together equations (6.28), (6.29), (6.30) and (6.33), we obtain an auxiliary Darcy-Brinkman system in $(\boldsymbol{v}_m^{(0)}, p_m^{(1)})$:

$$\begin{cases} -\nabla_{\boldsymbol{x}} p_m^{(0)}(\boldsymbol{x}) - \nabla_{\boldsymbol{y}} p_m^{(1)}(\boldsymbol{x}, \boldsymbol{y}) - \boldsymbol{K}_m^{-1}(\boldsymbol{x}, \boldsymbol{y}) \boldsymbol{v}_m^{(0)}(\boldsymbol{x}, \boldsymbol{y}) + \mu^* \Delta_{\boldsymbol{y}} \boldsymbol{v}_m^{(0)}(\boldsymbol{x}, \boldsymbol{y}) \\ \qquad\qquad\qquad\qquad + \boldsymbol{f}_m^{(0)}(\boldsymbol{x}, \boldsymbol{y}) = \boldsymbol{0} & \text{on } \Omega_m, \\ \nabla_{\boldsymbol{y}} \cdot \boldsymbol{v}_m^{(0)}(\boldsymbol{x}, \boldsymbol{y}) = 0 & \text{on } \Omega_m, \\ \boldsymbol{v}_m^{(0)}(\boldsymbol{x}, \boldsymbol{y}) \cdot \boldsymbol{n} = \boldsymbol{0} & \text{on } \Gamma, \\ \boldsymbol{v}_m^{(0)}(\boldsymbol{x}, \boldsymbol{y}) \cdot \boldsymbol{t} = -\frac{\sqrt{\boldsymbol{\mathcal{K}}_m(\boldsymbol{x}, \boldsymbol{y})}}{\alpha} \left[(\boldsymbol{n} \cdot \nabla_{\boldsymbol{y}}) \, \boldsymbol{v}_m^{(0)}(\boldsymbol{x}, \boldsymbol{y}) \right] \cdot \boldsymbol{t} & \text{on } \Gamma. \end{cases} \tag{6.43}$$

Since the problem is linear and the vector function $\nabla_{\boldsymbol{x}} p^{(0)}$ is $\boldsymbol{y}$-constant, we formulate the following ansatz for the solution:

$$p_m^{(1)}(\boldsymbol{x}, \boldsymbol{y}) = -\boldsymbol{g}_m(\boldsymbol{x}, \boldsymbol{y}) \cdot \nabla_{\boldsymbol{x}} p_m^{(0)}(\boldsymbol{x}) + \tilde{g}_m(\boldsymbol{x}, \boldsymbol{y}), \tag{6.44}$$

$$\boldsymbol{v}_m^{(0)}(\boldsymbol{x}, \boldsymbol{y}) = -\boldsymbol{W}_m(\boldsymbol{x}, \boldsymbol{y}) \nabla_{\boldsymbol{x}} p_m^{(0)}(\boldsymbol{x}) + \tilde{\boldsymbol{w}}_m(\boldsymbol{x}, \boldsymbol{y}). \tag{6.45}$$

We have that (6.44) and (6.45) are solutions of the problem (6.43) provided that the auxiliary vectors $\boldsymbol{g}_m, \tilde{g}_m, \boldsymbol{W}_m, \tilde{\boldsymbol{w}}_m$ solve the following cell problems:

$$\begin{cases} \boldsymbol{K}_m^{-1}(\boldsymbol{x}, \boldsymbol{y}) \boldsymbol{W}_m(\boldsymbol{x}, \boldsymbol{y}) - \mu^* \Delta_{\boldsymbol{y}} \boldsymbol{W}_m(\boldsymbol{x}, \boldsymbol{y}) - \boldsymbol{I} + (\nabla_{\boldsymbol{y}} \boldsymbol{g}_m(\boldsymbol{x}, \boldsymbol{y}))^T = \boldsymbol{0} & \text{in } \Omega_m, \\ \nabla_{\boldsymbol{y}} \cdot \boldsymbol{W}_m(\boldsymbol{x}, \boldsymbol{y}) = 0 & \text{in } \Omega_m, \\ \boldsymbol{W}_m(\boldsymbol{x}, \boldsymbol{y}) \cdot \boldsymbol{n} = 0 & \text{on } \Gamma, \\ \boldsymbol{W}_m(\boldsymbol{x}, \boldsymbol{y}) \boldsymbol{t} = -\frac{\sqrt{\boldsymbol{\mathcal{K}}_m(\boldsymbol{x}, \boldsymbol{y})}}{\alpha} \left[(\nabla_{\boldsymbol{y}} \boldsymbol{W}_m(\boldsymbol{x}, \boldsymbol{y})) \, \boldsymbol{n} \right] \boldsymbol{t} & \text{on } \Gamma, \end{cases} \tag{6.46}$$

$$\begin{cases} -\boldsymbol{K}_m^{-1}(\boldsymbol{x}, \boldsymbol{y}) \tilde{\boldsymbol{w}}_m(\boldsymbol{x}, \boldsymbol{y}) + \mu^* \Delta_{\boldsymbol{y}} \tilde{\boldsymbol{w}}_m(\boldsymbol{x}, \boldsymbol{y}) - \nabla_{\boldsymbol{y}} \tilde{g}_m(\boldsymbol{x}, \boldsymbol{y}) + \boldsymbol{f}_m^0(\boldsymbol{x}, \boldsymbol{y}) = \boldsymbol{0} & \text{in } \Omega_m, \\ \nabla_{\boldsymbol{y}} \cdot \tilde{\boldsymbol{w}}_m(\boldsymbol{x}, \boldsymbol{y}) = 0 & \text{in } \Omega_m, \\ \tilde{\boldsymbol{w}}_m(\boldsymbol{x}, \boldsymbol{y}) \cdot \boldsymbol{n} = 0 & \text{on } \Gamma, \\ \tilde{\boldsymbol{w}}_m(\boldsymbol{x}, \boldsymbol{y}) \cdot \boldsymbol{t} = -\frac{\sqrt{\boldsymbol{\mathcal{K}}_m(\boldsymbol{x}, \boldsymbol{y})}}{\alpha} \left[(\nabla_{\boldsymbol{y}} \tilde{\boldsymbol{w}}_m(\boldsymbol{x}, \boldsymbol{y})) \, \boldsymbol{n} \right] \boldsymbol{t} & \text{on } \Gamma. \end{cases} \tag{6.47}$$

Moreover, we impose that $\langle \boldsymbol{g}_m(\boldsymbol{x}, \boldsymbol{y}) \rangle_{\Omega_m} = 0$ and $\langle \tilde{g}_m(\boldsymbol{x}, \boldsymbol{y}) \rangle_{\Omega_m} = 0$ to ensure the uniqueness of the solution.

6.3 Macroscopic Model

Applying the operator $\langle \cdot \rangle_{\Omega_m}$ to the ansatz (6.45), we obtain:

$$\langle \boldsymbol{v}_m^{(0)}(\boldsymbol{x}, \boldsymbol{y}) \rangle_{\Omega_m} = -\langle \boldsymbol{W}_m(\boldsymbol{x}, \boldsymbol{y}) \rangle_{\Omega_m} \nabla_{\boldsymbol{x}} p_m^{(0)}(\boldsymbol{x}) + \langle \tilde{\boldsymbol{w}}_m(\boldsymbol{x}, \boldsymbol{y}) \rangle_{\Omega_m}, \tag{6.48}$$

where $\boldsymbol{W}_m$ and $\tilde{\boldsymbol{w}}_m$ solve (6.46) and (6.47), respectively.

We recall the equation of order ϵ^1 for the divergence (6.34):

$$\nabla_{\boldsymbol{x}} \cdot \boldsymbol{v}_m^{(0)}(\boldsymbol{x}, \boldsymbol{y}) + \nabla_{\boldsymbol{y}} \cdot \boldsymbol{v}_m^{(1)}(\boldsymbol{x}, \boldsymbol{y}) = 0. \tag{6.49}$$

Applying the average operator, we obtain (using the macroscopic uniformity assumption (6.17)):

$$\nabla_{\boldsymbol{x}} \cdot \langle \boldsymbol{v}_m^{(0)}(\boldsymbol{x}, \boldsymbol{y}) \rangle_{\Omega_m} + \langle \nabla_{\boldsymbol{y}} \cdot \boldsymbol{v}_m^{(1)}(\boldsymbol{x}, \boldsymbol{y}) \rangle_{\Omega_m} = 0. \tag{6.50}$$

Moreover, using the divergence theorem and the interface conditions (6.35):

$$\begin{aligned}
\langle \nabla_{\boldsymbol{y}} \cdot \boldsymbol{v}_m^{(1)} \rangle_{\Omega_m} &= \frac{1}{|\Omega_m|} \int_{\Omega_m} \nabla_{\boldsymbol{y}} \cdot \boldsymbol{v}_m^{(1)}(\boldsymbol{x}, \boldsymbol{y}) d\boldsymbol{y} \\
&= \frac{1}{|\Omega_m|} \int_{\Gamma} \boldsymbol{v}_m^{(1)}(\boldsymbol{x}, \boldsymbol{y}) \cdot \boldsymbol{n} dS \\
&= \frac{L_p S}{|\Omega_m|} \left[p_m^{(0)}(\boldsymbol{x}) - p_v^{(0)}(\boldsymbol{x}) - \bar{p} \right],
\end{aligned} \tag{6.51}$$

where $|\Omega_m|$ is the volume of the cell phase m and S is the surface area of fluid exchange between the two phases; hence we have

$$\nabla_{\boldsymbol{x}} \cdot \langle \boldsymbol{v}_m^{(0)}(\boldsymbol{x}, \boldsymbol{y}) \rangle_{\Omega_m} = -\frac{L_p S}{|\Omega_m|} \left[p_m^{(0)}(\boldsymbol{x}) - p_v^{(0)}(\boldsymbol{x}) - \bar{p} \right]. \tag{6.52}$$

For the Darcy problem, we apply the average operator to the equation (6.31) and, substituting the ansatz (6.39), we obtain:

$$\begin{aligned}
\langle \boldsymbol{v}_v^{(0)}(\boldsymbol{x}, \boldsymbol{y}) \rangle_{\Omega_v} =& - \langle \boldsymbol{K}_v(\boldsymbol{x}, \boldsymbol{y}) \nabla_{\boldsymbol{x}} p_v^{(0)}(\boldsymbol{x}) \rangle_{\Omega_v} - \langle \boldsymbol{K}_v(\boldsymbol{x}, \boldsymbol{y}) \nabla_{\boldsymbol{y}} \boldsymbol{g}_v(\boldsymbol{x}, \boldsymbol{y}) \cdot \nabla_{\boldsymbol{x}} p_v^{(0)}(\boldsymbol{x}) \rangle_{\Omega_v} \\
&- \langle \boldsymbol{K}_v(\boldsymbol{x}, \boldsymbol{y}) \nabla_{\boldsymbol{y}} \tilde{g}_v(\boldsymbol{x}, \boldsymbol{y}) \rangle_{\Omega_v} + \langle \boldsymbol{K}_v(\boldsymbol{x}, \boldsymbol{y}) \boldsymbol{f}_v^{(0)}(\boldsymbol{x}, \boldsymbol{y}) \rangle_{\Omega_v} \\
=& - \langle \boldsymbol{K}_v(\boldsymbol{x}, \boldsymbol{y}) + \boldsymbol{K}_v(\boldsymbol{x}, \boldsymbol{y}) (\nabla_{\boldsymbol{y}} \boldsymbol{g}_v(\boldsymbol{x}, \boldsymbol{y}))^T \rangle_{\Omega_v} \nabla_{\boldsymbol{x}} p_v^{(0)}(\boldsymbol{x}) \\
&- \langle \boldsymbol{K}_v(\boldsymbol{x}, \boldsymbol{y}) \nabla_{\boldsymbol{y}} \tilde{g}_v(\boldsymbol{x}, \boldsymbol{y}) \rangle_{\Omega_v} + \langle \boldsymbol{K}_v(\boldsymbol{x}, \boldsymbol{y}) \boldsymbol{f}_v^{(0)}(\boldsymbol{x}, \boldsymbol{y}) \rangle_{\Omega_v}.
\end{aligned} \tag{6.53}$$

Using the same technique, applying the average operator and the divergence theorem to equation (6.32), it follows that

$$\nabla_{\boldsymbol{x}} \cdot \langle \boldsymbol{v}_v^{(0)}(\boldsymbol{x}, \boldsymbol{y}) \rangle_{\Omega_v} = \frac{L_p S}{|\Omega_v|} \left[p_m^{(0)}(\boldsymbol{x}) - p_v^{(0)}(\boldsymbol{x}) - \bar{p} \right], \tag{6.54}$$

where we considered that $\boldsymbol{n}_v = -\boldsymbol{n}$.

We can write the total macroscale velocity as:

$$\begin{aligned}
\langle \boldsymbol{v}_v^{(0)}(\boldsymbol{x}, \boldsymbol{y}) \rangle_{\Omega_v} + \langle \boldsymbol{v}_m^{(0)}(\boldsymbol{x}, \boldsymbol{y}) \rangle_{\Omega_m} =& -\langle \boldsymbol{W}_m(\boldsymbol{x}, \boldsymbol{y}) \rangle_{\Omega_m} \nabla_{\boldsymbol{x}} p_m^{(0)}(\boldsymbol{x}) + \langle \tilde{\boldsymbol{w}}_m(\boldsymbol{x}, \boldsymbol{y}) \rangle_{\Omega_m} \\
&-\langle \boldsymbol{K}_v(\boldsymbol{x}, \boldsymbol{y}) + \boldsymbol{K}_v(\boldsymbol{x}, \boldsymbol{y}) (\nabla_{\boldsymbol{y}} \boldsymbol{g}_v(\boldsymbol{x}, \boldsymbol{y}))^T \rangle_{\Omega_v} \nabla_{\boldsymbol{x}} p_v^{(0)}(\boldsymbol{x}) \\
&-\langle \boldsymbol{K}_v(\boldsymbol{x}, \boldsymbol{y}) \nabla_{\boldsymbol{y}} \tilde{g}_v(\boldsymbol{x}, \boldsymbol{y}) \rangle_{\Omega_v} + \langle \boldsymbol{K}_v(\boldsymbol{x}, \boldsymbol{y}) \boldsymbol{f}_v^{(0)}(\boldsymbol{x}, \boldsymbol{y}) \rangle_{\Omega_v}.
\end{aligned} \tag{6.55}$$

Remark 3. *We notice that the fluid is macroscopically incompressible, indeed the sum of the two divergences is zero. The two phases can have non zero divergence due to the fluid exchange between them.*

Remark 4. *The* local periodicity *allows us to define the average operator on a single cell, which is computationally feasible; however we can replace this assumption with the* local boundedness*: denoting with B_R the ball centered in the origin with radius R, we can define a new average operator*

$$\langle f \rangle_{\Omega_\gamma} = \lim_{R\to\infty} \frac{1}{\frac{4}{3}\pi R^3} \int_{\Omega_\gamma \cap B_R} f d\boldsymbol{y} \tag{6.56}$$

for $\gamma = m, v$, where Ω_γ is the whole phase domain. For the details, we refer to [89].

Remark 5. *We can also remove the hypothesis of* macroscopic uniformity*, using an appropriate variant of the Reynolds Theorem [126]:*

$$\nabla_{\boldsymbol{x}} \cdot \langle \boldsymbol{v}^0_\gamma \rangle_{\Omega_\alpha} = \langle \nabla_{\boldsymbol{x}} \cdot \boldsymbol{v}^0_\gamma \rangle_{\Omega_\gamma} + \frac{1}{|\Omega_\gamma|} \int_\Gamma \boldsymbol{v}^0_\gamma \cdot (\nabla_{\boldsymbol{x}} \boldsymbol{r}(\boldsymbol{x}, \boldsymbol{y}))^T \boldsymbol{n} dS_y, \tag{6.57}$$

where $\boldsymbol{r}$ denotes the interface position vector.

Substituting (6.48) into equation (6.52) and (6.53) into equation (6.54), respectively, we obtain

$$\nabla_{\boldsymbol{x}} \cdot \Big(\langle \boldsymbol{W}_m(\boldsymbol{x}, \boldsymbol{y}) \rangle_{\Omega_m} \nabla_{\boldsymbol{x}} p_m^{(0)}(\boldsymbol{x}) \Big) = \nabla_{\boldsymbol{x}} \cdot \langle \tilde{\boldsymbol{w}}_m(\boldsymbol{x}, \boldsymbol{y}) \rangle_{\Omega_m} + \frac{L_p S}{|\Omega_m|} \Big[p_m^{(0)}(\boldsymbol{x}) - p_v^{(0)}(\boldsymbol{x}) - \bar{p} \Big], \tag{6.58}$$

$$\begin{aligned} \nabla_{\boldsymbol{x}} \cdot \Big(\langle \boldsymbol{K}_v(\boldsymbol{x}, \boldsymbol{y}) + \boldsymbol{K}_v(\boldsymbol{x}, \boldsymbol{y}) (\nabla_{\boldsymbol{y}} \boldsymbol{g}_v(\boldsymbol{x}, \boldsymbol{y}))^T \rangle_{\Omega_v} \nabla_{\boldsymbol{x}} p_v^{(0)} \Big) = &- \nabla_{\boldsymbol{x}} \cdot \langle \boldsymbol{K}_v(\boldsymbol{x}, \boldsymbol{y}) \nabla_{\boldsymbol{y}} \tilde{g}_v(\boldsymbol{x}, \boldsymbol{y}) \rangle_{\Omega_v} \\ &+ \nabla_{\boldsymbol{x}} \cdot \langle \boldsymbol{K}_v(\boldsymbol{x}, \boldsymbol{y}) \boldsymbol{f}_v^{(0)}(\boldsymbol{x}, \boldsymbol{y}) \rangle_{\Omega_v} \\ &- \frac{L_p S}{|\Omega_m|} \Big[p_m^{(0)}(\boldsymbol{x}) - p_v^{(0)}(\boldsymbol{x}) - \bar{p} \Big]. \end{aligned} \tag{6.59}$$

The equations (6.58) and (6.59) are the classical Darcy's law diffusion problem with additional terms related to the multiscale forces [119] and the fluid exchange between phases. We note that if the multiscale forces $\boldsymbol{f}_m$ and $\boldsymbol{f}_v$ are zero, the unique solutions $\tilde{g}_v(\boldsymbol{x}, \boldsymbol{y})$ and $\tilde{\boldsymbol{w}}_m(\boldsymbol{x}, \boldsymbol{y})$ of the systems (6.41) and (6.47) are $\boldsymbol{y}$-constant and zero, respectively. In this latter case, equations (6.58) and (6.59) reduce to the double Darcy's model with fluid exchange between phases as derived in [127] and subsequently solved and generalised in [128] and [126], respectively. However, even when ignoring the contributions related to the external volume loads, the final model that we have obtained differs from the one obtained in [127] due to the Darcy-Brinmann type cell problem which is to be solved to compute the hydraulic conductivity $\langle \mathsf{W} \rangle_{\Omega_m}$ for the matrix compartment Ω_m.

6.4 A comparison of the flow equations

In this section, we want to study the differences in using Darcy, Stokes, or Darcy-Brinkman in the domain Ω_v in the cell problem. We can see the cell problem domain in Figure 6.1.

Figure 6.1: The cell problem domains Ω_v (left) and Ω_m (right).

For simplicity we focus on the case $\boldsymbol{f}_v = \boldsymbol{0}$, replacing the interface boundary conditions with the no-slip condition $\boldsymbol{v}_v = \boldsymbol{0}$ and assuming the isotropy of the porous medium, that is $\boldsymbol{K}_v = K_v \boldsymbol{I}$. Hence the Darcy cell problems (6.40) and (6.41) reduce to

$$\begin{cases} \nabla_{\boldsymbol{y}} \cdot [\nabla_{\boldsymbol{y}} \boldsymbol{g}_v(\boldsymbol{x},\boldsymbol{y})] = 0, & \text{in } \Omega_v \\ \nabla_{\boldsymbol{y}} \boldsymbol{g}_v(\boldsymbol{x},\boldsymbol{y}) \cdot \boldsymbol{n} = -\boldsymbol{n} & \text{on } \Gamma, \end{cases} \tag{6.60}$$

while the Darcy-Brinkman cell problems (6.46) and (6.47) reduce to

$$\begin{cases} K^{*-1} \boldsymbol{W}_v(\boldsymbol{x},\boldsymbol{y}) - \mu^* \Delta_{\boldsymbol{y}} \boldsymbol{W}_v(\boldsymbol{x},\boldsymbol{y}) - \boldsymbol{I} + (\nabla_{\boldsymbol{y}} \boldsymbol{g}_v(\boldsymbol{x},\boldsymbol{y}))^T = \boldsymbol{0} & \text{in } \Omega_v, \\ \nabla_{\boldsymbol{y}} \cdot \boldsymbol{W}_v(\boldsymbol{x},\boldsymbol{y}) = 0 & \text{in } \Omega_v, \\ \boldsymbol{W}_v(\boldsymbol{x},\boldsymbol{y}) = \boldsymbol{0} & \text{on } \Gamma, \end{cases} \tag{6.61}$$

where $K^* = \dfrac{K_v \mu}{d^2}$. Finally, the cell problem for the Stokes equation is [32, 70]

$$\begin{cases} -\Delta_{\boldsymbol{y}} \boldsymbol{W}_v(\boldsymbol{x},\boldsymbol{y}) - \boldsymbol{I} + (\nabla_{\boldsymbol{y}} \boldsymbol{g}_v(\boldsymbol{x},\boldsymbol{y}))^T = \boldsymbol{0} & \text{in } \Omega_v, \\ \nabla_{\boldsymbol{y}} \cdot \boldsymbol{W}_v(\boldsymbol{x},\boldsymbol{y}) = 0 & \text{in } \Omega_v, \\ \boldsymbol{W}_v(\boldsymbol{x},\boldsymbol{y}) = \boldsymbol{0} & \text{on } \Gamma. \end{cases} \tag{6.62}$$

We want to solve and compare the problems above in the cell domain Ω_v; therefore we need to compare the same quantity at the macroscale. For Darcy-Brinkman and Stokes, the dimensionalized macroscopic velocity is given by (6.48):

$$\langle \boldsymbol{v}_v \rangle_{\Omega_v} = -\frac{d^2}{\mu} \langle \boldsymbol{W}_v \rangle_{\Omega_v} \nabla_{\boldsymbol{x}} p^0, \tag{6.63}$$

where $\boldsymbol{W}_v$ takes different expressions in Darcy-Brinkman's and Stokes' cases. On the other hand, for the Darcy case we have, by equation (6.53):

$$\langle \boldsymbol{v}_v \rangle_{\Omega_v} = -K^* \frac{d^2}{\mu} \langle \boldsymbol{I} + (\nabla_{\boldsymbol{y}} \boldsymbol{g}_v)^T \rangle_{\Omega_v} \nabla_{\boldsymbol{x}} p^0. \tag{6.64}$$

Hence we compare $\langle \boldsymbol{W} \rangle_{\Omega_v}$ for the Darcy-Brinkman and the Stokes problem and $K^* \langle \boldsymbol{I} + (\nabla_{\boldsymbol{y}} \boldsymbol{g}_v)^T \rangle_{\Omega_v}$ for the Darcy problem.

If we consider cylinders with a small radius, so that they have a small overlap region, we can analytically solve the previous systems up to a small error. The differential problems (6.61) and (6.62) are three standard Darcy-Brinkman and Stokes' problems in $\boldsymbol{W}_{1,v} = \boldsymbol{W}_v \boldsymbol{e}_1$, $\boldsymbol{W}_{2,v} = \boldsymbol{W}_v \boldsymbol{e}_2$ and $\boldsymbol{W}_{3,v} = \boldsymbol{W}_v \boldsymbol{e}_3$ connected to the rows of $\boldsymbol{I}$; hence, using the rotation invariance property of our geometry, we can fix one arbitrary row (*i.e.* direction) of $\boldsymbol{I}$, say, for example, $\boldsymbol{e}_3$ (the third row of $\boldsymbol{I}$). In this case, the solution is non-zero only in the branch directed along $\boldsymbol{e}_3$, which means the only non-zero component is $\boldsymbol{W}_{3,v}\boldsymbol{e}_3 = W_{33,v}$.

Hence the solution of the system (6.62) is (see [128]):

$$W_{33,v} = \frac{R^2 - r^2}{4}, \quad W_{31,v} = W_{32,v} = 0, \quad 0 \leq r \leq R, \tag{6.65}$$

where R is the radius of the cylinder. Hence we have that the resulting permeability is:

$$\langle W_{33,v} \rangle_{\Omega_v} = \frac{1}{|\Omega_v|} \int_0^{l_c} dz \int_0^{2\pi} d\theta \int_0^R \frac{R^2 - r^2}{4} r dr = \frac{\pi l_c R^4}{8|\Omega_v|}. \tag{6.66}$$

For the system (6.61) the problem reduces to

$$W''_{33,v}(r) + \frac{1}{r} W'_{33,v}(r) - \frac{W_{33,v}(r)}{\mu^* K^*} = -\frac{1}{\mu^*}, \quad 0 \leq r \leq R \tag{6.67}$$

and the solution is

$$W_{33,v}(r) = K^* \left[1 - \frac{J_0\left(i\sqrt{\dfrac{1}{\mu^* K^*}} r \right)}{J_0\left(i\sqrt{\dfrac{1}{\mu^* K^*}} R \right)} \right], \quad W_{31,v} = W_{32,v} = 0, \tag{6.68}$$

where J_0 is the Bessel function of the first kind of order zero. Hence we have (using the property $x^\nu J_{\nu-1} = \frac{d}{dx}\left(x^\nu J_\nu(x) \right)$):

$$\begin{aligned} \langle W_{33,v} \rangle_{\Omega_v} &= \frac{1}{|\Omega_v|} \int_0^{l_c} dz \int_0^{2\pi} d\theta \int_0^R K^* \left[1 - \frac{J_0\left(i\sqrt{\dfrac{1}{\mu^* K^*}} r \right)}{J_0\left(i\sqrt{\dfrac{1}{\mu^* K^*}} R \right)} \right] r dr \\ &= \frac{2\pi l_c}{|\Omega_v|} K^* \left[\frac{R^2}{2} + i\sqrt{\mu^* K^*} R \frac{J_1\left(i\sqrt{\dfrac{1}{\mu^* K^*}} R \right)}{J_0\left(i\sqrt{\dfrac{1}{\mu^* K^*}} R \right)} \right]. \end{aligned} \tag{6.69}$$

To solve system (6.60), we recall that $\boldsymbol{n} = (n_1, n_2, 0) = (\cos\theta, \sin\theta, 0)$. First of all, we focus on the case $n_1 = \cos\theta$, and we call the solution $g_{v,1}$. From the periodicity condition in the $\boldsymbol{e}_3$ direction, we have that $\boldsymbol{g}_v$ does not depend on the z variable. Hence the problem reduces to

$$\frac{1}{r}\frac{\partial}{\partial r}\left(r \frac{\partial g_{v,1}}{\partial r} \right) + \frac{1}{r^2}\frac{\partial^2 g_{v,1}}{\partial \theta^2} = 0, \quad 0 \leq r \leq R, \quad 0 \leq \theta \leq 2\pi. \tag{6.70}$$

Using the separation of variables $g_{v,1} = R(r)\Theta(\theta)$ and substituting into the equation above, we obtain

$$\begin{cases} r^2 R''(r) + rR'(r) - cR(r) = 0, \\ \Theta''(\theta) + c\Theta(\theta) = 0, \end{cases} \tag{6.71}$$

where c is the constant obtained by the separation of variables. From the second equation of the system (6.71), we have

$$\Theta(\theta) = A\sin(n\theta) + B\cos(n\theta), \quad n \in \mathbb{N}. \tag{6.72}$$

From the boundary condition of the system (6.60), it follows that $n = 1$. Hence the solution of the first equation of the system (6.71) is

$$R(r) = \frac{C_1}{r} + C_2 r, \tag{6.73}$$

and, from the boundary condition of (6.60) and the non-degeneracy condition in $r = 0$, we have $C_1 = 0$ and $C_2 = 1$. Hence we have

$$g_{v,1} = -r\cos\theta. \tag{6.74}$$

In the same way, for the case $n_2 = \sin\theta$ we get:

$$g_{v,2} = -r\sin\theta. \tag{6.75}$$

Hence it follows:

$$\langle(\nabla_{\boldsymbol{y}} \boldsymbol{g}_v)^T\rangle_{\Omega_v} = \frac{1}{|\Omega_v|}\int_{\Omega_v} (\nabla_{\boldsymbol{y}} \boldsymbol{g}_v)^T \, dV = -\frac{2}{3}. \tag{6.76}$$

These results are shown in Figure 6.2, where we set $r_c = 7.7 \times 10^{-3}$, $|\Omega_v| = 3\pi R^2 l_c$ (the volume is indeed a bit smaller, but we are supposing that the intersection between the cylinders is negligible).

As expected, the Darcy-Brinkman equation has a Stokes/Darcy duality behavior. Indeed, suppose we decrease the relevance of the Laplace operator in the Darcy-Brinkman cell problem (6.61). In that case, we have that the solution tends to the solution of the Darcy cell problem (6.60). We can see this behavior in the left Figure 6.2. The resulting permeability of the cell problem (6.61) tends to the one of the cell problems (6.60). We can see this behavior even if we decrease the permeability instead of the relevance of the Laplace operator because, in this case, both the Darcy and the Darcy-Brinkman equations tend to zero. In the right Figure 6.2 we can see that if we increase K^* in the Darcy-Brinkman cell problem (6.61), the solution tends to that of the Stokes cell problem (6.62).

Table 6.1 shows that, if the permeability is not too small or the Laplace operator is relevant, then the Darcy (resp. Stokes) and the Darcy-Brinkman equation give very different results; otherwise the solutions of the two problems are similar.

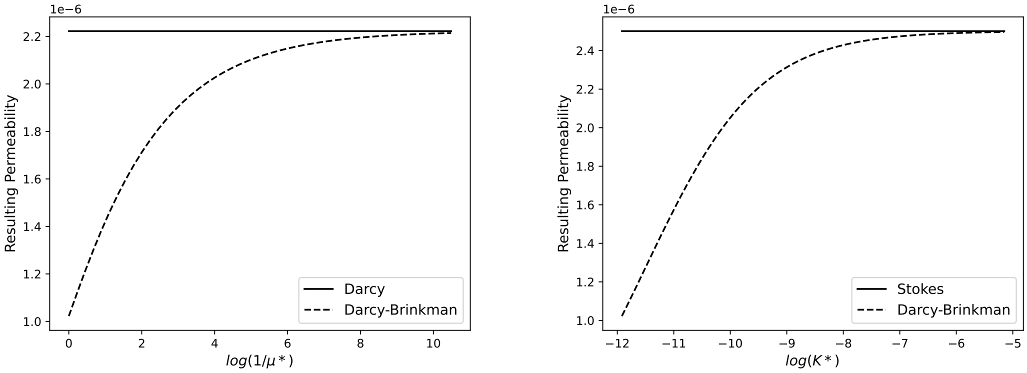

Figure 6.2: On the left: Darcy-Brinkman/Darcy comparison with respect to $1/\mu^*$, for $K^* = 6.67 \times 10^{-6}$. On the right: Darcy-Brinkman/Stokes comparison with respect to K^*, for $\mu^* = 1$.

μ^*	K^*	relative error
1	6.67×10^{-6}	74%
10^{-4}	6.67×10^{-6}	0.67%
10^{-6}	6.67×10^{-6}	0.067%
1	10^{-12}	0.026%

μ^*	K^*	relative error
1	6.67×10^{-6}	84%
1	10^{-4}	9.5%
1	10^{-2}	0.1%
1	1	0.001%

Table 6.1: Comparison between Darcy-Brinkman and Darcy (left), Darcy-Brinkman and Stokes (right).

6.5 Explicit Solution

In this section, we find an explicit solution of the macroscopic problem given in Section 6.3. For simplicity, we assume that the multiscale forces $\boldsymbol{f}_v^\epsilon$, $\boldsymbol{f}_m^\epsilon$ vanish and that both porous media are isotropic, that is:

$$\bar{\boldsymbol{K}}_v = \bar{K}_v \boldsymbol{I}, \quad \bar{\boldsymbol{K}}_m = \bar{K}_m \boldsymbol{I}, \tag{6.77}$$

where $\bar{K}_v$ and $\bar{K}_m$ are constants found solving the cell problems (6.40) and (6.46), respectively, using Comsol Multiphysics, with $\alpha = 1$. Our problem is

$$\begin{cases} \Delta p_v = -M_v \left[p_m - p_v - \bar{p} \right] & \text{in } \Omega, \\ \Delta p_m = M_m \left[p_m - p_v - \bar{p} \right] & \text{in } \Omega, \\ p_v = \bar{p}_v, \quad p_m = \bar{p}_m & \text{on } \partial\Omega, \end{cases} \tag{6.78}$$

where $M_v = \dfrac{L_p S}{|\Omega_v| \bar{K}_v}$ and $M_m = \dfrac{L_p S}{|\Omega_m| \bar{K}_m}$.

We consider a spherical domain Ω, denoting by r the radial coordinate, θ the polar coordinate, and ϕ the azimuthal angle. Moreover, we assume axisymmetry with respect to the azimuthal angle ϕ. Hence problem (6.78) becomes:

$$\begin{cases} \Delta p_v(r,\theta) = -M_v\left[p_m(r,\theta) - p_v(r,\theta) - \bar{p}\right] & r < R,\ \theta \in [0, 2\pi[, \\ \Delta p_m(r,\theta) = M_m\left[p_m(r,\theta) - p_v(r,\theta) - \bar{p}\right] & \text{in } r < R,\ \theta \in [0, 2\pi[, \\ p_v(r,\theta)_{|r=R_1} = \bar{p}_v(\theta), \quad p_m(r,\theta)_{|r=R_1} = \bar{p}_m(\theta) & r = R,\ \theta \in [0, 2\pi[, \\ \text{non-degenericity} & r = 0,\ \theta \in [0, 2\pi[, \end{cases} \tag{6.79}$$

where R is the radius of the spherical domain.

We define the quantity

$$\psi(r,\theta) = p_m(r,\theta) - p_v(r,\theta), \tag{6.80}$$

and, taking the difference between the second and the first equation of the system (6.79), we obtain the new problem

$$\begin{cases} \Delta\psi(r,\theta) = M\left[\psi(r,\theta) - \bar{p}\right] & r < R,\ \theta \in [0, 2\pi[, \\ \psi(r,\theta)_{|r=R_1} = \bar{p}_m(\theta) - \bar{p}_v(\theta), & r = R,\ \theta \in [0, 2\pi[, \\ \text{non-degenericity} & r = 0,\ \theta \in [0, 2\pi[, \end{cases} \tag{6.81}$$

where $M = M_v + M_m$. Defining

$$\hat{\psi}(r,\theta) = \psi(r,\theta) - \bar{p}, \tag{6.82}$$

we can reformulate the first equation of the system (6.81) as

$$\Delta\hat{\psi}(r,\theta) = M\hat{\psi}(r,\theta). \tag{6.83}$$

In spherical coordinates, we have:

$$\frac{1}{r^2}\frac{\partial}{\partial r}\left(r^2\frac{\partial\hat{\psi}(r,\theta)}{\partial r}\right) + \frac{1}{r^2}\frac{1}{\sin\theta}\frac{\partial}{\partial\theta}\left(\sin\theta\frac{\partial\hat{\psi}(r,\theta)}{\partial\theta}\right) = M\hat{\psi}(r,\theta), \tag{6.84}$$

calling $\zeta = \cos\theta$, we obtain

$$\frac{1}{r^2}\frac{\partial}{\partial r}\left(r^2\frac{\partial\hat{\psi}(r,\zeta)}{\partial r}\right) + \frac{1}{r^2}\frac{\partial}{\partial\zeta}\left(\left(1-\zeta^2\right)\frac{\partial\hat{\psi}(r,\zeta)}{\partial\zeta}\right) = M\hat{\psi}(r,\zeta). \tag{6.85}$$

We search for a solution in the form

$$\hat{\psi}(r,\zeta) = R(r)Z(\zeta) \tag{6.86}$$

we obtain (multiplying by r^2, dividing by $\hat{\psi}$ and rearranging the terms):

$$\frac{1}{R(r)}\frac{\partial}{\partial r}\left(r^2\frac{\partial R(r)}{\partial r}\right) - r^2 M = -\frac{1}{Z(\zeta)}\frac{\partial}{\partial\zeta}\left(\left(1-\zeta^2\right)\frac{\partial Z(\zeta)}{\partial\zeta}\right), \tag{6.87}$$

and we obtain the two differential equations:

$$r^2\frac{\partial^2 R(r)}{\partial r^2}+2r\frac{\partial R(r)}{\partial r}-(Mr^2+n(n+1))R(r)=0, \tag{6.88}$$

$$\frac{\partial}{\partial\zeta}\left(\left(1-\zeta^2\right)\frac{\partial Z(\zeta)}{\partial\zeta}\right)+n(n+1)Z(\zeta)=0, \tag{6.89}$$

where $n\in\mathbb{N}$.

The differential equation (6.88) is in the form of a spherical Bessel equation, of which the solution is

$$R(r)=Aj_{-n-1}\left(i\sqrt{M}r\right)+By_{-n-1}\left(i\sqrt{M}r\right), \tag{6.90}$$

where j_{-n-1} and y_{-n-1} are the *spherical Bessel function of the first and second kind*, respectively, and are connected to the classical Bessel function with the relations:

$$j_{-n-1}\left(x\right)=\sqrt{\frac{\pi}{2x}}J_{-n-1+\frac{1}{2}}\left(x\right),\quad y_{-n-1}\left(x\right)=\sqrt{\frac{\pi}{2x}}Y_{-n-1+\frac{1}{2}}\left(x\right), \tag{6.91}$$

where $J_{-n-\frac{1}{2}}$ and $Y_{-n-\frac{1}{2}}$ are the *Bessel function of the first and second kind.* The differential equation (6.89) is in the form of the Legendre differential equation (Section 2.2), of which the solution is

$$Z(\zeta)=CP_n(\zeta)+DQ_n(\zeta), \tag{6.92}$$

where P_n and Q_n are the *Legendre polynomials* of the first and second kind, respectively. From the non-degeneracy at $r=0$, we obtain

$$A=D=0. \tag{6.93}$$

Using the property that

$$Y_{-n-\frac{1}{2}}(x)=(-1)^nJ_{n+\frac{1}{2}}(x), \tag{6.94}$$

and the fact that

$$J_n(ix)=i^nI_n(x), \tag{6.95}$$

where I_n is the modified Bessel function of the first kind of order n, we have that the solution is

$$\hat{\psi}(r,\zeta)=\sum_{n=0}^{\infty}\tilde{A}_n\frac{1}{\sqrt{r}}I_{n+\frac{1}{2}}\left(\sqrt{M}r\right)P_n\left(\zeta\right), \tag{6.96}$$

and then, using (6.82), we obtain

$$\psi(r,\zeta)=\bar{p}+\sum_{n=0}^{\infty}\tilde{A}_n\frac{1}{\sqrt{r}}I_{n+\frac{1}{2}}\left(\sqrt{M}r\right)P_n\left(\zeta\right), \tag{6.97}$$

with the boundary condition from the second equation in the system (6.81)

$$\psi(R,\zeta)=\bar{p}_m(\zeta)-\bar{p}_v(\zeta). \tag{6.98}$$

From the properties of the orthogonal Legendre polynomials (Section 2.2) [31, 68], we can rewrite

$$\bar{p}_m(\zeta) - \bar{p}_v(\zeta) = \sum_{n=0}^{\infty} b^{(n)} P_n(\zeta), \tag{6.99}$$

where

$$b^{(n)} = \frac{1}{2}(2n+1) \int_{-1}^{1} \left[\bar{p}_m(\zeta) - \bar{p}_v(\zeta)\right] P_n(\zeta) d\zeta, \tag{6.100}$$

and, remembering that $P_0(\zeta) = 1$, we can rewrite equation (6.98) in this form

$$\begin{aligned} \psi(R,\zeta) - (\bar{p}_m(\zeta) - \bar{p}_v(\zeta)) = &\left[\bar{p} + \tilde{A}_0 \frac{1}{\sqrt{R}} I_{n+\frac{1}{2}}\left(\sqrt{M}R\right) - b^{(0)}\right] P_0(\zeta) \\ &+ \sum_{n=1}^{\infty} \left[\tilde{A}_n \frac{1}{\sqrt{R}} I_{n+\frac{1}{2}}\left(\sqrt{M}R\right) - b^{(n)}\right] P_n(\zeta) = 0, \end{aligned} \tag{6.101}$$

and using the linearly independent property of the Legendre polynomials, we obtain, for $n = 0$:

$$\tilde{A}_0 = \frac{\left[b^{(0)} - \bar{p}\right]\sqrt{R}}{I_{\frac{1}{2}}\left(\sqrt{M}R\right)}, \tag{6.102}$$

and for $n \in \mathbb{N}$, $n \neq 0$:

$$\tilde{A}_n = \frac{b^{(n)}\sqrt{R}}{I_{n+\frac{1}{2}}\left(\sqrt{M}R\right)}. \tag{6.103}$$

Exploiting the function ψ found in equation (6.97) with (6.102), (6.103) and (6.82), we can rewrite the first two equations in the system (6.79) in this way:

$$\Delta p_m(r,\zeta) = M_m \hat{\psi}(r,\zeta) = M_m \sum_{n=0}^{\infty} \tilde{A}_n \frac{1}{\sqrt{r}} I_{n+\frac{1}{2}}\left(\sqrt{M}r\right) P_n(\zeta) \tag{6.104}$$

$$\Delta p_v(r,\zeta) = -M_v \hat{\psi}(r,\zeta) = -M_v \sum_{n=0}^{\infty} \tilde{A}_n \frac{1}{\sqrt{r}} I_{n+\frac{1}{2}}\left(\sqrt{M}r\right) P_n(\zeta). \tag{6.105}$$

Now we search the solutions of equations (6.104) and (6.105) in these forms:

$$p_m(r,\zeta) = \sum_{n=0}^{\infty} m_n(r) P_n(\zeta), \tag{6.106}$$

$$p_v(r,\zeta) = \sum_{n=0}^{\infty} v_n(r) P_n(\zeta). \tag{6.107}$$

We focus on the equations for p_m (6.104) and (6.106), but for the equations in p_v the computations are similar. Substituting (6.106) into the equation (6.104), we obtain:

$$\begin{aligned} \sum_{n=0}^{\infty} \left(\frac{1}{r^2}\frac{\partial}{\partial r}\left(r^2 \frac{\partial m_n(r)}{\partial r}\right)\right) P_n(\zeta) + \frac{1}{r^2}\frac{\partial}{\partial \zeta}\left(\left(1-\zeta^2\right)\frac{\partial P_n(\zeta)}{\partial \zeta}\right) m_n(r) \\ - M_m \tilde{A}_n \frac{1}{\sqrt{r}} I_{n+\frac{1}{2}}(\sqrt{M}r) P_n(\zeta) = 0, \end{aligned} \tag{6.108}$$

using the fact that $P_n(\zeta)$ is the Legendre polynomial and the form of the Legendre differential equation (6.89), we have

$$\sum_{n=0}^{\infty}\left[\left(\frac{1}{r^2}\frac{\partial}{\partial r}\left(r^2\frac{\partial m_n(r)}{\partial r}\right)\right)-\frac{n(n+1)}{r^2}m_n(r)-M_m\tilde{A}_n\frac{1}{\sqrt{r}}I_{n+\frac{1}{2}}(\sqrt{M}r)\right]P_n(\zeta)=0, \tag{6.109}$$

and, from the linear independence of the Legendre polynomials and for every n, we obtain:

$$m_n''(r)+\frac{2}{r}m_n'(r)-\frac{n(n+1)}{r^2}m_n(r)=M_m\tilde{A}_n r^{\frac{1}{2}}I_{n+\frac{1}{2}}\left(\sqrt{M}r\right). \tag{6.110}$$

The homogeneous part of equation (6.110) is

$$m_n''(r)+\frac{2}{r}m_n'(r)-\frac{n(n+1)}{r^2}m_n(r)=0, \tag{6.111}$$

in which the solution is

$$m_n^{(0)}(r)=c_1^{(n)}r^n+c_2^{(n)}r^{-n-1}. \tag{6.112}$$

For the particular part of the solution of equation (6.110), we calculate the Wronskian Wr:

$$Wr=\frac{-2n-1}{r^2}, \tag{6.113}$$

and we have that the particular solution is:

$$m_n^{(p)}(r)=\bar{c}_1^{(n)}(r)y_1(r)+\bar{c}_2^{(n)}(r)y_2(r), \tag{6.114}$$

where y_1 and y_2 are the independent solutions of the homogeneous equation and

$$\bar{c}_1^{(n)}(r)=-\int\frac{y_2(r)f(r)}{Wr(r)}dr, \quad \bar{c}_2^{(n)}(r)=\int\frac{y_1(r)f(r)}{Wr(r)}dr. \tag{6.115}$$

We have

$$\bar{c}_1^{(n)}(r)=\frac{M_m\tilde{A}_n}{2n+1}\int r^{-n+\frac{1}{2}}I_{n+\frac{1}{2}}\left(\sqrt{M}r\right)dr, \tag{6.116}$$

calling $t=\sqrt{M}r$ we obtain

$$\frac{M_m\tilde{A}_n}{2n+1}\int r^{-n+\frac{1}{2}}I_{n+\frac{1}{2}}\left(\sqrt{M}r\right)dr=\frac{M_m\tilde{A}_n}{2n+1}\left(\frac{1}{\sqrt{M}}\right)^{-n+\frac{3}{2}}\int t^{-n+\frac{1}{2}}I_{n+\frac{1}{2}}(t)\,dt, \tag{6.117}$$

and using the property

$$\int x^{-p+1}I_p(x)dx=x^{1-p}I_{p-1}(x)dx, \tag{6.118}$$

we have

$$\frac{M_m\tilde{A}_n}{2n+1}\left(\frac{1}{\sqrt{M}}\right)^{-n+\frac{3}{2}}\int t^{-n+\frac{1}{2}}I_{n+\frac{1}{2}}(t)\,dt=\frac{M_m\tilde{A}_n}{2n+1}\left(\frac{1}{\sqrt{M}}\right)^{-n+\frac{3}{2}}t^{-n+\frac{1}{2}}I_{n-\frac{1}{2}}(t), \tag{6.119}$$

and it follows that

$$\bar{c}_1^{(n)}(r) = \frac{M_m \tilde{A}_n}{(2n+1)\sqrt{M}} r^{-n+\frac{1}{2}} I_{n-\frac{1}{2}}\left(\sqrt{M}r\right). \tag{6.120}$$

For $\bar{c}_2^{(n)}(r)$ we have

$$\bar{c}_2^{(n)}(r) = -\frac{M_m \tilde{A}_n}{2n+1} \int r^{n+\frac{3}{2}} I_{n+\frac{1}{2}}\left(\sqrt{M}r\right) dr, \tag{6.121}$$

calling $t = \sqrt{M}r$ we obtain

$$-\frac{M_m \tilde{A}_n}{2n+1} \int r^{n+\frac{3}{2}} I_{n+\frac{1}{2}}\left(\sqrt{M}r\right) dr = -\frac{M_m \tilde{A}_n}{2n+1} \left(\frac{1}{\sqrt{M}}\right)^{n+\frac{5}{2}} \int t^{n+\frac{3}{2}} I_{n+\frac{1}{2}}(t)\, dt, \tag{6.122}$$

and using the property of Bessel function

$$\int x^{p+1} I_p(x) dx = x^{p+1} I_{p+1}(x) dx, \tag{6.123}$$

we have

$$-\frac{M_m \tilde{A}_n}{2n+1} \left(\frac{1}{\sqrt{M}}\right)^{n+\frac{5}{2}} \int t^{n+\frac{3}{2}} I_{n+\frac{1}{2}}(t)\, dt = -\frac{M_m \tilde{A}_n}{2n+1} \left(\frac{1}{\sqrt{M}}\right)^{n+\frac{5}{2}} t^{n+\frac{3}{2}} I_{n+\frac{3}{2}}(t),$$

and it follows that

$$\bar{c}_2^{(n)}(r) = -\frac{M_m \tilde{A}_n}{(2n+1)\sqrt{M}} r^{n+\frac{3}{2}} I_{n+\frac{3}{2}}\left(\sqrt{M}r\right). \tag{6.124}$$

Finally, the particular solution is

$$\begin{aligned} m_n^{(p)}(r) &= \frac{M_m \tilde{A}_n \sqrt{r}}{(2n+1)\sqrt{M}} \left(I_{n-\frac{1}{2}}\left(\sqrt{M}r\right) - I_{n+\frac{3}{2}}\left(\sqrt{M}r\right)\right) \\ &= \frac{M_m \tilde{A}_n}{M} \frac{1}{\sqrt{r}} I_{n+\frac{1}{2}}\left(\sqrt{M}r\right), \end{aligned} \tag{6.125}$$

where we used the Bessel function relationship

$$I_{p-1}(x) - I_{p+1}(x) = \frac{2p}{x} I_p(x). \tag{6.126}$$

Hence we have that the solution is:

$$m_n(r) = m_n^{(0)}(r) + m_n^{(p)}(r) = c_1^{(n)} r^n + c_2^{(n)} r^{-n-1} + \frac{M_m \tilde{A}_n}{M} \frac{1}{\sqrt{r}} I_{n+\frac{1}{2}}\left(\sqrt{M}r\right). \tag{6.127}$$

By similar computations we obtain that $v_n(r)$ in (6.107) is

$$v_n(r) = d_1^{(n)} r^n + d_2^{(n)} r^{-n-1} - \frac{M_v \tilde{A}_n}{M} \frac{1}{\sqrt{r}} I_{n+\frac{1}{2}}\left(\sqrt{M}r\right). \tag{6.128}$$

We impose the boundary conditions (6.79). To have non-degeneracy at $r = 0$, we need to have (for every n)

$$c_2^{(n)} = d_2^{(n)} = 0; \tag{6.129}$$

instead, from the boundary condition at $r = R$, rewriting the boundary condition in terms of Legendre polynomials

$$\bar{p}_m(R, \zeta) = \sum_{n=0}^{\infty} b_m^{(n)} P_n(\zeta), \quad \bar{p}_v(R, \zeta) = \sum_{n=0}^{\infty} b_v^{(n)} P_n(\zeta), \tag{6.130}$$

where

$$b_m^{(n)} = \frac{1}{2}(2n+1)\int_{-1}^{1} \bar{p}_m(\zeta)P_n(\zeta)d\zeta, \quad b_v^{(n)} = \frac{1}{2}(2n+1)\int_{-1}^{1} \bar{p}_v(\zeta)P_n(\zeta)d\zeta, \tag{6.131}$$

we obtain (using the property of linear independence of the Legendre polynomials):

$$c_1^{(n)} = \frac{\left[b_m^{(n)} - \dfrac{M_m \tilde{A}_n}{M\sqrt{R}} I_{n+\frac{1}{2}}\left(\sqrt{M}R\right)\right]}{R^n}, \tag{6.132}$$

$$d_1^{(n)} = \frac{\left[b_v^{(n)} + \dfrac{M_v \tilde{A}_n}{M\sqrt{R}} I_{n+\frac{1}{2}}\left(\sqrt{M}R\right)\right]}{R^n}. \tag{6.133}$$

6.6 Application to the Lymph Node

In this section, we show the results given by the explicit solution with physiological data obtained or estimated by an idealized spherical mouse popliteal lymph node [10]. The lymph node is basically formed by two parts: a porous bulk region called lymphoid compartment (LC) and a thin layer against the wall where the fluid can flow freely, called subcapsular sinus (SCS) [37, 108]. Due to the fact that the whole blood vasculature in the lymph node is in the LC [5, 53, 54], in this section, we apply the explicit solution found in the previous section to the LC, implemented in Matlab.

Here we have that Ω_v is the *blood vessels phase*, and Ω_m is the *interstitial phase*. The fluid exchange between these two phases is described by the *Starling equation*, which corresponds to choose $\bar{p} = \sigma(\pi_m - \pi_v)$. We assume a radius $R = 0.49\,\mathrm{mm}$ of the LC [12, 53]. The lymph that flows inside the lymph node is modeled as an incompressible Newtonian fluid similar to water [1] with viscosity $\mu = 1\,\frac{\mathrm{mg}}{\mathrm{mm\ s}}$ and density $\rho_0 = 1\,\frac{\mathrm{mg}}{\mathrm{mm}^3}$. The interstitial permeability is considered homogeneous [101] with value $\hat{K}_m = 3.84 \times 10^{-9}\,\mathrm{mm}^2$ [11]. The effective viscosity is taken as $\mu_e = \frac{\mu}{\phi}$ [106, 107], where ϕ is the *porosity* taken as $\phi = 0.75$ [11].

The parameters that regulate the fluid exchange between the lymph node and the blood vessels are very heterogeneous in the literature, but we try to summarize them here. The Staverman's reflection coefficient σ is estimated between $\sigma =$

$0.88 - 0.9$. In [50–52] they estimate the oncotic pressure difference $\pi_v - \pi_m$ in a canine popliteal lymph node as $\approx 2080\,\text{Pa} = 2.08 \times 10^6\,\text{mPa}$, in [5] they estimate the values $\pi_v \approx 1.53 \times 10^6\,\text{mPa}$ and $\pi_m \approx 5.06 \times 10^6\,\text{mPa}$ in a mouse using the assumption that the protein content of lymph is 40% of that of the plasma, [6, 7] found $\pi_v - \pi_m \approx 3.41 \times 10^5\,\text{mPa}$ by fitting the wild type mouse model to experimental data, [129] measured the value $\pi_v - \pi_m \approx 1.5 \times 10^6\,\text{mPa}$ in the skin of mice and [8] estimates $\pi_v - \pi_m \approx 1.69 \times 10^6\,\text{mPa}$.

For the hydraulic conductivity of the blood vessel wall L_p, we have that [5] assumed a value of $L_p = 5.475 \times 10^{-12}\,\frac{\text{mm}}{\text{s mPa}}$ based on the measured hydraulic conductivity of rat mesenteric venular microvessels, [6, 7] assumed a range of $L_p \approx 1.02 \times 10^{-11} - 6.7 \times 10^{-10}\,\frac{\text{mm}}{\text{s mPa}}$ from the values of the blood capillaries, [8] estimates directly $L = L_p \frac{S}{|\Omega_m|} \approx 10^{-6}\,\frac{1}{\text{s mPa}}$ (that means, in our case, $L_p \approx 3.667 \times 10^{-8}\,\frac{\text{mm}}{\text{s mPa}}$, see below).

Moreover, we have that the mean blood vessels pressure $\bar{p}_v$ in the node is estimated as $\bar{p}_v \approx 6.67 \times 10^5\,\text{mPa}$ in [5], as $\bar{p}_v \approx 9.73 \times 10^5\,\text{mPa}$ in [6, 7] and as $\bar{p}_v \approx 1.06 \times 10^6\,\text{mPa}$ in [8].

The surface of fluid exchange S between the lymph node and the blood vessels is given by an average of the values found in [53] and is $S = 13.4\,\text{mm}^2$; the volume of the blood vessels inside the node $|\Omega_v|$ is about the 6.15% of the whole lymph node volume, and hence we have (supposing that the SCS height is $\approx 10^{-2}\,\text{mm}$ [5, 10, 12]) $|\Omega_v| = 0.0322\,\text{mm}^3$ [53, 54].

We suppose a geometry of the cell domain as in Section 6.4. This microscale geometry is simpler with respect to the physiological one [53, 54]; we can assume this simplified microscale geometry because we start with a formulation that is already smoothed out (our starting point was a Darcy/Darcy-Brinkman formulation), and hence we do not need precise information about the microstructure geometry (see Section 6.4). What we want to keep in the physiological geometry are the surface area of the blood vessels S and the volume of the blood vessels $|\Omega_v|$. For this reason, we estimate the normalized radius of the cylinders $\bar{r} = r_c/d$, where r_c is the radius of the cylinders and d is the microscale variable that indicates the distance between blood vessels, in such a way that we keep the physiological parameter S and $|\Omega_v|$. We have that the surface area S_v of the whole domain Ω_v can be found with the formula

$$S_v = 3N\left[2\pi r_c d - (16 - 8\sqrt{2})r_c^2\right], \tag{6.134}$$

where N is the number of cells in our domain, and remember that $3(16 - 8\sqrt{2})r_c^2$ is the intersection surface of a tricylinder. From the fact that $S_v = S$, we find

$$d = \frac{(16 - 8\sqrt{2})r_c}{2\pi} + \frac{S}{6N\pi r_c}. \tag{6.135}$$

From here, we can vary r_c so that we can calculate numerically the volume of $|\Omega_v|$ and we compare the results given numerically to the physiological data. We found that $r_c = 5.495 \times 10^{-3}\,\text{mm}$, $d = 2.4 \times 10^{-2}\,\text{mm}$ and hence $\bar{r} \approx 0.229$ gives the desired physiological volume. Thanks to this estimation, we have that, at the macroscale, S and $|\Omega_v|$ are the same as in the physiological data. Hence we can use these parameters to estimate the permeability of the blood vessels K_v using the Kozeny-Carman formula [130, 131]:

$$K_v = \frac{1}{c_0 \left(\frac{S}{|\Omega_v|}\right)^2}, \tag{6.136}$$

where c_0 is the *Kozeny constant*, and depends on the tortuosity of the vessels [128]. Thanks to the fact that we start from a formulation that is already smoothed out, we can take into account the tortuosity effect by varying only the constant c_0 and not the geometry of the cell problem; this is true, especially in the case with little tortuosity. With no tortuosity effect, $c_0 = 5.6$, and this implies $K_v = 1.03 \times 10^{-6}\,\mathrm{mm}^2$. With these data, we have

$$\epsilon = \frac{d}{L} \approx 10^{-2}. \tag{6.137}$$

To find the permeabilities $\bar{K}_v$ and $\bar{K}_m$ of the macroscale problems (6.48) and (6.53) that comes out from the microstructure problem, we need to solve the cell problems (6.40) and (6.46) with the body forces $\boldsymbol{f}_m = \boldsymbol{f}_v = \boldsymbol{0}$ and using the microstructure parameters described above (note that $\hat{K}_m$ is the microstructure permeability that we use in the cell problem (6.46) to find $\bar{K}_m$).

These parameters are summarized in Table 6.2.

As boundary conditions we choose, for p_v:

$$p_v(R, \zeta) = \bar{p}_v, \tag{6.138}$$

where $\bar{p}_v$ is a constant value given by the literature (mean blood vessels pressure), and for p_m:

$$p_m(R, \zeta) = \bar{p}_m(\zeta), \tag{6.139}$$

where $\bar{p}_m(\zeta)$ can be any function sufficiently regular of ζ.

To begin with (and for simplicity), we assume that $\bar{p}_m(\zeta) = \bar{p}_m$ is a fixed constant value. In this case, we can see the direction of the fluid exchange between the interstitial space and the blood vessels explicitly. Indeed, in this case remains only the $n = 0$ term (from equations (6.98), (6.99) and (6.100), from the fact that $P_0(x) = 1$ we have $b^{(0)} = b_m^{(0)} - b_n^{(0)} = \bar{p}_m - \bar{p}_v$), and this implies that equation (6.96) reduces to

$$\hat{\psi}(r) = \tilde{A}_0 \frac{I_{1/2}\left(\sqrt{M}r\right)}{\sqrt{r}} = \frac{\sqrt{R} I_{1/2}\left(\sqrt{M}r\right)}{\sqrt{r} I_{1/2}\left(\sqrt{M}R\right)} \left[\bar{p}_m - \bar{p}_v - \sigma\left(\pi_m - \pi_v\right)\right], \tag{6.140}$$

and from the fact that (6.54) can be written as

$$\nabla_{\boldsymbol{x}} \cdot \langle \boldsymbol{v}_v^{(0)}(\boldsymbol{x}, \boldsymbol{y}) \rangle_{\Omega_v} = \frac{L_p S}{|\Omega_v|} \left[p_m^{(0)}(\boldsymbol{x}) - p_v^{(0)}(\boldsymbol{x}) - \bar{p} \right] = \frac{L_p S}{|\Omega_v|} \hat{\psi}(r), \tag{6.141}$$

and remembering that

$$I_{1/2}(x) = \frac{\sqrt{\frac{2}{\pi}} \sinh(x)}{\sqrt{x}} \tag{6.142}$$

Name	Physiological Range/Value	Description
R	$0.49\,\text{mm}$	Macroscopic radius [10, 12].
μ	$1\,\frac{\text{mg}}{\text{mm s}}$	Viscosity [1, 17].
ϕ	0.75	Porosity [11].
μ_e	$\frac{\mu}{\phi}$	Effective viscosity [79, 106, 109].
ρ_0	$1\,\frac{\text{mg}}{\text{mm}^3}$	Density [1, 17].
$\hat{K}_m$	$3.84 \times 10^{-9}\,\text{mm}^2$	Permeability of the interstitium [11, 101].
σ	$0.88 - 0.9$	Staverman's coefficient [5–8].
$\pi_v - \pi_m$	$3.41 \times 10^5 - 2.08 \times 10^6\,\text{mPa}$	Oncotic pressure difference [5–8, 51, 52].
L_p	$5.475 \times 10^{-12} - 3.67 \times 10^{-8}\,\frac{\text{mm}}{\text{s mPa}}$	Hydraulic conductivity of the blood vessel walls[5–8].
$\bar{p}_v$	$6.67 \times 10^5 - 1.066 \times 10^6\,\text{mPa}$	Mean blood vessel pressure [5–8].
S	$13.4\,\text{mm}^2$	Blood vessel surface [53].
$\lvert\Omega_v\rvert$	$0.0322\,\text{mm}^3$	Blood vessel volume [53].
N	6500	Number of cells.
r_c	$5.495 \times 10^{-3}\,\text{mm}$	Blood vessel radius.
d	$2.4 \times 10^{-2}\,\text{mm}$	Blood vessel mean distance.
K_v	$1.03 \times 10^{-6}\,\text{mm}^2$	Blood vessels permeability.
c_0	5.6	Kozeny constant [128].
$\boldsymbol{f}_m$, $\boldsymbol{f}_v$	0	Body forces.
$\bar{K}_m$	$2.85 \times 10^{-9}\,\frac{\text{mm}^3\text{s}}{\text{mg}}$	Macroscopic interstitial hydraulic conductivity (solving equation (6.46)).
$\bar{K}_v$	$5.8 \times 10^{-7}\,\frac{\text{mm}^3\text{s}}{\text{mg}}$	Macroscopic blood hydraulic conductivity (solving equation (6.40)).

Table 6.2: Physiological and estimated parameters.

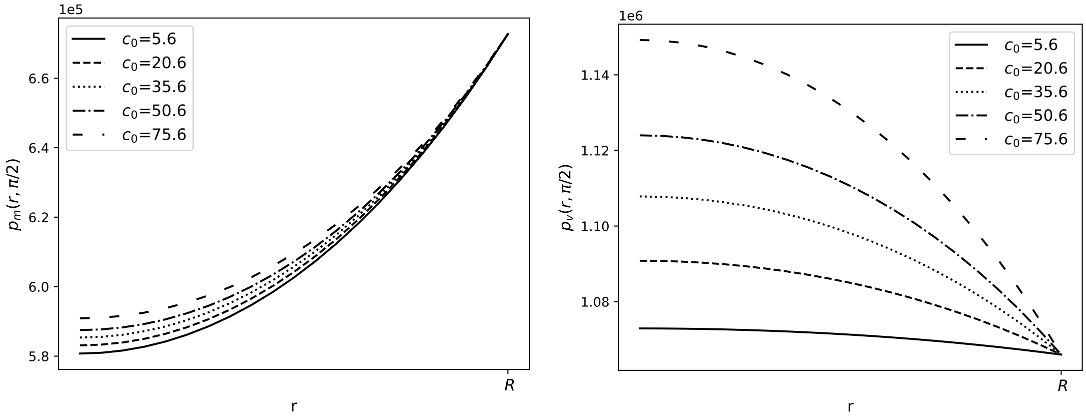

Figure 6.3: The variation of p_m and p_v in mPa at $\theta = \pi/2$, for some values of the Kozeny constant c_0, with $\pi_v - \pi_m = 1.02 \times 10^6\,\mathrm{mPa}$, $\bar{p}_v = 1.066 \times 10^6\,\mathrm{mPa}$, $L_p = 5.475 \times 10^{-10}\,\frac{\mathrm{mm}}{\mathrm{s\,mPa}}$, $\bar{p}_m = 6.727 \times 10^5\,\mathrm{mPa}$ and the parameters in Table 6.2.

is positive for every $x > 0$, we have that, the sign of the divergence (6.54) (that is the opposite sign of (6.52)) is given by the sign of

$$\bar{p}_m - \bar{p}_v - \sigma\left(\pi_m - \pi_v\right). \tag{6.143}$$

The work [111] measured that the average pressure in a lymph node is about $6.86 \pm 0.56\,\mathrm{mmH_2O} \approx 6.7 \times 10^5 \pm 5.5 \times 10^4\,\mathrm{mPa}$, so, for now, we fix $\bar{p}_m = 6.7 \times 10^5\,\mathrm{mPa}$. With this value, $\sigma = 0.88$ and $\Delta\pi = 1.02 \times 10^6\,\mathrm{mPa}$, we have that the sign of (6.143) is negative for $\bar{p}_v \lessapprox 1.5676 \times 10^6\,\mathrm{mPa} \approx 11.8\,\mathrm{mmHg}$ (which means that the fluid goes from the interstitial space to the blood phase), and start to have an inversion of the flow at $\bar{p}_v \approx 1.5676 \times 10^6\,\mathrm{mPa} \approx 11.8\,\mathrm{mmHg}$.

In Figure 6.3 we can see the resulting pressures p_m and p_v varying with respect to the Kozeny constant c_0. Increasing c_0 means increasing the tortuosity of the blood vessels [128], and this is related to an increase of p_v and p_m at the center of the node, and that means that there is lesser flow from the interstitial space to the blood vessels. This is related to the fact that, an increase in c_0 in the relation (6.136) means a decrease in K_v, and consequently, an increase of the pressure p_v at the center of the node, and an increase in the pressure p_v means an increase of p_m; we can see better this behavior in Figure 6.5. This is a parametric study with the variation of c_0 that is related to the tortuosity effect [128], but to study the role of the tortuosity in more detail we need to take it into account in the geometry of the microscale problem, which we did not do in this case.

In Figure 6.4 we can see the resulting pressures p_m and p_v varying with respect to the hydraulic conductivity of the blood vessel walls L_p. Increasing L_p means a decrease of p_m and an increase of p_v at the center of the node, meaning a higher flow from the interstitial space to the blood vessels (as expected).

In Figure 6.6 we can see the resulting pressures p_m and p_v varying with respect to $\Delta\pi = \pi_v - \pi_m$. Increasing $\Delta\pi$ means increasing the concentration difference between the interstitial space and the blood vessels, and consequently the increase of the fluid flow from Ω_m to Ω_v.

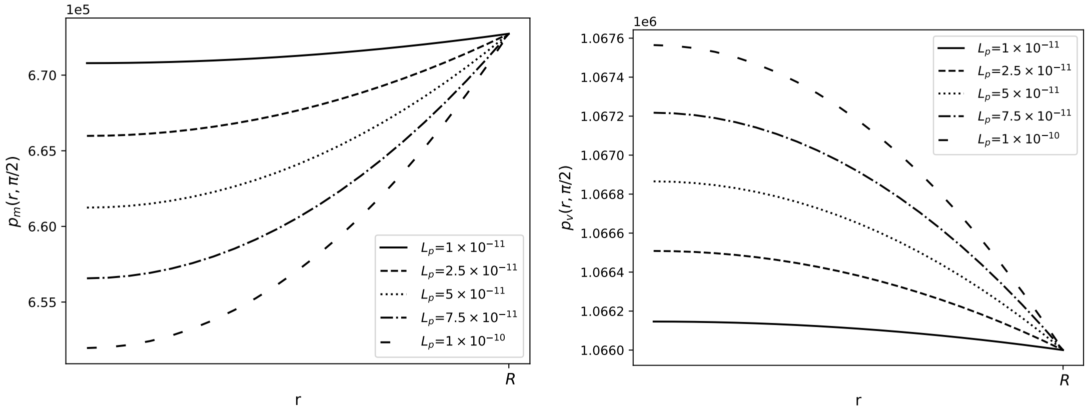

Figure 6.4: The variation of p_m and p_v in mPa at $\theta = \pi/2$, for some values of the hydraulic conductivity L_p in $\frac{\mathrm{mm}}{\mathrm{s\,mPa}}$, with $\pi_v - \pi_m = 1.02 \times 10^6\,\mathrm{mPa}$, $\bar{p}_v = 1.066 \times 10^6\,\mathrm{mPa}$, $\bar{p}_m = 6.727 \times 10^5\,\mathrm{mPa}$ and the parameters in Table 6.2.

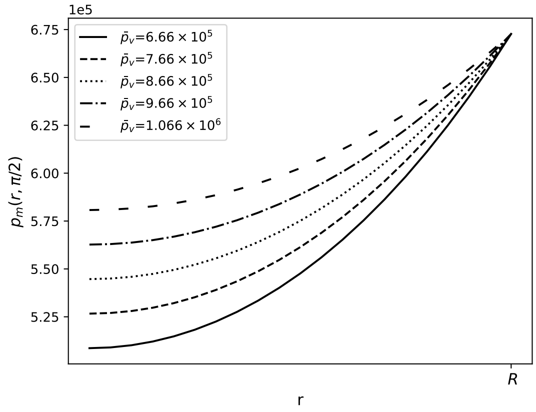

Figure 6.5: The variation of p_m in mPa at $\theta = \pi/2$, for some values of the blood vessel pressure $\bar{p}_v$ in mPa, with $\pi_v - \pi_m = 1.02 \times 10^6\,\mathrm{mPa}$, $L_p = 5.475 \times 10^{-10}\,\frac{\mathrm{mm}}{\mathrm{s\,mPa}}$, $\bar{p}_m = 6.727 \times 10^5\,\mathrm{mPa}$ and the parameters in Table 6.2.

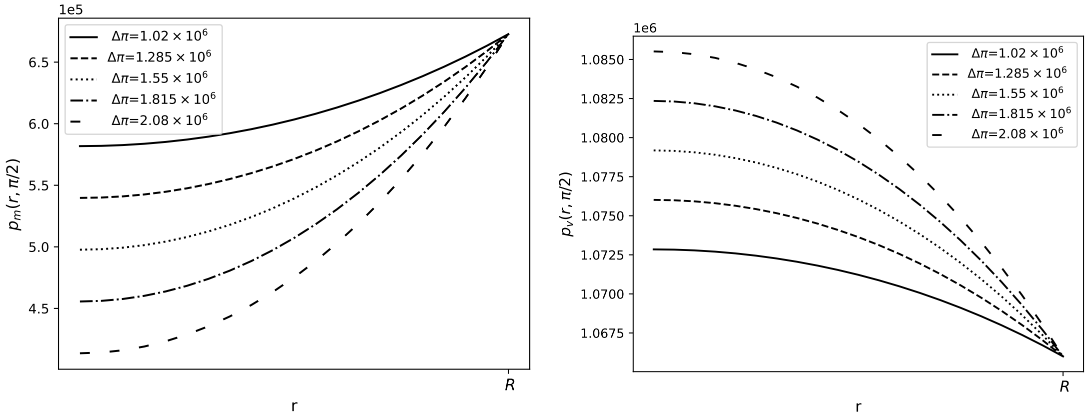

Figure 6.6: The variation of p_m and p_v in mPa at $\theta = \pi/2$, for some values of the oncotic pressure difference $\Delta\pi = \pi_v - \pi_m$ in mPa, with $\bar{p}_v = 1.066 \times 10^6\,\mathrm{mPa}$, $L_p = 5.475 \times 10^{-10}\,\frac{\mathrm{mm}}{\mathrm{s\,mPa}}$, $\bar{p}_m = 6.727 \times 10^5\,\mathrm{mPa}$ and the parameters in Table 6.2.

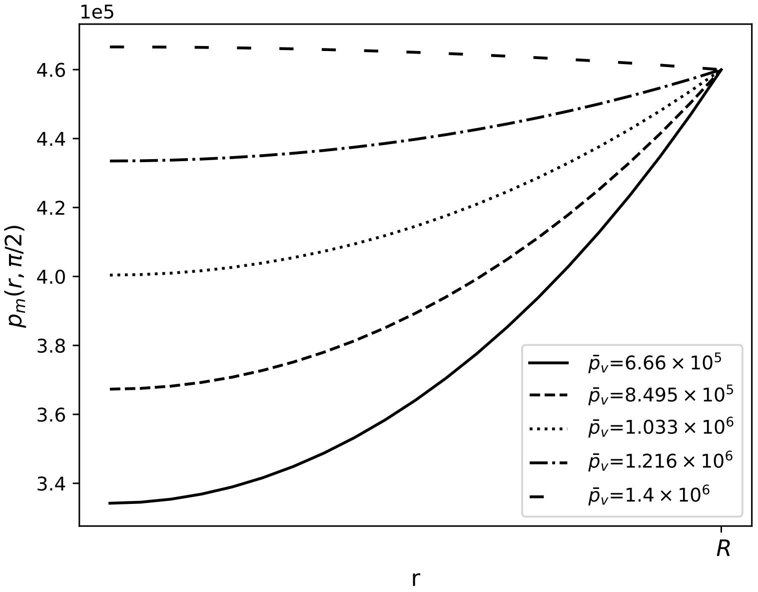

Figure 6.7: The variation of p_m in mPa at $\theta = \pi/2$, for some values of the mean blood vessel pressure $\bar{p}_v$ in mPa, with $\pi_v - \pi_m = 1.02 \times 10^6\,\text{mPa}$, $L_p = 5.475 \times 10^{-10}\,\frac{\text{mm}}{\text{s}\,\text{mPa}}$, the boundary conditions (6.144) and the parameters in Table 6.2.

The strength of the explicit solution we found in Section 6.5 is to take into account the variation with respect to θ of the boundary condition $\bar{p}_m$ to mimic the pressure distribution in the SCS. Unfortunately, as far as we know, there are no precise physiological data available for the pressure distribution in the SCS. Hence, inspired by [59], we take a linear variation of the pressure along the θ coordinate between the values $\bar{p}_{m,max} = 3.9$ mmHg $\approx 5.2 \times 10^5$ mPa and $\bar{p}_{m,min} = 3$ mmHg $\approx 4 \times 10^5$ mPa; these values are taken from the resulting pressure in [5]. Hence we can write:

$$\bar{p}_m(\zeta) = \bar{p}_{m,min} + \frac{\zeta + 1}{2}(\bar{p}_{m,max} - \bar{p}_{m,min}). \tag{6.144}$$

Given this boundary condition, if we use the physiological values used in [5] ($\sigma = 0.88$ and $\pi_v - \pi_m = 1.02 \times 10^6$ mPa), we have an inversion of the flow at $\approx 1.4 \times 10^6$ mPa ≈ 10.5 mmHg, the same found in [5]. We can see this behavior in Figure 6.7.

In Figure 6.8 we show the interstitial pressure distribution in the whole domain (remembering that we assume axisymmetry) varying the hydraulic conductivity of the blood vessel walls L_p. As we can see, we have that the position and the value of the minimum of the pressure vary with respect to L_p; as L_p increases, the minimum of the pressure decreases (see Figure 6.4) and moves towards the center of the node. This is due to a combination of the pressure variation given by the boundary conditions (6.144) and the fluid exchange between phases. These results confirm that the θ dependence in our explicit solution is essential to describe the fluid motion and the pressure distribution inside a lymph node.

In Figure 6.9 we can see the interstitial pressure distribution in the whole

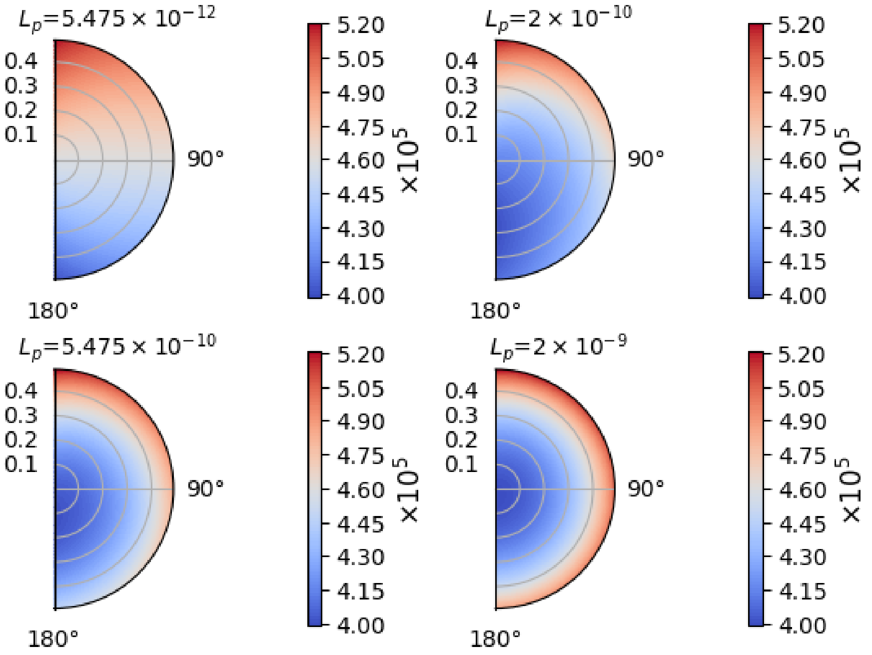

Figure 6.8: The variation of p_m in mPa in all the domain, for some values of L_p, with $\pi_v - \pi_m = 1.02 \times 10^6\,\mathrm{mPa}$, $\bar{p}_v = 6.66 \times 10^6\,\mathrm{mPa}$, the boundary conditions (6.144) and the parameters in Table 6.2.

domain varying the blood vessel pressure $\bar{p}_v$. As we can see, we have that increasing $\bar{p}_v$ increases the minimum of the pressure p_m and moves the minimum from the center to the lower part ($\zeta = -1$ where we have the minimum in equation (6.144)) of the node. This behavior is the opposite of what we have in Figure 6.8, in accordance with the results found in Figures 6.4 and 6.5.

As we mentioned before, we can choose as boundary condition $\bar{p}_m(\zeta)$ what we want; hence we can choose the more complicated pressure distribution found with the stream function approach in the steady case (see Section 2.3.1 for more details):

$$\bar{p}_m(R,\zeta) = C_{\text{steady}} - \mu \sum_{n=1}^{\infty} \left[\frac{(4(n+1)+2)}{n} C_n^s R^n + \frac{(4(n+1)-6)}{n+1} D_n^s R^{-n-1} \right] P_n(\zeta) \tag{6.145}$$

where the constants C_{steady}, C_n^s and D_n^s are calculated as in Chapter 5 [10] in a steady case without fluid-exchange (div-free solution), where we fix the pressure at one point $\bar{p}_m(R_2,-1) = 6.17 \times 10^5\,\mathrm{mPa}$ and with an inlet and outlet boundary condition defined in the domain $[-1,-1+\zeta_0]$ (outlet condition) and $[1-\zeta_0,1]$ (inlet condition), where $\zeta_0 = \cos\left[\arcsin\left(\frac{R_{LV}}{\sqrt{R_{LV}^2+R_2^2}}\right)\right] = \frac{R_2}{\sqrt{R_{LV}^2+R_2^2}}$, $R_{LV} = 0.04\,\mathrm{mm}$ and $R_2 = 0.5\,\mathrm{mm}$. The boundary pressure distribution is plotted in Figure 6.10. We can see that we have a fast increment of pressure near the inlet boundary condition (and a fast decrement near the outlet boundary condition). With this boundary conditions and the parameters $\bar{p}_v = 1.06 \times 10^6\,\mathrm{mPa}$, $\pi_v - \pi_m = 1.02 \times 10^6\,\mathrm{mPa}$ and $L_p = 5.475 \times 10^{-10}\,\frac{\mathrm{mm}}{\mathrm{s\,mPa}}$ we obtain the pressure distribution shown in Figure

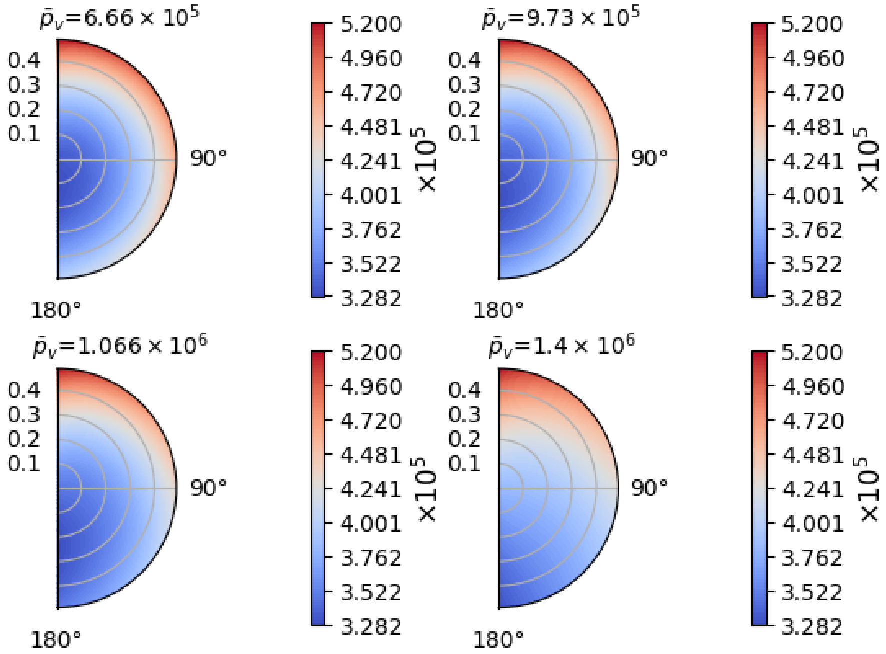

Figure 6.9: The variation of p_m in mPa in all the domain, for some values of $\bar{p}_v$ in mPa, with $\pi_v - \pi_m = 1.02 \times 10^6\,\text{mPa}$, $L_p = 5.475 \times 10^{-10}\,\frac{\text{mm}}{\text{s}\,\text{mPa}}$, $\bar{p}_m = 6.727 \times 10^5\,\text{mPa}$, the boundary conditions (6.144) and the parameters in Table 6.2.

6.11. Varying the parameters that regulate the fluid exchange, we obtain the same behavior obtained above. As we can see, we have a pressure distribution similar to those found earlier, but we have a higher (lower) pressure distribution near the inlet (outlet). In this case, we have an inversion of flow with the mean blood vessels pressure $\bar{p}_v \approx 1.53 \times 10^6\,\text{mPa} \approx 11.476\,\text{mmHg}$, similar to the one found with the constant value $\bar{p}_m \approx 6.7 \times 10^5\,\text{mPa}$.

6.7 Numerical Simulation

In this section we propose numerical simulations related to the model described in the previous sections aimed at coupling the motion of the flow in the subcapsular sinus (SCS) and the lymphoid compartment (LC). Indeed, in the previous section, we suppose a given pressure distribution for the SCS and we impose this pressure as a boundary condition for the porous bulk region (the LC). However, in general, we need to couple these two domains. We suppose that the lymph is a Newtonian fluid similar to water, wherein the SCS we can describe the fluid behavior with the steady Stokes equation (due to the small velocities and small characteristic length, see Section 2.1)

$$\Delta \boldsymbol{v}^f = \nabla p^f, \tag{6.146}$$

where $\boldsymbol{v}^f$ and p^f are the velocity and the pressure, respectively, in the SCS, and for the LC we use the model obtained in the previous sections. The physiological

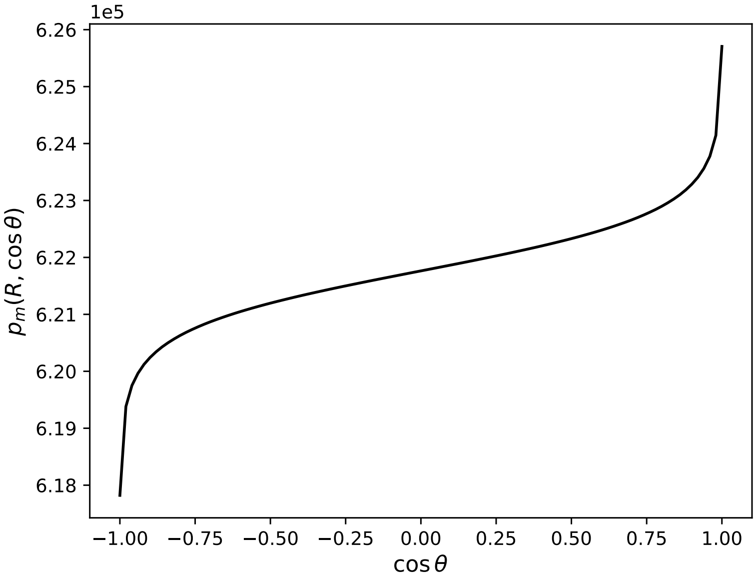

Figure 6.10: The pressure distribution of equation (6.145) with the values calculated in [10].

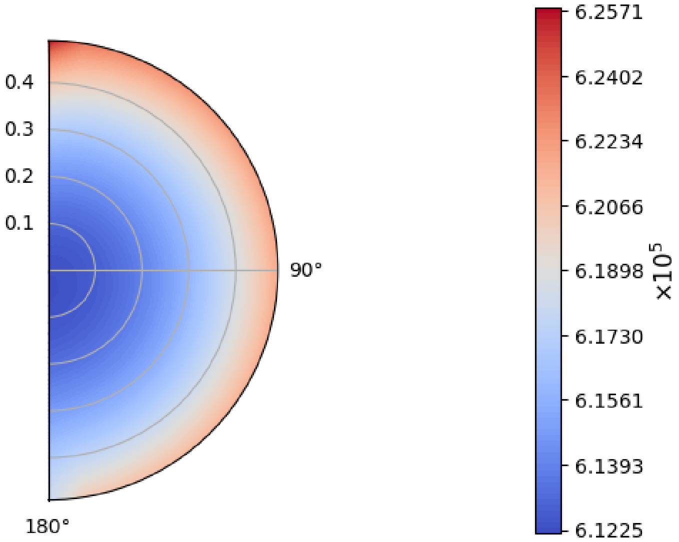

Figure 6.11: The pressure distribution of p_m with boundary conditions (6.145) (values calculated in [10]), $\bar{p}_v = 1.06 \times 10^6\,\mathrm{mPa}$, $\pi_v - \pi_m = 1.02 \times 10^6\,\mathrm{mPa}$ and $L_p = 5.475 \times 10^{-11}\,\frac{\mathrm{mm}}{\mathrm{s\,mPa}}$.

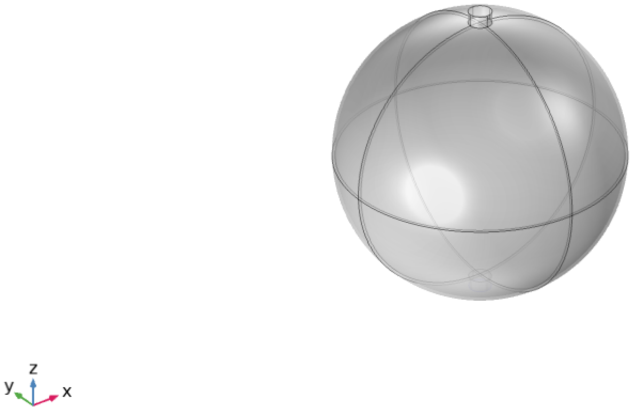

Figure 6.12: The 3D simplified geometry of our problem, inspired by a mouse popliteal lymph node as in Chapter 5 and in [10].

data are the same exposed in Section 6.5, and the cell problems (6.40) and (6.46) are solved using Comsol Multiphysics (as in the previous section).

We use the finite element method to solve numerically the Stokes equation and the macroscopic model given in Section 6.3 using Comsol Multiphysics. To have more information about the weak formulation of the Stokes equation, we refer to Section 5.2 and to [56]. Moreover, from equations (6.58) and (6.59), we have that the Darcy problems can be written as diffusion problems for the pressure and we refer to [132–134] for more information about the weak formulation and the numerical methods used to solve this kind of problem.

We suppose a simplified spherical geometry as in Chapter 5 and [10], but in this case, we have a 3D geometry (hence we do not assume the axisymmetry of the flow). The geometrical parameters are the same as given in the previous section and in the Subsection 5.1.2 [10]. We can see the 3D geometry of our problem in Figure 6.12.

The boundary conditions that we impose are: uniform flow velocity v_{in} as inlet condition in the upper lymphatic vessel, the pressure p_{out} as outlet condition in the lower lymphatic vessel, no-slip condition at the external wall, and at the interface between the SCS and the LC we have [121]

$$\boldsymbol{v}^f \cdot \boldsymbol{n} = \boldsymbol{v}^p \cdot \boldsymbol{n} \quad \text{on } \Gamma_M, \tag{6.147}$$

$$-\Big(\boldsymbol{T}(\boldsymbol{v}^f, p^f) \cdot \boldsymbol{n}\Big) \cdot \boldsymbol{n} = p^p \quad \text{on } \Gamma_M, \tag{6.148}$$

$$\boldsymbol{v}^f(\boldsymbol{x}) \cdot \boldsymbol{t}_j = -\frac{\sqrt{\mathcal{K}_m(\boldsymbol{x})}}{\alpha_M} \Big[(\boldsymbol{n} \cdot \nabla)\, \boldsymbol{v}^f(\boldsymbol{x})\Big] \cdot \boldsymbol{t}_j \quad \text{on } \Gamma_M, \tag{6.149}$$

where Γ_M is the *macroscopic interface* between the free fluid region (SCS) and the porous region (LC), $\boldsymbol{v}^f$ if the *velocity in the free-fluid region*, $\boldsymbol{v}^p$ is the *velocity* *in the porous region*, $\boldsymbol{T}$ is the *Cauchy stress tensor of the free-fluid region* (see Section 2.1), p^f is the *pressure of the free-fluid region*, p^p is the *pressure in the porous region*, $\boldsymbol{\mathcal{K}}_m$ is the macroscopic permeability (obtained from the cell problem (6.46) of the phase Ω_m, that in our specific case is constant $\boldsymbol{\mathcal{K}}_m(\boldsymbol{x}) \equiv \mathcal{K}\mathbf{I}$, where $\mathbf{I}$ is the identical tensor), α_M is a parameter that needs to be estimated, $\boldsymbol{n}$ is the normal vector related to Γ_M, and $\boldsymbol{t}_j$ for $j = 1, ..., d-1$ (where d is the dimension of our problem) are the tangents related to the normal $\boldsymbol{n}$. The last interface condition is the so-called *Beaver-Joseph-Saffman boundary condition* (BJS). The BJS is an interface condition formulated experimentally in [122, 123]. Unlike the interface between Stokes and Darcy-Brinkman in which we have the same differential formulation of the equations and we can impose the continuity of the velocities (see Section 5), here we have a Stokes differential equation in the free fluid region and a diffusion-type equation for the pressure in the porous region.

An approximation that we can use to treat the equation (6.149) is [121, 124]

$$\boldsymbol{v}^f \cdot \boldsymbol{t}_j = 0 \quad \text{on } \Gamma_M, \tag{6.150}$$

where, if we use this new boundary condition, we have an error of $\approx \epsilon$.

In the general case, we have that, if we take a test function $\boldsymbol{w} \in W_g = \{\boldsymbol{w} \in H^1(\Omega) : \boldsymbol{w}_{\Gamma_D} = g\}$ (where Ω is the domain of the problem and Γ_D is the portion of the boundary in which we have the Dirichlet boundary conditions, see Section 5.2), the weak formulation of the interface conditions (6.147-6.149) can be written as [121]

$$\begin{aligned} &-\int_{\Gamma_M} \boldsymbol{n} \cdot \boldsymbol{T}(\boldsymbol{v}^f, p^f) \boldsymbol{w} dV = \\ &-\int_{\Gamma_M} \Big[\boldsymbol{n} \cdot \boldsymbol{T}(\boldsymbol{v}^f, p^f) \cdot \boldsymbol{n}\Big]\, \boldsymbol{w} \cdot \boldsymbol{n} - \int_{\Gamma_M} \sum_{j=1}^{d-1} \Big[\boldsymbol{n} \cdot \boldsymbol{T}(\boldsymbol{v}^f, p^f) \cdot \boldsymbol{t}_j\Big]\, \boldsymbol{w} \cdot \boldsymbol{t}_j, \end{aligned} \tag{6.151}$$

and hence we have, using (6.148) and (6.149)

$$\begin{aligned} -\int_{\Gamma_M} \boldsymbol{n} \cdot \boldsymbol{T}(\boldsymbol{v}^f, p^f) \boldsymbol{w} dV &= \int_{\Gamma_M} p^p(\boldsymbol{w} \cdot \boldsymbol{n}) + \int_{\Gamma_M} \sum_{j=1}^{d-1} \frac{\mu \alpha_M}{\sqrt{\mathcal{K}}} \left(\boldsymbol{v}^f \cdot \boldsymbol{t}_j\right) (\boldsymbol{w} \cdot \boldsymbol{t}_j) \\ &= \int_{\Gamma_M} (p^p \cdot \boldsymbol{n}) \boldsymbol{w} + \int_{\Gamma_M} \sum_{j=1}^{d-1} \left[\frac{\mu \alpha_M}{\sqrt{\mathcal{K}}} \left(\boldsymbol{v}^f \cdot \boldsymbol{t}_j\right) \cdot \boldsymbol{t}_j\right] \boldsymbol{w}. \end{aligned} \tag{6.152}$$

First of all, we want to see the effect of the Beaver-Joseph-Saffman parameter α_M in the interface condition (6.149). If we have that $\alpha_M \to \infty$, we obtain the simplified interface condition (6.150). In Figure 6.13 we can see the velocity magnitude and the pressure values with $\alpha_M = 1$ and $\alpha_M \to \infty$, and, as we can see, we have that this parameter does not influence much the velocity and the pressure in the whole domain, but mainly affects the quantities on the interface Γ_M. Figure 6.14 shows the shear stress at the interface Γ_M varying α_M, with these chosen parameters: $v_{\text{in}} = 0.22\,\frac{\text{mm}}{\text{s}}$, $p_{\text{out}} = 6.18 \times 10^5$ mPa, $\pi_v - \pi_m = 1.02 \times 10^6$ mPa, $L_p = 5.475 \times 10^{-11}\,\frac{\text{mm}}{\text{s mPa}}$ and $\bar{p}_v = 1.06 \times 10^6$ mPa. As we can see, α_M has a relevant effect on the shear stress on the interface Γ_M, but all the values are qualitatively similar to the results found in Section 5.2.2. We note that when we have a small value of α_M, we need a finer mesh to get a smooth line. For this reason, and from the fact that we want to study the lymph behavior inside the lymph node qualitatively (because we do not have precise physiological information), from now on we fix the value $\alpha_M \to \infty$, which means we use the simplified interface condition (6.150), even though a lesser value of α may give a shear stress result more similar to the one found in Section 5.2.2.

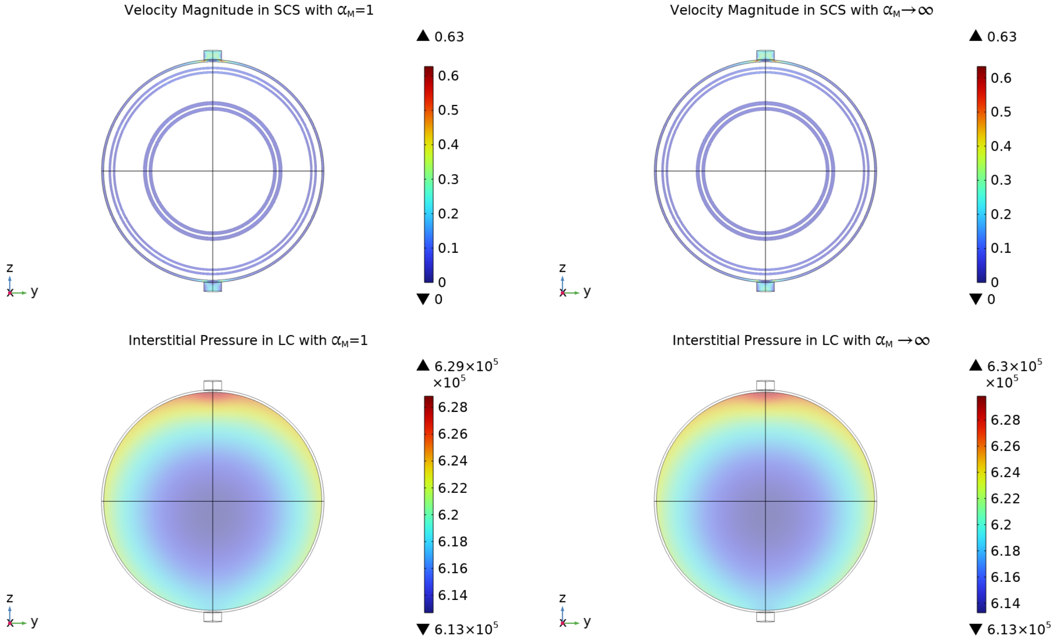

Figure 6.13: The first two plots (upper plots) represent the velocity magnitude in the SCS in $\frac{\text{mm}}{\text{s}}$ and the other two plots (lower plots) represent the pressure values in the LC in mPa, with two different value of $\alpha_M = 1$ and $\alpha_M \to \infty$. As we can see, the general value does not change much with respect to α_M. Here we used the parameters $v_{\text{in}} = 0.22\,\frac{\text{mm}}{\text{s}}$, $p_{\text{out}} = 6.18 \times 10^5$ mPa, $\pi_v - \pi_m = 1.02 \times 10^6$ mPa, $L_p = 5.475 \times 10^{-11}\,\frac{\text{mm}}{\text{s mPa}}$ and $\bar{p}_v = 1.06 \times 10^6$ mPa.

In Figure 6.15 we can see the interstitial pressure p_m values in the LC varying the parameter L_p. We have similar behavior to the one found in Section 6.6 (Figure 6.8): increasing L_p decreases the minimum of the interstitial pressure p_m (and increasing the maximum of the blood vessels pressure p_v) and moves the minimum towards the center of the node. This behavior is due to a combination of the pressure variation given by the pressure of the Stoke flow in the SCS and the fluid exchange between phases.

Given an uniform inlet velocity of $v_{\text{in}} = 0.22\,\frac{\text{mm}}{\text{s}}$, the inlet fluid flow calculated numerically is $\approx 1.083 \times 10^{-3}\,\frac{\text{mm}^3}{s}$ (with a relative error of about 1.5% from the value calculated explicitly of $1.1 \times 10^{-3}\,\frac{\text{mm}^3}{s}$). Part of the lymph goes from the SCS to the LC (and then back to the blood circulation), and the remaining part goes out from the efferent lymphatic vessels: these quantities change with the

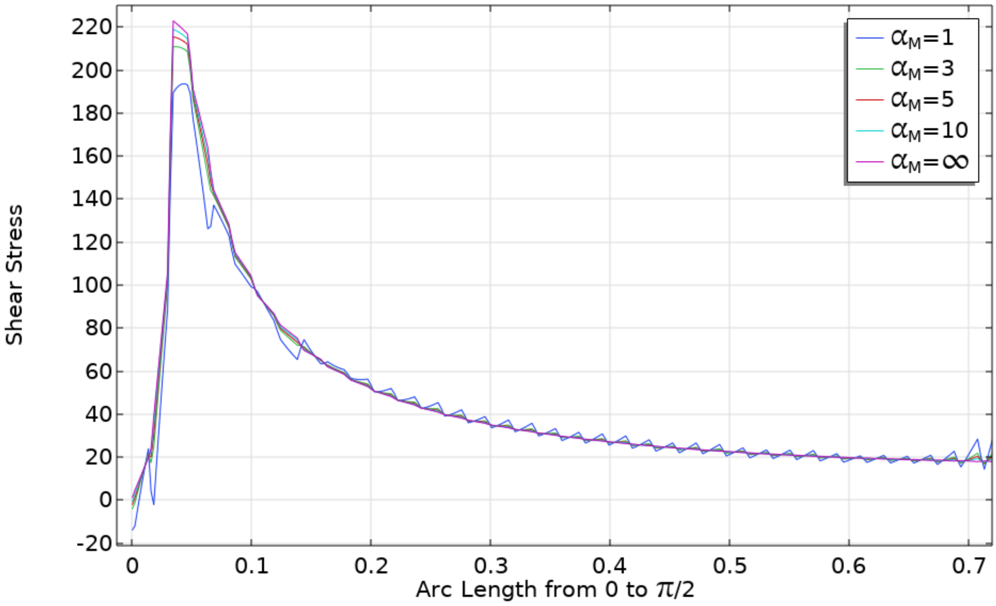

Figure 6.14: Shear Stress in mPa calculated at the interface Γ_M between the LC and the SCS with respect to the arc length calculated between the angles $\theta = 0$ (where we have the inlet condition) and $\theta = \pi/2$ (in the middle between the inlet and the outlet condition) varying α_M. Here we used the parameters $v_{\text{in}} = 0.22 \frac{\text{mm}}{\text{s}}$, $p_{\text{out}} = 6.18 \times 10^5$ mPa, $\pi_v - \pi_m = 1.02 \times 10^6$ mPa, $L_p = 5.475 \times 10^{-11} \frac{\text{mm}}{\text{s mPa}}$ and $\bar{p}_v = 1.06 \times 10^6$ mPa.

parameter L_p, and we can see some results in Table 6.3. The sum of the columns "Outlet Flow" and "SCS → LC" must result approximately in the inlet fluid flow value $\approx 1.083 \times 10^{-3} \frac{\text{mm}^3}{s}$. As expected, increasing L_p means increasing the fluid flow from the SCS to the LC, and it follows a lesser outlet fluid flow. We can see this behavior in Figure 6.16, where the velocity near the efferent lymphatic vessel decreases as L_p increases.

Varying the other parameters give results with behavior similar to what we found in Section 6.6.

The plots and the data above are obtained with $p_{\text{out}} = 6.18 \times 10^5$ mPa, that is a value inspired by the experiments of [111] (the minimum of the value range); in [5] they used a value of $p_{\text{out}} = 4 \times 10^5$ mPa and in [6, 7] they used a value of $p_{\text{out}} = 0$ mPa. Considering that the value of the pressure is important to study the fluid exchange between phases, we want to see the differences between using a different outlet pressure. Hence now we fix $p_{\text{out}} = 4 \times 10^5$ mPa. In Table 6.4 we can see the fluid flow calculated with different L_p in this case; as we can see, to have the same outlet fluid flow (and the same SCS → LC fluid flow) as in the case with $p_{\text{out}} = 6.18 \times 10^5$ mPa, we need a higher value of L_p. If we fix the same outlet fluid flow value of $\approx 9.83 \times 10^{-4} \frac{\text{mm}^3}{s}$ (that is chosen by the fact that more than 90% of the lymph remain in the SCS without entering the LC [5]), we have $L_p = 1.6 \times 10^{-11} \frac{\text{mm}}{\text{s mPa}}$ for $p_{\text{out}} = 6.18 \times 10^5$ mPa and a value of $L_p = 3 \times 10^{-11} \frac{\text{mm}}{\text{s mPa}}$ for $p_{\text{out}} = 4 \times 10^5$ mPa. As we can see in Figure 6.17, with these different values we have the same pressure behavior and range but with different pressure values.

L_p	Outlet Flow	SCS $\rightarrow$ LC
$5.475 \times 10^{-12} \frac{\text{mm}}{\text{s mPa}}$	$1.05 \times 10^{-3} \frac{\text{mm}^3}{s}$	$3.44 \times 10^{-5} \frac{\text{mm}^3}{s}$
$1 \times 10^{-11} \frac{\text{mm}}{\text{s mPa}}$	$1.02 \times 10^{-3} \frac{\text{mm}^3}{s}$	$6.28 \times 10^{-5} \frac{\text{mm}^3}{s}$
$1.6 \times 10^{-11} \frac{\text{mm}}{\text{s mPa}}$	$9.83 \times 10^{-4} \frac{\text{mm}^3}{s}$	$1 \times 10^{-4} \frac{\text{mm}^3}{s}$
$3 \times 10^{-11} \frac{\text{mm}}{\text{s mPa}}$	$8.97 \times 10^{-4} \frac{\text{mm}^3}{s}$	$1.87 \times 10^{-4} \frac{\text{mm}^3}{s}$
$5.475 \times 10^{-11} \frac{\text{mm}}{\text{s mPa}}$	$7.44 \times 10^{-4} \frac{\text{mm}^3}{s}$	$3.398 \times 10^{-4} \frac{\text{mm}^3}{s}$
$7.94 \times 10^{-11} \frac{\text{mm}}{\text{s mPa}}$	$5.94 \times 10^{-4} \frac{\text{mm}^3}{s}$	$4.9 \times 10^{-4} \frac{\text{mm}^3}{s}$

Table 6.3: Outlet fluid flow and the fluid flow passing through the external surface of the LC from the SCS in $\frac{\text{mm}^3}{s}$ varying the capillaries permeability L_p. Here we used the parameters $v_{\text{in}} = 0.22 \frac{\text{mm}}{\text{s}}$, $p_{\text{out}} = 6.18 \times 10^5$ mPa, $\pi_v - \pi_m = 1.02 \times 10^6$ mPa, and $\bar{p}_v = 1.06 \times 10^6$ mPa.

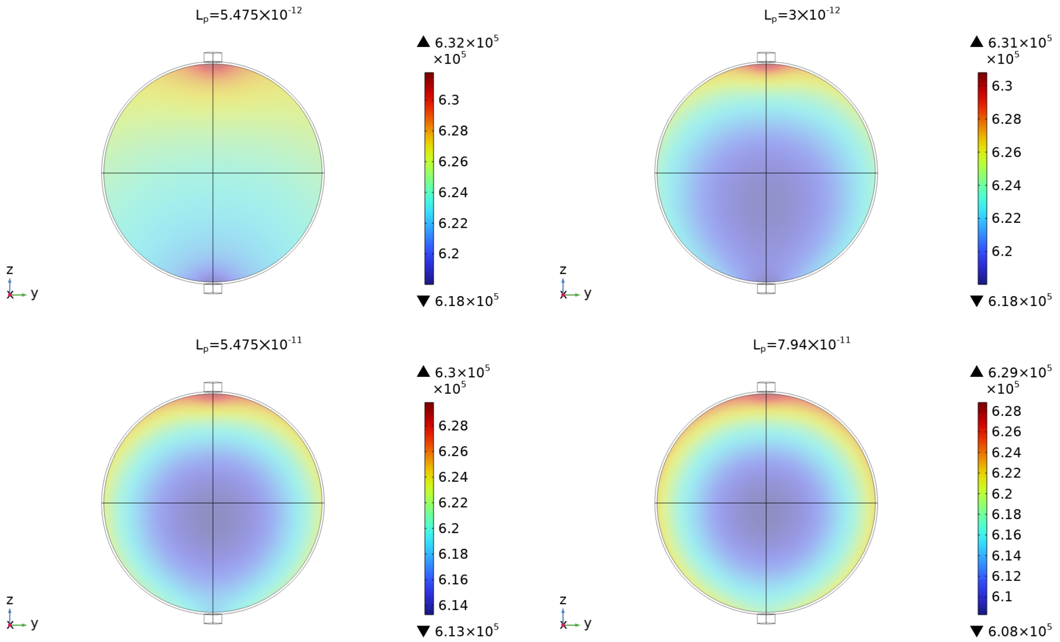

Figure 6.15: The interstitial pressure values p_m in the LC with different values of L_p. Here we used the parameters $v_{\text{in}} = 0.22 \frac{\text{mm}}{\text{s}}$, $p_{\text{out}} = 6.18 \times 10^5$ mPa, $\pi_v - \pi_m = 1.02 \times 10^6$ mPa, and $\bar{p}_v = 1.06 \times 10^6$ mPa.

L_p	Outlet Flow	SCS $\rightarrow$ LC
$5.475 \times 10^{-12} \frac{\text{mm}}{\text{s mPa}}$	$1.06 \times 10^{-3} \frac{\text{mm}^3}{s}$	$1.84 \times 10^{-5} \frac{\text{mm}^3}{s}$
$1.5 \times 10^{-11} \frac{\text{mm}}{\text{s mPa}}$	$1.03 \times 10^{-3} \frac{\text{mm}^3}{s}$	$5.05 \times 10^{-5} \frac{\text{mm}^3}{s}$
$2 \times 10^{-11} \frac{\text{mm}}{\text{s mPa}}$	$1.017 \times 10^{-3} \frac{\text{mm}^3}{s}$	$6.7 \times 10^{-5} \frac{\text{mm}^3}{s}$
$3 \times 10^{-11} \frac{\text{mm}}{\text{s mPa}}$	$9.83 \times 10^{-4} \frac{\text{mm}^3}{s}$	$1 \times 10^{-4} \frac{\text{mm}^3}{s}$

Table 6.4: Outlet fluid flow and the fluid flow passing through the external surface of the LC from the SCS in $\frac{\text{mm}^3}{s}$ varying the capillaries permeability L_p with $p_{\text{out}} = 4 \times 10^5$ mPa. The others parameters are $v_{\text{in}} = 0.22 \frac{\text{mm}}{\text{s}}$, $\pi_v - \pi_m = 1.02 \times 10^6$ mPa, and $\bar{p}_v = 1.06 \times 10^6$ mPa.

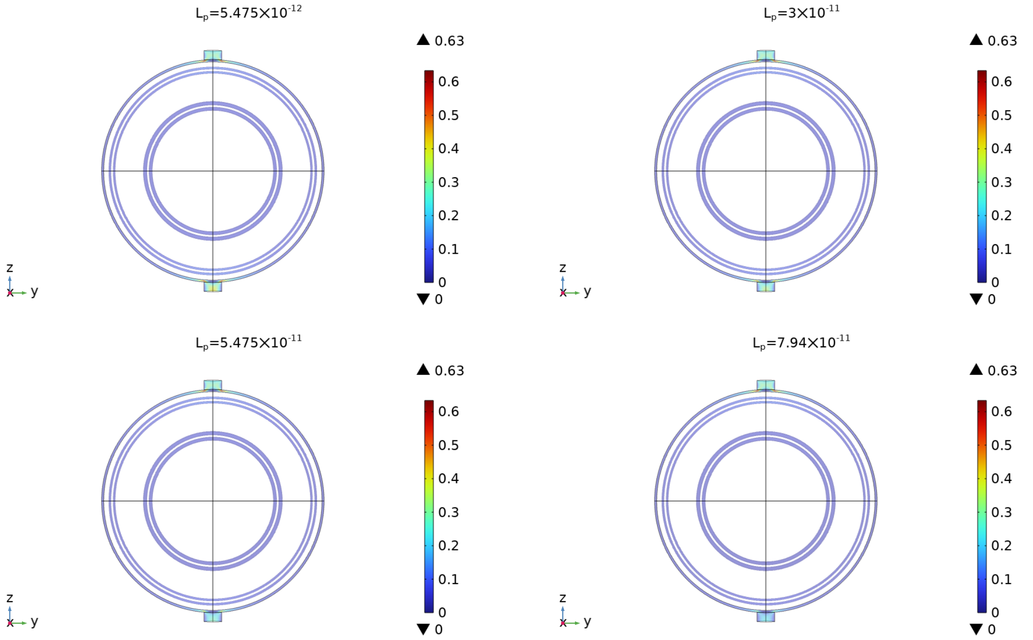

Figure 6.16: The Velocity magnitude in the SCS with different values of L_p. Here we used the parameters $v_{\text{in}} = 0.22\,\frac{\text{mm}}{\text{s}}$, $p_{\text{out}} = 6.18 \times 10^5$ mPa, $\pi_v - \pi_m = 1.02 \times 10^6$ mPa, and $\bar{p}_v = 1.06 \times 10^6$ mPa.

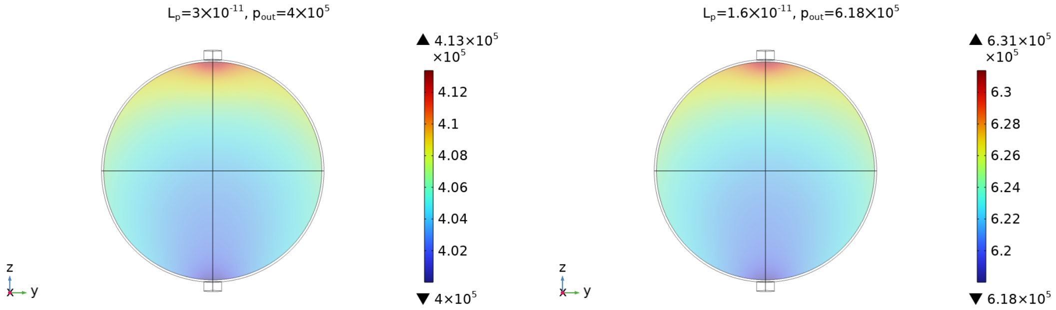

Figure 6.17: The pressure values in the LC with different values of p_{out} and L_p but with the same fluid flow values of Tables 6.3 and 6.4. Here we used the parameters $v_{\text{in}} = 0.22\,\frac{\text{mm}}{\text{s}}$, $\pi_v - \pi_m = 1.02 \times 10^6$ mPa, and $\bar{p}_v = 1.06 \times 10^6$ mPa.

6.8 Conclusions

In this chapter we proposed a macroscopic model using the asymptotic homogenization technique resulting from the starting equations (6.1)-(6.2) and the interface condition (6.4), which account for blood transcapillary exchange across the vessels walls, under the assumption of local periodicity and macroscopic uniformity in a steady setting. Our starting point was the Darcy/Darcy-Brinkman equation, so we considered the pore structure already smoothed out, and this simplified the model because we did not need precise information about the microscale geometry (this information is encoded in the hydraulic conductivity $\hat{\boldsymbol{K}}_\gamma$, $\gamma = m, v$). After that, in Section 6.4 we analyzed in detail the differences between using Darcy, Darcy-Brinkman, or Stokes as our starting point, and we found that the Darcy-Brinkman equation has a Darcy-Stokes duality behavior depending on the value of the permeability (and the relevance of the Laplace operator). Moreover, the choice of these equations allowed the separation of the cell problems into two distinct phases, one involving blood vessels and the other involving the FRC network so that we could solve the cell problems in the two domains separately. Although it is less theoretically justified than the Darcy equation, the Darcy-Brinkman equation is a valid starting point for our multiscale formulation since it has a Stokes-like structure of the differential equation, which allows us to specify in more detail the boundary condition without the need for a precise structure of the microscale, which is described by the permeability parameter (that in most cases is easier to obtain).

After this model analysis, in Section 6.5 we found the macroscopic explicit solution of the resulting equation of the proposed model (described in Section 6.3) in a spherical domain (under certainly simplified hypothesis) in terms of Bessel and Legendre polynomials. Then, in Section 6.6 we applied this explicit solution to an idealized spherical lymph node using physiological data from the literature; our multiscale formulation of the problem allowed us to study the fluid behavior and the fluid exchange in the interstitial space and the blood vessels within the node. Despite the blood vessel pressure being higher than the interstitial pressure of the node, the blood vessels have a higher concentration of protein too, and this leads to the fact that the lymph goes from the node to the blood circulation, making the lymph nodes important in the fluid regulation within the lymphatic system [39]. After that, in Section 6.7 we solved the lymphoid compartment problem coupled with the free-fluid thin layer (the subcapsular sinus).

We analyzed how the parameters affect the fluid absorption and the pressure (*i.e.* the velocity) with different boundary pressure, and the behavior of the results are in line with those found in the literature [5, 50–52, 111].

Chapter 7

Time-dependent Darcy-Brinkman Homogenization with Application to a Vascularized Lymph Node

The Darcy-Brinkman equation is a differential equation that describes the fluid flow in porous media (see Section 2.1). It is based on the Darcy's law proposed by Henry Darcy [77], and later modified by Brinkman adding a Laplacian (viscous) term (called Brinkman term) [79], weighed by an effective viscosity μ_e. Moreover, the Darcy-Brinkman equation enables us to examine the interface and boundary layer in more detail when there is an interaction between a free-fluid region and a porous region [80]. In general, the Darcy-Brinkman formulation allows for specifying boundary conditions in more detail [81], and its differential form is similar to that of the Stokes equation. Moreover, the Darcy-Brinkman equation is also valid in a time-dependent setting [76, 118, 135].

As we mentioned in Chapter 6, the Darcy-Brinkman equation is theoretically well justified from a multiscale point of view only in particular cases [32, 78, 118], but we saw that it is a valid starting point for a multiscale formulation.

In this chapter we present a preliminary multiscale model using the *asymptotic homogenization technique* (see Section 2.4) that couples two time-dependent Darcy-Brinkman equations with inhomogeneous body forces as our starting point (it can be generalized easily to the case with multiple equations).

The time dependence is taken into consideration because we aim to apply this model to a lymph node in which the inlet flow is time-dependent (see Chapter 1). To see the time-dependent term on the first order approximation of the asymptotic homogenization technique, we need to assume that

$$ShRe = \frac{\rho_0 L^2}{\mu T_0} \approx \frac{1}{\epsilon^2},$$

where Sh is the *Strouhal number*, Re is the *Reynolds number*, L is the *characteristic macroscopic length*, T_0 is the *characteristic time*, ρ_0 is the density and μ is the viscosity.

Moreover, we consider a multiscale volume load that drives the coarse scale fluid flow acting on both the Darcy-Brinkman problems [119]. The source mentioned above includes both the average force of the body and an additional component linked to the solution of a separate cell problem that is only affected by small scale changes of the specified force. These forces can occur from the use of electromagnetic fields, in magnetorheological fluids, and in electrolytes that permeate non-uniform tissues.

The main differences between the model that we propose in this chapter and the one described in Chapter 6 lie in the fact that here we consider the time-dependence of the flow and we have a coupling between two Darcy-Brinkman equations, instead of a coupling between a Darcy-Brinkman equation and a Darcy equation as in Chapter 6.

In Section 7.1 we define the starting equations of our problem. We formulate the balance equations of Continuum Mechanics and the corresponding boundary conditions. In Section 7.2 we use the asymptotic homogenization technique to find the equations that describe the motion of the fluid at the macroscale. In Section 7.3 we find the macroscopic equations by averaging the leading order terms of the asymptotic expansion. In Section 7.4 we describe the numerical scheme that we use to solve the problem presented in Section 7.3. Unlike the previous chapter, here we immediately use numerical methods as the inclusion of time makes the problem more complex. Finally, in Section 7.5 we run numerical simulations with physiological data obtained from the literature.

The results presented in this chapter are not yet complete and have to be considered preliminary. Since the research is ongoing, further analysis is needed before any definitive conclusions can be reached. We are still working on the subject.

7.1 Statement of the Problem

Let us consider a domain $\Omega = \Omega_v \cup \Omega_m$, where Ω_m and Ω_v are the portions of the domain that correspond to two different phases. The labels m and v stand for the *matrix* and the *vessel* regions, respectively. Without loss of generality and for the sake of ease of presentation, we focus on a single inclusion within the cell, but this model can be easily generalized to N inclusions.

To model the unsteady fluid flow within these phases, we use the *Darcy-Brinkman* equation [79] with inhomogeneous body forces [119] in both phases Ω_γ, with $\gamma = m, v$, which can be written as:

$$\begin{cases} \rho_0 \dfrac{\partial \boldsymbol{v}_\gamma(\boldsymbol{x},t)}{\partial t} = -\nabla p_\gamma(\boldsymbol{x},t) - \hat{\boldsymbol{K}}_\gamma^{-1}(\boldsymbol{x})\boldsymbol{v}_\gamma(\boldsymbol{x},t) & \text{in } \Omega_\gamma \times [0,T] \\ \qquad\qquad\qquad + \mu_e \Delta \boldsymbol{v}_\gamma(\boldsymbol{x},t) + \boldsymbol{f}_\gamma(\boldsymbol{x},t) & \\ \nabla \cdot \boldsymbol{v}_\gamma(\boldsymbol{x},t) = 0 & \text{in } \Omega_\gamma \times [0,T], \end{cases} \tag{7.1}$$

For $\gamma = v, m$, $\boldsymbol{v}_\gamma$ is the velocity of the fluid, p_γ the pressure, $\boldsymbol{f}_\gamma$ the inhomogeneous external force density, $\hat{\boldsymbol{K}}_\gamma(\boldsymbol{x})$ is *hydraulic conductivity tensor*, which is given by the permeability tensor divided by the viscosity μ of the fluid, μ_e is the *effective viscosity* and ρ_0 is the fluid *density.* We assume that the hydraulic conductivity tensor is symmetric and positive definite, that is, for $\gamma = v, m$

$$\hat{\boldsymbol{K}}_\gamma(\boldsymbol{x}) = \hat{\boldsymbol{K}}_\gamma^T(\boldsymbol{x}), \quad \forall \boldsymbol{a} \neq \boldsymbol{0} : \boldsymbol{a} \cdot \hat{\boldsymbol{K}}_\gamma(\boldsymbol{x}) \cdot \boldsymbol{a} > 0. \tag{7.2}$$

As our starting point we have the Darcy-Brinkman representations: the pore structure is considered already smoothed out, and the microscale geometry information is encoded in the hydraulic conductivity $\hat{\boldsymbol{K}}_\gamma(\boldsymbol{x})$.

The interface conditions are prescribed as follows:

$$\begin{cases} \boldsymbol{v}_m(\boldsymbol{x},t) \cdot \boldsymbol{n} = \boldsymbol{v}_v(\boldsymbol{x},t) \cdot \boldsymbol{n} = L_p(p_m(\boldsymbol{x},t) - p_v(\boldsymbol{x},t) - \bar{p}(t)) & \text{on } \Gamma \times [0,T] \\ \boldsymbol{v}_m(\boldsymbol{x},t) \cdot \boldsymbol{t} = \boldsymbol{v}_v(\boldsymbol{x},t) \cdot \boldsymbol{t} & \text{on } \Gamma \times [0,T], \end{cases} \tag{7.3}$$

where $\boldsymbol{n}$ is taken as the outward normal of the domain Ω_m, $\boldsymbol{t}$ is any tangential component, $\Gamma = \partial\Omega_m \cap \partial\Omega_v$ is the interface between phases, and $\bar{p}$ depends only on t. As in Chapter 6, the first equation of (7.3) is the interface condition for the normal component of the velocity; we impose this type of interface condition having in mind biological applications of this model (such as lymph nodes, tumors, etc). The quantity L_p is given by experimental measurements and depends on both the geometry and the tissue wall material of the intersection Γ. Nevertheless, our model remains valid for other choices of boundary conditions.

The initial conditions are:

$$\boldsymbol{v}_\gamma(\boldsymbol{x},0) = \boldsymbol{v}_{\gamma,0}(\boldsymbol{x}) \quad \text{in } \Omega_\gamma, \tag{7.4}$$

where the initial conditions $\boldsymbol{v}_{\gamma,0}(\boldsymbol{x})$ ($\gamma = m, v$) must be compatible with the interface conditions (7.3) and need to satisfy

$$\nabla \cdot \boldsymbol{v}_{\gamma,0}(\boldsymbol{x}) = 0. \tag{7.5}$$

Now we want to write the Darcy-Brinkman equation and the interface conditions in a non-dimensional form for the domain Ω_γ, with $\gamma = m, v$; we define the following non-dimensional quantities (denoted with a prime symbol):

$$p_\gamma = P_\gamma p'_\gamma, \quad \boldsymbol{v}_\gamma = U_\gamma \boldsymbol{v}'_\gamma, \quad \epsilon = \frac{d}{L}, \tag{7.6}$$

where P_γ is the *characteristic pressure*, U_γ is the *characteristic velocity*, d is the *fine scale length* and L is the *coarse scale length.* C_γ is a representative pressure gradient, with

$$P_\gamma = C\gamma L. \tag{7.7}$$

For the time, we consider

$$t_\gamma = T_0 t'_\gamma, \tag{7.8}$$

where T_0 is the characteristic time; moreover, we set

$$\boldsymbol{K}'_\gamma = \frac{\hat{\boldsymbol{K}}_\gamma}{K_{\text{ref},\gamma}}, \qquad \boldsymbol{f}'_\gamma = \frac{\boldsymbol{f}_\gamma}{F_\gamma}, \tag{7.9}$$

where $K_{\mathrm{ref},\gamma}$ is the representative (scalar) value for the hydraulic conductivity and F_γ is the representative force.

Substituting into (7.1), we obtain (leaving the primes):

$$\begin{cases} Sh\dfrac{\partial \boldsymbol{v}_\gamma(\boldsymbol{x},t)}{\partial t} = - Eu\nabla p_\gamma(\boldsymbol{x},t) - \boldsymbol{K}_\gamma^{-1}(\boldsymbol{x})\boldsymbol{v}_\gamma(\boldsymbol{x},t) \\ \qquad\qquad + \dfrac{1}{Re}\Delta \boldsymbol{v}_\gamma(\boldsymbol{x},t) + Fr\boldsymbol{f}_\gamma(\boldsymbol{x},t) & \text{in } \Omega_\gamma \times [0,T], \\ \nabla \cdot \boldsymbol{v}_\gamma(\boldsymbol{x},t) = 0 & \text{in } \Omega_\gamma \times [0,T], \end{cases} \tag{7.10}$$

where $Sh = \dfrac{L}{T_0 U_\gamma}$ is the *Strouhal Number*, $Eu = \dfrac{CL}{\rho_0 U_\gamma^2}$ is the *Euler Number*, $Re = \dfrac{\rho_0 U_\gamma L}{\hat{\mu}}$ is the *Reynolds Number*, $Fr = \dfrac{U_\gamma^2}{F_\gamma L}$ is the *Froude Number*, and we set the new non-dimensional number

$$Nk = \frac{L}{\rho_0 U_\gamma K_{\mathrm{ref},\gamma}}. \tag{7.11}$$

We assume that [33]

$$ShRe \approx EuRe \approx NkRe \approx \frac{1}{\epsilon^2}, \tag{7.12}$$

which means

$$\frac{\rho_0 L^2}{\mu T_0} \approx \frac{1}{\epsilon^2}, \quad \frac{CL^2}{\mu U_\gamma} \approx \frac{1}{\epsilon^2}, \quad \frac{L^2}{\mu K_{\mathrm{ref},\gamma}} \approx \frac{1}{\epsilon^2}. \tag{7.13}$$

Now we want to non-dimensionalize the interface conditions (7.3): by the Starling equation, the flux J_v passing through the blood vessel wall is given by

$$J_v = L_p \bar{S}\left(p_m(\boldsymbol{x},t) - p_v(\boldsymbol{x},t) - \bar{p}(t)\right), \tag{7.14}$$

where $\bar{S}$ is the total exchange surface density. From the fact that d is related to the distance between the vessels of the domain Ω_v, we have

$$S \propto \frac{L}{d} = \frac{1}{\epsilon}, \tag{7.15}$$

hence we need to rescale the interface condition by ϵ to have a finite flux (see Chapter 6 and [126] for more details).

Substituting into (7.10), we obtain

$$\begin{cases} \dfrac{\partial \boldsymbol{v}_\gamma(\boldsymbol{x},t)}{\partial t} = - \nabla p_\gamma(\boldsymbol{x},t) - \hat{\boldsymbol{K}}_\gamma^{-1}(\boldsymbol{x})\boldsymbol{v}_\gamma(\boldsymbol{x},t) \\ \qquad\qquad + \epsilon^2\mu^*\Delta \boldsymbol{v}_\gamma(\boldsymbol{x},t) + \boldsymbol{f}_\gamma(\boldsymbol{x},t) & \text{in } \Omega_\gamma \times [0,T], \\ \nabla \cdot \boldsymbol{v}_\gamma(\boldsymbol{x}) = 0 & \text{in } \Omega_\gamma \times [0,T], \end{cases} \tag{7.16}$$

with $\mu^* = \frac{\mu_e}{\mu}$, and the interface conditions (7.3):

$$\begin{cases} \boldsymbol{v}_v(\boldsymbol{x},t)\cdot\boldsymbol{n} = \boldsymbol{v}_v(\boldsymbol{x},t)\cdot\boldsymbol{n} = \epsilon L_p(p_m(\boldsymbol{x},t) - p_v(\boldsymbol{x},t) - p(t)) & \text{on } \Gamma \times [0,T] \\ \boldsymbol{v}_m(\boldsymbol{x},t)\cdot\boldsymbol{t} = \boldsymbol{v}_m(\boldsymbol{x},t)\cdot\boldsymbol{t} & \text{on } \Gamma \times [0,T]. \end{cases} \tag{7.17}$$

7.2 Asymptotic Homogenization

In this section we employ the asymptotic homogenization technique (Section 2.4) [32, 70, 90] to derive a continuum macroscale model for the system of equations (7.17), (7.26), (7.4). Since $\epsilon \ll 1$, we enforce the sharp length scale separation between d (fine scale) and L (coarse scale) and we decouple spatial scales by introducing a new local variable

$$\boldsymbol{y} = \frac{\boldsymbol{x}}{\epsilon}, \tag{7.18}$$

where $\boldsymbol{x}$ and $\boldsymbol{y}$ represent the coarse and fine scale spatial coordinates, respectively (see Chapter 2.4). They have to be formally considered independent variables. From now on, p_γ, $\boldsymbol{v}_\gamma$, $\boldsymbol{K}_\gamma$ and $\boldsymbol{f}_\gamma$ (where $\gamma = m, v$) are assumed to depend on both $\boldsymbol{x}$ and $\boldsymbol{y}$.

Before we start with the asymptotic homogenization technique, we recall some assumptions concerning the geometry of the multiscale problem:

- *Local periodicity*: we assume that p_γ, $\boldsymbol{v}_\gamma$, $\boldsymbol{K}_\gamma$ and $\boldsymbol{f}_\gamma$ are $\boldsymbol{y}$-periodic. This assumption allows us to study fine scale variations of the fields on a restricted portion of the domain. In particular, we have that Ω is the periodic cell domain, and Ω_m and Ω_v are the portions of the domain Ω related to the two different phases.

- *Macroscopic uniformity*: we neglect geometric variations of the cell and inclusions with respect to the coarse scale variable $\boldsymbol{x}$. Thanks to this assumption, we can consider only one periodic cell Ω_γ for every macroscale point $\boldsymbol{x}$, and we have that

$$\nabla_{\boldsymbol{x}} \cdot \int_{\Omega_\gamma} (\cdot) d\boldsymbol{y} = \int_{\Omega_\gamma} \nabla_{\boldsymbol{x}} \cdot (\cdot) d\boldsymbol{y}. \tag{7.19}$$

The differential operator transforms accordingly

$$\nabla \to \nabla_{\boldsymbol{x}} + \frac{1}{\epsilon} \nabla_{\boldsymbol{y}}; \tag{7.20}$$

now we employ a power series expansion with respect to ϵ as follows (with $\gamma = m, v$):

$$\boldsymbol{v}_\gamma(\boldsymbol{x}, \boldsymbol{y}, t) \equiv \boldsymbol{v}^\epsilon_\gamma(\boldsymbol{x}, \boldsymbol{y}, t) = \sum_{l=0}^{\infty} \boldsymbol{v}^{(l)}_\gamma(\boldsymbol{x}, \boldsymbol{y}, t)\epsilon^l, \tag{7.21}$$

$$p_\gamma(\boldsymbol{x}, \boldsymbol{y}, t) \equiv p^\epsilon_\gamma(\boldsymbol{x}, \boldsymbol{y}, t) = \sum_{l=0}^{\infty} p^{(l)}_\gamma(\boldsymbol{x}, \boldsymbol{y}, t)\epsilon^l, \tag{7.22}$$

$$\boldsymbol{f}_\gamma(\boldsymbol{x}, \boldsymbol{y}, t) \equiv \boldsymbol{f}^\epsilon_\gamma(\boldsymbol{x}, \boldsymbol{y}, t) = \sum_{l=0}^{\infty} \boldsymbol{f}^{(l)}_\gamma(\boldsymbol{x}, \boldsymbol{y}, t)\epsilon^l, \tag{7.23}$$

$$\boldsymbol{v}_{\gamma,0}(\boldsymbol{x}, \boldsymbol{y}, t) \equiv \boldsymbol{v}^\epsilon_{\gamma,0}(\boldsymbol{x}, \boldsymbol{y}, t) = \sum_{l=0}^{\infty} \boldsymbol{v}^{(l)}_{\gamma,0}(\boldsymbol{x}, \boldsymbol{y}, t)\epsilon^l, \tag{7.24}$$

Substituting the expansions (7.21), (7.22), (7.23), (7.24) and the differential operator (7.20) into the non-dimensionalized Darcy-Brinkman equations (7.16), we have:

$$\begin{cases} \epsilon \dfrac{\partial \boldsymbol{v}_\gamma^\epsilon(\boldsymbol{x},\boldsymbol{y},t)}{\partial t} = & - \epsilon \nabla_{\boldsymbol{x}} p_\gamma^\epsilon(\boldsymbol{x},\boldsymbol{y},t) - \nabla_{\boldsymbol{y}} p_\gamma^\epsilon(\boldsymbol{x},\boldsymbol{y},t) \\ & - \epsilon \boldsymbol{K}_\gamma^{-1}(\boldsymbol{x},\boldsymbol{y}) \boldsymbol{v}_\gamma^\epsilon(\boldsymbol{x},\boldsymbol{y},t) + \mu^* \epsilon^3 \Delta_{\boldsymbol{x}} \boldsymbol{v}_\gamma^\epsilon(\boldsymbol{x},\boldsymbol{y},t) \qquad \text{in } \Omega_\gamma \times [0,T] \\ & + \mu^* \epsilon \Delta_{\boldsymbol{y}} \boldsymbol{v}_\gamma^\epsilon(\boldsymbol{x},\boldsymbol{y},t) + \mu^* \epsilon^2 \nabla_{\boldsymbol{x}} \cdot (\nabla_{\boldsymbol{y}} \boldsymbol{v}_\gamma^\epsilon(\boldsymbol{x},\boldsymbol{y},t)) \\ & + \mu^* \epsilon^2 \nabla_{\boldsymbol{y}} \cdot (\nabla_{\boldsymbol{x}} \boldsymbol{v}_\gamma^\epsilon(\boldsymbol{x},\boldsymbol{y},t)) + \epsilon \boldsymbol{f}_\gamma^\epsilon(\boldsymbol{x},\boldsymbol{y},t) \\ \epsilon \nabla_{\boldsymbol{x}} \cdot \boldsymbol{v}_\gamma^\epsilon(\boldsymbol{x},\boldsymbol{y},t) + \nabla_{\boldsymbol{y}} \cdot \boldsymbol{v}_\gamma^\epsilon(\boldsymbol{x},\boldsymbol{y},t) = 0 & \qquad \text{in } \Omega_\gamma \times [0,T], \end{cases} \tag{7.25}$$

and if we substitute them into the interface conditions (7.17) and the initial conditions (7.4), we obtain

$$\begin{cases} \boldsymbol{v}_v^\epsilon(\boldsymbol{x},\boldsymbol{y},t) \cdot \boldsymbol{n} = \boldsymbol{v}_m^\epsilon(\boldsymbol{x},\boldsymbol{y},t) \cdot \boldsymbol{n} & \\ \qquad = \epsilon L_p (p_m^\epsilon(\boldsymbol{x},\boldsymbol{y},t) - p_v^\epsilon(\boldsymbol{x},\boldsymbol{y},t) - \bar{p}(t)) & \text{on } \Gamma \times [0,T] \\ \boldsymbol{v}_m^\epsilon(\boldsymbol{x},\boldsymbol{y},t) \cdot \boldsymbol{t} = \boldsymbol{v}_v^\epsilon(\boldsymbol{x},\boldsymbol{y},t) \cdot \boldsymbol{t} & \text{on } \Gamma \times [0,T]; \end{cases} \tag{7.26}$$

$$\boldsymbol{v}_\gamma^\epsilon(\boldsymbol{x},\boldsymbol{y},0) = \boldsymbol{v}_{\gamma,0}^\epsilon(\boldsymbol{x},\boldsymbol{y}) \quad \text{in } \Omega_\gamma. \tag{7.27}$$

If we collect the terms of order ϵ^0 from system (7.25), we obtain:

$$\nabla_{\boldsymbol{y}} p_\gamma^{(0)}(\boldsymbol{x},\boldsymbol{y},t) = \mathbf{0} \implies p_\gamma^0 = p_\gamma^{(0)}(\boldsymbol{x},t) \quad \text{in} \quad \Omega_\gamma \times [0,T], \tag{7.28}$$

$$\nabla_{\boldsymbol{y}} \cdot \boldsymbol{v}_\gamma^{(0)}(\boldsymbol{x},\boldsymbol{y},t) = 0 \quad \text{in} \quad \Omega_\gamma \times [0,T]. \tag{7.29}$$

If we collect the terms of order ϵ^0 in the interface conditions (7.26), we obtain

$$\boldsymbol{v}_m^{(0)}(\boldsymbol{x},\boldsymbol{y},t) \cdot \boldsymbol{n} = \boldsymbol{v}_v^{(0)}(\boldsymbol{x},\boldsymbol{y},t) \cdot \boldsymbol{n} = \mathbf{0} \quad \text{on} \quad \Gamma \times [0,T], \tag{7.30}$$

$$\boldsymbol{v}_m^{(0)}(\boldsymbol{x},\boldsymbol{y},t) \cdot \boldsymbol{t} = \boldsymbol{v}_v^{(0)}(\boldsymbol{x},\boldsymbol{y},t) \cdot \boldsymbol{t} \quad \text{on} \quad \Gamma \times [0,T], \tag{7.31}$$

and for the initial condition (7.27) we have

$$\boldsymbol{v}_\gamma^{(0)}(\boldsymbol{x},\boldsymbol{y},0) = \boldsymbol{v}_{\gamma,0}^{(0)}(\boldsymbol{x},\boldsymbol{y}) \quad \text{in } \Omega_\gamma. \tag{7.32}$$

For the terms of order ϵ^1 from equations (7.25), (7.26), and (7.27):

$$\begin{aligned} \frac{\partial \boldsymbol{v}_\gamma^{(0)}(\boldsymbol{x},\boldsymbol{y},t)}{\partial t} = & - \nabla_{\boldsymbol{x}} p_\gamma^{(0)}(\boldsymbol{x},t) - \nabla_{\boldsymbol{y}} p_\gamma^{(1)}(\boldsymbol{x},\boldsymbol{y},t) - \boldsymbol{K}_\gamma^{-1}(\boldsymbol{x},\boldsymbol{y}) \boldsymbol{v}_\gamma^{(0)}(\boldsymbol{x},\boldsymbol{y},t) \\ & + \mu^* \Delta_{\boldsymbol{y}} \boldsymbol{v}_\gamma^{(0)}(\boldsymbol{x},\boldsymbol{y},t) + \boldsymbol{f}_\gamma^{(0)}(\boldsymbol{x},\boldsymbol{y},t) \quad \text{on } \Omega_\gamma \times [0,T], \end{aligned} \tag{7.33}$$

$$\nabla_{\boldsymbol{x}} \cdot \boldsymbol{v}_\gamma^{(0)}(\boldsymbol{x},\boldsymbol{y},t) + \nabla_{\boldsymbol{y}} \cdot \boldsymbol{v}_\gamma^{(1)}(\boldsymbol{x},\boldsymbol{y},t) = 0 \quad \text{on } \Omega_\gamma \times [0,T], \tag{7.34}$$

$$\boldsymbol{v}_m^{(1)}(\boldsymbol{x},\boldsymbol{y},t) \cdot \boldsymbol{n} = \boldsymbol{v}_v^{(1)}(\boldsymbol{x},\boldsymbol{y},t) \cdot \boldsymbol{n} = L_p \left(p_m^{(0)}(\boldsymbol{x},t) - p_v^{(0)}(\boldsymbol{x},t) - \bar{p}(t) \right) \quad \text{on } \Gamma \times [0,T], \tag{7.35}$$

$$\boldsymbol{v}_m^{(1)}(\boldsymbol{x},\boldsymbol{y},t) \cdot \boldsymbol{t} = \boldsymbol{v}_v^{(1)}(\boldsymbol{x},\boldsymbol{y},t) \cdot \boldsymbol{t} \quad \text{on } \Gamma \times [0,T], \tag{7.36}$$

$$\boldsymbol{v}_\gamma^{(1)}(\boldsymbol{x},\boldsymbol{y},0)=\boldsymbol{v}_{\gamma,0}^{(1)}(\boldsymbol{x},\boldsymbol{y}) \quad \text{in } \Omega_\gamma. \tag{7.37}$$

Putting together (7.33), (7.29), (7.30), (7.31) and (7.32) in Ω_m, we obtain the following *auxiliary Darcy-Brinkman problem in* $(\boldsymbol{v}^{(0)}, p^{(1)})$:

$$\begin{cases}
\begin{aligned}\dfrac{\partial \boldsymbol{v}_\gamma^{(0)}(\boldsymbol{x},\boldsymbol{y},t)}{\partial t} =& -\nabla_{\boldsymbol{x}} p_\gamma^{(0)}(\boldsymbol{x},t)-\nabla_{\boldsymbol{y}} p_\gamma^{(1)}(\boldsymbol{x},\boldsymbol{y},t)\\ &-\boldsymbol{K}_\gamma^{-1}(\boldsymbol{x},\boldsymbol{y})\boldsymbol{v}_\gamma^{(0)}(\boldsymbol{x},\boldsymbol{y},t)+\mu^*\Delta_{\boldsymbol{y}}\boldsymbol{v}_\gamma^{(0)}(\boldsymbol{x},\boldsymbol{y},t)\\ &+\boldsymbol{f}_\gamma^{(0)}(\boldsymbol{x},\boldsymbol{y},t)\end{aligned} & \text{in } \Omega_\gamma\times[0,T],\\
\nabla_{\boldsymbol{y}}\cdot \boldsymbol{v}_\gamma^{(0)}(\boldsymbol{x},\boldsymbol{y},t)=0 & \text{in } \Omega_\gamma\times[0,T],\\
\boldsymbol{v}_m^{(0)}(\boldsymbol{x},\boldsymbol{y},t)\cdot\boldsymbol{n}=\boldsymbol{v}_v^{(0)}(\boldsymbol{x},\boldsymbol{y},t)\cdot\boldsymbol{n}=\boldsymbol{0} & \text{on } \Gamma\times[0,T],\\
\boldsymbol{v}_m^{(0)}(\boldsymbol{x},\boldsymbol{y},t)\cdot\boldsymbol{t}=\boldsymbol{v}_v^{(0)}(\boldsymbol{x},\boldsymbol{y},t)\cdot\boldsymbol{t} & \text{on } \Gamma\times[0,T],\\
\boldsymbol{v}_\gamma^{(0)}(\boldsymbol{x},\boldsymbol{y},0)=\boldsymbol{v}_{\gamma,0}^{(0)}(\boldsymbol{x},\boldsymbol{y}) & \text{in } \Omega_\gamma.
\end{cases} \tag{7.38}$$

We apply the Fourier transformation defined by

$$\mathcal{F}[\phi(t)]=\hat{\phi}(\omega)=\frac{1}{\sqrt{2\pi}}\int_{-\infty}^{\infty}\phi(t)e^{-it\omega}dt,$$

to the equations of the system (7.38), and we obtain

$$\begin{aligned} i\omega\hat{\boldsymbol{v}}_\gamma^{(0)}(\boldsymbol{x},\boldsymbol{y},\omega) =& -\nabla_{\boldsymbol{x}}\hat{p}_\gamma^{(0)}(\boldsymbol{x},\omega)-\nabla_{\boldsymbol{y}}\hat{p}_\gamma^{(1)}(\boldsymbol{x},\boldsymbol{y},\omega)-\boldsymbol{K}_\gamma^{-1}(\boldsymbol{x},\boldsymbol{y})\hat{\boldsymbol{v}}_\gamma^{(0)}(\boldsymbol{x},\boldsymbol{y},\omega)\\ &+\mu^*\Delta_{\boldsymbol{y}}\hat{\boldsymbol{v}}_\gamma^{(0)}(\boldsymbol{x},\boldsymbol{y},\omega)+\hat{\boldsymbol{f}}_\gamma^{(0)}(\boldsymbol{x},\boldsymbol{y},\omega) \quad \text{in } \Omega_\gamma\times[0,T], \end{aligned} \tag{7.39}$$

$$\nabla_{\boldsymbol{y}}\cdot\hat{\boldsymbol{v}}_\gamma^{(0)}(\boldsymbol{x},\boldsymbol{y},\omega)=0 \quad \text{in } \Omega_\gamma\times[0,T], \tag{7.40}$$

$$\hat{\boldsymbol{v}}_m^{(0)}(\boldsymbol{x},\boldsymbol{y},\omega)\cdot\boldsymbol{n}=\hat{\boldsymbol{v}}_v^{(0)}(\boldsymbol{x},\boldsymbol{y},\omega)\cdot\boldsymbol{n}=0 \quad \text{on } \Gamma\times[0,T] \tag{7.41}$$

$$\hat{\boldsymbol{v}}_m^{(0)}(\boldsymbol{x},\boldsymbol{y},\omega)\cdot\boldsymbol{t}=\hat{\boldsymbol{v}}_v^{(0)}(\boldsymbol{x},\boldsymbol{y},\omega)\cdot\boldsymbol{t} \quad \text{on } \Gamma\times[0,T]. \tag{7.42}$$

Since the problem is linear and the vector function $\nabla_{\boldsymbol{x}}p^{(0)}$ depends on the macroscale only, we formulate the following ansatz for the solutions:

$$\hat{p}_\gamma^{(1)}(\boldsymbol{x},\boldsymbol{y},\omega)=-\hat{\boldsymbol{g}}_\gamma(\boldsymbol{x},\boldsymbol{y},\omega)\cdot\nabla_{\boldsymbol{x}}\hat{p}_\gamma^{(0)}(\boldsymbol{x},\omega)+\hat{\tilde{g}}_\gamma(\boldsymbol{x},\boldsymbol{y},\omega), \tag{7.43}$$

$$\hat{\boldsymbol{v}}_\gamma^{(0)}(\boldsymbol{x},\boldsymbol{y},\omega)=-\hat{\boldsymbol{W}}_\gamma(\boldsymbol{x},\boldsymbol{y},\omega)\nabla_{\boldsymbol{x}}\hat{p}_\gamma^{(0)}(\boldsymbol{x},\omega)+\hat{\tilde{\boldsymbol{w}}}_\gamma(\boldsymbol{x},\boldsymbol{y},\omega). \tag{7.44}$$

We have that (7.43) and (7.44) are the unique solutions of the auxiliary Darcy-Brinkman problem (7.38) provided that the auxiliary vectors $\hat{\boldsymbol{g}}_\gamma, \hat{\tilde{g}}_\gamma, \hat{\boldsymbol{W}}_\gamma, \hat{\tilde{\boldsymbol{w}}}_\gamma$ solve the following cell problems:

$$\begin{cases}
\begin{aligned}-i\omega\hat{\boldsymbol{W}}_\gamma(\boldsymbol{x},\boldsymbol{y},\omega) =& -\boldsymbol{I}+\Big(\nabla_{\boldsymbol{y}}\hat{\boldsymbol{g}}_\gamma(\boldsymbol{x},\boldsymbol{y},\omega)\Big)^T\\ &+\boldsymbol{K}_\gamma^{-1}(\boldsymbol{x},\boldsymbol{y})\hat{\boldsymbol{W}}_\gamma(\boldsymbol{x},\boldsymbol{y},\omega)\\ &-\mu^*\Delta_{\boldsymbol{y}}\hat{\boldsymbol{W}}_\gamma(\boldsymbol{x},\boldsymbol{y},\omega)\end{aligned} & \text{in } \Omega_\gamma\times[0,T],\\
\nabla_{\boldsymbol{y}}\cdot\hat{\boldsymbol{W}}_\gamma(\boldsymbol{x},\boldsymbol{y},\omega)=0 & \text{in } \Omega_\gamma\times[0,T],\\
\hat{\boldsymbol{W}}_\gamma(\boldsymbol{x},\boldsymbol{y},\omega)\cdot\boldsymbol{n}=\boldsymbol{0} & \text{on } \Gamma\times[0,T]\\
\hat{\boldsymbol{W}}_m(\boldsymbol{x},\boldsymbol{y},\omega)\cdot\boldsymbol{t}=\hat{\boldsymbol{W}}_v(\boldsymbol{x},\boldsymbol{y},\omega)\cdot\boldsymbol{t} & \text{on } \Gamma\times[0,T],\\
\boldsymbol{W}_\gamma(\boldsymbol{x},\boldsymbol{y},0)=\boldsymbol{0} & \text{in } \Omega_\gamma,
\end{cases} \tag{7.45}$$

$$\begin{cases} i\omega\hat{\tilde{\boldsymbol{w}}}_\gamma(\boldsymbol{x},\boldsymbol{y},\omega) = -\boldsymbol{K}_\gamma^{-1}(\boldsymbol{x},\boldsymbol{y})\hat{\tilde{\boldsymbol{w}}}_\gamma(\boldsymbol{x},\boldsymbol{y},\omega) + \mu^*\Delta_{\boldsymbol{y}}\hat{\tilde{\boldsymbol{w}}}_\gamma(\boldsymbol{x},\boldsymbol{y}) \\ \qquad\qquad - \nabla_{\boldsymbol{y}}\hat{\tilde{g}}_\gamma(\boldsymbol{x},\boldsymbol{y},\omega) + \hat{\boldsymbol{f}}^0_\gamma(\boldsymbol{x},\boldsymbol{y},\omega) & \text{in } \Omega_\gamma\times[0,T], \\ \nabla_{\boldsymbol{y}}\cdot\hat{\tilde{\boldsymbol{w}}}_\gamma(\boldsymbol{x},\boldsymbol{y},\omega) = 0 & \text{in } \Omega_\gamma\times[0,T], \\ \hat{\tilde{\boldsymbol{w}}}_\gamma(\boldsymbol{x},\boldsymbol{y},\omega)\cdot\boldsymbol{n} = 0 & \text{on } \Gamma\times[0,T], \\ \hat{\tilde{\boldsymbol{w}}}_m(\boldsymbol{x},\boldsymbol{y},\omega)\cdot\boldsymbol{t} = \hat{\tilde{\boldsymbol{w}}}_v(\boldsymbol{x},\boldsymbol{y},\omega)\cdot\boldsymbol{t} & \text{on } \Gamma\times[0,T], \\ \tilde{\boldsymbol{w}}_\gamma(\boldsymbol{x},\boldsymbol{y},0) = \boldsymbol{v}^{(0)}_{\gamma,0}(\boldsymbol{x},\boldsymbol{y}) & \text{in } \Omega_\gamma, \end{cases} \tag{7.46}$$

If we apply the inverse Fourier transform $\mathscr{F}^{-1}$ to (7.45) and (7.46), we obtain

$$\begin{cases} \dfrac{\partial \boldsymbol{W}_\gamma(\boldsymbol{x},\boldsymbol{y},t)}{\partial t} = -\boldsymbol{K}_\gamma^{-1}(\boldsymbol{x},\boldsymbol{y})\boldsymbol{W}_m(\boldsymbol{x},\boldsymbol{y},t) + \mu^*\Delta_{\boldsymbol{y}}\boldsymbol{W}_\gamma(\boldsymbol{x},\boldsymbol{y},t) \\ \qquad\qquad + \delta(t)\boldsymbol{I} - \nabla_{\boldsymbol{y}}\boldsymbol{g}_\gamma^T(\boldsymbol{x},\boldsymbol{y},t) & \text{in } \Omega_\gamma\times[0,T], \\ \nabla_{\boldsymbol{y}}\cdot\boldsymbol{W}_\gamma(\boldsymbol{x},\boldsymbol{y},t) = 0 & \text{in } \Omega_\gamma\times[0,T], \\ \boldsymbol{W}_\gamma(\boldsymbol{x},\boldsymbol{y},t)\cdot\boldsymbol{n} = 0 & \text{on } \Gamma\times[0,T], \\ \boldsymbol{W}_m(\boldsymbol{x},\boldsymbol{y},t)\cdot\boldsymbol{t} = \boldsymbol{W}_v(\boldsymbol{x},\boldsymbol{y},t)\cdot\boldsymbol{t} & \text{on } \Gamma\times[0,T], \\ \boldsymbol{W}_\gamma(\boldsymbol{x},\boldsymbol{y},0) = \boldsymbol{0} & \text{in } \Omega_\gamma, \end{cases} \tag{7.47}$$

$$\begin{cases} \dfrac{\partial \tilde{\boldsymbol{w}}_\gamma(\boldsymbol{x},\boldsymbol{y},t)}{\partial t} = -\boldsymbol{K}_\gamma^{-1}(\boldsymbol{x},\boldsymbol{y})\tilde{\boldsymbol{w}}_\gamma(\boldsymbol{x},\boldsymbol{y},t) + \mu^*\Delta_{\boldsymbol{y}}\tilde{\boldsymbol{w}}_\gamma(\boldsymbol{x},\boldsymbol{y},t) \\ \qquad\qquad - \nabla_{\boldsymbol{y}}\tilde{g}_\gamma(\boldsymbol{x},\boldsymbol{y},t) + \boldsymbol{f}^0_\gamma(\boldsymbol{x},\boldsymbol{y},t) & \text{in } \Omega_\gamma\times[0,T], \\ \nabla_{\boldsymbol{y}}\cdot\tilde{\boldsymbol{w}}_\gamma(\boldsymbol{x},\boldsymbol{y},t) = 0 & \text{in } \Omega_\gamma\times[0,T], \\ \tilde{\boldsymbol{w}}_\gamma(\boldsymbol{x},\boldsymbol{y},t)\cdot\boldsymbol{n} = 0 & \text{on } \Gamma\times[0,T], \\ \tilde{\boldsymbol{w}}_m(\boldsymbol{x},\boldsymbol{y},t)\cdot\boldsymbol{t} = \tilde{\boldsymbol{w}}_v(\boldsymbol{x},\boldsymbol{y},t)\cdot\boldsymbol{t} & \text{on } \Gamma\times[0,T], \\ \tilde{\boldsymbol{w}}_\gamma(\boldsymbol{x},\boldsymbol{y},0) = \boldsymbol{v}^{(0)}_{\gamma,0}(\boldsymbol{x},\boldsymbol{y}) & \text{in } \Omega_\gamma, \end{cases} \tag{7.48}$$

where $\delta(t)$ is the *Dirac delta*. For system (7.48), we can search a solution in the form $\tilde{\boldsymbol{w}}_\gamma(\boldsymbol{x},\boldsymbol{y},t) = \tilde{\boldsymbol{w}}_{\gamma,1}(\boldsymbol{x},\boldsymbol{y},t) + \tilde{\boldsymbol{w}}_{\gamma,2}(\boldsymbol{x},\boldsymbol{y},t)$ and $\tilde{g}_\gamma(\boldsymbol{x},\boldsymbol{y},t) = \tilde{g}_{\gamma,1}(\boldsymbol{x},\boldsymbol{y},t) + \tilde{g}_{\gamma,2}(\boldsymbol{x},\boldsymbol{y},t)$, where $\tilde{\boldsymbol{w}}_{\gamma,1}(\boldsymbol{x},\boldsymbol{y},t)$ and $\tilde{g}_{\gamma,1}(\boldsymbol{x},\boldsymbol{y},t)$ are just the evolution (without any forcing term) of the initial condition $\boldsymbol{v}^{(0)}_{\gamma,0}(\boldsymbol{x},\boldsymbol{y})$. Hence we can split (7.48) in two systems:

$$\begin{cases} \dfrac{\partial \tilde{\boldsymbol{w}}_{\gamma,1}(\boldsymbol{x},\boldsymbol{y},t)}{\partial t} = -\boldsymbol{K}_\gamma^{-1}(\boldsymbol{x},\boldsymbol{y})\tilde{\boldsymbol{w}}_{\gamma,1}(\boldsymbol{x},\boldsymbol{y},t) + \mu^*\Delta_{\boldsymbol{y}}\tilde{\boldsymbol{w}}_{\gamma,1}(\boldsymbol{x},\boldsymbol{y},t) \\ \qquad\qquad - \nabla_{\boldsymbol{y}}\tilde{g}_{\gamma,1}(\boldsymbol{x},\boldsymbol{y},t) & \text{in } \Omega_\gamma\times[0,T], \\ \nabla_{\boldsymbol{y}}\cdot\tilde{\boldsymbol{w}}_{\gamma,1}(\boldsymbol{x},\boldsymbol{y},t) = 0 & \text{in } \Omega_\gamma\times[0,T], \\ \tilde{\boldsymbol{w}}_{\gamma,1}(\boldsymbol{x},\boldsymbol{y},t)\cdot\boldsymbol{n} = 0 & \text{on } \Gamma\times[0,T], \\ \tilde{\boldsymbol{w}}_{m,1}(\boldsymbol{x},\boldsymbol{y},t)\cdot\boldsymbol{t} = \tilde{\boldsymbol{w}}_{v,1}(\boldsymbol{x},\boldsymbol{y},t)\cdot\boldsymbol{t} & \text{on } \Gamma\times[0,T], \\ \tilde{\boldsymbol{w}}_{\gamma,1}(\boldsymbol{x},\boldsymbol{y},0) = \boldsymbol{v}^{(0)}_{\gamma,0}(\boldsymbol{x},\boldsymbol{y}) & \text{in } \Omega_\gamma, \end{cases} \tag{7.49}$$

$$
\begin{cases}
\dfrac{\partial \tilde{\boldsymbol{w}}_{\gamma,2}(\boldsymbol{x},\boldsymbol{y},t)}{\partial t} = -\boldsymbol{K}_{\gamma}^{-1}(\boldsymbol{x},\boldsymbol{y})\tilde{\boldsymbol{w}}_{\gamma,2}(\boldsymbol{x},\boldsymbol{y},t) + \mu^{*}\Delta_{\boldsymbol{y}}\tilde{\boldsymbol{w}}_{\gamma,2}(\boldsymbol{x},\boldsymbol{y},t) & \\
\qquad\qquad - \nabla_{\boldsymbol{y}}\tilde{g}_{\gamma,2}(\boldsymbol{x},\boldsymbol{y},t) + \boldsymbol{f}_{\gamma}^{0}(\boldsymbol{x},\boldsymbol{y},t) & \text{in } \Omega_{\gamma}\times[0,T], \\
\nabla_{\boldsymbol{y}}\cdot\tilde{\boldsymbol{w}}_{\gamma,2}(\boldsymbol{x},\boldsymbol{y},t) = 0 & \text{in } \Omega_{\gamma}\times[0,T], \\
\tilde{\boldsymbol{w}}_{\gamma,2}(\boldsymbol{x},\boldsymbol{y},t)\cdot\boldsymbol{n} = 0 & \text{on } \Gamma\times[0,T], \\
\tilde{\boldsymbol{w}}_{m,2}(\boldsymbol{x},\boldsymbol{y},t)\cdot\boldsymbol{t} = \tilde{\boldsymbol{w}}_{m,2}(\boldsymbol{x},\boldsymbol{y},t)\cdot\boldsymbol{t} & \text{on } \Gamma\times[0,T], \\
\tilde{\boldsymbol{w}}_{\gamma,2}(\boldsymbol{x},\boldsymbol{y},0) = \boldsymbol{0} & \text{in } \Omega_{\gamma},
\end{cases}
\tag{7.50}
$$

where (7.49) describes the evolution of the initial condition (and gives null result if the initial condition is zero), and (7.50) describes the action of the multiscale force $\boldsymbol{f}_{\gamma}$ (and gives null result if $\boldsymbol{f}_{\gamma}$ is zero).

For system (7.47), we define the quantities

$$
\bar{\boldsymbol{g}}_{\gamma}(\boldsymbol{x},\boldsymbol{y},t) = \int_{0}^{t}\boldsymbol{g}_{\gamma}(\boldsymbol{x},\boldsymbol{y},s)ds, \tag{7.51}
$$

$$
\bar{\boldsymbol{W}}_{\gamma}(\boldsymbol{x},\boldsymbol{y},t) = \int_{0}^{t}\boldsymbol{W}_{\gamma}(\boldsymbol{x},\boldsymbol{y},s)ds, \tag{7.52}
$$

so that

$$
\boldsymbol{g}_{\gamma}(\boldsymbol{x},\boldsymbol{y},t) = \frac{\partial\bar{\boldsymbol{g}}_{\gamma}(\boldsymbol{x},\boldsymbol{y},t)}{\partial t}, \tag{7.53}
$$

$$
\boldsymbol{W}_{\gamma}(\boldsymbol{x},\boldsymbol{y},t) = \frac{\partial\bar{\boldsymbol{W}}_{\gamma}(\boldsymbol{x},\boldsymbol{y},t)}{\partial t}; \tag{7.54}
$$

substituting these equations into (7.47) and integrating over time, we have

$$
\begin{cases}
\dfrac{\partial\bar{\boldsymbol{W}}_{\gamma}(\boldsymbol{x},\boldsymbol{y},t)}{\partial t} = -\boldsymbol{K}_{\gamma}^{-1}(\boldsymbol{x},\boldsymbol{y})\bar{\boldsymbol{W}}_{\gamma}(\boldsymbol{x},\boldsymbol{y},t) & \\
\qquad\qquad + \mu^{*}\Delta_{\boldsymbol{y}}\bar{\boldsymbol{W}}_{\gamma}(\boldsymbol{x},\boldsymbol{y},t) + \boldsymbol{I} - \nabla_{\boldsymbol{y}}\bar{\boldsymbol{g}}_{\gamma}^{T}(\boldsymbol{x},\boldsymbol{y},t) & \text{in } \Omega_{\gamma}\times[0,T], \\
\nabla_{\boldsymbol{y}}\cdot\bar{\boldsymbol{W}}_{\gamma}(\boldsymbol{x},\boldsymbol{y},t) = 0 & \text{in } \Omega_{\gamma}\times[0,T], \\
\bar{\boldsymbol{W}}_{\gamma}(\boldsymbol{x},\boldsymbol{y},t)\cdot\boldsymbol{n} = 0 & \text{on } \Gamma\times[0,T], \\
\bar{\boldsymbol{W}}_{m}(\boldsymbol{x},\boldsymbol{y},t)\cdot\boldsymbol{t} = \bar{\boldsymbol{W}}_{v}(\boldsymbol{x},\boldsymbol{y},t)\cdot\boldsymbol{t} & \text{on } \Gamma\times[0,T], \\
\bar{\boldsymbol{W}}_{\gamma}(\boldsymbol{x},\boldsymbol{y},0) = \boldsymbol{0} & \text{in } \Omega_{\gamma}.
\end{cases}
\tag{7.55}
$$

Applying the inverse Fourier transform $\mathcal{F}^{-1}$ to the ansatz (7.43)–(7.44), we obtain

$$
\begin{aligned}
\boldsymbol{v}_{\gamma}^{(0)}(\boldsymbol{x},\boldsymbol{y},t) &= -\mathcal{F}^{-1}[\hat{\boldsymbol{W}}_{\gamma}(\boldsymbol{x},\boldsymbol{y},\omega)\nabla_{\boldsymbol{x}}\hat{p}_{\gamma}^{(0)}(\boldsymbol{x},\omega)] + \tilde{\boldsymbol{w}}_{\gamma,1}(\boldsymbol{x},\boldsymbol{y},t) + \tilde{\boldsymbol{w}}_{\gamma,2}(\boldsymbol{x},\boldsymbol{y},t) \\
&= -\mathcal{F}^{-1}[\mathcal{F}[\boldsymbol{W}_{\gamma}(\boldsymbol{x},\boldsymbol{y},t) * \nabla_{\boldsymbol{x}}p_{\gamma}^{(0)}(\boldsymbol{x},t)]] + \tilde{\boldsymbol{w}}_{\gamma,1}(\boldsymbol{x},\boldsymbol{y},t) + \tilde{\boldsymbol{w}}_{\gamma,2}(\boldsymbol{x},\boldsymbol{y},t) \\
&= -\int_{-\infty}^{\infty}\boldsymbol{W}_{\gamma}(\boldsymbol{x},\boldsymbol{y},t-s)\nabla_{\boldsymbol{x}}p_{\gamma}^{(0)}(\boldsymbol{x},s)ds + \tilde{\boldsymbol{w}}_{\gamma,1}(\boldsymbol{x},\boldsymbol{y},t) + \tilde{\boldsymbol{w}}_{\gamma,2}(\boldsymbol{x},\boldsymbol{y},t) \\
&= -\int_{0}^{t}\boldsymbol{W}_{\gamma}(\boldsymbol{x},\boldsymbol{y},t-s)\nabla_{\boldsymbol{x}}p_{\gamma}^{(0)}(\boldsymbol{x},s)ds + \tilde{\boldsymbol{w}}_{\gamma,1}(\boldsymbol{x},\boldsymbol{y},t) + \tilde{\boldsymbol{w}}_{\gamma,2}(\boldsymbol{x},\boldsymbol{y},t) \\
&= -\int_{0}^{t}\frac{\partial\bar{\boldsymbol{W}}_{\gamma}(\boldsymbol{x},\boldsymbol{y},t-s)}{\partial t}(\boldsymbol{x},\boldsymbol{y},t-s)\nabla_{\boldsymbol{x}}p_{\gamma}^{(0)}(\boldsymbol{x},s)ds \\
&\quad + \tilde{\boldsymbol{w}}_{\gamma,1}(\boldsymbol{x},\boldsymbol{y},t) + \tilde{\boldsymbol{w}}_{\gamma,2}(\boldsymbol{x},\boldsymbol{y},t),
\end{aligned}
\tag{7.56}
$$

where $*$ denotes the convolution with respect to time. This is *Darcy's law with memory* and is in the same form presented in [32, 33, 136].

By the same computations, we obtain

$$p_\gamma^{(1)}(\boldsymbol{x},\boldsymbol{y},t) = -\int_0^t \frac{\bar{\boldsymbol{g}}_\gamma^T(\boldsymbol{x},\boldsymbol{y},t-s)}{\partial t}\nabla_{\boldsymbol{x}} p_\gamma^{(0)}(\boldsymbol{x},s)ds + \tilde{g}_{\gamma,1}(\boldsymbol{x},\boldsymbol{y},t) + \tilde{g}_{\gamma,2}(\boldsymbol{x},\boldsymbol{y},t). \tag{7.57}$$

Moreover, we need that $\langle \bar{\boldsymbol{g}}_\gamma(\boldsymbol{x},\boldsymbol{y},t)\rangle_{\Omega_\gamma} = 0$, $\langle \tilde{g}_{\gamma,1}(\boldsymbol{x},\boldsymbol{y},t)\rangle_{\Omega_\gamma} = 0$ and $\langle \tilde{g}_{\gamma,2}(\boldsymbol{x},\boldsymbol{y},t)\rangle_{\Omega_\gamma} = 0$ to ensure the uniqueness of the solution, where $\langle(.)\rangle_{\Omega_\gamma}$ is the average operator

$$\langle(.)\rangle_{\Omega_\gamma} = \frac{1}{|\Omega_\gamma|}\int_{\Omega_\gamma}(\cdot)d\boldsymbol{y}. \tag{7.58}$$

7.3 Macroscopic Model

We now apply the average operator $\langle(\cdot)\rangle_{\Omega_\gamma}$ to the ansatz (7.43) and we obtain:

$$\begin{aligned}\langle \boldsymbol{v}_\gamma^{(0)}(\boldsymbol{x},\boldsymbol{y},t)\rangle_{\Omega_\gamma} = &-\int_0^t \langle \frac{\partial \bar{\boldsymbol{W}}_\gamma(\boldsymbol{x},\boldsymbol{y},t-s)}{\partial t}(\boldsymbol{x},\boldsymbol{y},t-s)\rangle_{\Omega_\gamma}\nabla_{\boldsymbol{x}} p_\gamma^{(0)}(\boldsymbol{x},s)ds \\ &+ \langle \tilde{\boldsymbol{w}}_{\gamma,1}(\boldsymbol{x},\boldsymbol{y},t)\rangle_{\Omega_\gamma} + \langle \tilde{\boldsymbol{w}}_{\gamma,2}(\boldsymbol{x},\boldsymbol{y},t)\rangle_{\Omega_\gamma},\end{aligned} \tag{7.59}$$

where $\bar{\boldsymbol{W}}_\gamma$,$\tilde{\boldsymbol{w}}_{\gamma,1}$ and $\tilde{\boldsymbol{w}}_{\gamma,2}$ are computed by problems (7.55), (7.49) and (7.50), respectively.

Applying the average operator (7.58) to the equation (7.34), we obtain (using the macroscopic uniformity):

$$\nabla_{\boldsymbol{x}} \cdot \langle \boldsymbol{v}_\gamma^{(0)}(\boldsymbol{x},\boldsymbol{y},t)\rangle_{\Omega_\gamma} + \langle \nabla_{\boldsymbol{y}} \cdot \boldsymbol{v}_\gamma^{(1)}(\boldsymbol{x},\boldsymbol{y},t)\rangle_{\Omega_\gamma} = 0, \tag{7.60}$$

where, using the divergence theorem and the interface conditions (7.35), we have, for the phase $\gamma = m$

$$\begin{aligned}\langle \nabla_{\boldsymbol{y}} \cdot \boldsymbol{v}_m^{(1)}(\boldsymbol{x},\boldsymbol{y},t)\rangle_{\Omega_m} &= \frac{1}{|\Omega_m|}\int_{\Omega_m} \nabla_{\boldsymbol{y}} \cdot \boldsymbol{v}_m^{(1)}(\boldsymbol{x},\boldsymbol{y},t)d\boldsymbol{y} \\ &= \frac{1}{|\Omega_m|}\int_\Gamma \boldsymbol{v}_m^{(1)}(\boldsymbol{x},\boldsymbol{y},t)\cdot \boldsymbol{n}_m dS \\ &= \frac{1}{|\Omega_v|}\int_\Gamma \boldsymbol{v}_v^{(1)}(\boldsymbol{x},\boldsymbol{y},t)\cdot \boldsymbol{n} dS \\ &= \frac{L_p S}{|\Omega_m|}\left[p_m^{(0)}(\boldsymbol{x},t) - p_v^{(0)}(\boldsymbol{x},t) - \bar{p}(t)\right],\end{aligned} \tag{7.61}$$

hence

$$\nabla_{\boldsymbol{x}} \cdot \langle \boldsymbol{v}_m^{(0)}(\boldsymbol{x},\boldsymbol{y},t)\rangle_{\Omega_m} = -\frac{L_p S}{|\Omega_m|}\left[p_m^{(0)}(\boldsymbol{x},t) - p_v^{(0)}(\boldsymbol{x},t) - \bar{p}(t)\right]. \tag{7.62}$$

For the phase $\gamma = v$, we have:

$$\nabla_{\boldsymbol{x}} \cdot \langle \boldsymbol{v}_v^{(0)}(\boldsymbol{x},\boldsymbol{y},t)\rangle_{\Omega_v} + \langle \nabla_{\boldsymbol{y}} \cdot \boldsymbol{v}_v^{(1)}(\boldsymbol{x},\boldsymbol{y},t)\rangle_{\Omega_v} = 0, \tag{7.63}$$

and using the divergence theorem and the interface conditions (7.35):

$$\begin{aligned}
\langle \nabla_{\boldsymbol{y}} \cdot \boldsymbol{v}_v^{(1)}(\boldsymbol{x},\boldsymbol{y},t)\rangle_{\Omega_v} &= \frac{1}{|\Omega_v|}\int_{\Omega_v} \nabla_{\boldsymbol{y}} \cdot \boldsymbol{v}_v^{(1)}(\boldsymbol{x},\boldsymbol{y},t)d\boldsymbol{y} \\
&= \frac{1}{|\Omega_v|}\int_{\Gamma} \boldsymbol{v}_v^{(1)}(\boldsymbol{x},\boldsymbol{y},t)\cdot \boldsymbol{n}_v dS \\
&= -\frac{1}{|\Omega_v|}\int_{\Gamma} \boldsymbol{v}_v^{(1)}(\boldsymbol{x},\boldsymbol{y},t)\cdot \boldsymbol{n} dS \\
&= -\frac{L_pS}{|\Omega_v|}\left[p_m^{(0)}(\boldsymbol{x},t) - p_v^{(0)}(\boldsymbol{x},t) - \bar{p}(t)\right], \qquad (7.64)
\end{aligned}$$

where we used the fact that $\boldsymbol{n}_v = -\boldsymbol{n}$; hence

$$\nabla_{\boldsymbol{x}} \cdot \langle \boldsymbol{v}_v^0(\boldsymbol{x},\boldsymbol{y},t)\rangle_{\Omega_v} = \frac{L_pS}{|\Omega_v|}\left[p_m^{(0)}(\boldsymbol{x},t) - p_v^{(0)}(\boldsymbol{x},t) - \bar{p}(t)\right]. \qquad (7.65)$$

Remark 6. *We notice that the fluid is macroscopically incompressible, indeed the sum of the two divergences is zero. The two phases can have non-zero divergence due to the fluid exchange between them.*

7.4 Numerical Simulations

In this section we solve numerically the problems given by (7.59) (for $\gamma = m, v$), (7.62), and (7.65). Unlike the previous chapter, we immediately use numerical methods in this chapter as the inclusion of time makes the problem more complex. We focus on phase $\gamma = m$, but the computations for phase $\gamma = v$ are very similar.

For simplicity, we suppose $\boldsymbol{v}_{m,0} = \boldsymbol{0}$ and $\boldsymbol{f}_m = \boldsymbol{0}$ (and the same for the phase v, that means $\boldsymbol{v}_{v,0} = \boldsymbol{0}$ and $\boldsymbol{f}_v = \boldsymbol{0}$). We denote

$$\boldsymbol{A}_m(\boldsymbol{x},t) = \langle \frac{\partial \boldsymbol{W}_m(\boldsymbol{x},\boldsymbol{y},t)}{\partial t}\rangle_{\Omega_m}, \qquad (7.66)$$

where $\boldsymbol{A}_m$ is symmetric, positive definite, and decays exponentially with time [32]. Moreover, we assume that the porous medium is isotropic, which means that $\boldsymbol{A}_m = A_m\boldsymbol{I}$ depends only on t ($A_m(t)$, and the same for $A_v(t)$).

Putting together (7.59) and (7.62), we obtain

$$\int_0^t A_m(t-s)\Delta p_m^{(0)}(\boldsymbol{x},s)ds = \bar{L}_p\left[p^{(0)}(\boldsymbol{x},t)_m - p_v^{(0)}(\boldsymbol{x},t) - \bar{p}(t)\right], \qquad (7.67)$$

where

$$\bar{L}_p = \frac{L_pS}{|\Omega_m|}. \qquad (7.68)$$

The problem here is the presence of a convolutional integral in (7.59). First of all, we want to treat that term.

We discretize the time $t \in [0,T]$ with a uniform time step Δt such that

$$0 = t_0 < t_1 < ... < t_{j-1} < t_j < ... < t_N = T,$$

with

$$t_j - t_{j-1} = \Delta t, \quad \text{for } j = 1, ..., N.$$

For the first time step $t = t_1$ we have, using the trapezoidal rule:

$$\begin{aligned}\int_0^{t_1} A_m(t_1 - s)\Delta p_m^{(0)}(\boldsymbol{x}, s)ds &= \frac{t_1}{2}\left(A_m(t_1)\Delta p_m^{(0)}(\boldsymbol{x}, 0) + A_m(0)\Delta p_m^{(0)}(\boldsymbol{x}, t_1)\right) \\ &= \frac{\Delta t}{2}\left(A_m(t_1)\Delta p_m^{(0)}(\boldsymbol{x}, 0) + A_m(0)\Delta p_m^{(0)}(\boldsymbol{x}, t_1)\right).\end{aligned} \tag{7.69}$$

For the second time step $t = t_2$ we have:

$$\begin{aligned}\int_0^{t_2} A_m(t_2 - s)\Delta p_m^{(0)}(\boldsymbol{x}, s)ds =& \int_0^{t_1} A_m(t_2 - s)\Delta p_m^{(0)}(\boldsymbol{x}, s)ds \\ &+ \int_{t_1}^{t_2} A_m(t_2 - s)\Delta p_m^{(0)}(\boldsymbol{x}, s)ds \\ =&\frac{\Delta t}{2}A_m(t_2)\Delta p_m^{(0)}(\boldsymbol{x}, 0) + \Delta t A_m(t_2 - t_1)\Delta p_m^{(0)}(\boldsymbol{x}, t_1) \\ &+ \frac{\Delta t}{2}A_m(0)\Delta p_m^{(0)}(\boldsymbol{x}, t_2).\end{aligned} \tag{7.70}$$

For the third time step $t = t_3$ we have:

$$\begin{aligned}\int_0^{t_3} A_m(t_3 - s)\Delta p_m^{(0)}(\boldsymbol{x}, s)ds =& \int_0^{t_1} A_m(t_3 - s)\Delta p_m^{(0)}(\boldsymbol{x}, s)ds \\ &+ \int_{t_1}^{t_2} A_m(t_3 - s)\Delta p_m^{(0)}(\boldsymbol{x}, s)ds \\ &+ \int_{t_2}^{t_3} A_m(t_3 - s)\Delta p_m^{(0)}(\boldsymbol{x}, s)ds \\ =&\frac{\Delta t}{2}A_m(t_3)\Delta p_m^{(0)}(\boldsymbol{x}, 0) + \Delta t A_m(t_3 - t_1)\Delta p_m^{(0)}(\boldsymbol{x}, t_1) \\ &+ \Delta t A_m(t_3 - t_2)\Delta p_m^{(0)}(\boldsymbol{x}, t_2) + \frac{\Delta t}{2}A_m(0)\Delta p_m^{(0)}(\boldsymbol{x}, t_3).\end{aligned} \tag{7.71}$$

Hence, for a generic $t = t_k \in [0, T]$, we have

$$\begin{aligned}\frac{\Delta t}{2}A_m(0)\Delta p_m^{(0)}(\boldsymbol{x}, t_k) - \bar{L}_p p_m^{(0)}(\boldsymbol{x}, t_k) =& - \bar{L}_p\left(p_v^{(0)}(\boldsymbol{x}, t_k) + \bar{p}(t_k)\right) \\ &+ \frac{\Delta t}{2}A_m(t_k)\Delta p_m^{(0)}(\boldsymbol{x}, 0) \\ &+ \Delta t\sum_{j=1}^{k-1} A_m(t_k - t_j)\Delta p_m^{(0)}(\boldsymbol{x}, t_j).\end{aligned} \tag{7.72}$$

For the phase v we have (by similar computations, for a generic $t = t_k \in [0, T]$):

$$\begin{aligned}\frac{\Delta t}{2} A_v(0) \Delta p_v^{(0)}(\boldsymbol{x}, t_k) - \bar{L}_p p_v^{(0)}(\boldsymbol{x}, t_k) =& \bar{L}_p \left(-p_m^{(0)}(\boldsymbol{x}, t_k) + \bar{p}(t_k) \right) \\ &+ \frac{\Delta t}{2} A_v(t_k) \Delta p_v^{(0)}(\boldsymbol{x}, 0) \\ &+ \Delta t \sum_{j=1}^{k-1} A_v(t_k - t_j) \Delta p_v^{(0)}(\boldsymbol{x}, t_j). \end{aligned} \tag{7.73}$$

Remark 7. *From the fact that A_m and A_v decay exponentially with time, we can truncate the sum in equations (7.72) and (7.73) at a certain $N_{trunc} < k-1$, making the computational cost more feasible with a small error.*

For the spatial discretization, we use the classical finite element method for a diffusion problem [132–134].

7.5 Application to the Lymph Node

In this section, we use the numerical method presented in the previous section to model the fluid flow in a lymph node, using physiological data obtained or inspired by a mouse popliteal lymph node [10]. The lymph node is basically formed by two parts: a porous bulk region called lymphoid compartment (LC) and a thin layer near the wall where the fluid can flow freely, called subcapsular sinus (SCS) [37, 108]. Since the whole blood vasculature in the lymph node is in the LC [5, 53, 54], in this section we solve numerically the macroscopic model we found in the previous sections in the LC, using Comsol Multiphysics.

Here we have that Ω_v is the *blood vessels phase*, and Ω_m is the *interstitial phase.* The fluid exchange between these two phases is described by the *Starling equation*, which corresponds to choose $\bar{p} = \sigma\left(\pi_m - \pi_v\right)$, where π_m is the *oncotic pressure of the phase m*, and π_v is the *oncotic pressure of the phase v.* We can see the cell domain in Figure 7.1. We have that the cell problems (7.55) in the two domains Ω_m and Ω_v are coupled, unlike the cell problems presented in the previous chapter; this is because we have to impose the continuity of the tangential component of the velocity between the two phases.

We use the same parameters as in Section 6.6; we recall these parameters in Table 7.1.

We plot $A_v(t)$ and $A_m(t)$ in Figure 7.2, and we note that they decrease quickly with respect to time. The permeabilities obtained by the cell problem, in this case, are higher than the ones found for the cell problems in Chapter 6; hence in these simulations we expect a lesser fluid exchange between phases. We fix as boundary pressure for the phase Ω_m

$$\bar{p}_m = \left(4 \times 10^5\right) 0.5(1 - \cos(\pi t)) + 2.7 \times 10^5, \tag{7.74}$$

and we fix a constant blood vessels boundary pressure $\bar{p}_v$. In Figure 7.3 we can see the result of our numerical simulation at time $t = 1\,\mathrm{s}$, with the parameters

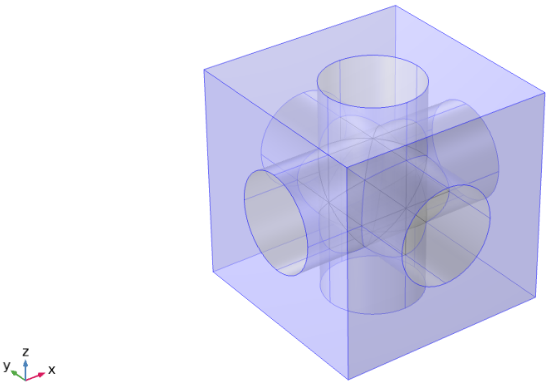

Figure 7.1: The cell problem domain. The grey region (internal part) is the blood vessels domain Ω_v, the blue region (external part) is the matrix domain Ω_m.

Name	Physiological Range/Value	Description
R	$0.49\,\mathrm{mm}$	Macroscopic radius [10, 12].
μ	$1\,\frac{\mathrm{mg}}{\mathrm{mm\ s}}$	Viscosity [1, 17].
ϕ	0.75	Porosity [11].
μ_e	$\frac{\mu}{\phi}$	Effective viscosity [79, 106, 109].
ρ_0	$1\,\frac{\mathrm{mg}}{\mathrm{mm}^3}$	Density [1, 17].
$\hat{K}_m$	$3.84 \times 10^{-9}\,\mathrm{mm}^2$	Permeability of the interstitium [11, 101].
σ	$0.88 - 0.9$	Staverman's coefficient [5–8].
$\pi_v - \pi_m$	$3.41 \times 10^5 - 2.08 \times 10^6\,\mathrm{mPa}$	Oncotic pressure difference [5–8, 51, 52].
L_p	$5.475 \times 10^{-12} - 3.67 \times 10^{-8}\,\frac{\mathrm{mm}}{\mathrm{s\ mPa}}$	Hydraulic conductivity of the blood vessel walls[5–8].
$\bar{p}_v$	$6.67 \times 10^5 - 1.066 \times 10^6\,\mathrm{mPa}$	Mean blood vessel pressure [5–8].
S	$13.4\,\mathrm{mm}^2$	Blood vessel surface [53].
$\lvert\Omega_v\rvert$	$0.0322\,\mathrm{mm}^3$	Blood vessel volume [53].
N	6500	Number of cells.
r_c	$5.495 \times 10^{-3}\,\mathrm{mm}$	Blood vessel radius.
d	$2.4 \times 10^{-2}\,\mathrm{mm}$	Blood vessel mean distance.
K_v	$1.03 \times 10^{-6}\,\mathrm{mm}^2$	Blood vessels permeability.
c_0	5.6	Kozeny constant [128].
$\boldsymbol{f}_m$, $\boldsymbol{f}_v$	0	Body forces.

Table 7.1: Physiological and estimated parameters. For a complete review of these parameters, see Section 6.6.

$L_p = 10^{-9}\,\frac{\text{mm}}{\text{s mPa}}$, $\pi_v - \pi_m = 1.02 \times 10^6$ mPa, and $\bar{p}_v = 1.06 \times 10^6$ mPa. As we can see, we have a lesser fluid exchange between the phases respect to the steady case (Figure 6.4), but remains the fact that, for a lymph node, the fluid inside the lymphoid compartment goes from the interstitial space Ω_m to the blood vessels phase Ω_v.

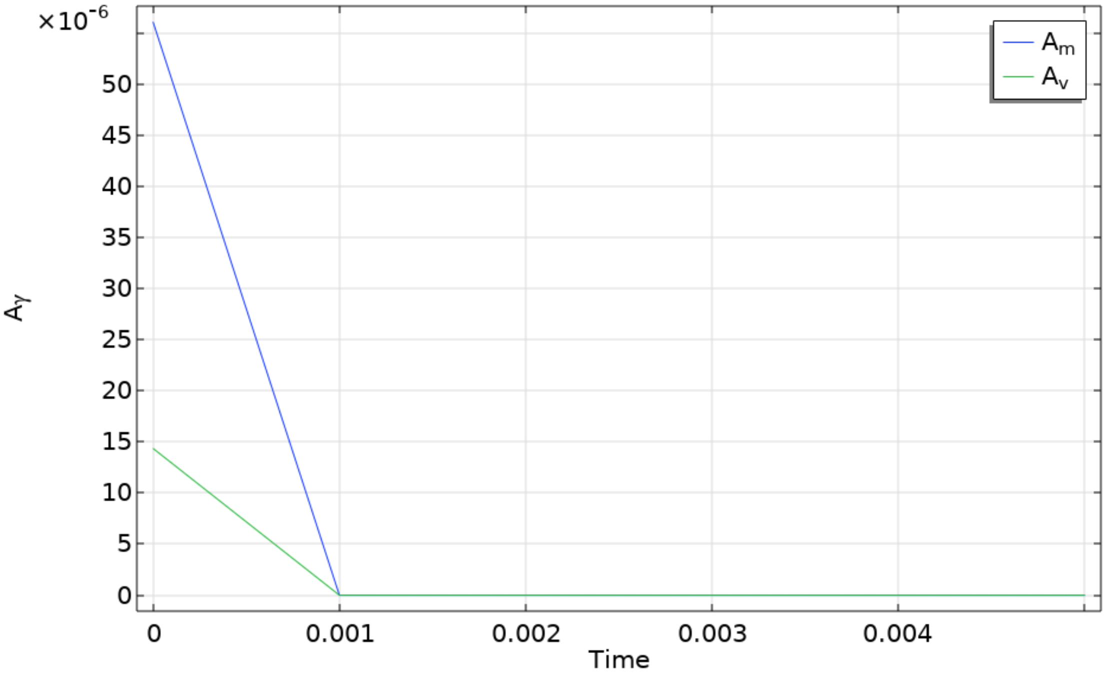

Figure 7.2: The permeability A_γ plotted with respect to time in $\frac{\text{mm}^3\text{s}}{\text{mg}}$.

If we vary the boundary pressure $\bar{p}_v$, we have different behavior for the inversion of the fluid exchange direction between phases. In Figure 7.4 we can see the interstitial pressure p_m varying $\bar{p}_v$; as we can see, for the value $\bar{p}_v \approx 1.4 \times 10^6$ mPa, we have an inversion of the flow for the first ≈ 0.5 s, after that time the behavior is the classical one found in Figure 7.3. Instead, with a higher boundary pressure of $\bar{p}_v \approx 1.6 \times 10^6$ mPa, we have a flow inversion for every time. For the value $\bar{p}_v \approx 1.5676 \times 10^6$ that is the same value found for the flow inversion in Section 6.6 (with $\bar{p}_m = 6.7 \times 10^5$ mPa), we have the flow inversion only for the first ≈ 0.9 s; hence we need a higher $\bar{p}_v$ to have flow inversion, in this case, respect to the steady case. The variation of the values in this Figure is minimal because we are plotting the results with pressure values very close to have the flow inversion.

Now we want to define a boundary pressure $\bar{p}_m$ that varies with respect to time and space to mimic the pressure behavior with a pulsatile inlet condition (inspired by the results found in Section 5). We define the following boundary pressure

$$\bar{p}_m = 0.5(1 - \cos(\pi t)) f(z, y, z) \times 10^4 + 6.6 \times 10^5, \tag{7.75}$$

where

$$f(x, y, z) = \frac{(z/R)}{\sqrt{x^2 + y^2 + (z/R)^2}} \tag{7.76}$$

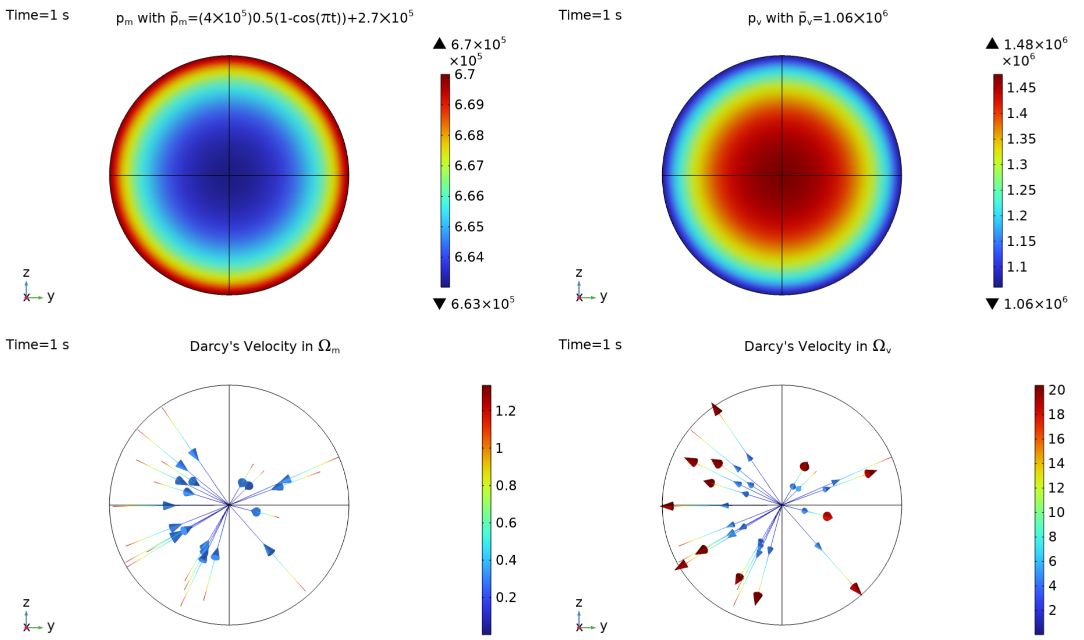

p_m with $\bar{p}_m$=(4×10^5)0.5(1-cos(πt))+2.7×10^5

p_v with $\bar{p}_v$=1.06×10^6

Darcy's Velocity in Ω_m

Darcy's Velocity in Ω_v

Figure 7.3: In the upper plots, the interstitial pressure p_m and the blood vessels pressure p_v in mPa; in the lower plots, the Darcy's velocity in Ω_m and in Ω_v in $\frac{\text{mm}}{\text{s}}$. We use the boundary conditions (7.74) and the parameters $L_p = 10^{-9}\,\frac{\text{mm}}{\text{s mPa}}$, $\pi_v - \pi_m = 1.02 \times 10^6$ mPa, and $\bar{p}_v = 1.06 \times 10^6$ mPa. The time is fixed as $t = 1$ s.

is a function defined on the boundary of a sphere with radius R and gives 1 in the upper pole, 0 in the other pole, and decreases smoothly between these two values. We run numerical simulations with the fixed parameters $L_p = 10^{-9}\,\frac{\text{mm}}{\text{s mPa}}$, $\pi_v - \pi_m = 1.02 \times 10^6$ mPa, and $\bar{p}_v = 1.06 \times 10^6$ mPa. We can see the results in Figure 7.5. As we can see, as time increases, the interstitial pressure's minimum moves from the node's center towards the lower pole (where $f(x, y, z)$ has the minimum value). We have this result due to the combination between the effects of the boundary pressure and the fluid exchange in the center of the node. Instead, when we are in a fluid inversion situation, we have the opposite behavior, and we can see this in Figure 7.6, where we used the same parameters as before but with $\bar{p}_v = 2 \times 10^6$ mPa.

In Figure 7.7 we can see the behavior of the interstitial pressure p_m varying L_p with the boundary condition (7.75), with the parameters $\pi_v - \pi_m = 1.02 \times 10^6$ mPa and $\bar{p}_v = 1.06 \times 10^6$ mPa, at $t = 1$ s. When L_p is small, we have that the effect of the boundary condition is the prevailing one, but as L_p increases, the two effects add up.

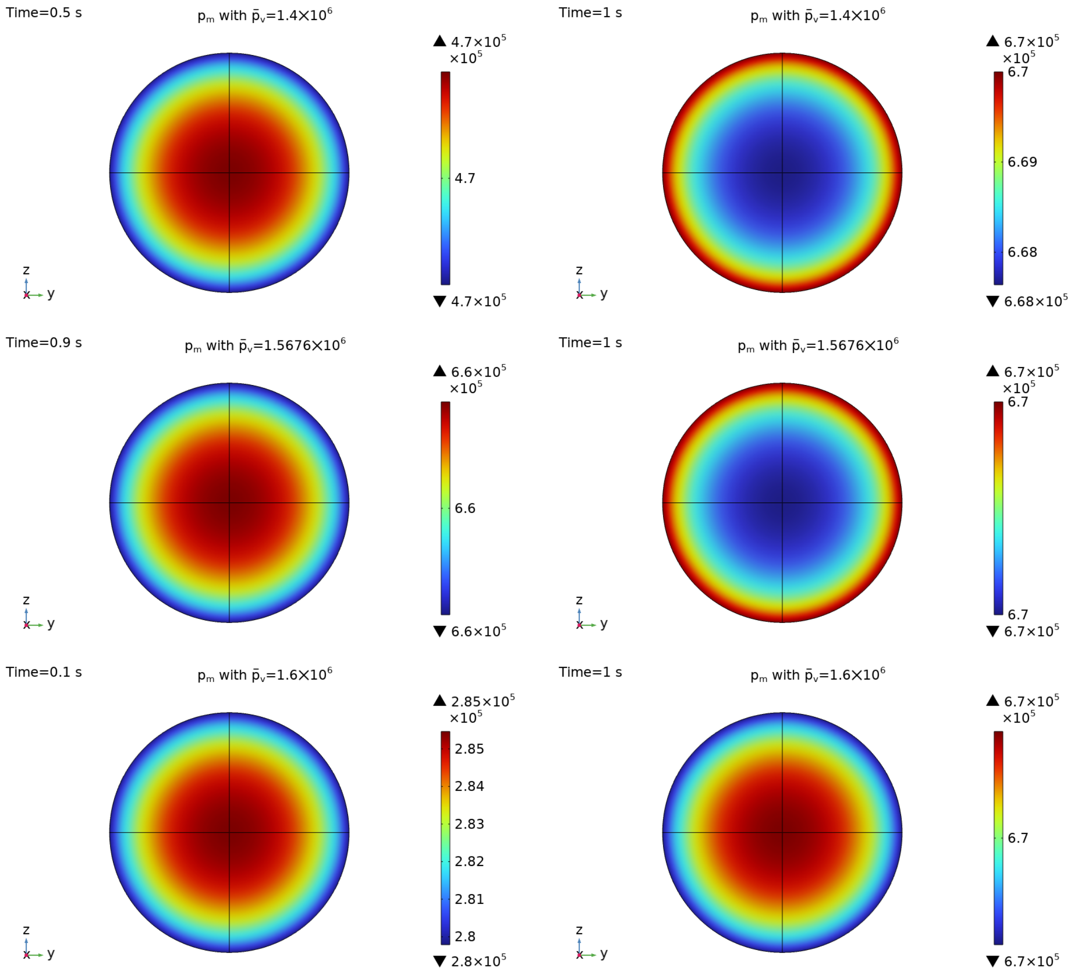

Figure 7.4: The interstitial pressure p_m varying the boundary blood vessels pressure $\bar{p}_v$, in mPa, at different times. We use the parameters $L_p = 10^{-9}\,\frac{\text{mm}}{\text{s mPa}}$, $\pi_v - \pi_m = 1.02 \times 10^6$ mPa, and $\bar{p}_v = 1.06 \times 10^6$ mPa.

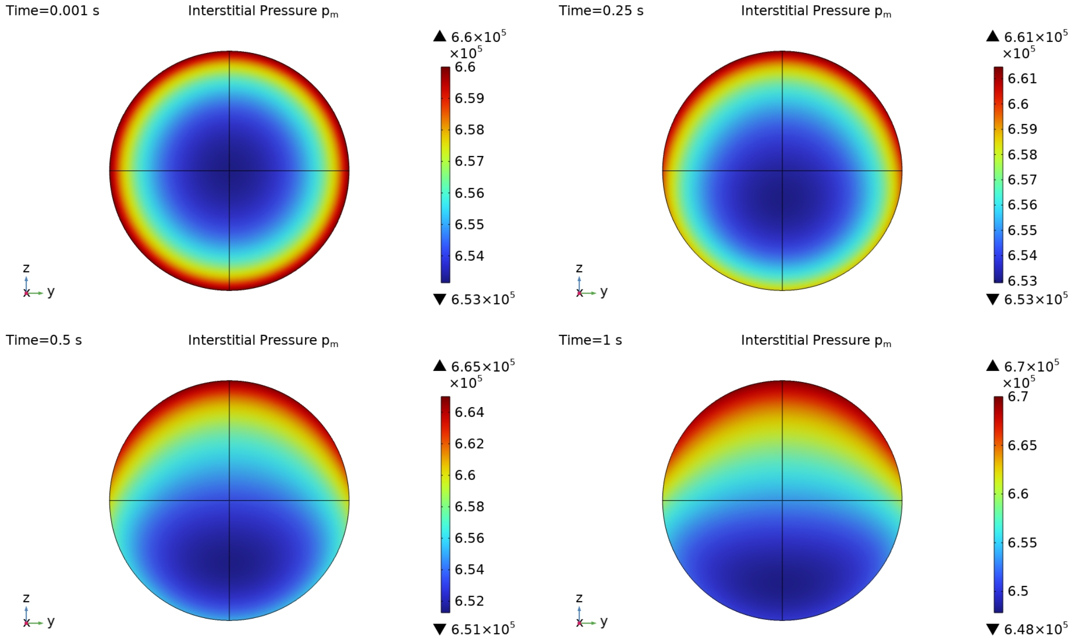

Figure 7.5: The interstitial pressure p_m varying the at different times with the boundary condition given in equation (7.75). We use the parameters $L_p = 10^{-9}\,\frac{\text{mm}}{\text{s mPa}}$, $\pi_v - \pi_m = 1.02 \times 10^6$ mPa, and $\bar{p}_v = 1.06 \times 10^6$ mPa.

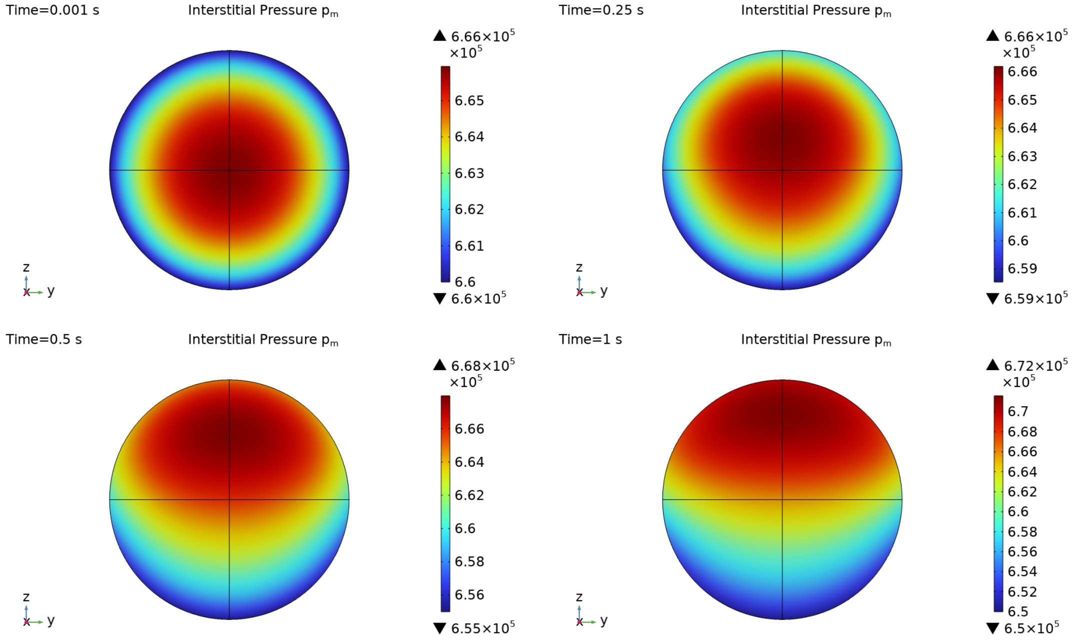

Figure 7.6: The interstitial pressure p_m varying the at different times with the boundary condition given in equation (7.75). We use the parameters $L_p = 10^{-9}\,\frac{\text{mm}}{\text{s mPa}}$, $\pi_v - \pi_m = 1.02 \times 10^6$ mPa, and $\bar{p}_v = 2 \times 10^6$ mPa.

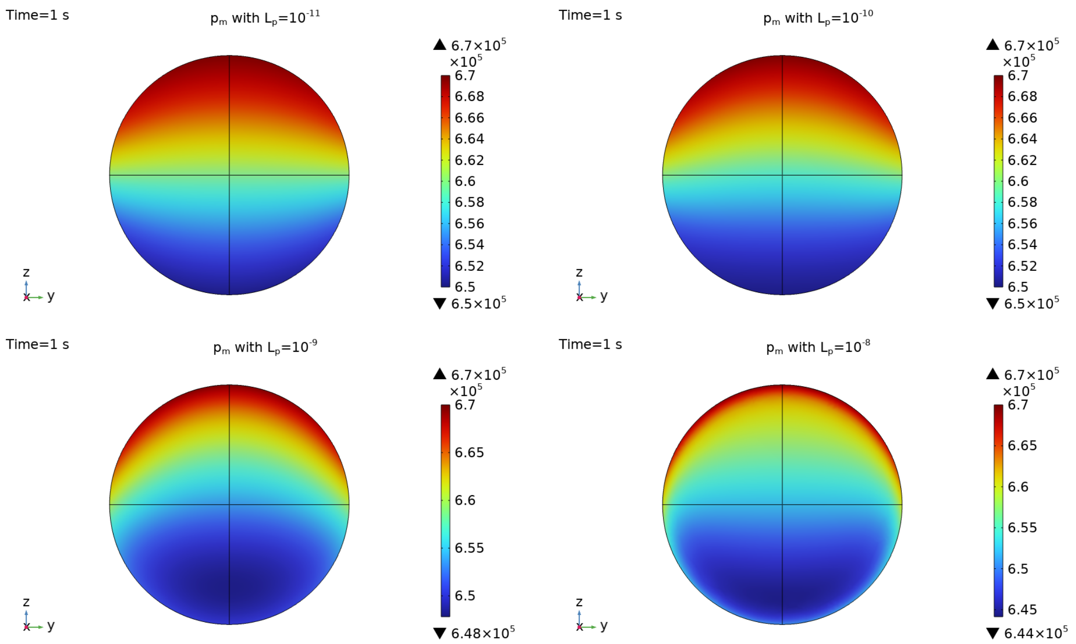

Figure 7.7: The interstitial pressure p_m the at different times with the boundary condition given in equation (7.75) varying L_p (in mPa), at $t = 1\,\mathrm{s}$. We use the parameters $\pi_v - \pi_m = 1.02 \times 10^6$ mPa, and $\bar{p}_v = 1.06 \times 10^6$ mPa.

7.6 Conclusions

In this chapter we proposed a macroscopic model using the asymptotic homogenization technique resulting from the starting equations (7.1) and the interface conditions (7.3), which account for blood transcapillary exchange across the vessels walls, under the assumption of local periodicity and macroscopic uniformity in a time-dependent setting. Our starting point was the Darcy-Brinkman equation, so we considered the pore structure already smoothed out, and the information about the microscale geometry was encoded in the hydraulic conductivity $\hat{\boldsymbol{K}}_\gamma$, $\gamma = m, v$. Since we used the Darcy-Brinkman equation for both Ω_m and Ω_v and imposed continuity of the tangential component of velocity between them, the two-phase cell problems were coupled. After that, in Section 7.4 we proposed numerical simulations to treat the memory term in the macroscopic equation (7.59). Then, in Section 7.5 we used the model and the numerical simulations to study an idealized spherical lymph node using physiological data from the literature; the multiscale formulation of the problem allowed us to study the fluid behavior in the interstitial space and the blood vessels within the lymph node.

In this model, we have considered the time-dependent behavior of the lymph pulsation with the time-derivative term in the Darcy-Brinkman equation (7.1). To see the time-dependent term on the first order approximation of the asymptotic homogenization technique, we needed that

$$ShRe = \frac{\rho_0 L^2}{\mu T_0} \approx \frac{1}{\epsilon^2},$$

where Sh is the *Strouhal number*, Re is the *Reynolds number*, L is the *characteristic macroscopic length*, T_0 is the *characteristic time*, ρ_0 is the density, and μ is the viscosity. As we can see, we need a small characteristic time to see the time-dependent term at the first order: this may not be true for the lymph node case.

From the time-dependent cell problem, we found a higher permeability result for both the interstitial and the blood vessel phases and a lesser fluid exchange between these two phases. Moreover, we found that we need a higher blood vessel pressure to have the flow inversion with respect to the steady case of Chapter 6.

Conclusions

In this thesis, we proposed and analyzed mathematical models describing lymph flow through the lymphatic system.

The first proposed model (Chapter 3) referred to the movement of lymph in a lymphangion, the part of the lymphatic vessel between two valves. Thanks to the lymphangion geometry, we were able to propose a 1D model using the theory of the quasilinear hyperbolic systems. Several models tried to describe the lymph flow in a lymphangion; we proposed a model that took into account realistic data, with the shear stress inhibition and regulation phenomena related to the contractions (eNOS) by fitting the well-known tube law with experimental data found in the literature (for a mesenteric lymphangion of a mouse). We chose this approach because it prioritized fluid behavior while maintaining realistic wall deformation results with more feasible numerical simulations. The results found by our model are in agreement with the literature.

The other models of this thesis referred to the lymph flow through a lymph node; we focused most of our attention here because, to our knowledge, few models tried to describe the behavior of the lymph node from a mechanical point of view. The lymph node has a complex structure and functioning, and the attempt to describe the lymphatic flow within it raised some exciting mathematical questions worth studying in detail. Indeed, as far as we know, this thesis is the first attempt to explicitly study the lymph flow through a lymph node.

As the first lymph node mathematical model (Chapter 4), we presented a highly idealized model for lymph flow in a cylindrical lymph node, assuming laminar flow and driven by a pulsatile pressure gradient. We found an explicit solution in terms of Bessel functions, and we analyzed the eigenvalues of the problem.

After that, we proposed a more realistic mathematical model of the fluid flow in a spherical lymph node (Chapter 5) inspired by a mouse popliteal lymph node; the geometry remained idealized, but it was more similar to a real one. We found an explicit solution using the stream function approach. Compared to the simpler cylindrical case in which we found all the constants of integration explicitly, here we had to solve a 6×6 system for every term of the series expansion of the solution to find them. After we found the explicit solution, we proposed numerical simulations and compared the results with the ones found explicitly. Moreover, thanks to these numerical simulations, we were able to study the fluid flow in more general cases (for example, in a spheroidal geometry).

The previous models described the fluid flow in a lymph node macroscopically, and they did not consider its vascularization. To account for the multiscale nature of the lymph node and the blood vessels within it, we proposed two models using the asymptotic homogenization technique, coupling two different phases: the matrix phase, describing the fluid flow in the FRC network, and the blood vessel phase, describing the fluid flow in the blood vessels within the node, with inhomogeneous body forces. For this analysis, we mainly focused on the porous part of the lymph node (the lymphoid compartment, LC) since the blood vessels are all in this area. The first model (Chapter 6) coupled a Darcy-Brinkman equation for the matrix phase with a Darcy equation for the blood vessel phase in a steady setting. The choice of these equations allowed the separation of the cell problems into two distinct phases, one involving blood vessels and the other involving the FRC network so that we could solve the cell problems in the two domains separately. We studied in detail the difference between using the Stokes, Darcy, and Darcy-Brinkman equation for the microscale problem. After that, we found the explicit macroscopic solution of the resulting equation of the proposed model in a spherical domain (under certainly simplified hypothesis), and we applied the results we found to a lymph node using physiological data from the literature. After that, we numerically solved the lymphoid compartment problem coupled with the free-fluid thin layer (the subcapsular sinus, SCS).

In the second model (Chapter 7) we considered the time dependence of the flow in the lymph node. We coupled two Darcy-Brinkman equations for the FRC and blood vessel phases. We used the Darcy-Brinkman equation because it seems more justified in the time-dependent setting. In this case, the blood vessels and the FRC phases of the cell problems are coupled, unlike the cell problems presented in Chapter 6; this is because we chose as starting point two Darcy-Brinkman equations, and we had to impose the continuity of the tangential component of the velocity between the two phases. To have the time-dependent component in the first-order approximation of the asymptotic homogenization method, we had to assume that

$$ShRe = \frac{\rho_0 L^2}{\mu T_0} \approx \frac{1}{\epsilon^2},$$

where Sh is the *Strouhal number*, Re is the *Reynolds number*, L is the *characteristic macroscopic length*, T_0 is the *characteristic time*, ρ_0 is the density and μ is the viscosity. In this case, we got Darcy's law with memory, and we solved it using numerical simulations with physiological parameters obtained from a lymph node. The hypothesis above may not be valid for the lymph node case; this model is still a work in progress, and further analysis needs to be conducted.

The mathematical models presented here represent a step forward in understanding lymph flow through the lymphatic system and consequently to various pathologies. These models can be a starting point for a more accurate physiological analysis, perhaps by collaborating with medical research institutions. Moreover, this thesis demonstrates the importance of mathematical modeling in understanding the complex dynamics of the lymphatic system and highlights the need for further research in this field.

Future Developments

Mathematical models are a fundamental tool for understanding the physics and the physiology of biological phenomena; moreover, the mathematical description of the lymph flow through the lymphatic system is in its infancy, which means that there are still many things to do.

The lymphangion model can be improved in different ways.

- We can treat the wall mechanics with a more detailed model and not only using phenomenological behavior and data [28–30]. The difficulty is that the wall deformations are highly nonlinear, and coupling this behavior with the system of differential equations described in Chapter 3 is quite difficult and computationally demanding.
- We can consider not only the NO production given by the eNOS but also by iNOS [44, 45].
- We can improve the model by adding to the system given in Section 3.2 the following differential equation that describes the concentration of proteins inside the lymphangion [56]:

  $$\frac{\partial \Gamma}{\partial t} + \frac{\partial}{\partial z}\left(\omega \frac{\Gamma Q}{A}\right) + K_c \frac{\Gamma}{A} = 0, \tag{7.77}$$

  where

  $$\Gamma = A\bar{c}, \tag{7.78}$$

  A is the *cross-sectional area*, $\bar{c}$ is the *average concentration*, ω is the *velocity-concentration correlation coefficient*, Q is the *average flow* and K_c is a coefficient depending on the permeability of the wall χ and the protein concentration of the interstitial space c_{ext}. Indeed, we have that the concentration of proteins affects the fluid behavior and some pathologies (like lymphœdema) [137, 138].

As for the lymph node, we can improve the model in the following ways.

- We can study and analyze in more detail the time-dependent case exposed in Chapter 7. To start with, we can add the subcapsular sinus to the simulations in Section 7.5. Moreover, we can study in detail the role of the characteristic time in the lymph node case, maybe considering different scale separations.
- It may be interesting to take into account the variation over time and space of the protein concentration and the exchange of the latter with the blood vessels within the node, adding the following differential equations [126] to the problems given in Chapter 6 and 7:

  $$\frac{\partial c_v}{\partial t} + \nabla \cdot (c_v \boldsymbol{v}_v - D_v \nabla c_v) = 0 \quad \text{in } \Omega_v, \tag{7.79}$$

$$\frac{\partial c_m}{\partial t} + \nabla \cdot (c_m \boldsymbol{v}_m - D_m \nabla c_m) = 0 \quad \text{in } \Omega_m, \tag{7.80}$$

where $\gamma = m, v$ define the phase cell domain, D_γ is the diffusivity of the phase Ω_γ, c_γ is the *protein concentration* of the phase Ω_γ, and $\boldsymbol{v}_\gamma$ is the *fluid velocity* of the phase Ω_γ. The protein concentration plays a key role in the fluid exchange within the node. Indeed, as we can see in Chapter 6, despite the blood vessel pressure being higher than the interstitial pressure of the node, the higher protein concentration of the blood vessels leads to the fact that the lymph goes from the node to the blood circulation, making the lymph nodes important in the fluid regulation within the lymphatic system [39]. Moreover, it would be interesting to see how the lymph flow within the node affects protein exchange and concentration.

- We can take into account a more realistic microscale and macroscale geometry [6, 7, 59]. Lymph nodes have a very heterogeneous physiology, hence it may be difficult to obtain precise data regarding the geometry (both microscale and macroscale geometry).
- The rigid porous matrix hypothesis can be too restrictive, and a further extension of this thesis can be to treat the lymph node as a deformable porous medium. As mentioned in the previous point, the physiology of the lymph node is very complex, hence it may be difficult to obtain precise biological data to deal with this case.

A final improvement can be to couple the lymphangion model with the lymph node model, so as to have more information about the interaction between these two organs and about the lymph flow through the lymphatic system.

Bibliography

[1] J. E. Moore Jr and C. D. Bertram, "Lymphatic system flows," *Annual review of fluid mechanics*, vol. 50, pp. 459–482, 2018. DOI: `doi.org/10.1146/annurev-fluid-122316-045259`.

[2] A. Quarteroni, A. Manzoni, and C. Vergara, "The cardiovascular system: Mathematical modelling, numerical algorithms and clinical applications," *Acta Numerica*, vol. 26, 365–590, 2017. DOI: `10.1017/S0962492917000046`.

[3] N. P. Reddy, T. A. Krouskop, and P. H. Newell Jr., "Biomechanics of a lymphatic vessel," *Blood Vessels*, vol. 12, no. 5, pp. 261–278, 1975. DOI: `10.1159/000158062`.

[4] M. Novkovic, L. Onder, H.-W. Cheng, G. Bocharov, and B. Ludewig, "Integrative computational modeling of the lymph node stromal cell landscape," *Frontiers in Immunology*, p. 2428, 2018. DOI: `doi.org/10.3389/fimmu.2018.02428`.

[5] M. Jafarnejad, M. C. Woodruff, D. C. Zawieja, M. C. Carroll, and J. Moore Jr., "Modeling lymph flow and fluid exchange with blood vessels in lymph nodes," *Lymphatic research and biology*, vol. 13, no. 4, pp. 234–247, 2015. DOI: `doi.org/10.1089/lrb.2015.0028`.

[6] L. J. Cooper, J. P. Heppell, G. F. Clough, B. Ganapathisubramani, and T. Roose, "An image-based model of fluid flow through lymph nodes," *Bulletin of mathematical biology*, vol. 78, no. 1, pp. 52–71, 2016. DOI: `doi.org/10.1007/s11538-015-0128-y`.

[7] L. J. Cooper, B. Zeller-Plumhoff, G. F. Clough, B. Ganapathisubramani, and T. Roose, "Using high resolution X-ray computed tomography to create an image based model of a lymph node," *Journal of Theoretical Biology*, vol. 449, pp. 73–82, 2018. DOI: `doi.org/10.1016/j.jtbi.2018.04.021`.

[8] R. Tretiakova, A. Setukha, R. Savinkov, D. Grebennikov, and G. Bocharov, "Mathematical modeling of lymph node drainage function by neural network," *Mathematics*, vol. 9, no. 23, p. 3093, 2021. DOI: `doi.org/10.3390/math9233093`.

[9] G. Giantesio, A. Girelli, and A. Musesti, "A model of the pulsatile fluid flow in the lymph node," *Mechanics Research Communications*, vol. 116, p. 103 743, 2021. DOI: `doi.org/10.1016/j.mechrescom.2021.103743`.

[10] G. Giantesio, A. Girelli, and A. Musesti, "A mathematical description of the flow in a spherical lymph node," *Bulletin of Mathematical Biology*, vol. 84, no. 142, 2022. DOI: `doi.org/10.1007/s11538-022-01103-6`.

[11] A. Shanti *et al.*, "Multi-compartment 3D-cultured organ-on-a-chip: Towards a biomimetic lymph node for drug development," *Pharmaceutics*, vol. 12, no. 5, p. 464, 2020. DOI: `doi.org/10.3390/pharmaceutics12050464`.

[12] K. G. Birmingham *et al.*, "Lymph node subcapsular sinus microenvironment-on-a-chip modeling shear flow relevant to lymphatic metastasis and immune cell homing," *Iscience*, vol. 23, no. 11, p. 101 751, 2020. DOI: `doi.org/10.1016/j.isci.2020.101751`.

[13] A. Shanti, J. Teo, and C. Stefanini, "In vitro immune organs-on-chip for drug development: A review," *Pharmaceutics*, vol. 10, no. 4, p. 278, 2018. DOI: `doi.org/10.3390/pharmaceutics10040278`.

[14] A. J. Macdonald, K. P. Arkill, G. R. Tabor, N. G. McHale, and C. P. Winlove, "Modeling flow in collecting lymphatic vessels: One-dimensional flow through a series of contractile elements," *American Journal of Physiology-Heart and Circulatory Physiology*, vol. 295, no. 1, H305–H313, 2008. DOI: `https://doi.org/10.1152/ajpheart.00004.2008`.

[15] C. D. Bertram, C. Macaskill, and J. E. Moore Jr., "Incorporating measured valve properties into a numerical model of a lymphatic vessel," *Computer Methods in Biomechanics and Biomedical Engineering*, vol. 17, no. 14, pp. 1519–1534, 2014. DOI: `doi.org/10.1080/10255842.2012.753066`.

[16] C. D. Bertram, C. Macaskill, and J. E. Moore Jr., "Development of a model of a multi-lymphangion lymphatic vessel incorporating realistic and measured parameter values," *Biomechanics and Modeling in Mechanobiology*, vol. 13, pp. 401–416, 2014. DOI: `doi.org/10.1007/s10237-013-0505-0`.

[17] C. D. Bertram, C. Macaskill, M. J. Davis, and J. E. Moore Jr., "Valve-related modes of pump failure in collecting lymphatics: Numerical and experimental investigation," *Biomechanics and modeling in mechanobiology*, vol. 16, no. 6, pp. 1987–2003, 2017. DOI: `doi.org/10.1007/s10237-017-0933-3`.

[18] C. D. Bertram, C. Macaskill, and J. E. Moore Jr., "Inhibition of contraction strength and frequency by wall shear stress in a single-lymphangion model," *Journal of biomechanical engineering*, vol. 141, no. 11, 2019. DOI: `doi.org/10.1115/1.4043724`.

[19] C. Contarino and E. F. Toro, "A one-dimensional mathematical model of collecting lymphatics coupled with an electro-fluid-mechanical contraction model and valve dynamics," *Biomechanics and Modeling in Mechanobiology*, vol. 17, no. 6, pp. 1687–1714, 2018. DOI: `doi.org/10.1007/s10237-018-1050-7`.

[20] R. M. Tretyakova, G. I. Lobov, and G. A. Bocharov, "Simulation of lymph flow with consideration of natural gravity force influence," *Math. Model. Nat. Phenom*, vol. 13, no. 45, 2018. DOI: `doi.org/10.1051/mmnp/2018044`.

[21] A. S. Mozokhina and S. I. Mukhin, "Pressure gradient influence on global lymph flow," *Trends in Biomathematics: Modeling, Optimization and Computational Problems*, 2018. DOI: `doi.org/10.1007/978-3-319-91092-5\_22`.

[22] J. T. Wilson, R. van Loon, W. Wang, D. C. Zawieja, and J. E. Moore Jr., "Determining the combined effect of the lymphatic valve leaflets and sinus on resistance to forward flow," *Journal of Biomechanics*, vol. 48, pp. 3584–3590, 2015. DOI: `doi.org/10.1016/j.jbiomech.2015.07.045`.

[23] J. T. Wilson, L. T. Edgar, S. Prabhakar, M. Horner, R. van Loon, and J. E. Moore Jr., "A fully coupled fluid-structure interaction model of the secondary lymphatic valve," *Computer Methods in Biomechanics and Biomedical Engineering*, vol. 21, pp. 813–823, 2018. DOI: `doi.org/10.1080/10255842.2018.1521964`.

[24] C. D. Bertram, "Modelling secondary lymphatic valves with a flexible vessel wall: How geometry and material properties combine to provide function," *Biomechanics and Modeling in Mechanobiology*, vol. 19, no. 6, pp. 2081–2098, 2020. DOI: `doi.org/10.1007/s10237-020-01325-4`.

[25] K. T. Wolf, J. B. Dixon, and A. Alexeev, "Fluid pumping of peristaltic vessel fitted with elastic valves," *Journal of Fluid Mechanics*, vol. 918, no. A28, 2021. DOI: `doi.org/10.1017/jfm.2021.302`.

[26] J. In, J. Ryu, D. K. Yu, K. Taeyoung, and K. Jungwook, "Microfluidic valvular chips and a numerical lymphatic vessel model for the study of lymph transport characteristics," *Lab on a Chip*, vol. 21, no. 11, pp. 2283–2293, 2021. DOI: `dx.doi.org/10.1039/D1LC00022E`.

[27] H. Li, Y. Mei, M. Nir, T. P. Padera, J. W. Baish, and L. L. Munn, "The effects of valve leaflet mechanics on lymphatic pumping assessed using numerical simulations," *Scientific Reports*, vol. 9, 2019. DOI: `doi.org/10.1038/s41598-019-46669-9`.

[28] A. W. Caulk, Z. V. Nepiyushchikh, R. Shaw, and J. B. Dixon, "Quantification of the passive and active biaxial mechanical behaviour and microstructural organization of rat thoracic ducts," *Journal of the Royal Society Interface*, vol. 12, 2015. DOI: `doi.org/10.1098/rsif.2015.0280`.

[29] A. W. Caulk, J. B. Dixon, and R. L. Gleason Jr., "A lumped parameter model of mechanically mediated acute and long-term adaptations of contractility and geometry in lymphatics for characterization of lymphedema," *Journal of Physiology*, vol. 15, pp. 1601–1618, 2016. DOI: `doi.org/10.1007/s10237-016-0785-2`.

[30] M. S. Razavi, J. B. Dixon, and R. L. Gleason, "Characterization of rat tail lymphatic contractility and biomechanics: Incorporating nitric oxide-mediated vasoregulation," *Journal of the Royal Society Interface*, vol. 17, 2020. DOI: `doi.org/10.1098/rsif.2020.0598`.

[31] J. Happel and H. Brenner, *Low Reynolds number hydrodynamics: with special applications to particulate media.* The Hague: Martinus Nijhoff Publishers, 1983.

[32] U. Hornung, *Homogenization and Porous Media.* Springer Science + Business Media New York: Springer, 1997.

[33] A. Mikelić, "Mathematical derivation of the darcy-type law with memory effects, governing transient flow through porous media," *Glasnik Matematicki*, vol. 29, 1994.

[34] K. N. Margaris and R. A. Black, "Modelling the lymphatic system: Challenges and opportunities," *Journal of the Royal Society, Interface*, vol. 9, no. 69, pp. 601–612, 2012. DOI: `https://doi.org/10.1098/rsif.2011.07511`.

[35] A. Mozokhina and R. Savinkov, "Mathematical modelling of the structure and function of the lymphatic system," *Mathematics*, vol. 8, no. 9, p. 1467, 2020.

[36] J. Arasa, V. Collado-Diaz, and C. Halin, "Structure and immune function of afferent lymphatics and their mechanistic contribution to dendritic cell and T cell trafficking," *Cells*, vol. 10, no. 5, p. 1269, 2021. DOI: `doi.org/10.3390/cells10051269`.

[37] M. J. O'Melia, A. W. Lund, and S. N. Thomas, "The biophysics of lymphatic transport: Engineering tools and immunological consequences," *Iscience*, vol. 22, pp. 28–43, 2019. DOI: `doi.org/10.1016/j.isci.2019.11.005`.

[38] A. D. Permana, F. Nainu, K. Moffatt, E. Larrañeta, and R. F. Donnelly, "Recent advances in combination of microneedles and nanomedicines for lymphatic targeted drug delivery," *Wiley Interdisciplinary Reviews: Nanomedicine and Nanobiotechnology*, vol. 13, no. 3, 2021. DOI: `https://doi.org/10.1002/wnan.1690`.

[39] D. Tobbia, J. Semple, A. Baker, D. Dumont, A. Semple, and M. Johnston, "Lymphedema development and lymphatic function following lymph node excision in sheep," *Journal of vascular research*, vol. 46, no. 5, pp. 426–434, 2009. DOI: `doi.org/10.1159/000194273`.

[40] J. Trzewik, S. K. Mallipattu, G. M. Artmann, F. A. Delano, and G. W. Schmid-Schonbein, "Evidence for a second valve system in lymphatics: Endothelial microvalves," *FASEB J.*, vol. 15, no. 10, pp. 1711–1717, 2001. DOI: `10.1096/fj.01-0067com`.

[41] A. A. Gashev, R.-Z. Zhang, M. Muthuchamy, D. C. Zaqieja, and M. J. Davis, "Regional heterogeneity of length–tension relationships in rat lymph vessels," *Lymphatic research and biology*, vol. 10, no. 1, 2012. DOI: `doi.org/10.1089/lrb.2011.0013`.

[42] I. Quéré, "Lymphatic system: Anatomy, histology and physiology," *La-Presse Médicalel*, vol. 39, no. 12, pp. 1269–1278, 2010. DOI: `doi.org/10.1016/j.lpm.2010.09.009`.

[43] A. A. Gashev, M. j. Davis, and D. C. Zawieja, "Inhibition of the active lymph pump by flow in rat mesenteric lymphatics and thoracic duct," *Journal of Physiology*, vol. 540, no. 3, pp. 1023–1037, 2002. DOI: `doi.org/10.1113/jphysiol.2001.016642`.

[44] S. Liao, E. M. Bouta, L. M. Morris, D. Jones, R. K. Jain, and T. P. Padera, "Inducible nitric oxide synthase and cd11b$^+$gr1$^+$ cells impair lymphatic contraction of tumor-draining lymphatic vessels," *Lymphatic Research and Biology*, vol. 17, no. 3, pp. 294–300, 2019. DOI: `doi.org/10.1089/lrb.2018.0013`.

[45] S. Liao *et al.*, "Impaired lymphatic contraction associated with immunosuppression," *PNAS*, vol. 108, no. 46, pp. 18 748–18 789, 2011. DOI: `doi.org/10.1073/pnas.1116152108`.

[46] M. J. Davis, E. Rahbar, A. A. Gashev, D. C. Zawieja, and J. E. Moore Jr., "Determinants of valve gating in collecting lymphatic vessels from rat mesentery," *Am J Physiol Heart Circ Physiol*, vol. 301, no. 1, H48–H60, 2011. DOI: `doi.org/10.1152/ajpheart.00133.2011`.

[47] C. Blatter *et al.*, "In vivo label-free measurement of lymph flow velocity and volumetric flow rates using Doppler optical coherence tomography," *Scientific reports*, vol. 6, no. 1, pp. 1–10, 2016. DOI: `doi.org/10.1038/srep29035`.

[48] J. B. Dixon, S. T. Greiner, A. A. Gashev, G. L. Cote, J. E. Moore, and D. C. Zawieja, "Lymph flow, shear stress, and lymphocyte velocity in rat mesenteric prenodal lymphatics," *Microcirculation*, vol. 13, no. 597, pp. 597–610, 2006. DOI: `doi.org/10.1080/10739680600893909`.

[49] R. Roozendaal, R. E. Mebius, and G. Kraal, "The conduit system of the lymph node," *International immunology*, vol. 20, no. 12, pp. 1483–1487, 2008. DOI: `doi.org/10.1093/intimm/dxn110`.

[50] T. H. Adair, D. S. Moffatt, A. W. Paulsen, and A. C. Guyton, "Quantitation of changes in lymph protein concentration during lymph node transit," *American Journal of Physiology-Heart and Circulatory Physiology*, vol. 243, no. 3, H351–H359, 1982. DOI: `doi.org/10.1152/ajpheart.1982.243.3.H351`.

[51] T. H. Adair and A. C. Guyton, "Modification of lymph by lymph nodes. II. Effect of increased lymph node venous blood pressure," *American Journal of Physiology-Heart and Circulatory Physiology*, vol. 245, no. 4, H616–H622, 1983. DOI: `doi.org/10.1152/ajpheart.1983.245.4.H616`.

[52] T. H. Adair and A. C. Guyton, "Modification of lymph by lymph nodes. III. Effect of increased lymph hydrostatic pressure," *American Journal of Physiology-Heart and Circulatory Physiology*, vol. 249, no. 4, H777–H782, 1985. DOI: `doi.org/10.1152/ajpheart.1985.249.4.H777`.

[53] M. Jafarnejad *et al.*, "Quantification of the whole lymph node vasculature based on tomography of the vessel corrosion casts," *Nature Scientific Reports*, vol. 9, no. 13380, 2019. DOI: `doi.org/10.1038/s41598-019-49055-7`.

[54] I. D. Kelch, G. Bogle, G. B. Sands, A. R. J. Phillips, I. J. LeGrice, and P. R. Dunbar, "Organ-wide 3d-imaging and topological analysis of the continuous microvascular network in a murine lymph node," *Nature Scientific Reports*, vol. 16, no. 5, 2015. DOI: `doi.org/10.1038/srep16534`.

[55] J. Waniewski, "Mathematical modeling of fluid and solute transport in hemodialysis and peritoneal dialysis," *Journal of Membrane Sciences*, vol. 274, pp. 24–37, 2006. DOI: `doi.org/10.1016/j.memsci.2005.11.038`.

[56] L. Formaggia, A. Quarteroni, and A. Veneziani, *Cardiovascular Mathematics: Modeling and Simulation of the Circulatory System.* Milano: Springer-Verlag, 2009.

[57] F. Apoorva *et al.*, "How biophysical forces regulate human B cell lymphomas," *Cell reports*, vol. 23, no. 2, pp. 499–511, 2018. DOI: `10.1016/j.celrep.2018.03.069`.

[58] A. Schudel, D. M. Francis, and S. N. Thomas, "Material design for lymph node drug delivery," *Nature Reviews Materials*, vol. 4, pp. 415–428, 2019. DOI: `doi.org/10.1038/s41578-019-0110-7`.

[59] D. Grebennikov *et al.*, "Critical issues in modelling lymph node physiology," *Computation*, vol. 5, no. 1, 2016. DOI: `https://doi.org/10.3390/computation5010003`.

[60] M. H. Ulvmar *et al.*, "The atypical chemokine receptor CCRL1 shapes functional CCL21 gradients in lymph nodes," *Nature immunology*, vol. 15, no. 7, pp. 623–630, 2014. DOI: `doi.org/10.1038/ni.2889`.

[61] T. Junt *et al.*, "Subcapsular sinus macrophages in lymph nodes clear lymph-borne viruses and present them to antiviral B cells," *Nature*, vol. 450, 2007. DOI: `10.1038/nature06287`. [Online]. Available: `doi.org/10.1038/nature06287`.

[62] S. Das *et al.*, "Tumor cell entry into the lymph node is controlled by CCL1 chemokine expressed by lymph node lymphatic sinuses," *Journal of Experimental Medicine*, vol. 210, no. 8, pp. 1509–1528, 2013. DOI: `doi.org/10.1084/jem.20111627`.

[63] U. H. von Andrian and T. R. Mempel, "Homing and cellular traffic in lymph nodes," *Nature Reviews Immunology*, vol. 3, no. 11, pp. 867–878, 2003. DOI: `doi.org/10.1038/nri1222`.

[64] L. Kähäri *et al.*, "Transcytosis route mediates rapid delivery of intact antibodies to draining lymph nodes," *The Journal of Clinical Investigation*, vol. 129, no. 8, pp. 3086–3102, 2019. DOI: `doi.org/10.1172/JCI125740`.

[65] A. L. Fletcher, S. E. Acton, and K. Knoblich, “Lymph node fibroblastic reticular cells in health and disease,” *Nature Reviews Immunology*, vol. 15, pp. 350–361, 2015. DOI: `https://doi.org/10.1038/nri3846`.

[66] S. E. Acton *et al.*, “Dendritic cells control fibroblastic reticular network tension and lymph node expansion,” *Nature*, vol. 514, pp. 498–502, 2014. DOI: `https://doi.org/10.1038/nature13814`.

[67] S. E. Acton, L. Onder, M. Novkovic, V. G. Martinez, and B. Ludewig, “Communication, construction, and fluid control: Lymphoid organ fibroblastic reticular cell and conduit networks,” *Trends in Immunology*, vol. 42, no. 9, pp. 782–794, 2021. DOI: `https://doi.org/10.1016/j.it.2021.07.003`.

[68] M. Abramowitz and I. A. Stegun, *Handbook of mathematical functions with formulas, graphs, and mathematical tables.* Washington, D.C.: US Government printing office, 1964, vol. 55.

[69] G. Dassios, M. Hadjinicolaou, and A. C. Payatakes, “Generalized eigenfunctions and complete semiseparable solutions for stokes flow in spheroidal coordinates,” *Quarterly of Applied Mathematics*, vol. 52, pp. 157–191, 1994. DOI: `10.1090/QAM/1262325`.

[70] A. Gerisch, R. Penta, and J. Lang, *Multiscale Models in Mechano and Tumor Biology.* Gewerbestrasse 11, 6330 Cham, Switzerland: Springer, 2018.

[71] T. Ruggeri and S. Simic, “On the hyperbolic system of a mixture of eulerian fluids: A comparison between single- and multi-temperature models,” *Mathematical Methods in the Applied Sciences*, vol. 30, no. 7, pp. 827–849, 2007. DOI: `https://doi.org/10.1002/mma.813`.

[72] T. Ruggeri and S. Taniguchi, “Shock waves in hyperbolic systems of nonequilibrium thermodynamics,” *Applied Wave Mathematics II*, vol. 6, 2019. DOI: `https://doi.org/10.1007/978-3-030-29951-4\_8`.

[73] A. C. L. Barnard, W. A. Hunt, W. P. Timlake, and E. Varley, “A theory of fluid flow in compliant tubes,” *Biophysical Journal*, vol. 6, no. 6, pp. 717–724, 1966. DOI: `doi.org/10.1016/S0006-3495(66)86690-0`.

[74] S. Čanić and E. H. Kim, “Mathematical analysis of the quasilinear effects in a hyperbolic model blood flow through compliant axi-symmetric vessels,” *Mathematical Methods in the Applied Sciences*, vol. 26, pp. 1161–1186, 2003. DOI: `doi.org/10.1002/mma.407`.

[75] M. S. Hassanizadeh, “Derivation of basic equations of mass transport in porous media, part 2. generalized darcy’s and fick’s laws,” *Adv. Water Resources*, vol. 9, pp. 207–222, 1986. DOI: `https://doi.org/10.1016/0309-1708(86)90025-4`.

[76] J. Bear and Y. Bachmat, *Introduction to Modelling of Transport Phenomena in Porous Media.* Dordrecht, The Netherlands: Kluwer, 1990.

[77] H. Darcy, *Les fontaines publiques de la ville de Dijon.* Paris: Victor Dalmont, 1856.

[78] J.-L. Auriault, C. Geindreau, and C. Boutin, "Filtration law in porous media with poor separation of scales," *Transport in Porous Media*, vol. 60, no. 1, pp. 89–108, 2005. DOI: `doi.org/10.1007/s11242-004-3649-7`.

[79] H. Brinkman, "A calculation of the viscous force exerted by a flowing fluid on a dense swarm of particles," *Applied Scientific Research*, vol. A1, no. 27, pp. 27–34, 1949. DOI: `doi.org/10.1007/BF02120313`.

[80] G. Naele and W. Nader, "Practical signihcance of Brinkman's extension of Darcy's law: Coupled parallel flows within a channel and a bounding porous medium," *The Canadian lournal of Chemical Engineering*, vol. 52, pp. 475–478, 1974. DOI: `doi.org/10.1002/cjce.5450520407`.

[81] E. Marusic-Paloka, I. Pazanin, and S. Marusic, "Comparison between darcy and brinkman laws in a fracture," *Applied Mathematics and Computation*, vol. 218, pp. 7538–7545, 2012. DOI: `doi.org/10.1016/j.amc.2012.01.021`.

[82] T. Zlatanovski, "Axisymmetric creeping flow past a porous prolate spheroidal particle using the Brinkman model," *The Quarterly Journal of Mechanics and Applied Mathematics*, vol. 52, no. 1, pp. 111–126, 1999. DOI: `doi.org/10.1093/qjmam/52.1.111`.

[83] P. K. Yadav and S. Deo, "Stokes flow past a porous spheroid embedded in another porous medium," *Meccanica*, vol. 47, no. 6, pp. 1499–1516, 2012. DOI: `doi.org/10.1007/s11012-011-9533-y`.

[84] W. L. Haberman and R. M. Sayre, "Motion of rigid and fluid spheres in stationary and moving liquids inside cylindrical tubes," David Taylor Model Basin Washington DC, Tech. Rep., 1958.

[85] G. Allaire, "Homogenization and two-scale convergence," *SIAM Journal on Mathematical Analysis*, vol. 23, no. 6, pp. 1482–1518, 2001. DOI: `doi.org/10.1137/0523084`.

[86] D. Cioranescu and P. Donato, *An Introduction to Homogenization.* Oxford: Oxford University Pres, 1999.

[87] A. Bensoussan, J.-L. Lions, and G. Papanicolaou, *Asymptotic Analysis for Periodic Structures.* New York: Elsevier, 1978.

[88] E. Sanchez-Palencia, *Non-Homogeneous Media and Vibration Theory.* Berlin: Springer, 1980.

[89] R. Burridge and J. B. Keller, "Poroelasticity equations derived from microstructure," *The Journal of the Acoustical Society of America*, vol. 70, no. 4, pp. 1140–1146, 1981. DOI: `doi.org/10.1121/1.386945`.

[90] J.-L. Auriault, C. Boutin, and C. Geindreau, *Homogenization of Coupled Phenomena in Heterogenous Media.* France: Wiley, 2009.

[91] F. M. White, *Viscous Fluid Flow.* New York: McGraw-Hill, 2009.

[92] E. F. Toro, *Riemann Solvers and Numerical Methods for Fluid Dynamics.* Verlag Berlin Heidelberg: Springer, 2009.

[93] T. Li and S. Čanić, "Critical thresholds in a quasilinear hyperbolic model of blood flow," *Networks and Heterogeneous Media*, vol. 4, no. 3, pp. 527–536, 2009. DOI: `10.3934/nhm.2009.4.527`.

[94] J. P. Mynard, M. R. Davidson, D. J. Penny, and J. J. Smolich, "A simple, versatile valve model for use in lumped parameter and one-dimensional cardiovascular models," *International Journal for Numerical Methods in Biomedical Engineering*, vol. 28, no. 6-7, pp. 626–641, 2012. DOI: `doi.org/10.1002/cnm.1466`.

[95] P. Marcati and B. Rubino, "Hyperbolic to parabolic relaxation theory for quasilinear first order systems," *Journal of Differential Equations*, vol. 162, no. 2, pp. 359–399, 2000. DOI: `doi.org/10.1006/jdeq.1999.3676`.

[96] P. Lax and B. Wendroff, "Systems of conservation laws," *Communications on pure and applied mathematics*, vol. 13, pp. 217–237, 1960. DOI: `https://doi.org/10.1002/cpa.3160130205`.

[97] R. J. LeVeque, *Numerical Methods for Conservation Laws.* Basilea: Birkhäuser, 1992.

[98] A. K. Diem and N. W. Bressloff, "Vampy: A python package to solve 1d blood flow problems," *Journal of Open Research Software*, vol. 5, no. 17, 2017. DOI: `doi.org/10.5334/jors.159`.

[99] A. Tümer, C. Öztürk Demir, and A. N. Basar-Eroglu, "Spontaneous contractions and stretch-evoked responses of isolated lymph nodes," *J. Muscle Res. Cell Motil.*, vol. 4, no. 1, pp. 103–113, 2001. DOI: `doi.org/10.1007/BF00711961`.

[100] G. N. Watson, *A Treatise on the Theory of Bessel Functions.* Cambridge University Press, 1944, pp. vi+804.

[101] R. Savinkov *et al.*, "Data-driven modelling of the FRC network for studying the fluid flow in the conduit system," *Engineering Applications of Artificial Intelligence*, vol. 62, pp. 341–349, 2017, ISSN: 0952-1976. DOI: `10.1016/j.engappai.2016.10.007`.

[102] F. Hecht, "New development in FreeFem++," *J. Numer. Math.*, vol. 20, no. 3-4, pp. 251–265, 2012, ISSN: 1570-2820. [Online]. Available: `https://freefem.org/`.

[103] D. A. Nield, "Modelling fluid flow and heat transfer in a saturated porous medium," *Journal of applied mathematics and decision sciences*, vol. 4, no. 2, pp. 165–173, 2000. DOI: `doi.org/10.1155/S1173912600000122`.

[104] A. Kislitsyn, R. Savinkov, M. Novkovic, L. Onder, and G. Bocharov, "Computational approach to 3D modeling of the lymph node geometry," *Computation*, vol. 3, no. 2, pp. 222–234, 2015. DOI: `doi.org/10.3390/computation3020222`.

[105] Z. Zhang *et al.*, "High resolution MRI for non-invasive mouse lymph node mapping," *Journal of immunological methods*, vol. 400, pp. 23–29, 2013. DOI: `doi.org/10.1016/j.jim.2013.06.013`.

[106] J. A. Ochoa-Tapia and S. Whitaker, "Momentum transfer at the boundary between a porous medium and a homogeneous fluid I. Theoretical development," *International Journal of Heat and Mass Transfer*, vol. 38, no. 14, pp. 2635–2646, 1995. DOI: `doi.org/10.1016/0017-9310(94)00346-W`.

[107] H. Tan and K. M. Pillai, "Finite element implementation of stress-jump and stress-continuity conditions at porous-medium, clear-fluid interface," *Computers & Fluids*, vol. 38, no. 6, pp. 1118–1131, 2009. DOI: `doi.org/10.1016/j.compfluid.2008.11.006`.

[108] O. Ohtani and Y. Ohtani, "Structure and function of rat lymph nodes," *Archives of histology and cytology*, vol. 71, no. 2, pp. 69–76, 2008. DOI: `doi.org/10.1679/aohc.71.69`.

[109] J. A. Ochoa-Tapia and S. Whitaker, "Momentum transfer at the boundary between a porous medium and a homogeneous fluid II. Comparison with experiment," *International Journal of Heat and Mass Transfer*, vol. 38, no. 14, pp. 2647–2655, 1995. DOI: `doi.org/10.1016/0017-9310(94)00347-X`.

[110] J. Prakash, "Hydrodynamic mobility of a porous spherical particle with variable permeability in a spherical cavity," *Microsystem Technologies*, vol. 26, no. 8, pp. 2601–2614, 2020. DOI: `doi.org/10.1007/s00542-020-04801-0`.

[111] E. M. Bouta, R. W. Wood, E. B. Brown, H. Rahimi, C. T. Ritchlin, and E. M. Schwarz, "In vivo quantification of lymph viscosity and pressure in lymphatic vessels and draining lymph nodes of arthritic joints in mice," *The Journal of physiology*, vol. 592, no. 6, pp. 1213–1223, 2014. DOI: `doi.org/10.1113/jphysiol.2013.266700`.

[112] E. W. Jenkins, V. John, A. Linke, and L. G. Rebholz, "On the parameter choice in grad-div stabilization for the Stokes equations," *Advances in Computational Mathematics*, vol. 40, no. 2, pp. 491–516, 2014. DOI: `doi.org/10.1007/s10444-013-9316-1`.

[113] M. Neilan and A. Zytoon, "Connection between grad-div stabilized Stokes finite elements and divergence-free Stokes finite elements," *International journal of numerical analysis and modeling*, vol. 17, no. 6, 2020.

[114] Y. Qin, Y. Hou, P. Huang, and Y. Wang, "Numerical analysis of two grad–div stabilization methods for the time-dependent Stokes/Darcy model," *Computers & Mathematics with Applications*, vol. 79, no. 3, pp. 817–832, 2020. DOI: `doi.org/10.1016/j.camwa.2019.07.032`.

[115] Y. Rong and J. A. Fiordilino, "Numerical analysis of a BDF2 modular grad–div stabilization method for the Navier–Stokes equations," *Journal of Scientific Computing*, vol. 82, no. 3, pp. 1–22, 2020. DOI: `doi.org/10.48550/arXiv.1806.10750`.

[116] X. Xie, J. Xu, and G. Xue, "Uniformly-stable finite element methods for Darcy-Stokes-Brinkman models," *Journal of Computational Mathematics*, pp. 437–455, 2008.

[117] C. Lamaison *et al.*, "Stromal cells regulate malignant B-cell spatial organization, survival, and drug response in a new 3D model mimicking lymphoma tumor niche," *bioRxiv*, 2020. DOI: `10.1101/2020.10.17.343657`.

[118] T. Lèvy, "Fluid flow through an array of fixed particles," *International Journal of Engineering Science*, vol. 21, no. 1, pp. 11–23, 1983. DOI: `doi.org/10.1016/0020-7225(83)90035-6`.

[119] R. Penta, A. D. Ramírez-Torres, J. Merodio, and R. Rodríguez-Ramos, "Effective governing equations for heterogenous porous media subject to inhomogeneous body forces," *Mathematics in Engineering*, vol. 3, no. 4, pp. 1–17, 2020. DOI: `10.3934/mine.2021033`.

[120] M. Novkovic, L. Onder, G. Bocharov, and B. Ludewig, "Topological structure and robustness of the lymph node conduit system," *Cell Reports*, vol. 30, no. 3, pp. 893–904, 2020. DOI: `doi.org/10.1016/j.celrep.2019.12.070`.

[121] M. Discacciati and A. Quarteroni, "Navier-Stokes/Darcy coupling: Modeling, analysis, and numerical approximation," *Revista Matemática Complutense*, vol. 22, no. 2, pp. 315–426, 2009. DOI: `doi.org/10.5209/rev\_REMA.2009.v22.n2.16263`.

[122] G. S. Beavers and D. D. Joseph, "Boundary conditions at a naturally permeable wall," *Journal of fluid mechanics*, vol. 30, no. 1, pp. 197–207, 1967. DOI: `dx.doi.org/10.1017/S0022112067001375`.

[123] P. G. Saffman, "On the boundary condition at the surface of a porous medium," *Studies in applied mathematics*, vol. 50, no. 2, pp. 93–101, 1971. DOI: `doi.org/10.1002/sapm197150293`.

[124] J.-L. Auriault, "About the beavers and joseph boundary condition," *Transport Porous Media*, vol. 83, pp. 257–266, 2010. DOI: `https://doi.org/10.1007/s11242-009-9435-9`.

[125] W. Jäger and A. Mikelić, "Modeling effective interface laws for transport phenomena between an unconfined fluid and a porous medium using homogenization," *Transport in Porous Media*, vol. 78, pp. 489–508, 2009. DOI: `hhttps://doi.org/10.1007/s11242-009-9354-9`.

[126] R. Penta, D. Ambrosi, and A. Quarteroni, "Multiscale homogenization for fluid and drug transport in vascularized malignant tissues," *Mathematical Models and Methods in Applied Sciences*, vol. 25, no. 1, pp. 79–108, 2015. DOI: `doi.org/10.1142/S0218202515500037`.

[127] R. J. Shipley and S. J. Chapman, "Multiscale modelling of fluid and drug transport in vascular tumours," *Bulletin of mathematical biology*, vol. 72, pp. 1464–1491, 2010. DOI: `https://doi.org/10.1007/s11538-010-9504-9`.

[128] R. Penta and D. Ambrosi, "The role of the microvascular tortuosity in tumor transport phenomena," *Journal of Theoretical Biology*, vol. 364, pp. 80–97, 2015. DOI: `doi.org/10.1016/j.jtbi.2014.08.007`.

[129] M. Stohrer, Y. Boucher, M. Stangassinger, and R. K. Jain, "Oncotic pressure in solid tumors is elevated," *Cancer Research*, vol. 60, pp. 4251–4255, 2000.

[130] J. Kozeny, "Ueber kapillare leitung des wassers im boden," *Sitzungsber Akad. Wiss.*, vol. 136, no. 2a, pp. 271–306, 1927.

[131] P. C. Carman, "Fluid flow through granular beds," *Chemical Engineering Research and Design*, vol. 75, S32–S48, 1997. DOI: `doi.org/10.1016/S0263-8762(97)80003-2`.

[132] A. Quarteroni and A. Valli, *Numerical Approximation of Partial Differential Equations.* Heidelberg: Springer, 1994.

[133] C. Johnson, *Numerical Solution of Partial Differential Equations by the Finite Element Method.* Dover: Cambridge University Press., 2008.

[134] A. Quarteroni, R. Sacco, and F. Saleri, *Numerical Mathematics.* Heidelberg: Springer, 2007.

[135] A.-T. Vuong, L. Yoshihara, and W. A. Wall, "A general approach for modeling interacting flow through porous media under finite deformations," *Comput. Methods Appl. Mech. Engrg*, vol. 283, no. 1, pp. 1240–1259, 2014. DOI: `doi.org/10.1016/j.cma.2014.08.018`.

[136] J.-L. Lions, *Some methods in the mathematical analysis of systems and their control.* New York: Science Press, 1981.

[137] J. P. Scallan and V. H. Huxley, "In vivo determination of collecting lymphatic vessel permeability to albumin: A role for lymphatics in exchange," *The Journal of Physiology*, vol. 588, pp. 243–254, 1 2010. DOI: `doi.org/10.1113/jphysiol.2009.179622`.

[138] V. H. Huxley and J. P. Scallan, "Lymphatic fluid: Exchange mechanisms and regulation," *The Journal of Physiology*, vol. 589, pp. 2935–2943, 12 2011. DOI: `doi.org/10.1113/jphysiol.2011.208298`.